

# **Controls on stable iron isotope variations in magmatic systems**

**Significance of mineral-melt isotopic fractionation  
in experiments and nature**

Von der Naturwissenschaftlichen Fakultät  
der Gottfried Wilhelm Leibniz Universität Hannover

zur Erlangung des Grades eines

DOKTORS DER NATURWISSENSCHAFTEN

Dr. rer. nat.

genehmigte Dissertation

von

Dipl.-Geow. Jan Arne Schübler

geboren am 19.05.1979 in Stuttgart

2008

Referent: Prof. Dr. Harald Behrens (Leibniz Universität Hannover)

Korreferent: Prof. Dr. Jochen Hoefs (Georg-August-Universität Göttingen)

Mitglieder der Prüfungskommission:

Prof. Dr. Jürgen Böttcher (Vorsitzender)

Prof. Dr. Harald Behrens

Prof. Dr. Jochen Hoefs

Prof. Dr. Friedhelm von Blanckenburg

Tag der Promotion: 19.02.2008

## Erklärung zur Dissertation

Hierdurch versichere ich, dass ich die Dissertation selbstständig verfasst und alle benutzten Hilfsmittel und Quellen sowie evtl. zur Hilfeleistung herangezogene Institutionen vollständig angegeben habe. Die Dissertation wurde nicht schon als Diplomarbeit oder ähnliche Prüfungsarbeit verwendet.

Hannover, den 06.12.2007

Jan A. Schübler

„Until only a few years, I would have never have imagined that a volume on the stable isotope geochemistry of elements like Mg, Fe or Cu would be written. In fact, a comic book of blank pages entitled „The Stable Isotope Geochemistry of Fluorine“ would have been a more likely prospect.”

James R. O’Neil, University of Michigan, Ann Arbor, USA

Foreword to *Geochemistry of Non-Traditional Stable Isotopes*,  
*Reviews in Mineralogy & Geochemistry*, 2004, Vol. 55

„Die Zeit ist immer reif, es fragt sich nur, wofür.“

François Charles Mauriac (1885-1970)  
*Nobel Prize winner for literature in 1952*

## DANKSAGUNG

Diese Arbeit wurde am Institut für Mineralogie der Leibniz Universität Hannover unter der Leitung von Dr. Ronny Schönberg und Prof. Dr. Harald Behrens durchgeführt. Ihnen möchte ich für die Initiierung des DFG-Projekts (Scho-1071/1-1&2) danken und für die Möglichkeit diese Arbeit durchzuführen. Ihre intensive Betreuung und Führung war mir stets eine große Hilfe. Neben zahlreichen anderen fachlichen Kompetenzen vermittelten sie mir vor allem die die Fähigkeit zur kritischen und trotzdem offenen Herangehensweise an wissenschaftliche Problemstellungen und Ergebnisse. Sehr dankbar bin ich auch für ihr Vertrauen in mich und die große Freiheit, eigenständig zu arbeiten. Prof. Dr. Jochen Hoefs danke ich für die Übernahme des Korreferats. Außerdem gilt mein Dank den Mitgliedern der Prüfungskommission, Prof. Dr. Jürgen Böttcher (Vorsitzender), Prof. Dr. Harald Behrens, Prof. Dr. Jochen Hoefs und Prof. Dr. Friedhelm von Blanckenburg.

Thanks to Prof. Dr. Olgeir Sigmarsson for generously providing samples from the Hekla volcano and for sharing his expertise on Hekla. Many thanks also to Dr. Jérôme Chmeleff and Dr. Severine Mouné for inspiring discussions about Icelandic volcanism. I gratefully acknowledge discussions and helpful comments on early versions of individual chapters in this thesis by Dr. Ronny Schönberg, Prof. Dr. Harald Behrens, Prof. Dr. Friedhelm von Blanckenburg, Dr. Roman Botcharnikov, Dr. Valeria Misiti, Dr. Franck Poitrasson, Prof. Dr. Edwin Schauble, Prof. Dr. Clark Johnson, Dr. Veniamin Polyakov, Dr. Roberto Moretti and Dr. Mathieu Roskosz.

Dr. Frank Melcher, Dr. Thomas Oberthür und U. Vetter danke ich für die Bereitstellung der Sulfidmineral-Proben und ihre Diskussionsbereitschaft. I am grateful to Dr. Roman Botcharnikov, Dr. Francesco Vetere, Dr. Valeria Misiti and Dr. Carmela Freda for supply of experimental samples for Fe redox analyses. Danke an die „iron girls“ Claudia Thürnagel und Anna Wegorzewski für ihre zuverlässige Unterstützung bei den Fe redox Analysen.

Danke an Prof. Dr. Francois Holtz, Dr. Renat Almeev, Dr. Jürgen Koepke, Prof. Dr. Marcus Nowak und Prof. Dr. Andreas Pack für ihr Interesse und neue Impulse. Mein Dank gilt außerdem Dr. Thorsten Gesing für die freundliche Unterstützung bei den Röntgenmessungen und insbesondere Dr. Ingo Horn für seine enthusiastische Unterstützung am *Laser*. Ich danke auch Sara Fanara und Henrike Baumgarten für *KFT*-Messungen. Großen Dank an Otto Diedrich für exzellente lichtgeschwindigkeitsnahe Dünnschliffpräparation. Für die technische Unterstützung danke ich den Mitarbeitern der Werkstatt, insbesondere Willi Hurkuck und Bettina Aichinger.

Vielen Dank an Francesco, Piero und Jérôme (Franz Ohse) für die tolle Bürogemeinschaft (It was fun!). Ganz besonders danke ich Grit „femtosecond“ Steinhöfel für so manche lange Abende am *Laser* und die zahlreichen wissenschaftlich-isotopisch-philosophischen Gespräche. Für die lustige Atmosphäre im und außerhalb des *clean lab* danke ich Sonja Zink, Alexandra Tangen, Prof. Dr. Michael Staubwasser, Monika Gülke, Kevin Norton und insbesondere Hella Wittmann, meiner langjährigen Mitstreiterin in den Geowissenschaften in Hannover (8 Jahre!). Danke auch an Dr. Francesco Vetere, Dr. Piero DelGaudio, Dr. Sandrin Feig, Holger Strauß, Jan Stelling, Kai Spickenbohm, Oliver Beermann und Sarah Cichy für Spaß im Hochdrucklabor.

Das beständige Engagement von Friedhelm, Harald und Ronny für eine motivierende und freundschaftliche Atmosphäre im Institut (z.B. durch Organisation von Seminaren und anderen Aktivitäten) habe ich stets sehr begrüßt. Ihnen und den anderen *Isos* und *Petros* danke ich für die zahlreichen „Seminare“ im *Klein Kröpke* und die leichten Diskussionen über schwere Isotope. Ein universelles Dankeschön gilt allen Mitarbeitern des Instituts für Mineralogie für die angenehme Arbeitsatmosphäre während meiner Zeit am Institut. Es ist fast als hätte ich gestern begonnen. Die Zeit verging wie im Flug!

Das größte Dankeschön geht an meine Familie (Schübler und Deutscher), insbesondere an meine Frau Stefanie für ihre kontinuierliche Unterstützung und Geduld und an meinen Sohn Luca für sein Lächeln.

# Contents

Abstract .....	I
Zusammenfassung.....	III
I. Introduction .....	1
I.I. Aim of the study and structure of the thesis.....	1
I.II. Iron in magmas.....	3
I.III. Stable iron isotopes.....	6
I.III.I. Stable isotope fractionation theory.....	7
I.III.II. Iron isotope variations in nature and experiment.....	13
Chapter 1. Oxidation state of iron in hydrous phono-tephritic melts.....	25
Abstract .....	25
1.1. Introduction.....	26
1.2. Experimental methods.....	28
1.3. Analytical methods .....	32
1.3.1 Electron microprobe analysis.....	32
1.3.2. Ferrous iron analyses .....	33
1.4. Results.....	40
1.4.1. Redox state of iron .....	42
1.5. Discussion.....	45
1.5.1. Influence of oxygen fugacity and dissolved water on the speciation of iron.....	45
1.5.2. Effect of temperature and pressure on the redox state of iron .....	50
1.6. Concluding remarks .....	53

Chapter 2. The experimental calibration of the iron isotope fractionation factor between pyrrhotite and peralkaline rhyolitic melt.....	54
Abstract.....	54
2.1. Introduction .....	55
2.2. Experimental methods .....	57
2.2.1. Starting materials.....	58
2.2.1.1. Natural pyrrhotite samples.....	58
2.2.1.2. Synthetic peralkaline, rhyolitic glass.....	59
2.2.1.3. <sup>57</sup> Fe enriched glasses.....	60
2.2.2. Experimental design .....	61
2.2.2.1. Kinetic tracer experiments.....	61
2.2.2.2. Isotope exchange experiments.....	61
2.2.2.3. Crystallisation experiments .....	62
2.2.2.4. Run conditions.....	63
2.2.2.5. Characterisation of run products.....	64
2.2.3. Isotope analysis.....	64
2.2.3.1. Phase separation.....	64
2.2.3.2. Mass spectrometry and data presentation.....	65
2.3. Results .....	66
2.3.1. Isotope exchange kinetics.....	73
2.3.2. Isotope exchange experiments.....	75
2.3.3. Crystallisation experiments .....	77
2.4. Discussion.....	79
2.4.1. Stability of pyrrhotite.....	79
2.4.2. Iron isotope fractionation.....	80
2.4.2.1. Kinetic or equilibrium isotope fractionation?.....	81
2.4.2.2. Effect of temperature on iron isotope fractionation.....	82
2.4.3. Mechanisms of isotope fractionation.....	83
2.4.4. Applications to natural systems – perspectives .....	86
2.5. Conclusions .....	88

Chapter 3. Iron and lithium isotope systematics of the Hekla volcano, Iceland – Evidence for stable Fe isotope fractionation during magma differentiation.....	90
Abstract .....	90
3.1. Introduction.....	91
3.2. Geological background and sample selection.....	94
3.3. Analytical methods .....	98
3.3.1. Sample preparation and purification.....	98
3.3.2. Mass spectrometry .....	100
3.3.2.1. Fe isotope analyses.....	100
3.3.2.2. Li isotope analyses .....	102
3.4. Results.....	106
3.4.1. Iron isotope compositions .....	106
3.4.2. Lithium concentrations and isotope compositions.....	109
3.5. Discussion.....	111
3.5.1. Behavior of Li and Li isotopes during fractional crystallisation .....	111
3.5.2. Behaviour of Li and Fe and their isotopes during fluid exsolution .....	112
3.5.2.1. Constraints from Li and Fe concentrations .....	113
3.5.2.2. Constraints from Li isotopes on the significance of fluids during magma differentiation.....	114
3.5.3. Fe isotope fractionation through crystal fractionation .....	116
3.6. Conclusions.....	122
References.....	123



Appendix A1 to chapter 1 .....	141
A1.1. Reagents used for wet-chemical colorimetric iron termination.....	141
A1.2. Water solubility in phono-tephritic melts .....	142
Appendix A2 to chapter 2 .....	144
A2.1. Details on the starting materials.....	144
A2.2. Characterisation of the run products.....	146
A2.3. Phase separation and corrections applied to the measured isotopic compositions.	147
A2.4. Iron isotope compositions of natural sulphides .....	153
Appendix A3 to chapter 3 .....	157
A3.1. Iron isotope analyses of reference materials.....	157
A3.2. Lithium isotope analytics.....	157
A3.3. Iron isotope fractionation between magnetite and rhyolitic melt .....	160
Lebenslauf.....	165

## Abstract

Iron is the forth-most abundant element in the Earth's crust and is an ubiquitous constituent of magmas. In nature, iron almost exclusively exists in the two oxidation states of ferrous ( $\text{Fe}^{2+}$ ) and ferric ( $\text{Fe}^{3+}$ ) iron both of which can coexist in melts, minerals, and fluids. This, for example, makes iron speciation, expressed as the  $\text{Fe}^{2+}/\Sigma\text{Fe}$  ratio, a valuable tool to depict changes in the oxidation state of evolving magmatic systems. Furthermore, differences in the bonding environment of ferrous and ferric iron lead to mass-dependent fractionation of stable iron isotopes between different phases. However, to use such shifts in the relative abundances of iron isotopes between two species or materials as geochemical tracer for natural processes, the nature of these processes (i.e., equilibrium or kinetic) and the magnitude of isotope fractionation they cause need to be determined. To date, little is known about the nature and extent of iron isotope fractionation in magmatic systems. As a consequence, the objective of this thesis is to investigate the parameters controlling iron isotope fractionation in magmatic systems by laboratory experiments and analyses of natural samples.

An improved analytical method for the determination of the Fe speciation in geological materials was applied to investigate the Fe redox state in hydrous ultrapotassic (phono-tephritic) melts, coexisting with mixed  $\text{H}_2\text{O}-\text{CO}_2$  fluids, at 1200 and 1250°C and pressures from 50 to 500 MPa. The oxygen fugacity ( $f\text{O}_2$ ), relative to the Ni/NiO oxygen buffer ( $\Delta\text{NNO}$ ), was systematically varied from  $\Delta\text{NNO}-2.9$  to  $\Delta\text{NNO}+2.6$  in  $\log f\text{O}_2$ , with associated variations in water activity from 0.05 to 1. The  $\text{Fe}^{2+}/\Sigma\text{Fe}$  ratios of the experimental glasses range from 0.41 to 0.85 and are negatively correlated with oxygen fugacity, water activity, and – less pronounced – with the amount of dissolved water as a chemical component in the melt, i.e., leaving all other parameters such as pressure, temperature or  $f\text{O}_2$  constant. The results are consistent with commonly used empirical and thermodynamic models.

A prerequisite for the interpretation of natural Fe isotope variations is knowledge of Fe isotope fractionation factors between different phases in magmatic systems. Therefore, a first experimental study was conducted to determine the equilibrium iron isotope fractionation between pyrrhotite ( $\text{Fe}_{1-x}\text{S}$ ) and peralkaline rhyolitic melt at magmatic conditions. Experiments were performed at 500 MPa and temperatures between 840 and 1000°C. The results show that isotopically light iron is preferentially incorporated in pyrrhotite relative to the silicate melt. No temperature dependence of the fractionation factor was found, within experimental and analytical precision. An average fractionation factor of  $\Delta^{56/54}\text{Fe}_{\text{pyrrhotite-melt}} = 0.35 \pm 0.04\text{‰}$  (2SE,  $n=13$ ) was determined for the investigated temperature range. Kinetic experiments using a  $^{57}\text{Fe}$ -enriched tracer indicate that this value represents isotopic equilibrium. Predictions of Fe isotope fractionation between FeS and ferric iron-dominated silicate minerals are consistent with the experimental results, indicating that the marked contrast in both ligand and redox state of iron control the isotope fractionation between pyrrhotite and silicate melt. Consequently, the determined fractionation factor is representative for the specific  $\text{Fe}^{2+}/\Sigma\text{Fe}$  ratio of the peralkaline rhyolitic melt of  $0.38 \pm 0.02$ . At higher  $\text{Fe}^{2+}/\Sigma\text{Fe}$  ratios a smaller fractionation factor is expected. Consistent with the experimental results, analyses of natural sulphide minerals,

mainly pyrrhotites, from various ore deposits indicate that magmatic sulphides tend to be less fractionated (relative to mafic rocks) than sulphides of hydrothermal and metamorphic origin. This first observation opens the possibility that Fe isotopes may serve to identify sulphide ore genesis.

To study the behaviour of Fe isotopes during magma differentiation, the volcanic evolution of Hekla, Iceland, was traced by Fe isotopes. It was found that during differentiation of dacitic magma towards rhyolitic composition the  $\delta^{56/54}\text{Fe}_{\text{IRMM-014}}$  values increase successively from 0.051‰ to 0.168‰ ( $\pm 0.021\%$ , 2SD external reproducibility). No analytically resolvable Fe isotope fractionation was induced by crystal fractionation of basaltic to basaltic andesite magmas. Lithium concentrations and isotope compositions measured in Hekla's rocks do not indicate extensive fluid exsolution during the volcanic evolution. Hence, the heavy Fe isotope composition of the dacites and rhyolites can be predominately attributed to fractional crystallisation. Iron isotope fractionation between magnetite and peralkaline rhyolitic melt was determined experimentally at 100 and 200 MPa and 800°C fractionation ( $\Delta^{56/54}\text{Fe}_{\text{magnetite-melt}} \approx -0.2\%$ ). Hence, removal of isotopically light Fe from the evolving melt controlled by titanomagnetite crystallisation and subsequent crystal settling in the magma chamber is a possible mechanism to form the isotopically heavy dacites and rhyolites at Hekla. Iron isotope analyses on single samples from other Icelandic volcanoes (Torfajökull, Vestmannaeyjar) confirm heavy Fe isotope enrichment in evolving magmas. The results of this study suggest that the iron isotope composition of the crust can be slightly modified by magmatic processes.

Keywords: stable iron isotopes, iron oxidation state, silicate melt, pyrrhotite, magma differentiation, Hekla volcano

## Zusammenfassung

Eisen ist das viert-häufigste Element in der Erdkruste und ein allgegenwärtiger Bestandteil von Magmen. In der Natur kommt Eisen fast ausschließlich in den beiden Oxidationsstufen  $\text{Fe}^{2+}$  und  $\text{Fe}^{3+}$  vor, die gemeinsam in Schmelzen, Mineralen und Fluiden vorkommen. Dies macht die Fe-Speziation, ausgedrückt als  $\text{Fe}^{2+}/\Sigma\text{Fe}$ -Verhältnis, zu einem wertvollen Werkzeug um, zum Beispiel, Veränderungen des Oxidationszustands sich entwickelnder magmatischer Systeme zu bestimmen. Außerdem führen Unterschiede in der Bindungsumgebung zweiwertigen und dreiwertigen Eisens zwischen verschiedenen Phasen zu massenabhängiger Fraktionierung stabiler Eisenisotope. Um diese Verschiebungen in der relativen Häufigkeit der Eisenisotope als geochemischen Tracer nutzen zu können, müssen sowohl die Art (kinetisch oder im Gleichgewicht) und die Größe der Isotopenfraktionierung bestimmt werden. Derzeit ist nur wenig über die Art und Größe der Eisenisotopenfraktionierung in magmatischen Systemen bekannt. Aus diesem Grund ist das Ziel dieser Arbeit die Erforschung der Parameter, welche die Eisenisotopenfraktionierung in magmatischen Systemen kontrollieren, insbesondere durch experimentelle Untersuchungen im Labor und Isotopenmessungen an natürlichen Proben.

Eine verbesserte analytische Methode zur Bestimmung der Fe-Speziation in geologischen Materialien wurde angewendet, um den Fe-Oxidationszustand in wasser- und kaliumhaltigen (phono-tephritischen) Schmelzen, die mit  $\text{H}_2\text{O}$ - $\text{CO}_2$ -Fluiden koexistieren, bei 1200 und 1250°C und 50 bis 500 MPa zu untersuchen. Die Sauerstoff fugazität ( $f\text{O}_2$ ), relativ zum Ni/NiO-Sauerstoff-Puffer ( $\Delta\text{NNO}$ ), wurde systematisch von  $\Delta\text{NNO}-2.9$  bis  $\Delta\text{NNO}+2.6$  (in  $\log f\text{O}_2$ ) variiert, in Verbindung mit Variationen in der Wasseraktivität von 0.05 bis 1. Die  $\text{Fe}^{2+}/\Sigma\text{Fe}$ -Verhältnisse der experimentellen Gläser reichen von 0.41 bis 0.85 und zeigen eine negative Korrelation mit der Sauerstoff fugazität, der Wasseraktivität und – weniger deutlich ausgeprägt – mit dem Gehalt an gelöstem Wasser, in Bezug auf Wasser als chemische Komponente in der Schmelze, d.h. wenn alle anderen Parameter wie Druck, Temperatur und  $f\text{O}_2$  konstant sind. Diese Ergebnisse sind konsistent mit den im Allgemeinen verwendeten empirischen und thermodynamischen Modellen.

Eine Grundvoraussetzung für die Interpretation natürlicher Eisenisotopenvariationen ist die Kenntnis von Isotopenfraktionierungsfaktoren zwischen verschiedenen Phasen in magmatischen Systemen. Deshalb wurde eine erstmalige experimentelle Studie zur Bestimmung der Gleichgewichts isotopenfraktionierung zwischen Pyrrhotin ( $\text{Fe}_{1-x}\text{S}$ ) und Silikatschmelze bei magmatischen Bedingungen durchgeführt. Die Experimente erfolgten bei 500 MPa und Temperaturen zwischen 840 und 1000°C. Die Ergebnisse zeigen, dass relativ zur Silikatschmelze bevorzugt isotopisch leichteres Eisen in Pyrrhotin eingebaut wird. Im Rahmen der analytischen und experimentellen Präzision wurde keine Temperaturabhängigkeit des Fraktionierungsfaktors im untersuchten Temperaturbereich gefunden. Ein durchschnittlicher Fraktionierungsfaktor von  $\Delta^{56/54}\text{Fe}_{\text{pyrrhotite-melt}} = 0.35 \pm 0.04\%$  (2SE,  $n=13$ ) wurde für diesen Temperaturbereich bestimmt. Kinetische Experimente welche mit einem  $^{57}\text{Fe}$  Tracer angereichert wurden zeigen, dass dieser Wert isotopischem Gleichgewicht entspricht. Vorhersagen zur Eisenisotopenfraktionierung zwischen FeS und  $\text{Fe}^{3+}$ -dominierten Silikatmineralen sind konsistent mit den experimentellen Ergebnissen, was darauf hindeutet, dass der deutliche Unterschied in den

Liganden und dem Oxidationszustands des Eisens die Eisenisotopenfraktionierung zwischen Pyrrhotin und Silikatschmelze kontrollieren. Folglich, ist der bestimmte Fraktionierungsfaktor repräsentativ für das spezifische  $\text{Fe}^{2+}/\Sigma\text{Fe}$ -Verhältnis in der peralkalinen rhyolitischen Schmelze von  $0.38 \pm 0.02$ . Bei höheren  $\text{Fe}^{2+}/\Sigma\text{Fe}$ -Verhältnissen, ist ein kleinerer Fraktionierungsfaktor zu erwarten. Konsistent mit den experimentellen Ergebnissen, ergaben Analysen natürlicher Sulfidminerale, hauptsächlich Pyrrhotine, aus verschiedenen Erzlagerstätten, dass magmatisch gebildete Sulfide tendenziell eine geringe eisenisotopische Fraktionierung (relativ zu mafischen Gesteinen) aufweisen als solche hydrothermalen oder metamorphen Ursprungs. Diese ersten Beobachtungen eröffnen die Möglichkeit, dass Eisenisotope unter Umständen zur Identifizierung der Genese von sulfidischen Erzlagerstätten dienen könnten.

Um das Verhalten von Eisenisotopen während der Magmendifferentiation zu untersuchen, wurde die vulkanische Entwicklung des Hekla-Vulkans, Island, eisenisotopisch verfolgt. Die Ergebnisse zeigen, dass die  $\delta^{56/54}\text{Fe}_{\text{IRMM-014}}$ -Werte während der Differentiation dazitischer Magmen zu rhyolitischer Zusammensetzung sukzessive von 0.051‰ auf 0.168‰ ( $\pm 0.021\%$ , 2SD externe Reproduzierbarkeit) ansteigen. Durch fraktionierte Kristallisation von basaltischen zu basaltisch-andestischen Magmen wurde keine analytische auflösbare Eisenisotopenfraktionierung verursacht. Die in den Hekla-Gesteinen gemessenen Lithium-Konzentrationen und -Isotopenzusammensetzungen deuten nicht auf extensive Fluid-Entmischung während der vulkanischen Entwicklung hin. Infolgedessen kann die schwere Eisenisotopenzusammensetzung der Dazite und Rhyolite überwiegend auf fraktionierte Kristallisation zurückgeführt werden. Die Eisenisotopenfraktionierung zwischen Magnetit und peralkaliner rhyolitischer Schmelze wurde experimentell bei 800°C und 100 bzw. 200 MPa bestimmt ( $\Delta^{56/54}\text{Fe}_{\text{magnetite-melt}} \approx -0.2\%$ ). Folglich ist die Entfernung von isotopsch leichtem Eisen aus der Schmelze, kontrolliert durch Kristallisation von Titanomagnetit und darauf folgendem Absinken der Kristalle in der Magmakammer, ein möglicher Mechanismus, um die isotopisch schweren Dazite und Rhyolite des Hekla-Vulkans zu bilden. Eisenisotopenanalysen einzelner Proben von anderen isländischen Vulkanen (Torfajökull, Vestmannaeyjar) bestätigen eine Anreicherung isotopisch schweren Eisens in differenzierten Magmen. Die Ergebnisse dieser Arbeit legen nahe, dass die Eisenisotopenzusammensetzung der Erdkruste durch magmatische Prozesse leicht modifiziert werden kann.

Schlagworte: stabile Eisenisotope, Eisen-Oxidationszustand, Pyrrhotin, Magmendifferentiation, Vulkan Hekla

## **I. Introduction**

### **I.I. AIM OF THE STUDY AND STRUCTURE OF THE THESIS**

Iron is the the second-most abundant element (after oxygen) on Earth (Allegre et al., 2001). In the Earth's crust, iron is the fourth-most abundant element, after O, Si and Al (Wedepohl, 1995), and is an ubiquitous constituent of magmas in nature. Iron occurs in different oxidation states and has various bonding environments. This could lead to mass-dependent fractionation of stable iron isotopes between different phases. To date, little is known on stable iron isotope fractionation in magmatic systems. The main objective of this study is to explore the mechanisms that govern iron isotope fractionation in crustal magmatic systems. Therefore, experiments at high temperature and pressure were performed to investigate the controlling parameters, such as bonding environment and oxidation state of iron, on iron isotope fractionation between minerals and silicate melts. Furthermore, the behaviour of iron isotopes during magma differentiation was studied by analyses of natural rock samples from the Hekla volcano, Iceland.

This thesis is subdivided into three main chapters preceded by an introduction section. Each chapter contains separate introduction and conclusion sections and is aimed at being conclusive without the context of other chapters. Manuscripts that represent the three chapters of this thesis are either already published (chapter 2) or submitted for publication (chapters 1 and 3) in international journals. All experimental and analytical work as well as the interpretation of the results presented in this thesis was done by me unless stated otherwise.

The introduction section gives background information on the chemical behaviour and speciation of iron in magmas. Principles of stable isotope fractionation theory are briefly reviewed and the state of iron isotope research is presented based on a concise review of the recent literature.

Chapter 1 gives a detailed description of the analytical method for the determination of the Fe redox state in geological materials. The improvements of this method were developed during this study and tested by an experimental investigation on the influence of water activity and oxygen fugacity on the redox state of iron in hydrous phono-tephritic melts. The Fe redox measurements were done on well characterised samples previously used for a water and CO<sub>2</sub> solubility study (Misiti et al., 2007). The results are compared to the most widely used empirical and thermodynamic models. This work was accepted for publication in *American Mineralogist* (Schuessler J. A., Botcharnikov R. E., Behrens H., Misiti V., and Freda C., 2007, Oxidation state of iron in hydrous phonotephritic melts. *American Mineralogist*).

Chapter 2 presents the experimental calibration of the iron isotope fractionation factor between pyrrhotite (Fe<sub>1-x</sub>S) and a hydrous peralkaline silicate melt at magmatic conditions. This first experimental iron isotope study in a mineral-melt system discusses the mechanisms controlling iron isotope fractionation during iron sulphide crystallisation. This work was published as an article in *Geochimica et Cosmochimica Acta* (Schuessler J. A., Schoenberg R., Behrens H., and von Blanckenburg F., 2007, The experimental calibration of the iron isotope fractionation factor between pyrrhotite and peralkaline rhyolitic melt. *Geochimica et Cosmochimica Acta* 71(2), 417-433).

Chapter 3 presents a case study on well-characterised natural samples (previously investigated in other geochemical studies) from the Hekla volcano, Iceland. The aim was to investigate the behaviour of iron isotopes during magma evolution in combination with an

experimental approach on iron isotope fractionation between magnetite and silicate melt. Different mechanisms such as fractional crystallisation and magma/fluid interaction that may explain the Fe isotope variations observed in the volcanic eruption products are discussed. To unravel the influence of magma/fluid interaction of the Helka volcanic system on the Fe isotope composition of the evolving magmas, this study was complemented with analyses of Li concentrations and isotopes. This work was accepted for publication (pending minor revisions) in *Chemical Geology* (Schuessler J. A., Schoenberg R., and Sigmarsson O., 2007, Iron and lithium isotope systematics of the Hekla volcano, Iceland - Evidence for stable Fe isotope fractionation during magma differentiation. *Chemical Geology - Special Issue: Non-traditional stable isotope applications in high-temperature geochemistry*).

### I.II. IRON IN MAGMAS

Iron has a wide range of concentrations in natural magmas. Mafic volcanic rocks have generally higher total iron contents (total iron content comprising ferric and ferrous iron is expressed as  $\Sigma\text{FeO}$ ) compared to silicic ones (Fig. I.I). This reflects the processes governing their genesis and evolution and the chemical composition of their sources. On Earth, iron occurs commonly in three oxidation states, 0 (metallic), +2, and +3. Whereas ferrous iron is the dominant species in the Earth's mantle (Wood, 1991), the crust contains various proportions of ferric and ferrous iron (Frost, 1991). In particular, volcanic rocks show a wide range in  $\text{Fe}^{2+}/\Sigma\text{Fe}$  ratios (Fig. I.II), whereas basalts (mantle-derived melts) display a more narrow range towards ferrous Fe rich compositions compared to more evolved silicic rocks. These variations reflect the prevailing redox conditions during magma genesis and evolution.



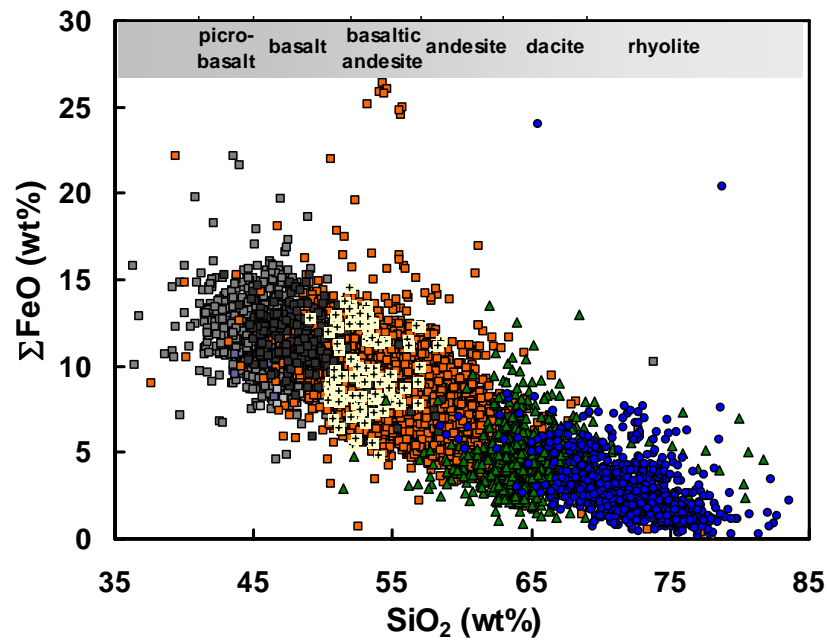


Figure I.I. Total iron content of volcanic rocks as function of  $\text{SiO}_2$  contents. Compiled from the GEOROC database (<http://georoc.mpch-mainz.gwdg.de/georoc/>) representing a total of 9603 whole rock analyses of various volcanic rocks. Symbol colors refer to different rock types as identified in Figure I.II.

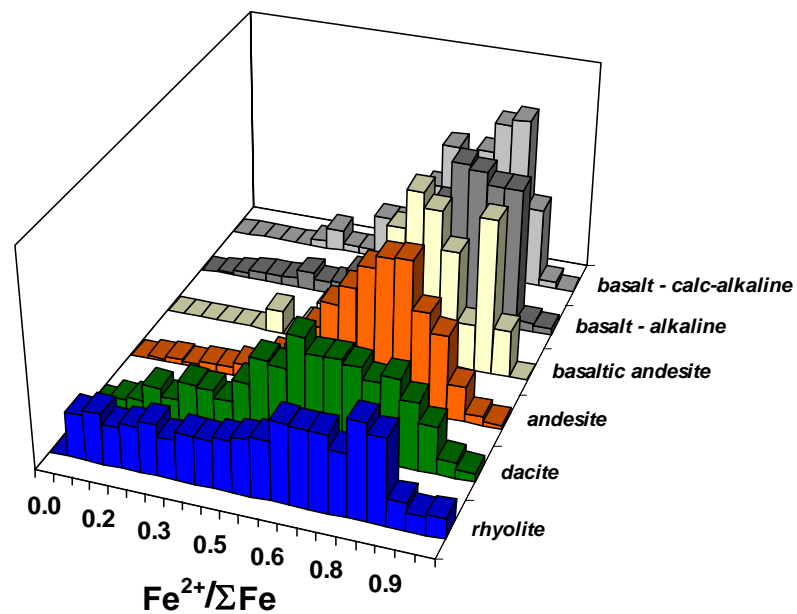


Figure I.II. Frequency distribution of the iron redox state in various volcanic rocks. Compilation of 9274 whole rock analyses from the GEOROC database (<http://georoc.mpch-mainz.gwdg.de/georoc/>).

The redox state of iron in the melt is related to the oxygen fugacity ( $f\text{O}_2$ ) which is a thermodynamic expression of the partial pressure ( $p\text{O}_2$ ) of oxygen in the system ( $f\text{O}_2 = \gamma\text{O}_2 \cdot p\text{O}_2$ , where  $\gamma\text{O}_2$  is the activity coefficient of  $\text{O}_2$ ). The present terrestrial atmosphere has

$fO_2 \approx pO_2 \approx 0.2$  bar. In the Earth's interior at high pressures and temperatures  $fO_2$  values are much lower and the Fe redox state is controlled via the reaction  $Fe(II)O_{\text{melt}} + \frac{1}{4} O_{2 \text{ gas}} = Fe(III)O_{1.5 \text{ melt}}$ . The equilibrium constant of the reaction can be expressed as  $K = a_{Fe(III)O_{1.5}} / ( a_{Fe(II)O} \cdot (fO_2)^{1/4} )$  where  $a$  denotes the activity of the respective components in the melt.  $K$  depends on temperature, pressure and melt composition. Oxygen fugacity is commonly expressed relative to a buffer, e.g.  $\Delta NNO$  ( $Ni + O = NiO$ ). Oxygen fugacities relevant for terrestrial magmas comprise a range of about eight log units, i.e. from about  $\Delta NNO-3$  to  $\Delta NNO+5$  (Carmichael, 1991). The valency of iron has strong influence on the physical and chemical properties of magmas, such as viscosity (e.g., Liebske et al., 2003; Vetere et al., 2006) and the stability of Fe-bearing minerals, respectively. The structural incorporation of iron in silicate melts also depends on the speciation. Ferrous iron is predominantly tetrahedrally coordinated by oxygen. However, some  $Fe^{3+}$  may also be present in five-fold or six-fold coordination (Mysen and Richet, 2005). The coordination of  $Fe^{2+}$  in silicate melts is still debated. A continuous distribution of  $Fe^{2+}$  environments from four-fold to six-fold coordination in silicate melts has been suggested (e.g., Seifert et al., 1979; Virgo and Mysen, 1985; Rossano et al., 2000; Farges et al., 2004; Wilke et al., 2006). The melt composition also plays an important role on the structural incorporation of iron. For example, in alkali-rich melts a stabilisation of tetrahedrally coordinated ferric iron by charge-balancing  $K_2O$  is suggested (Dickenson and Hess, 1986; Kilinc et al., 1983; Kress and Carmichael, 1988; Sack et al., 1980). This structural variability of iron in silicate melts and different minerals very likely influences the iron isotope distribution in magmas as well. This is because equilibrium stable isotope fractionation is sensitive to differences in the bonding environment that is linked to the redox state, the coordination and the bond character (ionic/covalent).

## I.III. STABLE IRON ISOTOPES

The investigation of stable isotope variations of H, C, O, N in nature has a long tradition (e.g., Valley and Cole, 2001, and references therein). Studies on these isotopic systems provided important constraints on various problems, such as the evolution of the solar system and the origin of life. On Earth stable isotopes were applied to thermometry, fingerprinting geochemical pathways and mass transfers for a better understanding of crust and mantle evolution, climate change and exploration of natural resources, for example.

The magnitude of maximally possible stable isotope fractionation depends (amongst other factors) on the mass of an element and the mass difference between the two isotopes of consideration. Hence, relatively large isotopic variations of tens to hundreds of permil are observed in nature for isotope systems of light elements such as  $^2\text{H}/^1\text{H}$ ,  $^7\text{Li}/^6\text{Li}$ ,  $^{18}\text{O}/^{16}\text{O}$  that have large relative mass differences of about 100%, 14%, and 11%, respectively). For heavier elements, such as iron with a mass difference of about 4% in  $^{56}\text{Fe}/^{54}\text{Fe}$ , natural isotopic variations are much smaller (<4‰) and therefore analytically more challenging. With the advent of new analytical methods, large portions of the Periodic Table are now accessible to stable isotope studies. High precision analyses by double spike thermal ionisation mass spectrometry (TIMS) (e.g., Beard and Johnson, 1999; Bullen et al., 2001), and in particular by multi collector inductively coupled plasma mass spectrometry (MC-ICP-MS) allow access to a new field of stable isotope geochemistry. *In situ* techniques, such as secondary ion mass spectrometry (SIMS) (e.g., Woodhead, 2006) and laser ablation coupled to MC-ICP-MS (e.g., Horn and von Blanckenburg, 2007) for these heavy stable isotope systems were also developed. This new field of *non-traditional stable isotope geochemistry*

has rapidly evolved during the past decade and isotopic variations of more than 20 elements, in particular of transition metals, can now be studied (Johnson et al., 2004). Variation in stable isotope compositions of Mg, Ca, Sr, Ti, Cr, Mo, Fe, Cu, Zn, Ag, Cd, Hg, Tl, B, Li, Si, Ge, Se, Sb, Te, Cl and Br have been reported (see Anbar and Rouxel, 2007, and references therein). Understanding the mechanisms that control the isotopic variations of these *new* systems is a prerequisite to enable application to problems in nature. Therefore, theoretical and experimental determination of fractionation factors are needed in addition to studies of isotope variations of natural samples.

### I.III.I. Stable isotope fractionation theory

Mass dependent stable isotope fractionation during chemical reactions is a fundamental thermodynamic/quantum mechanical phenomenon. It is driven by differences in the vibrational energies of molecules and crystals upon isotopic substitution resulting in different zero point energies and strengths of chemical bonds (Bigeleisen and Mayer, 1947; Urey, 1947). The theory has been reviewed frequently in the geochemical literature (e.g., Criss, 1999; Chacko et al., 2001; Hoefs, 2004; Schauble, 2004). Based on these literature sources, the principles of isotope fractionation are described in the following, with particular emphasis to iron isotopes.

We consider a simple isotope exchange reaction ( ${}^x A + {}^y B = {}^x B + {}^y A$ ) of two isotopes  $x$  and  $y$  between the two phases A and B. In the case of iron, the relative abundances of the two isotopes  ${}^{54}\text{Fe}$  and  ${}^{56}\text{Fe}$  in the two phases can be expressed in terms of an isotope ratio,  $({}^{56}\text{Fe}/{}^{54}\text{Fe})_A$  and  $({}^{56}\text{Fe}/{}^{54}\text{Fe})_B$ , respectively. The equilibrium constant for this reaction is

$$K_{eq} = \frac{({}^y A)({}^x B)}{({}^y B)({}^x A)}, \quad (\text{I.I})$$

defined as the quotient of the thermodynamic activities of the products and reactants. Assuming exchange of one atom of iron and ideal mixing of isotopes in both phases (Polyakov, 1993),  $K_{eq}$  is equivalent to the equilibrium isotope fractionation factor  $\alpha$

$$\alpha_{A-B} = \frac{\left( \frac{{}^{56}\text{Fe}}{{}^{54}\text{Fe}} \right)_A}{\left( \frac{{}^{56}\text{Fe}}{{}^{54}\text{Fe}} \right)_B}. \quad (\text{I.II})$$

Analogous to any chemical reaction the equilibrium constant is related to the change in standard state Gibbs free energy,

$$\Delta G_R^0(T,P) = \Delta H_R^0 - T \Delta S_R^0 + \Delta V_R^0 = -RT \ln K_{eq}. \quad (\text{I.II})$$

In principle, the free energy change and the equilibrium constant can be calculated for isotope exchange reactions from thermodynamic data of molar enthalpy ( $\Delta H_R^0$ ), entropy ( $\Delta S_R^0$ ) and volume ( $\Delta V_R^0$ ) as a function of pressure ( $P$ ) and absolute temperature ( $T$ ). However, even if such data on isotopically pure end members would be widely available the changes in  $\Delta G_R^0$  on isotopic substitution would be too small (< a few tens of joules) for precise classical thermodynamic calculations. Therefore, a quantum mechanical approach is required. For most isotope exchange reactions the change in volume and bond structure is negligibly small (except for some light elements), particularly for condensed phases, such as minerals. Then, following  $G = F + PV$ ,  $\Delta G$  of the reaction is equivalent to the Helmholtz free energy ( $\Delta F$ ) and the equilibrium constant is

$$K_{eq} = e^{\left( \frac{-\Delta F}{RT} \right)} \quad (\text{I.III})$$

The temperature dependence of this relation also demonstrates the potential usefulness of isotope fractionation as a geothermometer that has found wide application in geosciences for light stable isotope variations, particularly for those of oxygen (e.g., Valley and Cole, 2001). Specifically,  $\ln K_{eq}$  varies linearly with  $T^{-1}$  if the free energy change is independent of

temperature. In contrast to most cation exchange reactions, where  $\Delta G$  is approximately constant over a specific range of temperatures, the free energy change of isotope exchange reactions varies significantly with  $T$ . Therefore, isotope fractionation often depends on higher orders of inverse temperature ( $T^{-2}$ ).

The energy difference between two substances that differ only in their isotopic composition is a quantum mechanical effect caused by the influence of the mass on the atomic motions in a molecule (frequencies of translations, rotations and vibrations). In a simple diatomic molecule, the vibration of the bond can be approximated by a harmonic oscillator,  $Force = -k_F \cdot x$ , where the force exerted on the atoms is related to the force constant ( $k_F$ ) and the displacement of the atoms ( $x$ ) from the optimal distance, i.e. the minimum potential energy ( $E$ ) that is given by  $E = k_F \cdot x^2/2$ . This function defines a parabola with a minimum potential energy at  $x = 0$ . Quantum theory predicts that at a temperature of absolute zero the potential energy is not equal to the minimum of the potential well. Thus, even when all molecules are in the ground state ( $T = 0$  Kelvin) the vibrational energy (zero point energy = ZPE) has still a quantised level above the minimum of the potential well according to

$$E_{\text{vib}} = \left(n + \frac{1}{2}\right) \cdot h \cdot \Delta\nu, \quad (\text{I.IV})$$

where  $n$  ( $= 0, 1, 2, \dots$ ) corresponds to the energy level (i.e., the quantum number),  $h$  is the Planck's constant and  $\nu$  is the vibration frequency of the bond. The ZPE is equal to the half quantum of vibrational energy ( $E_{\text{vib}}$ ) when  $n = 0$  and is related to the masses of the atoms forming the bond by

$$\nu = \frac{1}{2\pi} \sqrt{\frac{k}{\mu}}, \quad \text{with} \quad \mu = \frac{m_1 \cdot m_2}{m_1 + m_2} \quad (\text{I.V})$$

where  $\mu$  is the reduced mass calculated from the masses ( $m_1$  and  $m_2$ ) of the atoms in the bond. Hence, when heavier isotopes are substituted for lighter ones ZPE decreases and bond

strength increases, while leaving the force constant ( $k$ ) unchanged. Differences in ZPEs between different molecules are the driving force for equilibrium stable isotope fractionation. For more complex molecules (e.g., minerals), with more than one vibrational frequency, the magnitude of isotope fractionation between two substances ( $A$  and  $B$ ) depends on the difference between the sums of vibrational frequencies of each substance that can be approximately described by

$$\Delta ZPE \approx \Delta F \approx \Sigma(\frac{1}{2} h \cdot \nu)_A - \Sigma(\frac{1}{2} h \cdot \nu)_B = \frac{1}{2} h \cdot \Delta \nu. \quad (\text{I.VI})$$

More accurately, the total vibrational energy of a substance, which depends on the masses of the involved isotopes, is determined by partition functions. The partition function ( $Q$ ) is the sum over all energy states taking into account the probabilities of particular states and that molecules are not always in their ground state. This means that a partition function comprises the total energy of atomic motion (translation, rotation, vibration) and is closely related to the Helmholtz free energy of a substance

$$F = -R \cdot T ( \ln(Q_{trans}) + \ln(Q_{rot}) + \ln(Q_{vib}) ) = -R \cdot T \ln( Q_{trans} \cdot Q_{rot} \cdot Q_{vib} ). \quad (\text{I.VI})$$

Therefore, the equilibrium constant (equation I.III) for an isotope exchange reaction between the phases  $A$  and  $B$  becomes

$$\begin{aligned} K_{eq} &= e^{\left( \Sigma \ln(Q_{trans} \cdot Q_{rot} \cdot Q_{vib})_A - \Sigma \ln(Q_{trans} \cdot Q_{rot} \cdot Q_{vib})_B \right)} \\ &= \frac{\prod (Q_{trans} \cdot Q_{rot} \cdot Q_{vib})_A}{\prod (Q_{trans} \cdot Q_{rot} \cdot Q_{vib})_B} \end{aligned} \quad (\text{I.VII})$$

The partition function of an unsubstituted molecule ( $Q$ ) differs from an isotopically substituted one ( $*Q$ ) and the quotient of both gives the partition function ratio  $*Q/Q$ . Then, the isotope fractionation factor  $\alpha_{A-B}$  (equation I.II) of an exchange reaction between phase  $A$  and  $B$  is equal to  $K_{eq}$  (equation I.VII). Urey (1947) derived a relation to link vibrational frequencies, momentums of inertia and molecular masses of isotopically substituted

molecules to calculate equilibrium isotope fractionation factors. When vibrational frequencies are known (from spectroscopic measurements or force-field modelling) and momentums of inertia can be determined from the molecular structure, the equilibrium constant of the isotope exchange reaction (and hence  $\alpha$ ) can be calculated analogous to equation I.I, following

$$\alpha = \frac{(*Q/Q)_A}{(*Q/Q)_B}, \quad (\text{I.VIII})$$

which illustrates (strongly simplified) the approach. Calculated partition function ratios are commonly expressed as  $\beta$ -factors. These are called reduced isotope partition function ratios because each  $Q$  represents the equilibrium constant between the substance of interest and its separated atoms and thus some mass terms in the calculations cancel out. From these  $\beta$ -values isotope fractionation factors between two phases can be conveniently calculated via

$$\alpha_{A-B} = \beta_A / \beta_B \quad \text{or} \quad 1000 \cdot \ln \alpha_{A-B} = 1000 \cdot \ln \beta_A - 1000 \cdot \ln \beta_B. \quad (\text{I.IX})$$

Besides stable isotope fractionation at equilibrium, kinetic isotope fractionation can occur due to differences in reaction rate constants (e.g., reaction  $A \rightarrow B$ ;  $k_R(^{54}\text{Fe}) \neq k_R(^{56}\text{Fe})$ ), i.e., when the rate of isotope exchange is slower than the reaction rate. Such processes can occur due to unequilibrated chemical reactions or unidirectional processes such as evaporation or condensation, rapid crystallisation or diffusion. Kinetic isotope fractionation is driven by higher velocities ( $v$ ) of isotopically lighter molecules relative to heavier ones according to

$$K_E = \frac{1}{2} m \cdot v^2 = \frac{3}{2} k_R \cdot T \quad (\text{I.IX})$$

if their translational kinetic energy ( $K_E$ ) is the same (such as in an ideal gas). Thus, in many kinetic reactions, the light isotopes are concentrates in the reaction products.



Some qualitative predictions governing equilibrium fractionation have been summarised by Schauble (2004):

- The magnitude of isotope fractionation decreases with increasing temperature, approximately with  $1/T^2$ .
- The magnitude of isotope fractionation decreases with increasing element mass and decreasing mass difference between the isotopes, roughly scaling with

$$\frac{m_{heavy} - m_{light}}{m_{heavy} \cdot m_{light}} \approx \frac{\Delta m}{m^2}.$$

- At equilibrium, the heavy isotopes are enriched in the substance where the element of interest is more strongly bound. Bond strength is positively correlated with high oxidation state of the element of interest, presence of highly covalent bonds (small differences in electronegativity between involved elements), low coordination number, low-spin electronic configuration.

To describe iron isotope fractionation quantitatively, the following nomenclature is used. Iron has four stable iron isotopes with the atomic masses 54, 56, 57, and 58, with relative abundances of ~5.845 at%, ~91.754 at%, ~2.1191 at% and ~0.2819 at%, respectively. Iron isotope data are reported in the  $\delta$ -notation, which gives the permil deviation of the isotopic ratio (e.g.,  $^{56}\text{Fe}/^{54}\text{Fe}$  or  $^{57}\text{Fe}/^{54}\text{Fe}$ ) of the sample relative to that of the IRMM-014 standard (Taylor et al., 1992b), e.g.:

$$\delta^{56}\text{Fe}_{\text{sample}} = \left[ \left( \frac{^{56}\text{Fe}}{^{54}\text{Fe}}_{\text{sample}} \bigg/ \frac{^{56}\text{Fe}}{^{54}\text{Fe}}_{\text{IRMM-014}} \right) - 1 \right] \cdot 1000 \quad [\text{‰}] \quad (\text{I.X})$$

whereby conversion between  $^{57}\text{Fe}/^{54}\text{Fe}$  and  $^{56}\text{Fe}/^{54}\text{Fe}$  isotope ratios is according to

$$\delta^{57}\text{Fe} = \delta^{56}\text{Fe} \cdot 1.4881 \quad (\text{I.XI})$$

Such a conversion between different isotopic ratios is based on the mass fractionation law

$$\left(\alpha^{57/54}\text{Fe}\right)=\left(\alpha^{56/54}\text{Fe}\right)^\beta, \text{ with } \beta_a = \frac{\left(\frac{\ln M^{57}\text{Fe}}{\ln M^{54}\text{Fe}}\right)}{\left(\frac{\ln M^{56}\text{Fe}}{\ln M^{54}\text{Fe}}\right)} \text{ or } \beta_b = \frac{\left(\frac{1}{M^{57}\text{Fe}} - \frac{1}{M^{54}\text{Fe}}\right)}{\left(\frac{1}{M^{56}\text{Fe}} - \frac{1}{M^{54}\text{Fe}}\right)}, \quad (\text{I.XII})$$

where the  $\beta_a$  is valid for kinetic fractionation and  $\beta_b$  is valid for equilibrium fractionation (e.g., Young et al., 2002). The conversion factor in equation I.XI is derived from the kinetic law. Such mass dependent fractionation laws have recently shown to be useful to distinguish between equilibrium and kinetic isotope fractionation in nature (e.g., Young et al., 2002).

Isotope fractionation between two substances, regardless whether kinetic or equilibrium fractionation is quantified by the fractionation factor  $\alpha$  (see equation I.I) which can be determined from measured  $\delta$ -values following

$$\alpha_{A-B} = \frac{1000 + \delta^{56}\text{Fe}_A}{1000 + \delta^{56}\text{Fe}_B}. \quad (\text{I.XIII})$$

Since iron isotope fractionation is relatively small ( $\alpha < 1.004$ ), the more convenient  $\Delta$ -values can be used

$$\Delta^{56}\text{Fe}_{A-B} = \delta^{56/54}\text{Fe}_A - \delta^{56/54}\text{Fe}_B \approx 1000 \cdot \ln \alpha^{56/54}\text{Fe}_{A-B} \quad (\text{I.XIV})$$

### **I.III.II. Iron isotope variations in nature and experiment**

The field of iron isotope research was pioneered only a decade ago and thus knowledge on parameters controlling iron isotope fractionation in nature is still limited. Before 1999 studies on stable iron isotope fractionation were virtually absent, since no variation in stable iron isotope compositions in meteorites and terrestrial rocks were found at the level of precision achieved by the available analytical techniques (Valley and Anderson, 1947). After 1999 analytical advancements in mass spectrometry (e.g., see Dauphas and Rouxel, 2006 and references therein) have accelerated the research in this area

and more than 150 research papers comprising a wide range of disciplines were published until 2007. Therefore, only a brief overview of the state of iron isotope research will be given here, with emphasis on high temperature processes relevant for this thesis. Reviews on iron isotope research are presented by Anbar (2004), Beard and Johnson (2004a), Johnson and Beard (2004), Dauphas and Rouxel (2006) and Anbar and Rouxel (2007).

The range in iron isotope composition observed in nature is about 4‰ in  $\delta^{56}\text{Fe}$  (Fig. I.III), excluding variations of several tens of permil found in cosmic spherules caused by fractional evaporative Fe loss during atmospheric entry (e.g., Engrand et al., 2005) and excluding mass independent Fe isotope anomalies that can be up to several hundreds of permil in presolar grains and calcium-aluminium rich inclusions in meteorites (e.g., Dauphas and Rouxel, 2006, and references therein).

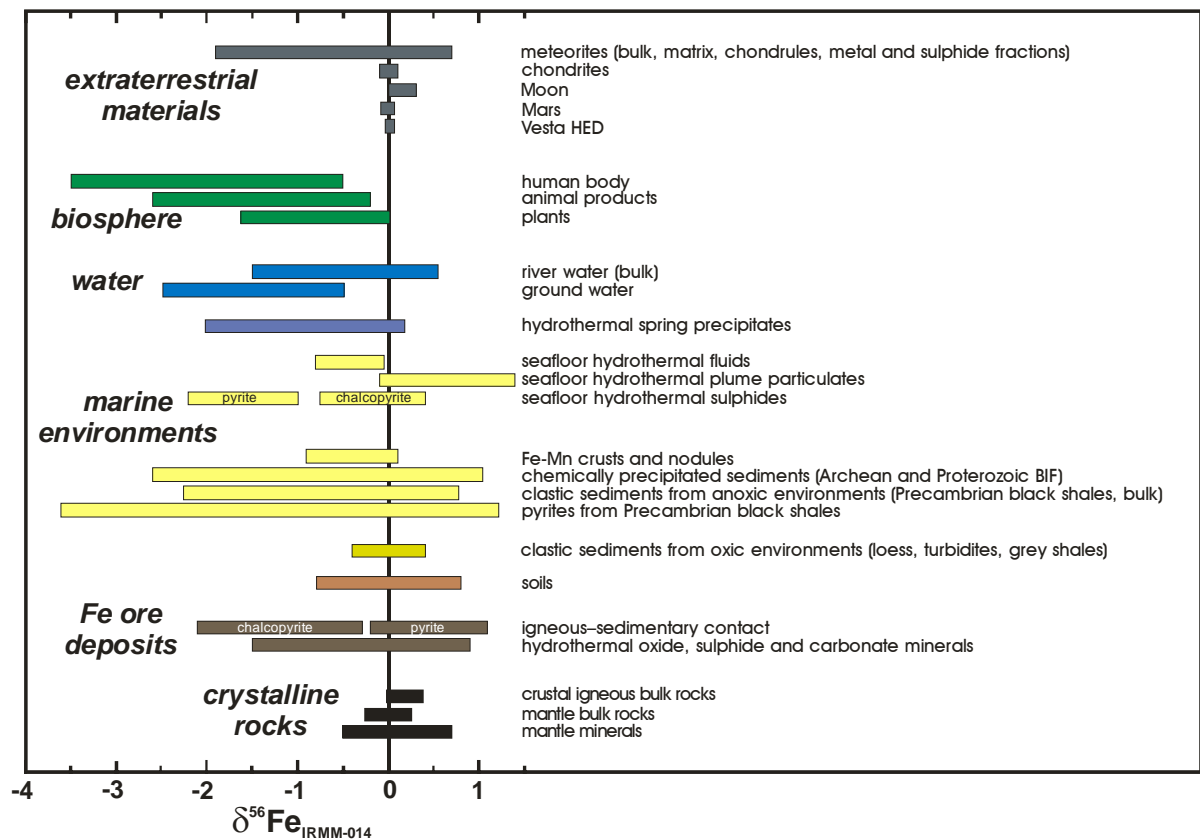


Figure I.III. Natural iron isotope variations. Data from Anbar (2004), Beard and Johnson (2004a), Johnson and Beard (2004), Dauphas and Rouxel (2006), Anbar and Rouxel (2007, and references therein).

Iron isotope compositions of various types of meteorites that follow mass dependent isotope fractionation show a more limited variability (Fig. I.III). In particular, bulk chondrites, eucrites, HED (supposedly from 4Vesta) and SNC (maritan) meteorites suggest inner-solar system homogeneity in Fe isotopes, although small differences between some planetary bodies may exist (Poitrasson, 2007; Schoenberg and von Blanckenburg, 2005). Large variations have been reported in the biosphere (Fig. I.III), i.e., the food chain, in human blood and within plants, suggesting applications in biological and medical research (e.g., Walczyk and von Blanckenburg, 2002; Walczyk and von Blanckenburg, 2005; Guelke and von Blanckenburg, 2007). Modern aqueous systems show a considerable variability in iron isotope composition (Fig. I.III). River waters and groundwaters tend to have lower  $\delta^{56}\text{Fe}$  values relative to IRMM-014. Studies on hydrothermal activity at mid-ocean ridges and ridge flanks revealed that Fe isotopes are fractionated during basalt alteration and hydrothermal mineral precipitation (Fig. I.III).

Marine environments comprise the largest natural range in Fe isotope composition (Fig. I.III). While modern marine sediments, such as clays, terrigenous sediments or turbidites have a more restricted range of about  $\pm 0.5\%$  in  $\delta^{56}\text{Fe}$ , ferromanganese precipitates are characterised by almost exclusively negative  $\delta^{56}\text{Fe}$  values (Fig. I.III). Large iron isotope variability was found in ancient sedimentary rocks (Fig. I.III) and several Fe isotope investigations on such deposits, in particular banded iron formations (BIF), were aimed at reconstructing the cycling of Fe in archaean oceans and the rise of atmospheric oxygen in the early Proterozoic (Dauphas and Rouxel, 2006, and references therein).

Iron isotope studies on ore deposits revealed large fractionations (Fig. I.III) between sulphides from porphyry and associated skarn deposits (e.g., Graham et al., 2004) and between oxide, sulphide and carbonate minerals interpreted to results from partial oxidation and mineral-fluid fractionation during hydrothermal ore formation (e.g., Markl et al., 2006).

Equilibrium iron isotope fractionation decreases with increasing temperature, and thus, reactions in low temperature environments produce much larger isotopic variations than in high temperature environments. Pioneering measurements reported by Beard and Johnson (1999) suggested that bulk igneous rocks are homogeneous within  $\pm 0.3\text{‰}$  (1SD) in  $\delta^{56}\text{Fe}$ , identical to the analytical precision available at that time using thermal ionisation mass spectrometry (TIMS). Therefore, most early studies focused on low temperature reactions, where larger effects are expected. The possibility that iron isotope signatures could be used to distinguish biologically processed iron from non-biological iron motivated initial research, particularly for investigating the possibility of life on Mars (e.g., Beard et al., 1999; Mandernack et al., 1999; Anbar et al., 2000). However, the application of iron isotopes as a biosignature turned out to be more complicated and subsequent laboratory studies identified various abiotic and biologically mediated reactions fractionating iron isotopes at equilibrium or through kinetic reactions (e.g., Bullen et al., 2001; Matthews et al., 2001; Johnson et al., 2002; Skulan et al., 2002; Beard et al., 2003a; Welch et al., 2003; Brantley et al., 2004; Icopini et al., 2004; Kappler and Newman, 2004; Teutsch et al., 2004; Wiesli et al., 2004; Butler et al., 2005; Crosby et al., 2005; Johnson et al., 2005). The importance of the oxidation state of iron on isotopic fractionation was highlighted by a first experimental determination of the equilibrium Fe isotope fractionation factor between Fe(III) complexes and Fe(II) complexes in aqueous solutions where ferric Fe complexes are isotopically heavier than ferrous Fe complexes by  $\sim 3\text{‰}$  in  $\delta^{56}\text{Fe}$  at temperatures between 0 and 22°C (Johnson et al., 2002; Welch et al., 2003). Subsequent laboratory studies determined Fe isotope fractionation factors (equilibrium and kinetic) at temperatures between 2 and 98°C caused by abiotic and biotic processes (e.g., Anbar, 2004, and references therein). These investigations comprised different aqueous Fe species, Fe reduction and oxidation reactions and mineral precipitations (e.g., magnetite, hematite, siderite) from aqueous Fe bearing

solutions (see Anbar, 2004; Beard and Johnson, 2004a; Johnson and Beard, 2004; Dauphas and Rouxel, 2006; and references therein) and found fractionation factors from close-to-zero-values up to  $\sim 3\%$  in  $\delta^{56}\text{Fe}$ .

The experimental and analytical work was accompanied by theoretical studies. Iron isotope fractionation of several per mil were predicted from vibrational force field modelling and from vibrational spectroscopic data, particularly, between Fe complexes in solution having different ligands and Fe oxidation states (Schauble et al., 2001; Jarzecki et al., 2004; Anbar et al., 2005). Predictions of equilibrium iron isotope fractionation between minerals based on Mössbauer spectroscopic data and nuclear inelastic resonant X-ray scattering revealed significant fractionation even at high temperatures (Polyakov, 1997; Polyakov and Mineev, 2000; Polyakov et al., 2007). For example, the calculations of these authors predict

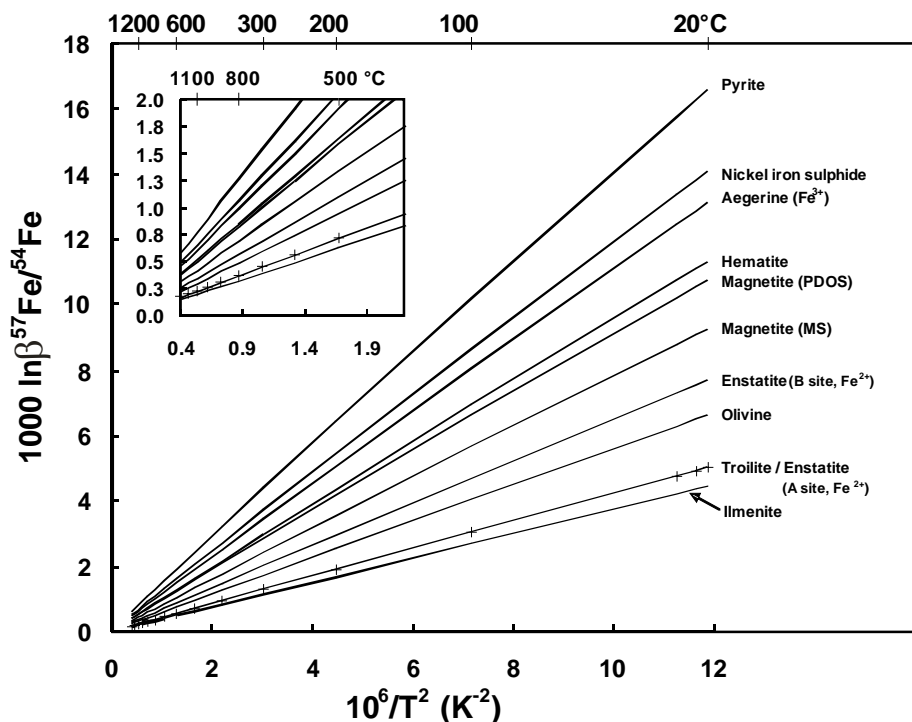


Figure I.IV. Reduced isotope partition function ratios ( $\beta$ -factors) derived from Mössbauer spectroscopy data (MS) or nuclear inelastic resonant X-ray scattering (PDOS) for different minerals as a function of inverse temperature (Polyakov and Mineev, 2000; Mineev et al., 2007; Polyakov et al., 2007). Isotope fractionation between two phases equilibrated at a given temperature can be deduced by subtraction of their respective  $\beta$ -factors. The inset magnifies the range relevant for iron isotope fractionation at magmatic conditions.

that at 800°C magnetite is  $\sim 0.2\%$  heavier in  $\delta^{56}\text{Fe}$  than coexisting olivine (Fig. I.IV). In particular, systematic relations between the potential energy of the cation site in crystalline materials and differences in oxidation state, coordination, and nature of the ligand of iron on isotope fractionation were found (Polyakov et al., 2007) – consistent with the general theoretical rules described earlier in chapter I.II.I: Heavier iron isotopes are enriched in minerals containing ferric iron, having highly covalent bonds and low Fe coordination numbers (compare also Fig. I.IV). From the inset in Figure I.IV it becomes apparent that iron isotope fractionation at high temperatures is generally much smaller compared to low temperature processes and therefore analytically more challenging. First exploration of high temperature iron isotope fractionation was done by analyses of natural rocks and minerals (Beard and Johnson, 1999; Zhu et al., 2002; Beard et al., 2003a; Williams et al., 2004). Iron isotope analyses of various igneous rocks comprise a relatively narrow range (Fig. I.V).

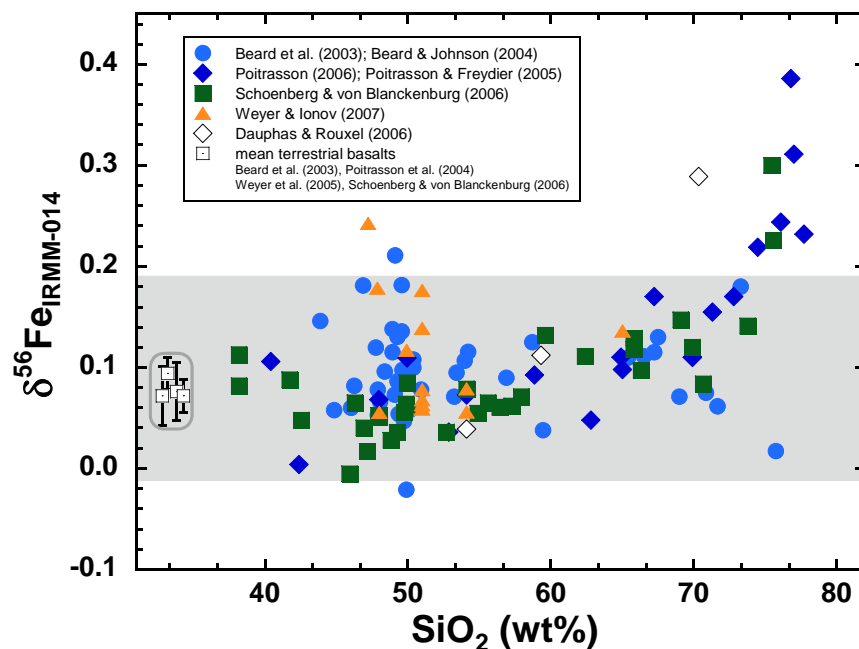


Figure I.V. Iron isotope compositions of igneous rocks (whole rock analyses) as a function of  $\text{SiO}_2$  contents. The grey area represents the average iron isotope composition of igneous rocks as defined by Beard et al. (2003a), i.e.  $\delta^{56}\text{Fe}_{\text{IRMM-014}} = 0.09 \pm 0.10\%$  (2SD). The mean iron isotope composition of terrestrial basalts (data from different research groups) is also shown (error bars represent 2SE).

Beard et al. (2003a) defined the average bulk igneous rock Fe isotope composition as  $\delta^{56}\text{Fe}_{\text{IRMM-014}} = 0.09 \pm 0.10\text{‰}$  (2SD) based on 46 bulk rock analyses of various types of igneous rocks. This homogeneous terrestrial Fe isotope baseline was proposed as a reference reservoir for the interpretation of biological Fe cycling or abiotic low temperature iron isotope fractionation (Beard et al., 2003a, b). Zhu et al. (2002) reported the first Fe isotope data for minerals from mantle xenoliths equilibrated at  $\sim 1000^\circ\text{C}$  and found that pyroxenes (opx and cpx) were systematically heavier in  $\delta^{56}\text{Fe}$  than olivines by  $\sim 0.2\text{‰}$  (Figure I.VI). Williams et al. (2004) found substantial (up to  $1.1\text{‰}$ ) systematic Fe isotope variations of spinels from mantle xenoliths and a correlation with oxygen fugacity and  $\text{Fe}^{2+}/\Sigma\text{Fe}$  of spinels. It was proposed that iron isotopes potentially provide a proxy of changes in mantle oxidation state, melting, and volatile recycling. Subsequent studies on mantle derived rocks suggested that these Fe isotope variations are the result of melt extraction in combination with changes in mantle redox conditions or metasomatism of the sub-arc mantle by iron-rich

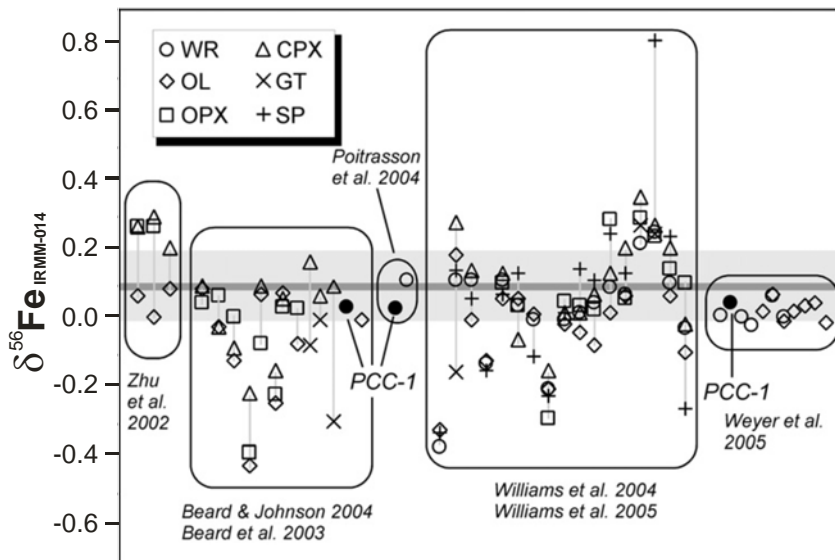


Figure I.VI. Iron isotope compositions of mantle samples (modified from Beard and Johnson, 2007). Different symbols represent different minerals (or whole rock samples) and vertical lines connect phases from the same sample. Abbreviations: WR = whole rock, OL = olivine, OPX = orthopyroxene, CPX = clinopyroxene, GT = garnet, SP = spinel. The horizontal grey line represents the average of igneous rocks ( $\pm 2\text{SD}$ ) as defined by Beard et al. (2003a).



silicate melts from the subducting slab (Beard and Johnson, 2004b; Williams et al., 2005). Further on, several studies explored inter-mineral iron isotope fractionation (Figure I.VI). Consistent with the study of Zhu et al. (2002), Poitrasson et al. (2004) and Williams et al. (2005) reported significant differences in  $\delta^{56}\text{Fe}$  of -0.1 to -0.2‰ between coexisting olivine and pyroxene in mantle rocks, but an absence of differences between ortho- and clinopyroxene. These authors suggested that their findings reflect isotopic equilibrium at high temperatures. Beard and Johnson (2004b) confirmed differences in iron isotopes between coexisting olivine and clinopyroxene for some spinel peridotites, but found no isotopic differences between olivine and orthopyroxene. In contrast to other studies, these authors attributed the isotopic inter-mineral differences to metasomatic alteration. So far, the largest inter-mineral fractionation in mafic rocks interpreted as equilibrium fractionation was observed for clinopyroxene and garnet in eclogites and in garnet-bearing ultramafic rocks ( $\Delta^{56}\text{Fe}_{\text{cpx-grt}} \approx +0.3\text{‰}$  in  $^{56}\text{Fe}/^{54}\text{Fe}$ ; Beard and Johnson, 2004b). In contrast, andesitic volcanic rocks did not reveal any differences in Fe isotope composition between silicate minerals (olivine, biotite, amphibole) and magnetite (Beard and Johnson, 2004b). However, a recent study reported significant differences between silicate minerals and magnetite in volcanic rocks and plutonic rocks that were interpreted to reflect open-system Fe exchange (Heimann et al., 2007). In particular, these authors suggested that the Fe isotope shifts likely occurred during exsolution of late stage Fe fluids, and as such reflect sub-solidus isotopic equilibration upon cooling.

Latest analytical improvements now allow resolving even smallest Fe isotope variations in planetary reservoirs, although their scientific significance is highly debated (Poitrasson and Freydier, 2005; Weyer et al., 2005; Beard and Johnson, 2006; Poitrasson, 2006; Schoenberg and von Blanckenburg, 2006; Beard and Johnson, 2007; Poitrasson, 2007; Weyer et al., 2007; Weyer and Ionov, 2007). Moreover, differences as small as 0.1‰ in

$\delta^{56}\text{Fe}$  were found between basaltic reservoirs of Earth, Moon, HED and SNC meteorites (Poitrasson et al, 2004; Weyer et al. 2005; Schoenberg and von Blanckenburg, 2006) and between terrestrial mantle peridotites and crustal basalts (Weyer et al. 2005; Schoenberg and von Blanckenburg, 2006). From these observations, it has been proposed that partial melting of mantle rocks induces Fe isotope fractionation, resulting in a heavier  $\delta^{56}\text{Fe}$  of basalts (+0.1‰) relative to residual mantle rocks (Weyer et al., 2005; Weyer et al., 2007; Weyer and Ionov, 2007). However, this interpretation has generated a vigorous debate (Beard and Johnson, 2007; Poitrasson, 2007; Weyer et al, 2007).

The question whether magma differentiation processes fractionate Fe isotopes has been addressed as well. From the absence of any correlation between Fe isotope composition and bulk rock  $\text{SiO}_2$  Beard and Johnson (2004b) concluded that magma differentiation does not induce Fe isotope fractionation. However, new data revealed that the Fe isotope range of the crust is more scattered than previously thought (Fig. I.V). In particular, Poitrasson and Freydier (2005) found that silica-rich plutonic rocks show significantly heavier Fe isotope compositions than mafic rocks. These authors ruled out magma differentiation to be responsible for the heavy Fe isotope signatures of highly evolved rocks (Fig. I.V), arguing that Fe-rich minerals, which could potentially fractionate Fe isotopes, become rare in evolved granitic magmas. Rather, Poitrasson and Freydier (2005) explained the heavy Fe isotope compositions of highly evolved granites by removal of isotopically light Fe through late stage fluid exsolution, leaving behind an isotopically heavier residual magma (Poitrasson and Freydier, 2005). Schoenberg and von Blanckenburg (2006) found systematic variations in the Fe isotope compositions of a genetically related suite of igneous rocks from the Bergell intrusion, Swiss Alps, but could not unambiguously be attributed to fractional crystallisation, due to simultaneous assimilation of host rocks with ongoing fractional crystallisation.

To date, it is still difficult to clearly identify the underlying processes causing the discussed Fe isotope variations in igneous rocks, because knowledge of mechanisms that fractionate Fe isotopes at high temperatures is limited. One cornerstone for the interpretation of iron isotope variations is knowledge of equilibrium isotope fractionation factors between different minerals, melts and fluids, preferably obtained by direct laboratory experiments. In 2005, when the project for this thesis started, no experimental studies on high temperature iron isotope fractionation existed. Apart from the experimental investigations described in this thesis, meanwhile published experimental studies of high temperature iron isotope fractionation are restricted to two research papers (Cohen et al., 2006; Roskosz et al., 2006) and two preliminary studies reported in conference abstracts (Huang and Lundstrom, 2006; Huang et al., 2007; Shahar et al., 2007). Cohen et al. (2006) reported a kinetic isotope effect during reduction of iron from a silicate melt with implications for chondrule formation. Their experiments were conducted at atmospheric pressure, at temperatures between 1450 and 1540°C and runtimes from two minutes to six hours. A gas mixing furnace (CO/CO<sub>2</sub>) was used to apply low oxygen fugacities (about 5 log units below the iron-wüstite buffer:  $2\text{FeO} = 2\text{Fe} + \text{O}_2$ ). Under these reducing conditions, iron from the starting material (fayalite-rich silicate glass) was reduced to metallic iron at the melt/gas interface. The  $\delta^{56}\text{Fe}$  values of the residual Fe depleted melt ranged between -0.22 and +2.0‰ relative to the starting material, depending on experiment duration. This was explained by kinetic isotope fractionation accompanied by the faster diffusion of lighter iron isotopes to the melt/gas interface where reduction occurred. As the reduction neared completion, isotopic re-equilibration between metal and melt caused a gradual decrease in  $\delta^{56}\text{Fe}$  of the melt approaching that of the metal and the initial value of the starting material. The metal-melt isotope fractionation factor at equilibrium was not determined. The investigations of Roskosz et al. (2006) were also conducted in a silicate melt–metal system with implications to iron meteorites. Experiments

were done at 1500°C and atmospheric pressure, using a starting glass of anorthite–diopside eutectic composition to which Fe<sub>2</sub>O<sub>3</sub> was added. The melt was in contact with Pt metal, resulting in the formation of Fe-Pt alloys during runs with 30 minutes to 24 hours duration. Different oxygen fugacities were applied using CO/CO<sub>2</sub> gas mixtures. The results show an initial kinetic isotope effect with  $\Delta^{56}\text{Fe}_{\text{silicate melt} - \text{metal alloy}}$  up to +4.7‰, consistent with the results from Cohen et al. (2006). After 24 hours the measured  $\Delta^{56}\text{Fe}_{\text{silicate melt} - \text{metal alloy}}$  was 0.4±0.3‰. The authors proposed that this values represents the equilibrium fractionation factor between silicate melt and the Fe-Pt alloy, although isotopic equilibrium was not proven (e.g., by reversal experiments or use of isotopically enriched tracers). The preliminary results of Huang and Lundstrom (2006) and Huang et al. (2007) reported Fe isotope fractionation of up to 9.9‰ in  $\delta^{56}\text{Fe}$  as a result of Soret diffusion, in which light isotopes preferentially migrate up a temperature gradient. In this thermal migration experiment at 0.5 GPa (66 days duration) hydrous andesite was used as starting material. Along a temperature gradient from 950 to 350°C over 2 cm the experimental products consisted of silicate melt (glass) and various proportions of minerals (apatite, magnetite, amphibole, biotite, plagioclase, quartz, and K-feldspar). From experiments at 800°C, 0.5 GPa, they proposed an equilibrium  $\Delta^{56}\text{Fe}_{\text{magnetite} - \text{silicate melt}}$  smaller than -0.26‰. Shahr et al. (2007) presented iron isotope exchange experiments between fayalite and magnetite using an enriched isotope tracer approach to determine equilibrium isotope fractionation at 1 GPa and 600, 700, and 800°C. The results show temperature dependent fractionation between fayalite and magnetite with  $\Delta^{56}\text{Fe}_{\text{magnetite-fayalite}}$  of 0.26‰, 0.21‰, and 0.18‰ ±0.017‰ at temperatures of 600°C, 700°C, and 800°C, respectively. These results agree well with those calculated from Mössbauer spectroscopy-derived  $\beta$ -factors (Polyakov and Mineev, 2000; Polyakov et al., 2007).

The status quo of high temperature iron isotope research as reviewed in this chapter illustrates that many questions regarding the mechanisms that control Fe isotope fractionation in igneous environments are still open. Some of these issues will be addressed in the following chapters.

## Chapter 1. Oxidation state of iron in hydrous phono-tephritic melts

### ABSTRACT

The oxidation state of iron in hydrous ultrapotassic (phono-tephritic) melts coexisting with mixed H<sub>2</sub>O-CO<sub>2</sub> fluids was experimentally studied at 1200 and 1250°C and pressures from 50 to 500 MPa. The oxygen fugacity ( $fO_2$ ) varied from NNO-2.9 to NNO+2.6, relative to the Ni/NiO oxygen buffer (NNO), as imposed by external redox conditions in experimental vessels and internal variations in water activity from 0.05 to 1 inside the capsules. The iron redox state of the quenched melts was determined by colorimetric wet-chemical analysis. This analytical method was optimized to measure the  $Fe^{2+}/\Sigma Fe$  ratio of mg-sized samples within  $\pm 0.03$  ( $2\sigma$ ). The accuracy and precision was tested with international reference materials and with standards analysed by other methods. The  $Fe^{2+}/\Sigma Fe$  ratio of the glasses covers a range of 0.41 to 0.85. A small negative effect of dissolved water on  $Fe^{2+}/\Sigma Fe$  at given  $fO_2$  was found, consistent with the thermodynamic model of Moretti (2005). No effect of pressure and temperature on the redox state of iron was resolvable in the investigated P-T range. Compared to hydrous ferrobaltic melts that were studied previously under similar conditions, systematically lower  $Fe^{2+}/\Sigma Fe$  ratios were found for the phono-tephritic melts, in particular at low oxygen fugacities. This effect is attributed to the much higher K<sub>2</sub>O contents of the phono-tephrite (7.5 compared to 0.3 wt%), but the difference in  $\Sigma FeO$  (7.8 wt% in the phono-tephrite and 12.9 wt% in the ferrobalt) may have an influence as well. Comparison of the experimentally obtained relationship

between  $\log fO_2$  and  $Fe^{3+}/Fe^{2+}$  for the studied hydrous ultrapotassic melts with commonly used empirical and thermodynamic models suggest that these models can be successfully applied to phono-tephrite melts, although such compositions were not implemented in the model calibrations. Furthermore, the new data can be used to improve the models with respect to the effects of  $H_2O$ ,  $K_2O$  and  $\Sigma FeO$  on the redox state of iron in silicate melts.

### 1.1. INTRODUCTION

The oxidation state of iron varies widely in natural magmas (e.g., Carmichael, 1991) and influences their physical and chemical properties as well as the phase equilibria for iron-bearing minerals. The redox state of iron in the melt is related to the oxygen fugacity via the reaction  $Fe(II)O_{melt} + \frac{1}{4} O_{2\ gas} = Fe(III)O_{1.5\ melt}$  and the equilibrium constant of the reaction can be expressed as  $K = a_{Fe(III)O_{1.5}} / ( a_{Fe(II)O} \cdot (a_{O_2})^{1/4} )$  where  $a$  denotes the activity of the respective components in the melt.  $K$  depends on temperature, pressure and melt composition. Knowledge of the Fe redox state in magmas is a pre-requisite to understand the physical and chemical properties of magmas, to constrain source regions of magmas and their redox states, and the processes occurring during magma genesis and evolution. Specifically, the redox state of iron has influence on the stability of iron bearing minerals that may crystallize during magma evolution, and hence, control the iron content of the residual melt, and the stability and composition of major silicate phases (e.g., Pichavant et al., 2002). Furthermore, the structural incorporation of ferric and ferrous iron in silicate melts may affect the viscosity of a magma (e.g., Liebske et al.; 2003; Vetere et al., 2006), which has strong influence on the dynamics of volcanic eruptions. In particular, interaction between various species of different elements may influence the partitioning of volatile

elements between silicate melts and coexisting gas phases, which strongly affects the degassing behavior of ascending magmas (e.g., Moretti and Ottonello, 2003; Moretti and Papale, 2004; Burgisser and Scaillet, 2007).

Several empirical relations have been proposed to quantify the effect of various parameters on the Fe redox state in silicate melts and to predict the prevailing oxygen fugacity in a magmatic system from Fe redox ratios of quenched melts (e.g., Sack et al., 1980; Kilinc et al., 1983; Kress and Carmichael, 1988; Mysen, 1988; Borisov and Shapkin, 1989; Kress and Carmichael, 1991; Nikolaev et al., 1996; Jayasuriya et al., 2004). The early empirical models were calibrated over a relatively wide range of melt compositions, temperatures and oxygen fugacities, but the data basis comprised dry silicate melts only. Subsequent experimental investigations on silicate melts of different chemical compositions and also on hydrous silicate melts revealed in part considerable discrepancies between predicted  $\text{Fe}^{2+}/\text{Fe}^{3+}$  ratio of the melts and experimental findings (Sisson and Grove, 1993; Moore et al., 1995; Baker and Rutherford, 1996; Gaillard et al., 2001; Wilke et al., 2002; Gaillard et al., 2003; Partzsch et al., 2004; Botcharnikov et al., 2005). The deviations might be either due to ignoring the component  $\text{H}_2\text{O}$  in the empirical models or due to differences in anhydrous melt compositions studied in the experiments compared to the compositions used to calibrate the models. As an alternative, a thermodynamic model based on a polymeric approach was developed for the prediction of the Fe redox state in dry silicate melts at atmospheric pressures by Ottonello et al. (2001). Recently, this model was extended by Moretti (2005) to account for the effects of dissolved water and pressure.

Here we use samples from a previous study on volatile solubility in phono-tephritic melts (Misiti et al., 2007) to test the predictive power of commonly used models for  $\text{Fe}^{2+}/\text{Fe}^{3+}$  ratios in ultrapotassic silicate melts because hydrous phono-tephritic melts have not been used in the calibration of those models. A positive effect of increasing  $\text{K}_2\text{O}$  on the



$\text{Fe}^{2+}/\Sigma\text{Fe}$  ratios has been proposed by Tangemann et al. (2001) for dry iron-rich  $\text{K}_2\text{O}$ - $\text{FeO}$ - $\text{Fe}_2\text{O}_3$ - $\text{SiO}_2$  liquids at atmospheric pressure, whereas other studies suggest a stabilization of tetrahedrally coordinated ferric iron by charge-balancing  $\text{K}_2\text{O}$  (Sack et al., 1980; Kilinc et al., 1983; Dickenson and Hess, 1986; Kress and Carmichael, 1988). To date, no experimental data exists on hydrous  $\text{K}_2\text{O}$ -rich melts at elevated pressures. The new data allow us to investigate the influence of water activity and oxygen fugacity on the redox state of iron in the melts as well as to evaluate the compositional effects of water, potassium and total iron content on the  $\text{Fe}^{2+}/\Sigma\text{Fe}$  ratio. The results are compared to the widely used empirical model of Kress and Carmichael (1991) and the thermodynamic model of Moretti (2005).

## 1.2. EXPERIMENTAL METHODS

The experimental strategies and procedures are described in detail in Misiti et al. (2007) and are summarized briefly here. The starting material for the experiments was a synthetic analogue of the phono-tephritic Mt. Mellone lava flow composition from the Alban Hills Volcanic District in Central Italy (Marra et al., 2003; Gaeta et al., 2006). For each experiment ~ 50 mg glass powder, 0 to 20  $\mu\text{L}$  deionised water and 0 to 15 mg silver oxalate ( $\text{Ag}_2\text{C}_2\text{O}_4$ ) were sealed in  $\text{Au}_{80}\text{Pd}_{20}$  capsules (~15 mm length, 2.6 mm inner diameter, 0.2 mm wall thickness). To reduce Fe loss to the capsule walls, for experiments under reducing conditions the capsules were pre-saturated with Fe as described in Botcharnikov et al. (2005). The experiments were performed in internally heated gas pressure vessels (IHPV) at temperatures of 1200 and 1250°C and pressures between 50 to 500 MPa for 1.5 to 72 hours (Table 1.1). Uncertainties in temperature and pressure are  $\pm 10^\circ\text{C}$  and  $\pm 5$  MPa, respectively.

Table 1.1 Summary of experimental conditions, results of wet-chemical colorimetric iron analyses and  $\text{Fe}^{2+}/\Sigma\text{Fe}$  ratios from model calculations after Moretti (2005) and Kress and Carmichael (1991).

sample	experimental conditions				wet-chemical colorimetric analyses						model calculations				
	run <sup>a</sup>	P (MPa)	T (°C)	t (h)	X <sup>f</sup> H <sub>2</sub> O <sup>b</sup>	aH <sub>2</sub> O <sup>c</sup>	logfO <sub>2</sub> <sup>d</sup>	$\Delta\text{NNO}^e$	sample weight (mg)	A <sub>523</sub> Fe <sup>2+</sup>	A <sub>523</sub> ΣFe	ΣFeO (wt%)	(2σ)	Fe <sup>2+</sup> /ΣFe (2σ)	Fe <sup>2+</sup> /ΣFe (Moretti) (K&C)
<b>Ar-IHPV (fH<sub>2</sub> intrinsic); H<sub>2</sub>O fluid, aH<sub>2</sub>O = 1</b>															
Alb1-20	A	50	1250	15	1.00	1.00	-4.39	2.60	4.65	0.2323	0.3880	7.07	0.24	0.60	0.40
Alb1-21	A	50	1250	15	1.00	1.00	-4.39	2.60	6.01	0.2999	0.5014	7.06	0.22	0.60	0.40
Alb1-22	B	100	1250	20	1.00	1.00	-4.38	2.60	5.76	0.2886	0.4852	7.12	0.22	0.59	0.48
Alb1-23	B	100	1250	20	1.00	1.00	-4.38	2.60	4.54	0.1953	0.3921	7.31	0.25	0.50	0.39
Alb1-36	C	200	1200	20	1.00	1.00	-4.90	2.60	4.57	0.1877	0.3775	6.99	0.24	0.50	0.48
Alb1-37	C	200	1200	20	1.00	1.00	-4.90	2.60	5.64	0.2307	0.4665	7.00	0.22	0.49	0.41
Alb1-10	D	200	1250	20	1.00	1.00	-4.35	2.60	3.50	0.1607	0.2994	7.25	0.28	0.54	0.42
Alb1-24 <sup>e</sup>	E	300	1250	14	1.00	1.00	-4.32	2.60	5.89	0.2176	0.4986	7.17	0.22	0.44	0.41
Alb1-25 <sup>e</sup>	E	300	1250	14	1.00	1.00	-4.32	2.60	4.78	0.1877	0.3918	6.94	0.23	0.48	0.43
Alb1-35 <sup>e</sup>	F	400	1200	72	1.00	1.00	-4.84	2.60	4.79	0.1870	0.3922	6.93	0.23	0.48	0.43
Alb1-26 <sup>e</sup>	G	400	1250	48	1.00	1.00	-4.29	2.60	5.53	0.2148	0.4477	6.85	0.22	0.48	0.45
Alb1-27 <sup>e</sup>	G	400	1250	48	1.00	1.00	-4.29	2.60	4.69	0.1848	0.3772	6.81	0.23	0.49	0.45
Alb1-5 <sup>e</sup>	H	500	1200	20	1.00	1.00	-4.81	2.60	4.58	0.1764	0.3630	6.72	0.23	0.49	0.45
Alb1-15 <sup>e</sup>	I	500	1250	20	1.00	1.00	-4.26	2.60	4.12	0.1500	0.3298	6.78	0.25	0.45	0.46
Alb1-28 <sup>e</sup>	L	500	1250	17	1.00	1.00	-4.26	2.60	4.55	0.1544	0.3759	6.99	0.24	0.41	0.48
Alb1-41	N	200	1200	24	1.00	1.00	-4.90	2.60	4.98	0.1619	0.3934	6.69	0.22	0.41	0.48
<b>Ar-IHPV (fH<sub>2</sub> intrinsic); H<sub>2</sub>O-CO<sub>2</sub> fluid</b>															
Alb1-7	D	200	1250	18	0.33	0.40	-5.15	1.80	4.46	0.2322	0.3805	7.23	0.25	0.61	0.58
Alb1-8	D	200	1250	18	0.50	0.57	-4.84	2.10	4.49	0.2183	0.3946	7.44	0.25	0.55	0.52
Alb1-6bis	M	200	1250	20	0.10	0.13	-6.10	0.85	4.52	0.2555	0.3277	6.13	0.22	0.78	0.75
Alb1-6a	M	200	1250	20	0.18	0.23	-5.62	1.33	4.97	0.2649	0.3822	6.51	0.22	0.69	0.68
Alb1-1 <sup>e</sup>	H	500	1200	18	n.a.	0.15 <sup>e</sup>	-6.47	0.93	4.45	0.2658	0.3187	6.07	0.22	0.83	0.78
Alb1-2	H	500	1200	18	0.22	0.28	-5.91	1.50	3.99	0.2191	0.3425	7.27	0.26	0.64	0.63
Alb1-3	H	500	1200	18	0.60	0.66	-5.17	2.23	4.56	0.1952	0.3653	6.78	0.23	0.53	0.56
Alb1-4 <sup>e</sup>	H	500	1200	18	0.83	0.85	-4.95	2.46	2.45	0.1013	0.2005	6.92	0.34	0.51	0.56
Alb1-12	I	500	1250	18	0.32	0.39	-5.08	1.78	4.18	0.1617	0.3537	7.17	0.25	0.46	0.50
Alb1-13 <sup>e</sup>	I	500	1250	18	0.75	0.78	-4.47	2.38	4.62	0.2167	0.4055	7.42	0.25	0.53	0.63
Alb1-14 <sup>e</sup>	I	500	1250	18	0.79	0.81	-4.44	2.42	3.55	0.1368	0.3052	7.27	0.27	0.45	0.51
									4.48	0.1714	0.3870	7.32	0.25	0.44	0.47

continued on next page

Table 1.1. - continued

sample	experimental conditions				wet-chemical colorimetric analyses					model calculations							
	run <sup>a</sup>	P (MPa)	T (°C)	t (h)	X <sup>i</sup> H <sub>2</sub> O <sup>b</sup>	a H <sub>2</sub> O <sup>c</sup>	log fO <sub>2</sub> <sup>d</sup>	ANNO <sup>e</sup>	sample weight (mg)	A <sub>523</sub> Fe <sup>2+</sup>	A <sub>523</sub> ΣFe	ΣFeO (wt%) (2σ)	Fe <sup>2+</sup> /ΣFe (2σ)	Fe <sup>2+</sup> /ΣFe (Moretti) (K&C)			
<b>Ar-H<sub>2</sub>-IHPV (fH<sub>2</sub> varied); H<sub>2</sub>O fluid or H<sub>2</sub>O-CO<sub>2</sub> fluid</b>																	
Alb1-H42	O	200	1200	18	1.00	1.00	-5.64	1.87	5.56	0.2302	0.4640	7.06	0.22	0.50	0.02	0.51	0.57
Alb1-H43	O	200	1200	18	0.76	0.78	-5.86	1.65	5.48	0.2357	0.4611	7.12	0.23	0.51	0.02	0.55	0.53
Alb1-H44	O	200	1200	18	0.30	0.34	-6.57	0.93	5.59	0.2863	0.4658	7.05	0.22	0.61	0.02	0.69	0.61
Alb1-H45	O	200	1200	18	0.07	0.09	-7.78	-0.28	4.47	0.2251	0.3705	7.02	0.24	0.61	0.03	0.69	0.61
Alb1-H47	P	200	1200	5	1.00	1.00	-7.70	-0.20	5.27	0.2921	0.4083	6.55	0.22	0.72	0.02	0.84	0.73
Alb1-H48	P	200	1200	5	0.71	0.73	-7.97	-0.47	4.37	0.2379	0.3359	6.50	0.23	0.71	0.03	0.84	0.73
Alb1-H49	P	200	1200	5	0.39	0.43	-8.43	-0.93	5.11	0.2883	0.3646	6.04	0.21	0.79	0.03	0.77	0.76
Alb1-H50	P	200	1200	5	0.23	0.27	-8.85	-1.35	5.20	0.3039	0.3893	6.34	0.21	0.78	0.03	0.81	0.74
Alb1-H51	P	200	1200	5	0.14	0.17	-9.26	-1.76	5.70	0.3057	0.3720	5.52	0.19	0.82	0.03	0.87	0.78
Alb1-H52	Q	200	1200	1.5	1.00	1.00	-7.80	-0.29	5.02	0.2371	0.2886	4.87	0.19	0.82	0.04	0.90	0.81
Alb1-H54	Q	200	1200	1.5	0.50	0.53	-8.35	-0.85	4.07	0.1949	0.2338	4.86	0.21	0.83	0.04	0.90	0.81
Alb1-H56	Q	200	1200	1.5	0.04 <sup>f</sup>	0.05	-10.40 <sup>f</sup>	-2.90 <sup>f</sup>	5.36	0.2084	0.2577	4.07	0.17	0.81	0.04	0.93	0.83
									3.82	0.1594	0.1976	4.37	0.21	0.81	0.05	0.93	0.86
									5.26	0.3419	0.4567	7.34	0.23	0.75	0.02	0.79	0.72
									6.24	0.4169	0.5276	7.16	0.22	0.79	0.02	0.86	0.76
									5.23	0.2842	0.3342	5.41	0.19	0.85	0.03	0.96	0.89

n.a. not available

a) Each letter refers to an individual run in the IHPV, containing one or more samples (capsules).

b) Mole fraction of water and CO<sub>2</sub> in the fluid phase measured by the weight loss method (see text).c) Water activities for mixed H<sub>2</sub>O-CO<sub>2</sub> fluids were calculated from X<sup>i</sup>H<sub>2</sub>O after Aranovich and Newton (1999) using molar volumes of pure H<sub>2</sub>O and CO<sub>2</sub> from Pitzer and Sterner (1994).d) Oxygen fugacity calculated from water activity:  $\log fO_2 = \log fO_2(\text{IHPV apparent}) + 2 \log(a_{H_2O})$ . ΔNNO is log fO<sub>2</sub> expressed relative to the Ni-NiO buffer (Huebner and Sato, 1970).

e) Experimental products which contain quench crystals formed during cooling at the end of the experiment. All other run products consist of glass and a fluid phase only; except sample Alb1-1, which additionally contains clinopyroxene crystals formed in equilibrium with the silicate melt at experimental conditions (see text).

f) Fluid composition (X<sup>i</sup>H<sub>2</sub>O, X<sup>i</sup>CO<sub>2</sub>, X<sup>i</sup>CO) for sample Alb1-H56 (that was used to calculate the oxygen fugacity) estimated from CO<sub>2</sub> solubility trends due to presence of other carbon species (beside CO<sub>2</sub>) in the fluid (see text).g) Water activity was calculated from an estimated X<sup>i</sup>H<sub>2</sub>O of 0.11 for Alb1-1 (see text).Notes for wet-chemical colorimetric analyses: A<sub>523</sub> values are the measured baseline-corrected absorbances at the Fe(II)-2,2-bipyridyl absorbance maximum at about 523 nm. Given uncertainties were calculated from error propagation of individual uncertainties in sample weight, dilution and absorbance measurements. The external reproducibility (2σ) of the Fe<sup>2+</sup>/ΣFe ratio with this method is 0.03 (see text). Multiple analyses for the same sample represent full wet-chemical replicates including individual dissolution of fragments from the experimental products.

Samples were rapidly quenched at the end of the experiment with an initial cooling rate of about 150°C/s (Berndt et al., 2002). Most of the experiments were performed at intrinsic redox conditions of the IHPV pressurized with Ar. The intrinsic oxygen fugacity in capsules with pure H<sub>2</sub>O fluid (mole fraction of water in the fluid  $X^f\text{H}_2\text{O} = 1$ ) in the IHPV used in this study was determined by NiPd-solid sensors (Taylor et al., 1992a) at 1200°C and 200 MPa. The obtained value of  $\log f\text{O}_2 = -7.5$  corresponds to NNO+2.6 ( $\pm 0.5$ ;  $1\sigma$  from microprobe analyses of the NiPd alloy) where NNO refers to the Ni-NiO buffer (Huebner and Sato, 1970). This  $f\text{O}_2$  value is about 0.9 log units lower than reported by Berndt et al. (2002) for a similar IHPV. The difference reflects the uncertainty in  $f\text{O}_2$  due to unbuffered hydrogen fugacity. The prevailing  $f\text{H}_2$  depends on the specific components used in the individual IHPV (furnace, sample holder, etc.). Experiments at low  $f\text{O}_2$  were performed in another IHPV pressurized with an Ar-H<sub>2</sub> mixture. The IHPV is equipped with a Shaw-membrane to monitor the  $f\text{H}_2$  at high pressure and temperature (Berndt et al., 2002). The  $f\text{H}_2$  controls the  $f\text{O}_2$  in the capsule through the equilibrium reaction  $\text{H}_2 + \frac{1}{2} \text{O}_2 \leftrightarrow \text{H}_2\text{O}$ . The accuracy of  $\log f\text{O}_2$  is estimated to be  $\pm 0.2$  log units for experiments with pure H<sub>2</sub>O fluids. In experiments with mixed H<sub>2</sub>O-CO<sub>2</sub> fluids the fugacity of H<sub>2</sub>O and hence the  $f\text{O}_2$  decreases with increasing  $f\text{CO}_2$ . The prevailing  $f\text{O}_2$  in the capsule was calculated from the fluid composition determined after the experiment. Hence, differences in oxygen fugacity in capsules processed in the same run are determined only by the variations in  $X^f\text{H}_2\text{O}$ . The precision of the latter is limited by the uncertainties associated with the weight-loss determination of H<sub>2</sub>O and CO<sub>2</sub> released from the capsules after the experiments. In this case the relative precision of  $\log f\text{O}_2$  processed in the same run was estimated from error propagation of weighing uncertainties to be approximately  $\pm 0.1$  log units. However, taking the uncertainty of the intrinsic redox condition in the IHPV into account, the error in absolute  $\log f\text{O}_2$  values of experiments processed in different runs is higher (approximately  $\pm 0.5$  log units).

### 1.3. ANALYTICAL METHODS

The composition of the fluid phase in equilibrium with the silicate melt (expressed in mole fractions of H<sub>2</sub>O and CO<sub>2</sub>, X<sup>f</sup>H<sub>2</sub>O and X<sup>f</sup>CO<sub>2</sub>, respectively) was determined by a conventional weight-loss technique. H<sub>2</sub>O and CO<sub>2</sub> concentrations in the glasses were measured by FT-IR spectroscopy. Bulk H<sub>2</sub>O contents of quenched melts were also measured by Karl-Fischer titration (KFT). Analytical details and results of these investigations are reported in Misiti et al. (2007) and results relevant to this study are given in appendix A1.2. Here, we focus on measurements relevant for the oxidation state of iron in the melt. The chemical composition of the post-experimental glasses was determined by electron microprobe analysis (EMPA). The redox state of iron (Fe<sup>2+</sup>/ΣFe) was analysed using a wet-chemical technique, which is based on the colorimetric method of Wilson (1960). Both techniques are described below.

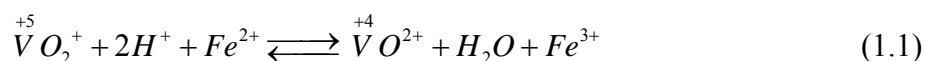
#### 1.3.1 Electron microprobe analysis

Glass fragments from representative samples were mounted in epoxy and polished for electron microprobe analysis. Analytical conditions were 5 nA, 15 kV and a beam diameter of 20 μm, with counting times of 8 s for Si, Al, Fe, Mg, Ca, Mn and Ti on the peak and 4 s on the background and 4 s for K and Na on the peak and 2 s on the background to minimize the lack of alkalis. Cameca supplied standards were used for calibration and PAP matrix correction according to Pouchou and Pichoir (1991) was applied. Between 8 and 20 spot analyses were made on each sample. The results are listed in Table 1.2

### 1.3.2. Ferrous iron analyses

Different wet-chemical techniques have been developed to determine the redox state of iron in geological materials, where most of them employ titration methods for quantification. Conventional techniques usually involve the acid dissolution of 100 to 500 mg of powdered sample material and subsequent precise determination of the absolute ferrous iron concentration. To obtain the  $Fe^{2+}/\Sigma Fe$  ratio, the total iron concentration is commonly determined by a second method, i.e., electron microprobe analysis or optical emission spectroscopy (ICP-OES). In experimental studies the amounts of samples are often limited to <50 mg and this material is subjected to several different analytical methods. This limits the amount of sample available for the wet-chemical ferrous iron determination. Here, we follow the colorimetric method of Wilson (1960) to measure the  $Fe^{2+}/\Sigma Fe$  ratio in mg-sized samples after acid dissolution. The original method was modified to minimize handling of toxic materials (i.e., beryllium sulfate was replaced by boric acid, see below) and to improve the reproducibility. To assess the accuracy and precision of this method, we have analysed international reference materials and in-house standards.

The critical point in ferrous iron analysis is to avoid an oxidation of  $Fe^{2+}$  during the analytical procedure. Here, samples are decomposed in a HF-H<sub>2</sub>SO<sub>4</sub> mixture in presence of excess pentavalent vanadium, which oxidizes ferrous iron as soon as it is released from the sample. According to the reaction



the amount of generated tetravalent vanadium, which is highly resistant to oxidation compared to  $Fe^{2+}$ , is equivalent to the amount of  $Fe^{2+}$  in the sample. The equilibrium of the reaction is shifted to the right hand side under the strongly acidic conditions during sample dissolution (pH < 1). After complete sample dissolution ferrous iron is regenerated from

Table 1.2. Electron microprobe analyses of the starting phono-tephritic glass and the experimental glasses. Analysis of the ferrobasalt SC1 studied by Botcharnikov et al. (2005) is shown for comparison, to highlight compositional differences. Given is the average and the standard deviation (1 $\sigma$ ) of n replicate analyses reported in wt%.

sample	n	SiO <sub>2</sub>	Al <sub>2</sub> O <sub>3</sub>	$\Sigma$ FeO	MgO	CaO	MnO	TiO <sub>2</sub>	Na <sub>2</sub> O	K <sub>2</sub> O	Total	$\Sigma$ FeO norm <sup>b</sup>
<i>phonotephritic starting glass</i>												
Alb-1	31	49.89 ± 0.42	15.57 ± 0.21	7.82 ± 0.32	5.75 ± 0.18	11.40 ± 0.21	0.02 ± 0.09	0.89 ± 0.03	1.95 ± 0.18	7.52 ± 0.16	100.83 ± 0.67	7.75
<i>ferrobasalt from Botcharnikov et. al (2005)</i>												
SC1		48.34 ± 0.29	14.61 ± 0.13	12.91 ± 0.28	6.40 ± 0.11	10.87 ± 0.15	-	2.86 ± 0.05	2.60 ± 0.11	0.30 ± 0.03	99.89 ± 0.67	12.92
<i>experimental products</i>												
Alb1-1	8	48.31 ± 0.40	15.65 ± 0.26	6.09 ± 0.32	5.22 ± 0.17	10.53 ± 0.19	0.04 ± 0.08	0.91 ± 0.06	2.14 ± 0.12	7.47 ± 0.08	96.36 ± 0.83	6.32
Alb1-2	11	46.20 ± 0.27	14.56 ± 0.14	6.92 ± 0.22	5.31 ± 0.10	10.44 ± 0.24	0.01 ± 0.06	0.83 ± 0.06	1.97 ± 0.12	6.90 ± 0.14	93.14 ± 0.62	7.43
Alb1-5 <sup>a</sup>	9	44.42 ± 0.68	13.94 ± 0.16	6.58 ± 0.73	4.93 ± 0.81	10.28 ± 1.56	0.05 ± 0.08	0.80 ± 0.04	1.78 ± 0.19	6.56 ± 0.53	89.35 ± 0.81	7.37
Alb1-8	11	46.82 ± 0.38	14.61 ± 0.18	7.01 ± 0.22	5.26 ± 0.11	10.38 ± 0.22	0.08 ± 0.08	0.83 ± 0.03	1.94 ± 0.12	7.04 ± 0.15	93.96 ± 0.67	7.46
Alb1-6a	11	48.08 ± 0.35	15.08 ± 0.16	6.74 ± 0.36	5.40 ± 0.10	10.91 ± 0.26	0.01 ± 0.08	0.87 ± 0.05	2.02 ± 0.09	7.14 ± 0.14	96.27 ± 0.63	7.00
Alb1-6bis	11	48.54 ± 0.49	15.29 ± 0.18	5.95 ± 0.26	5.50 ± 0.15	10.92 ± 0.25	0.03 ± 0.10	0.91 ± 0.04	2.06 ± 0.24	7.33 ± 0.11	96.55 ± 0.95	6.16
Alb1-14	11	44.56 ± 0.39	13.98 ± 0.16	6.77 ± 0.30	4.94 ± 0.19	9.96 ± 0.20	0.02 ± 0.05	0.79 ± 0.04	1.82 ± 0.10	6.74 ± 0.12	89.58 ± 0.61	7.56
Alb1-20	12	47.28 ± 0.49	14.83 ± 0.24	6.94 ± 0.23	5.44 ± 0.20	10.66 ± 0.26	0.01 ± 0.07	0.86 ± 0.02	2.01 ± 0.11	7.10 ± 0.14	95.14 ± 0.86	7.30
Alb1-23	12	47.06 ± 0.38	14.65 ± 0.15	7.04 ± 0.29	5.20 ± 0.11	10.49 ± 0.25	0.06 ± 0.06	0.84 ± 0.04	1.97 ± 0.11	6.93 ± 0.13	94.24 ± 0.54	7.47
Alb1-25	12	45.47 ± 0.35	14.06 ± 0.13	6.79 ± 0.22	5.00 ± 0.08	9.99 ± 0.16	0.06 ± 0.08	0.82 ± 0.03	1.81 ± 0.16	6.72 ± 0.16	90.73 ± 0.38	7.48
Alb1-26	12	44.77 ± 0.27	14.03 ± 0.19	6.69 ± 0.29	5.14 ± 0.16	9.89 ± 0.27	0.05 ± 0.07	0.79 ± 0.03	1.80 ± 0.14	6.62 ± 0.12	89.78 ± 0.61	7.45
Alb1-41	12	46.42 ± 0.41	14.56 ± 0.25	7.06 ± 0.33	5.27 ± 0.16	10.70 ± 0.24	0.01 ± 0.08	0.83 ± 0.04	1.81 ± 0.08	7.12 ± 0.13	93.78 ± 0.69	7.53
Alb1-H42	15	45.57 ± 0.35	14.18 ± 0.21	6.85 ± 0.25	5.03 ± 0.13	10.32 ± 0.28	0.02 ± 0.10	0.83 ± 0.03	1.77 ± 0.13	7.06 ± 0.11	91.66 ± 0.58	7.47
Alb1-H43	18	45.28 ± 0.35	14.22 ± 0.18	7.03 ± 0.33	5.21 ± 0.15	10.34 ± 0.27	0.06 ± 0.06	0.83 ± 0.05	1.87 ± 0.12	7.04 ± 0.15	91.86 ± 0.75	7.65
Alb1-H44	13	46.69 ± 0.41	14.63 ± 0.20	6.91 ± 0.39	5.36 ± 0.13	10.75 ± 0.21	0.01 ± 0.05	0.87 ± 0.06	1.91 ± 0.15	7.18 ± 0.17	94.31 ± 0.72	7.33
Alb1-H45	16	47.39 ± 0.83	14.98 ± 0.23	6.32 ± 0.35	5.29 ± 0.28	10.78 ± 0.31	0.03 ± 0.06	0.87 ± 0.05	1.87 ± 0.14	7.42 ± 0.19	94.95 ± 1.39	6.65
Alb1-H47	12	45.60 ± 0.27	14.18 ± 0.24	6.17 ± 0.24	5.14 ± 0.18	10.46 ± 0.24	-0.03 ± 0.08	0.87 ± 0.02	1.79 ± 0.14	7.10 ± 0.12	91.32 ± 0.65	6.75
Alb1-H48	14	46.24 ± 0.45	14.46 ± 0.16	6.40 ± 0.16	5.23 ± 0.11	10.37 ± 0.19	0.01 ± 0.07	0.84 ± 0.03	1.90 ± 0.22	7.13 ± 0.15	92.60 ± 0.47	6.91
Alb1-H49	16	46.97 ± 0.56	14.80 ± 0.24	5.52 ± 0.35	5.32 ± 0.16	10.64 ± 0.29	0.03 ± 0.07	0.86 ± 0.04	1.87 ± 0.15	7.37 ± 0.16	93.40 ± 0.71	5.91
Alb1-H50	16	48.01 ± 0.39	15.13 ± 0.21	4.72 ± 0.32	5.41 ± 0.15	10.83 ± 0.18	0.02 ± 0.06	0.85 ± 0.04	1.95 ± 0.15	7.56 ± 0.17	94.49 ± 0.59	5.00
Alb1-H51	20	47.93 ± 0.97	15.22 ± 0.23	4.50 ± 0.34	5.57 ± 0.15	10.95 ± 0.25	0.01 ± 0.08	0.89 ± 0.05	1.91 ± 0.18	7.60 ± 0.17	94.61 ± 1.29	4.76

a) Analysis represents glass and quench crystals (see text).

b)  $\Sigma$ FeO concentration in the glasses recalculated to a water-free basis (normalised to a sum of 100).

tetravalent vanadium by increasing the pH value to ~5, which shifts the equilibrium of reaction 1.1 to the left hand side.

The analytical procedure is as follows (employed reagents are listed in appendix A1.1): The powdered sample (in case of reference materials) or sub-millimeter-sized glass fragments (from experimental products) were weighed into a 15-mL Savillex® Teflon beaker containing 1 mL of an ammonium vanadate solution dissolved in sulfuric acid (1M to 5M H<sub>2</sub>SO<sub>4</sub>). After addition of 1 mL HF (24 or 48%), the beakers were tightly sealed and placed in an ultrasonic bath for ca. 15 minutes. Thereafter, the beakers were left for 3 to 24 hours at temperatures between 20 to 100°C until complete sample dissolution was attained. Acid concentrations, dissolution time and temperature were systematically varied to test for potential effects of these parameters on the analytical results (see discussion below). After sample dissolution, 5 mL saturated hot boric acid (at ~80°C) was added, instead of beryllium sulfate as proposed by Wilson (1960), to neutralize excess HF and to bring possibly formed fluorides back into solution. Upon cooling to room temperature the content of the beaker was quantitatively transferred into a 100-mL volumetric flask, containing 10 mL ammonium acetate solution, 5 mL 2:2'-bipyridyl solution, and the remaining volume was filled with distilled water. The ammonium acetate buffer adjusted the pH value to ~5. The regenerated Fe<sup>2+</sup> forms a very stable complex with 2:2'-bipyridyl in the solution which shows an intensive absorption band in the visible spectrum (Fig. 1.1).

Measurements of ferrous Fe and total Fe were made on the same solution before and after adding 5 to 10 mg solid hydroxylamine hydrochloride to an aliquot of about 10 mL. This reducing agent converts all ferric Fe into the ferrous state. Since both Fe<sup>2+</sup> and total Fe are measured in the same solution, the Fe<sup>2+</sup>/ΣFe ratio can be directly calculated by dividing the absorbances of the Fe<sup>2+</sup> and total Fe aliquots. The advantage compared to an absolute concentration measurement of ferrous iron and an additional total Fe determination by



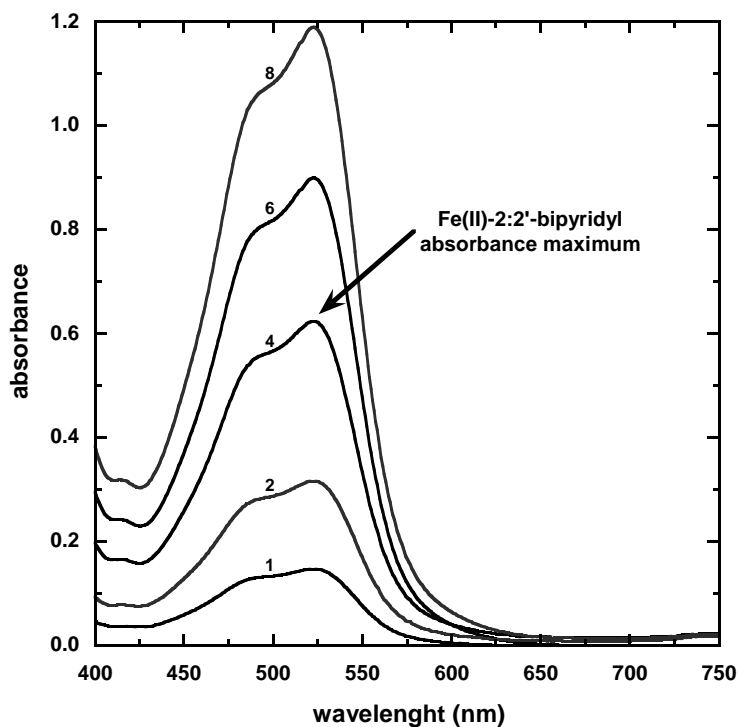


Figure 1.1. UV/VIS spectra of Fe(II)-2:2'-bipyridyl solutions. Ferrous iron concentrations are indicated (in  $\mu\text{g/mL Fe}$ ). Spectra recorded in 1 cm transmission cells.

another method (e.g., EMPA or ICP-OES) is that uncertainties in the  $\text{Fe}^{2+}/\Sigma\text{Fe}$  ratios arise mainly from the spectroscopic measurements, whereas weighing and dilution errors cancel out. Absolute concentrations were obtained as well after calibration of the spectrometric technique using ferrous ammonium sulfate solutions with different known  $\text{Fe}^{2+}$  concentrations. For all measurements 1 cm transmission cells and an UV/VIS spectrometer (Zeiss Specord S10) was used. The sample solutions show a characteristic absorption band at about 523 nm of the Fe(II)-2:2'-bipyridyl complex (Figure 1.1). The maximum peak height was determined relative to a baseline measured at 700 nm. No differences in the general appearance of the spectra and in the maximum peak position were observed between samples of different matrices, i.e. basaltic to rhyolitic rocks or pure Fe(II) solutions.

The results of the wet-chemical colorimetric iron analyses on international reference materials and in-house standards are given in Table 1.3. To assess the accuracy of the method, our results are compared to the recommended values obtained by other studies (Govindaraju,

1994; Govindaraju, 1995; Liebske et al., 2003; Bertoldi et al., 2007). There is good agreement between the recommended  $\text{Fe}^{2+}/\Sigma\text{Fe}$  ratios and the values obtained by this study (Figure 1.2). Furthermore, the results of our in-house standard PU-3 are in good agreement with measurements reported by Liebske et al. (2003). They analysed a synthetic andesitic glass similar in composition and synthesis conditions (1600°C, air atmosphere) to our PU-3. Noteworthy, the  $\text{Fe}^{2+}/\Sigma\text{Fe}$  ratios obtained for the granites GS-N and GA are significantly higher than the recommended values. Furthermore, the  $\Sigma\text{FeO}$  values ( $\Sigma\text{FeO}$  refers to total iron expressed as wt% FeO) of those samples are also systematically lower than the recommended values. Undissolved refractory minerals containing significant amounts of ferric iron may explain the discrepancy for these particular samples. The experimental products analysed in this study consist primarily of glass, which is readily dissolved within a few hours at room temperature. Thus, no attempts were made to optimise the method for analyses of highly resistant minerals, although this would be principally possible given some minor modifications and tests.

For the two reference materials, natural olivine and commercial ammonium iron(II) sulfate hexahydrate, the expected  $\text{Fe}^{2+}/\Sigma\text{Fe}$  ratios are close to unity (Table 1.3). The measured values of  $0.93\pm 0.08$  and  $0.95\pm 0.05$  ( $2\sigma$ ), respectively, are systematically lower, while for chlorite CA the reported value of  $0.90\pm 0.02$  from Bertoldi et al. (2007) is still well reproduced by our measurements ( $0.89\pm 0.04$ ). To test whether exclusion of atmospheric oxygen improves the recovery yield, some samples were dissolved under Ar atmosphere, but no difference in the  $\text{Fe}^{2+}/\Sigma\text{Fe}$  ratios was found. Whipple (1974) and later Yokoyama and Nakamura (2002) noted that variable concentrations of sulphuric acid and hydrofluoric acid may affect the accuracy of the measured  $\text{Fe}^{2+}/\Sigma\text{Fe}$  ratio as well. We have varied acid concentrations in the range from 1M to 5M  $\text{H}_2\text{SO}_4$  and 24% to 48% HF, respectively, but did

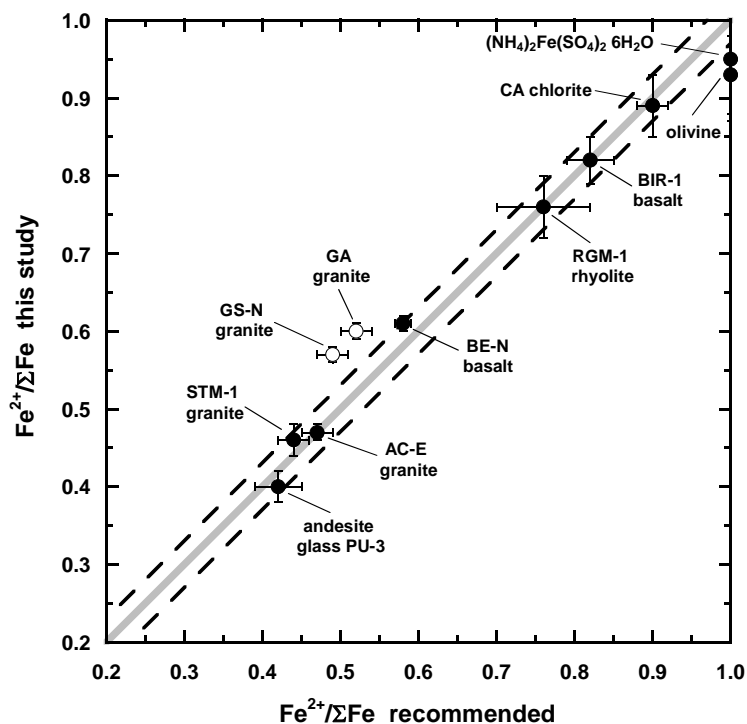


Figure 1.2. Comparison of measured  $\text{Fe}^{2+}/\Sigma\text{Fe}$  ratios from this study with other studies (recommended values). Open symbols refer to incomplete sample dissolution (see text). Solid line represents a 1:1 correlation. Dashed lines indicate the interval  $\pm 0.03$ .

not observe any systematic bias on the results. The potential effect of sample decomposition temperature on the  $\text{Fe}^{2+}/\Sigma\text{Fe}$  ratio was also studied (Table 1.3), since the dissolution kinetics at room temperature could be more sluggish for some rock samples. Results obtained from samples dissolved at  $25^\circ\text{C}$  are indistinguishable from those at  $100^\circ\text{C}$ , except for the granitic sample GS-N, as discussed above.

The precision of the method can be evaluated from replicate measurements (Table 1.3). Reproducibility was between  $\pm 0.01$  and  $\pm 0.05$  ( $2\sigma$ ) in the  $\text{Fe}^{2+}/\Sigma\text{Fe}$  ratio for different rocks and minerals containing between 8 and 1 wt% ferrous FeO. The long term reproducibility (over a time period of about one year) was assessed from  $n = 33$  replicate analyses of the synthetic andesitic glass PU-3. Based on these measurements the uncertainty assigned to the  $\text{Fe}^{2+}/\Sigma\text{Fe}$  ratios is  $\pm 0.03$  ( $2\sigma$ , external precision).

Table 1.3. Results of wet-chemical colorimetric iron analyses on international reference materials and in-house standards.

sample description	this study				recommended values														
	sample weight <sup>a</sup> (mg)	T <sup>b</sup> (°C)	n <sup>c</sup>	$\frac{\text{Fe}^{2+}}{\Sigma\text{Fe}}$ (2 $\sigma$ )	$\frac{\Sigma\text{FeO}}{\Sigma\text{Fe}}$ (wt%) (2 $\sigma$ )	ferrous FeO (wt%) (wt%) (2SE) (2 $\sigma$ )	$\frac{\text{Fe}^{2+}}{\Sigma\text{Fe}}$ (2SE) (2 $\sigma$ )	$\frac{\Sigma\text{FeO}}{\Sigma\text{Fe}}$ (wt%) (wt%) (2SE) (2 $\sigma$ )	ferrous FeO (wt%) (wt%) (2SE) (2 $\sigma$ )	Ref.									
<i>international reference materials</i>																			
BIR-1 basalt	6-7	20	9	0.82	0.03	10.20	0.21	8.35	0.35	0.82	n.a.	0.03	10.17	n.a.	0.22	8.34	n.a.	0.20	(1)
BE-N basalt	6-7	20	3	0.61	0.01	11.53	0.22	6.98	0.26	0.58	0.01	0.06	11.55	0.05	0.63	6.74	0.08	0.60	(2)
RGM-1 calc-alkaline rhyolite	19-22	20	15	0.76	0.04	1.63	0.05	1.25	0.06	0.76	n.a.	0.06	1.67	n.a.	0.05	1.27	n.a.	0.10	(1)
RGM-1 calc-alkaline rhyolite	19-23	100	3	0.78	0.02	1.63	0.04	1.28	0.07	0.76	n.a.	0.06	1.67	n.a.	0.05	1.27	n.a.	0.10	(1)
STM-1 peralkaline nepheline syenite	10-11	20	9	0.49	0.02	4.23	0.20	2.05	0.11	0.44	n.a.	0.02	4.70	n.a.	0.18	2.09	n.a.	0.06	(1)
STM-1 peralkaline nepheline syenite	10-12	100	3	0.46	0.02	4.63	0.10	2.15	0.05	0.44	n.a.	0.02	4.70	n.a.	0.18	2.09	n.a.	0.06	(1)
GS-N granite	15-21	20	5	0.63	0.04	2.88	0.34	1.82	0.10	0.49	0.02	0.12	3.37	0.04	0.25	1.65	0.07	0.38	(2)
GS-N granite	15-22	100	4	0.57	0.01	3.28	0.05	1.86	0.04	0.49	0.02	0.12	3.37	0.04	0.25	1.65	0.07	0.38	(2)
GA granite	20-21	20	5	0.61	0.01	2.28	0.11	1.39	0.06	0.52	0.02	0.11	2.55	0.05	0.38	1.32	0.04	0.18	(2)
GA granite	20-22	100	4	0.60	0.01	2.40	0.11	1.44	0.06	0.52	0.02	0.11	2.55	0.05	0.38	1.32	0.04	0.18	(2)
AC-E granite	20-21	20	2	0.47	0.01	2.19	0.04	1.04	0.01	0.47	0.02	0.12	2.28	0.02	0.23	1.07	0.04	0.26	(2)
AC-E granite	20-21	100	4	0.49	0.01	2.22	0.07	1.08	0.03	0.47	0.02	0.12	2.28	0.02	0.23	1.07	0.04	0.26	(2)
<i>in-house standards</i>																			
PU-3 <sup>d</sup> andesite glass (syn.)	5-9	20	33	0.39	0.03	7.44	0.15	2.87	0.24	0.42	n.a.	0.03	7.49	0.15	0.34	3.15	n.a.	0.21	(3,4)
PU-3 <sup>d</sup> andesite glass (syn.)	5-9	100	4	0.40	0.02	7.20	0.44	2.86	0.28	0.42	n.a.	0.03	7.49	0.15	0.34	3.15	n.a.	0.21	(3,4)
CT-1 <sup>e</sup> basalt glass (syn.)	5-6	20	8	0.39	0.03	12.78	0.23	5.02	0.29	n.a.	n.a.	n.a.	12.85	0.19	0.44	n.a.	n.a.	n.a.	(4)
CA chlorite	1.5	20	3	0.89	0.04	39.96	1.35	35.8	1.67	0.90	n.a.	0.02	41.56	0.12	0.79	37.32	0.11	0.71	(5)
olivine Mg <sub>0.829</sub> Fe <sub>0.171</sub> SiO <sub>4</sub> (natural)	3-6	20	13	0.93	0.05	8.30	0.74	7.75	0.74	1.00	n.a.	n.a.	8.38	0.06	0.07	8.38	0.06	0.07	(4,6)
ammonium iron(II) sulfate hexahydrate (NH <sub>4</sub> ) <sub>2</sub> Fe(SO <sub>4</sub> ) <sub>2</sub> · 6H <sub>2</sub> O (Merck, p.a.)	1-2	20	11	0.95	0.08	18.46	0.70	17.57	1.50	1.00	n.a.	n.a.	18.42	n.a.	n.a.	18.42	n.a.	n.a.	(6)

a) Range of sample weight used for analyses. b) Decomposition temperature. c) Number of replicate analyses.

d) Electron microprobe analysis of synthetic glass CT-1 (wt%): SiO<sub>2</sub> 47.40, Al<sub>2</sub>O<sub>3</sub> 14.24, FeO<sub>total</sub> 12.85, MgO 6.25, CaO 10.79, Na<sub>2</sub>O 2.68, K<sub>2</sub>O 0.32, TiO<sub>2</sub> 3.17

e) Electron microprobe analysis of synthetic glass PU-3 (wt%): SiO<sub>2</sub> 54.72, Al<sub>2</sub>O<sub>3</sub> 16.80, FeO<sub>total</sub> 7.49, MgO 4.15, CaO 9.00, Na<sub>2</sub>O 3.32, K<sub>2</sub>O 1.54, TiO<sub>2</sub> 0.79, MnO 0.12

References for recommended values: (1) Govindaraju (1994), (2) Govindaraju (1995), (3) Fe<sup>2+</sup>/ΣFe value calculated from ferrous iron analyses of sample Unzen-A given by Liebske et al. (2003), (4) ΣFeO values were measured by electron microprobe analysis (this study); FeO value of PU-3 calculated from ΣFeO (this study) and Fe<sup>2+</sup>/ΣFe from Liebske et al. (2003). (5) Bertoldi et al. (2007), (6) ΣFeO (= ferrous FeO) calculated from stoichiometry.

Despite the low sample mass used for wet-chemical analyses, the obtained  $\Sigma\text{FeO}$  agree well with electron microprobe analyses for experimental products and recommended values for the reference materials, most of them within <5% relative (Tables 1.1, 1.2 and 1.3). Thus, we conclude that the  $\text{Fe}^{2+}/\Sigma\text{Fe}$  ratio can be reliably determined in the range from 0.4 to 0.9 by our method. All  $\text{Fe}^{2+}/\Sigma\text{Fe}$  ratios of our experimental run products fall within this range. Procedural blanks were always below the detection limit of the method, i.e. <0.012 absorbance units ( $3\sigma$  of the background), which corresponds to less than 1  $\mu\text{g}$  Fe. This can be considered negligible relative to the processed amount of iron (100 to 500  $\mu\text{g}$  Fe), since the maximum bias in the measured  $\text{Fe}^{2+}/\Sigma\text{Fe}$  would be <0.01.

#### 1.4. RESULTS

Except for one sample (Alb1-1) with very low water content, which was probably at the liquidus and thus partially crystallized, all experiments with less than 6 wt% of dissolved water in the melt yield only glass and a fluid phase as experimental products (Fig. 1.3a, b). All melts with higher water contents contain crystals after quench. These crystals show typical features of non-equilibrium growth and were probably formed during quenching (Fig. 1.3c, d). The crystals were too small for a reliable quantitative microprobe analysis but semi-quantitative results, obtained by energy dispersive x-ray analyses (EDX), indicate a K-rich, Fe-bearing composition (Fig. 1.3d). X-ray powder diffraction on sample Alb1-5 gives evidence that the quench phases are mica. In experimental studies using basaltic melts under similar conditions no quench crystals were observed (e.g., Berndt et al., 2002; Botcharnikov et al., 2005). This discrepancy may be explained by the high potassium

content of the phono-tephrite facilitating K-rich mica crystallization from a H<sub>2</sub>O-rich melt of relatively low viscosity during cooling.

The results of electron microprobe analyses of representative post experimental glasses are given in Table 1.2. Sample Alb1-5 consists of glass and numerous quench crystals (Fig. 1.3d). Thus, the analyses were performed using a defocused electron beam (20  $\mu$ m) and represent the bulk composition. After normalizing to a sum of 100 wt% (i.e., anhydrous composition) most of the glass compositions are identical to the starting glass (Alb-1) and electron microprobe analyses show homogeneous  $\Sigma$ FeO concentrations in the glasses. Furthermore, from these data no indication for extensive dissolution of cations from the melt into the fluid phase is given. However, some samples (Alb1-1, Alb1-6a, Alb1-6bis, Alb1-H45, Alb1-H47 to Alb1-H51, Alb1-H56) have significantly lower  $\Sigma$ FeO (compare  $\Sigma$ FeO<sub>norm</sub> in Table 1.2 for samples with different water contents). These experiments were carried out under the most reducing conditions and at the lowest  $a_{\text{H}_2\text{O}}$ . At these conditions iron from the samples was partly dissolved as metallic Fe alloy in the capsule walls. As a consequence of the reduction of ferric and ferrous iron from the melt a small amount of oxygen is produced which reacts with hydrogen permeating from the pressure medium into the capsule forming some additional H<sub>2</sub>O. The generated H<sub>2</sub>O might have continuously increased the water activity and hence the oxygen fugacity within the capsule. The largest iron loss was observed for sample Alb1-H51 with a final  $\Sigma$ FeO of  $\sim$ 4.2 wt%. The corresponding increase in water content of the system was 0.5 mg. Considering the masses of glass, fluid and the partitioning of H<sub>2</sub>O between fluid and melt,  $f_{\text{O}_2}$  increased by about half a log unit during the experiment. The rate of iron reduction is controlled most likely by

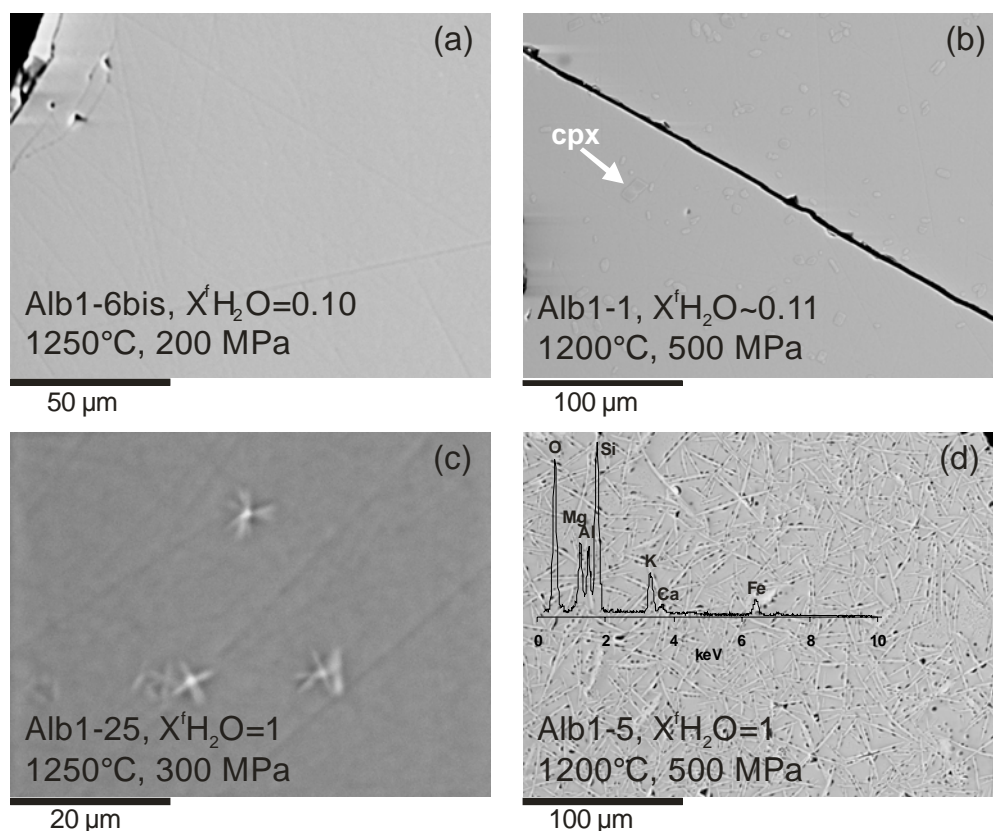


Figure 1.3. Representative backscattered electron images of experimental run products. (a) Glasses with water contents of less than about 6 wt% were crystal-free (Table 1.1), except of experiment Alb1-1 (b), where clinopyroxene crystallized during the experiment. (c, d) Experiments with water contents of more than about 6 wt% contained mica quench-crystals (Table 1.1) that were formed during cooling at the end of the experiments. An EDX spectrum of a needle-like mica is shown as inset in (d).

the sluggish diffusion of Fe in the silicate melt. Fe diffusion is much slower than water and hydrogen diffusion in the melt (Behrens et al., 2004; Gaillard et al., 2002; Watson and Baxter, 2007) and, therefore, we suggest that  $\text{Fe}^{2+}/\Sigma\text{Fe}$  is in near-equilibrium with the oxygen fugacity imposed by the fluid via the reaction  $2 \text{Fe(II)O} + \text{H}_2\text{O} = \text{Fe(III)}_2\text{O}_3 + \text{H}_2$ .

#### 1.4.1. Redox state of iron

The results of Fe redox analyses of the experimental run products are given in Table 1.1. The measured  $\text{Fe}^{2+}/\Sigma\text{Fe}$  ratios range from 0.41 at 1250°C, 200 MPa, NNO+2.6 (Alb1-15) to 0.85 at 1200°C, 200 MPa, NNO-2.9. A comparison of run P and run Q at 1200°C, 200 MPa with durations of 5 and 1.5 hours, respectively, reveals consistent results

in terms of the redox state of iron. This finding and the homogeneous Fe concentration in the run products (Table 1.3) suggest that the system is close to equilibrium, in terms of both chemical and redox equilibrium, after 1.5 hours at 1200°C. This is also consistent with a study on Fe redox kinetics in peralkaline hydrous rhyolitic melts (Gaillard et al., 2002), revealing that redox kinetics are fast enough to equilibrate the melt within 3 hours at 800°C, but slow enough to readily quench the  $\text{Fe}^{2+}/\Sigma\text{Fe}$  ratio of the melt in the experiments.

As mentioned above some samples are partially crystallized. Since the  $\text{Fe}^{2+}/\Sigma\text{Fe}$  analyses were done upon complete dissolution of fragments of the experimental products (including quench crystals) they represent bulk values for the quenched melts, assuming that the bulk  $\text{Fe}^{2+}/\Sigma\text{Fe}$  of the system is not significantly altered due to crystallization of Fe bearing mica during cooling. Despite an almost instantaneous permeation of  $\text{H}_2$  from the pressure medium through the capsule walls and a transfer of Fe from the melt to the crystals during cooling, at an initial quench rate of about 150 °C/s only a few seconds remain for a potential re-equilibration of the melt until the kinetics of the systems can be considered as virtually frozen, i.e., at  $T < 500^\circ\text{C}$ . During this time interval no significant change in the bulk  $\text{Fe}^{2+}/\Sigma\text{Fe}$  ratio is expected from redox kinetics (Gaillard et al., 2002) and thus the measured Fe redox ratios are considered to represent close-to-equilibrium values.

As shown in Figure 1.4, the  $\text{Fe}^{2+}/\Sigma\text{Fe}$  ratio decreases nonlinearly with increasing mole fraction of water in the coexisting fluid phase ( $X^f\text{H}_2\text{O}$ ). The change in  $\text{Fe}^{2+}/\Sigma\text{Fe}$  with  $X^f\text{H}_2\text{O}$  is more marked at oxygen fugacities  $> \text{NNO}-0.2$  compared to the series at  $< \text{NNO}-0.2$ . At constant temperature, pressure,  $X^f\text{H}_2\text{O}$  and water content, the  $\text{Fe}^{2+}/\Sigma\text{Fe}$  ratio increases with decreasing  $f\text{O}_2$  (Fig. 1.5).



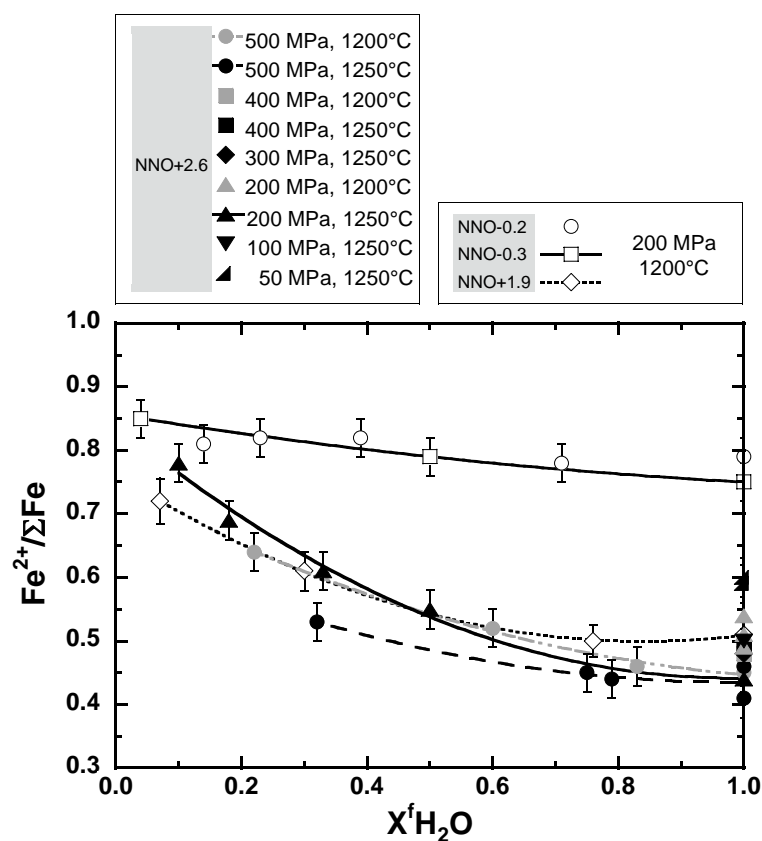


Figure 1.4. Oxidation state of iron as a function of  $\text{H}_2\text{O}$  mole fraction in the fluid. Lines represent second order polynomials for selected data sets to illustrate the non-linear relationships. Oxygen fugacity is expressed relative to the Ni-NiO buffer (NNO) and the given values represent the maximum  $\log f\text{O}_2$  values in the runs ( $X^f\text{H}_2\text{O} = 1$ ), i.e.,  $f\text{O}_2$  in the capsule is lower at  $X^f\text{H}_2\text{O} < 1$ .

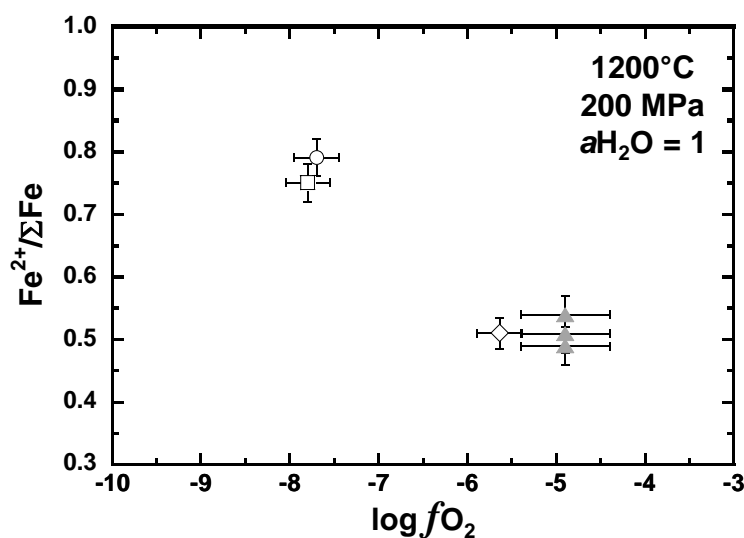


Figure 1.5. Oxidation state of iron as a function of  $\log f\text{O}_2$  for experiments at  $1200^\circ\text{C}$ , 200 MPa and pure  $\text{H}_2\text{O}$  fluid. Symbols as in Fig. 1.4.

## 1.5. DISCUSSION

### 1.5.1. Influence of oxygen fugacity and dissolved water on the speciation of iron

The main factors controlling the oxygen fugacity in the system are the water activity in the capsule and the hydrogen fugacity ( $fH_2$ ) in the IHPV at given P, T and melt composition. Permeability of hydrogen through the capsule walls is high at our experimental conditions facilitating  $fH_2$  equilibration between the capsule interior and the vessel atmosphere. The time needed to permeate the amount of  $H_2$  required for reduction of all ferric iron in the starting glass ( $Alb1 Fe^{2+}/\Sigma Fe = 0.29$ ) is less than two minutes based on permeation data for Au tubes (Chou, 1986). Assuming a negligible effect of reactions between carbon-bearing species on redox conditions at T and P of this study, the prevailing oxygen fugacity within the capsule is mainly determined by the dissociation reaction of water ( $H_2O = H_2 + \frac{1}{2} O_2$ ) for which the equilibrium constant can be expressed as

$$K_w = fH_2O / fH_2 \cdot fO_2^{0.5} \quad (1.2)$$

and the logarithm of oxygen fugacity is given as

$$\log fO_2 = 2 \log fH_2O - 2 \log fH_2 - 2 \log K_w . \quad (1.3)$$

$K_w$  was derived from thermodynamic data of Robie et al. (1978). The water fugacity in the capsule is the product of water activity ( $a_{H_2O}$ ) and standard state water fugacity ( $f^\theta_{H_2O}$ ). If the experimental pressure is chosen as standard state,  $f^\theta_{H_2O}$  equals the fugacity of the pure  $H_2O$  fluid and the water activity is calculated as  $a_{H_2O} = \gamma^f_{H_2O} \cdot X^f_{H_2O}$  where  $\gamma^f_{H_2O}$  is the activity coefficient of  $H_2O$  in the fluid. Activity coefficients of  $H_2O$  for mixed  $H_2O$ - $CO_2$  fluids were computed for given P, T,  $X^f_{H_2O}$  after Aranovich and Newton (1999) using molar

volumes of pure H<sub>2</sub>O and CO<sub>2</sub> from Pitzer and Sterner (1994). These calculations are only valid assuming that H<sub>2</sub>O and CO<sub>2</sub> are the dominant species in the fluid, which is a reasonable assumption for most of our experimental conditions (Botcharnikov et al., 2006, and references therein). However, especially at very reducing conditions, other species (e.g., CO, H<sub>2</sub>, CH<sub>4</sub>) can become more abundant. Except for sample Alb1-H56, no indication of an abrupt drop in CO<sub>2</sub> solubility in the melts with decreasing  $fO_2$  was observed (see appendix A1.2: Fig. A1.1) that would indicate a change of the dominant carbon species in the fluid. The anomalously low CO<sub>2</sub> concentration in the melt of sample Alb1-H56 indicates a lower prevailing  $fCO_2$  in the capsule than calculated by mass balance. A value of  $\sim 0.38$  is estimated for  $X^fCO_2$  from the relation between CO<sub>2</sub> concentration in the melt and  $X^fCO_2$  (Fig. A1.1). Assuming that the additional fluid component is mainly CO (Holloway and Blank, 1994) the fluid composition was recalculated to  $X^fH_2O \sim 0.04$  and  $X^fCO \sim 0.58$ . Based on the recalculated  $X^fH_2O$  the oxygen fugacity is  $\Delta NNO-2.9$ . For sample Alb1-1 the fluid composition could not be determined and  $X^fH_2O$  was estimated to be 0.11, using the measured H<sub>2</sub>O and CO<sub>2</sub> contents (0.94 and 0.90 wt%, respectively) and the CO<sub>2</sub> and H<sub>2</sub>O saturation curves at 500 MPa and 1200°C (Figures A1.1a and A1.2a).

The calculated oxygen fugacities are listed in Table 1.1. Additionally, the difference relative to the Ni-NiO ( $\Delta NNO$ ) buffer is given (Huebner and Sato, 1970). This allows a direct comparison of the experiments equilibrated at different temperatures and pressures to evaluate the effect of  $fO_2$  on the redox state of iron in the silicate melts. In Figure 1.6 the iron redox state (expressed as  $Fe^{3+}/Fe^{2+}$  ratio) is plotted as a function of oxygen fugacity ( $\Delta NNO$ ).

The data show a monotonous increase in  $Fe^{3+}/Fe^{2+}$  with  $\Delta NNO$ . The scatter of the data is due to superimposed variations in water content and experimental pressure as discussed below.

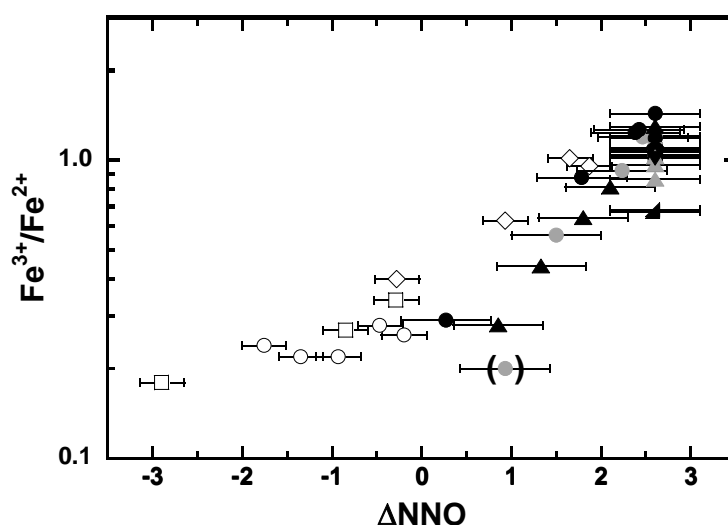


Figure 1.6. The dependence of the  $\text{Fe}^{3+}/\text{Fe}^{2+}$  ratio on oxygen fugacity expressed relative to the NNO buffer. Note the logarithmic scaling. Alb1-1 (in parentheses) is the only sample containing clinopyroxene crystals (see text). Symbols as in Fig. 1.4.

The experiment Alb1-1 deviates noticeably from the trend (Fig. 1.6). This sample with very low water content (0.94 wt%  $\text{H}_2\text{O}$ ) contains clinopyroxene crystals that may bias the measured iron redox ratio. Therefore, this sample is not considered further on in the systematics of the redox state of the melt. As shown in Fig. 1.7 the  $\text{Fe}^{2+}/\Sigma\text{Fe}$  ratios determined for the phono-tephritic melts are in general agreement with the predictions of the models of Kress and Carmichael (1991) and Moretti (2005). The dependence of the  $\text{Fe}^{3+}/\text{Fe}^{2+}$  ratio on  $\log f\text{O}_2$  at pressures of 200 MPa and 500 MPa and temperatures of 1200°C and 1250°C is shown in Figures 1.8. In such a plot, a slope of 0.25 is expected according to the reaction  $\text{Fe(II)O}_{\text{melt}} + \frac{1}{4} \text{O}_2_{\text{gas}} = \text{Fe(III)O}_{1.5 \text{ melt}}$ . This slope is also implemented in the thermodynamic model of Moretti (2005), whereas Kress and Carmichael obtained a slope close to 0.2 for their empirical modelling.

Considering the experiments done at relatively oxidizing conditions (IHPV intrinsic;  $f\text{H}_2 \sim 0.6$ ; Fig. 1.8a, b, d), the slope defined by the data points at given P, T and  $f\text{H}_2$  is 0.31 (1200°C, 500 MPa), 0.28 (1250°C, 500 MPa) and 0.37 (1200°C, 500 MPa), respectively,

which is much larger than expected. This finding is consistent with a positive dependence of the  $\text{Fe}^{3+}/\text{Fe}^{2+}$  ratio on the  $\text{H}_2\text{O}$  concentration (Fig. 1.8d) in the melt as suggested by Moretti (2005). The data obtained at  $1200^\circ\text{C}$ , 200 MPa (Fig. 1.8c) define a much smaller slope of 0.16. Here, due to different  $f\text{H}_2$  the oxygen fugacity is not directly correlated with the water fugacity over the entire experimental  $f\text{O}_2$  range.

Comparison of our data for phono-tephrite with the results of Botcharnikov et al. (2005) for ferrobasalt studied at similar conditions can be used to evaluate the effect of the chemical composition on the redox state of iron in mafic melts. The phono-tephrite has much higher  $\text{K}_2\text{O}$  content (0.3 vs. 7.5 wt%) and lower  $\Sigma\text{FeO}$  content (12.9 vs. 7.8 wt%) than the ferrobasalt (Table 1.2). The comparison between our experimental dataset at  $1200^\circ\text{C}$  and 200 MPa and the data from Botcharnikov et al. (2005) for hydrous ferrobasaltic melts obtained at the same P-T conditions (Fig. 1.7c) reveal slightly higher  $\text{Fe}^{3+}/\text{Fe}^{2+}$  ratios of the ultrapotassic hydrous melts relative to the ferrobasaltic melts.

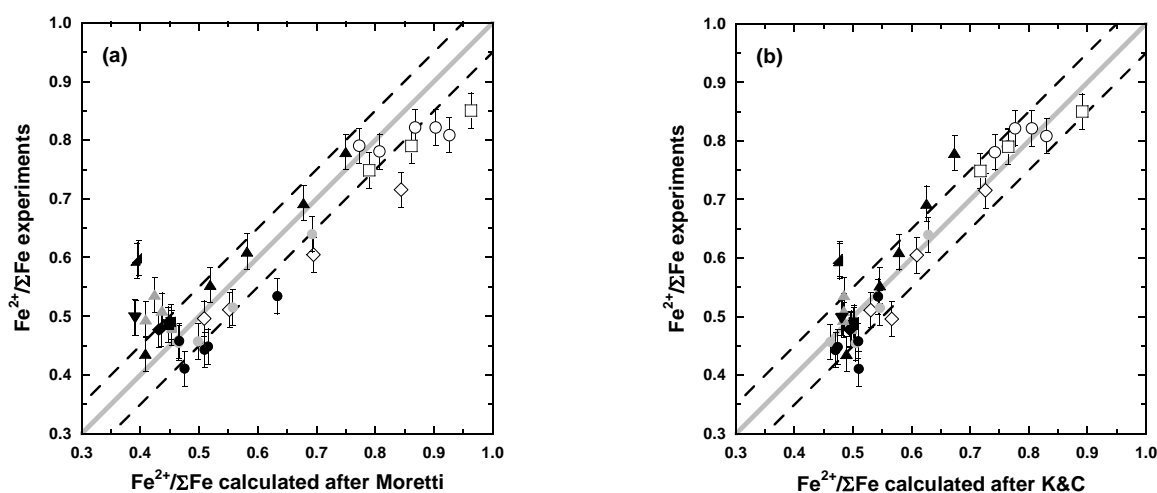


Figure 1.7. Comparison between measured and calculated  $\text{Fe}^{2+}/\Sigma\text{Fe}$  ratios from the experiments and models of (a) Moretti (2005) and (b) Kress and Carmichael (1991), respectively. The solid line is a 1:1 correlation and the dashed lines represent an envelope of  $\pm 0.05$ . Symbols as in Fig. 1.4.

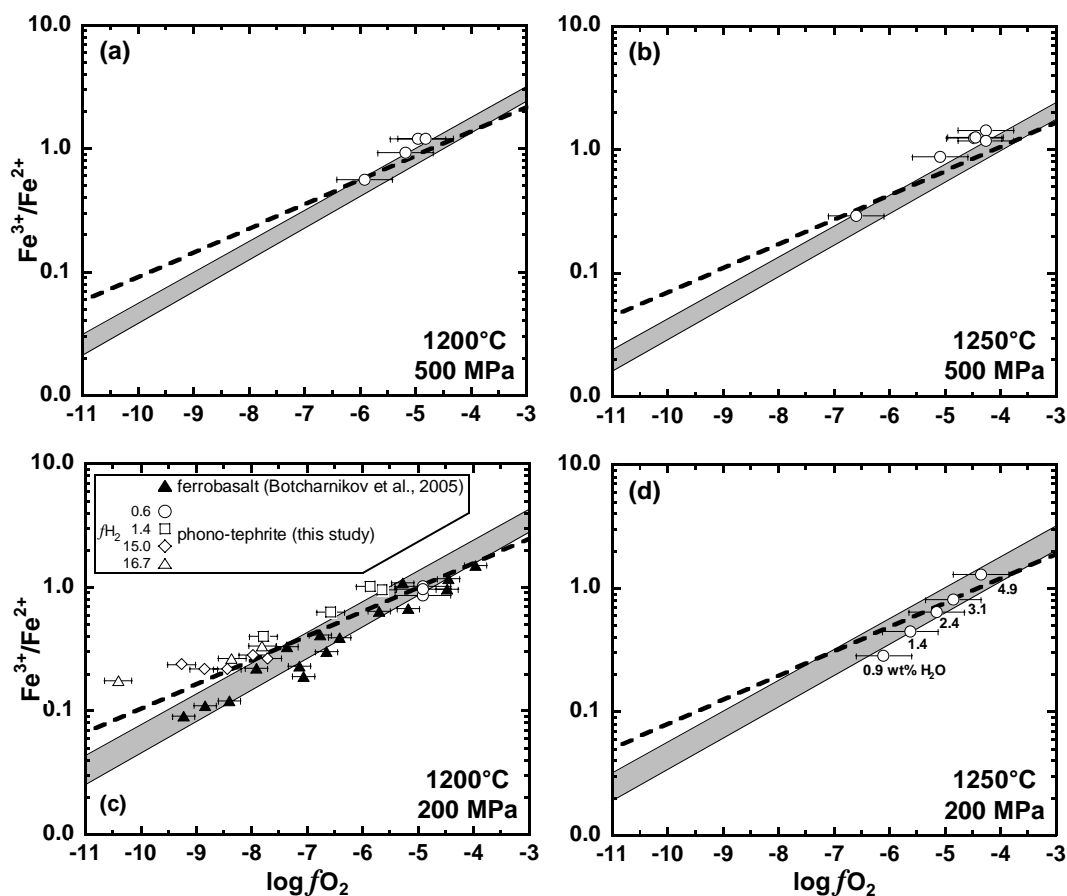


Figure 8.  $\text{Fe}^{3+}/\text{Fe}^{2+}$  ratio as a function of  $\log f\text{O}_2$  in comparison with the predictions of the empirical model of Kress and Carmichael (1991) (dashed lines) and the thermodynamic model of Moretti (2005) (grey areas) for the phono-tephritic melt at 200 and 500 MPa. All data in (a), (b) and (d) are all for constant hydrogen fugacity ( $f\text{H}_2 \sim 0.6$  bar) while for data shown in (c) the hydrogen fugacity varied from 0.6 to 16.7 bar (measured values). The model of Moretti (2005) takes the effect of water contents into account and the lower and upper limits of the grey areas comprise the range from 0 to 10 wt%  $\text{H}_2\text{O}$  at 500 MPa (a, b) and from 0 to 5 wt%  $\text{H}_2\text{O}$  at 200 MPa (c, d). This range covers the measured water concentrations in the experimental glasses. For comparison the experimental data of Botcharnikov et al. (2005) for hydrous ferrobasaltic melts are shown (c).

This effect is more pronounced at lower  $f\text{O}_2$ . From linear regressions through each of the two datasets the differences in  $\text{Fe}^{2+}/\Sigma\text{Fe}$  ratios can be quantified. At a  $\log f\text{O}_2$  of -9 the  $\text{Fe}^{2+}/\Sigma\text{Fe}$  ratio of the phono-tephrite is 0.08 lower than that of the ferrobasalt. At more oxidizing conditions of  $\log f\text{O}_2$  of -5 this difference decreases to a value of 0.01. This trend is consistent with the model of Kress and Carmichael (1991) which predicts a decrease of the  $\text{Fe}^{2+}/\Sigma\text{Fe}$  ratio with increasing  $\text{K}_2\text{O}$ . For an increase from 0.3 to 8 wt%  $\text{K}_2\text{O}$  (ferrobasalt vs.

phono-tephrite) at 1200°C, 200 MPa and  $\log fO_2 = -5$  a decrease in  $Fe^{2+}/\Sigma Fe$  by 0.05 is calculated. The corresponding increase at  $\log fO_2 = -9$  is only 0.03. Within this  $\log fO_2$  range and at water contents between 0 to 5 wt% in the melt, the model of Moretti (2005) predicts no significant variation in  $Fe^{2+}/\Sigma Fe$  with changing  $K_2O$  (i.e.,  $<0.003$ ). If the  $\Sigma FeO$  content is reduced from 13 wt% to 8 wt% (ferrobasalt vs. phono-tephrite), the decrease in the  $Fe^{2+}/\Sigma Fe$  ratio calculated by the model of Kress and Carmichael (1991) is 0.02 and 0.01 at  $\log fO_2$  of -9 and -5, respectively. Again, no significant variation ( $<0.005$ ) is predicted by the model of Moretti (2005). In conclusion, both an increase of  $K_2O$  and a decrease of  $\Sigma FeO$  are predicted by Kress and Carmichael (1991) to shift the  $Fe^{3+}/Fe^{2+}$  ratio in the same direction, whereas Moretti (2005) suggests an insignificant change. It is difficult to clearly attribute the observed shift in  $Fe^{3+}/Fe^{2+}$  to either  $K_2O$  or  $\Sigma FeO$ . A stabilization of tetrahedrally coordinated ferric iron by charge-balancing  $K_2O$  has been suggested by various authors (Dickenson and Hess, 1986; Kilinc et al., 1983; Kress and Carmichael, 1988; Sack et al., 1980) supporting that  $K_2O$  has a positive impact on the ferric-ferrous ratio.

Noteworthy, in contrast to the model predictions and our findings, Tangemann et al. (2001) proposed a negative effect of increasing  $K_2O$  and a positive effect of increasing  $\Sigma FeO$  on the  $Fe^{3+}/Fe^{2+}$  ratio. However, these discrepancies may be due to significant compositional differences, since these authors investigated dry  $K_2O$ - $FeO$ - $Fe_2O_3$ - $SiO_2$  liquids and their experiments were performed at atmospheric pressure.

### **1.5.2. Effect of temperature and pressure on the redox state of iron**

The models of Kress and Carmichael (1991) and Moretti (2005) both predict a small positive dependence of the  $Fe^{2+}/\Sigma Fe$  ratio on temperature (Fig. 1.9). At a given  $fO_2$ , both models calculate an increase of the  $Fe^{2+}/\Sigma Fe$  ratio by 0.01 - 0.08 when the temperature is

raised from 1200 to 1250°C. This effect is more pronounced at lower pressure and higher oxygen fugacity. The comparison of the experimental datasets obtained at 1200°C and 1250°C reveals no clearly resolvable systematic trend regarding experimental and analytical uncertainties. However, predicted effects on the iron redox state caused by this moderate temperature change are small and therefore difficult to resolve.

To evaluate the effect of pressure on the redox state of iron we performed experiments at pressures from 50 to 500 MPa (Table 1.1) at intrinsic redox conditions in the IHPV (NNO+2.6). All experiments were done with a pure H<sub>2</sub>O fluid to obtain a water saturated silicate melt. In Figure 1.9a, the Fe<sup>2+</sup>/ΣFe ratio of the silicate glasses is shown as a function of pressure.

The data suggest a slight negative trend with increasing pressure. However, this trend is basically defined by the 50 MPa experiments, whereas most of the other experimentally obtained Fe<sup>2+</sup>/ΣFe ratios agree within uncertainties. Furthermore, it is important to note that the water solubility in the melt increases with increasing pressure (Figure 1.9b) and hence for a comparison of the experiments a superimposed effect of water content – as suggested by Moretti (2005) – has to be considered as well. Both models (Kress and Carmichael, 1991; Moretti, 2005) predict a nonlinear positive dependence of the Fe<sup>2+</sup>/ΣFe ratio on increasing pressure (Fig. 1.9a). According to the model of Moretti (2005) the pressure effect is more prominent for water-rich than for dry melts. Our experiments at *a*H<sub>2</sub>O = 1 cover a range from about 2.4 to 12 wt% H<sub>2</sub>O and the measured Fe<sup>2+</sup>/ΣFe ratios are consistent with the range of Fe<sup>2+</sup>/ΣFe calculated by the model of Moretti (2005) for corresponding water contents. Thus, the dependence of the Fe redox state on water contents (linked to the specific pressures) that is superimposed on the pressure effect could explain the seeming negative trend mentioned above. No analytically resolvable change in the Fe redox ratio is found within the pressure range investigated in this study. An extension of the experimental data



set to higher pressures is needed to better constrain the effect of pressure on  $\text{Fe}^{2+}/\Sigma\text{Fe}$  in hydrous silicate melts and to allow a comparison to anhydrous silicate melts, e.g. O'Neill et al. (2006), where a pressure effect was observed.

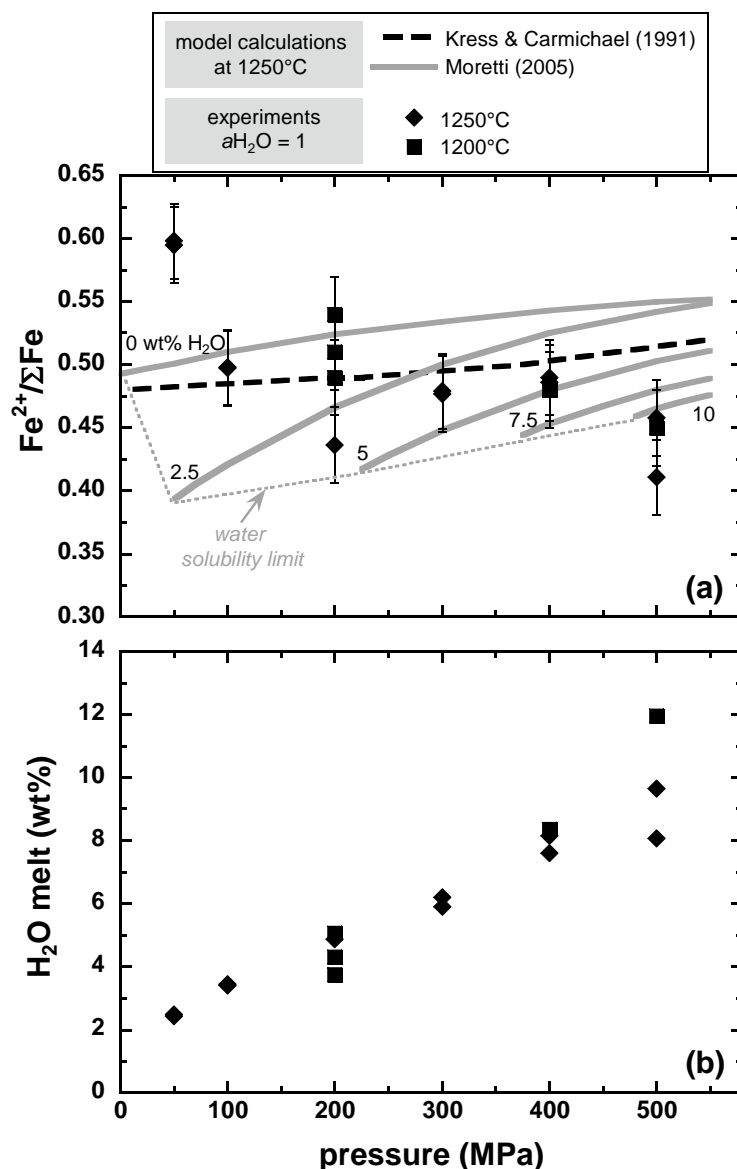


Figure 1.9. (a) Redox state of iron in the phono-tephritic melt as a function of pressure for experiments with pure H<sub>2</sub>O fluid and at intrinsic redox conditions in the IHPV (NNO+2.6). For comparison the pressure dependence of the  $\text{Fe}^{2+}/\Sigma\text{Fe}$  ratio calculated after Moretti (2005) and Kress and Carmichael (1991) at 1250°C are shown. The corresponding water contents of the experimental samples are shown in (b).

## 1.6. CONCLUDING REMARKS

An experimental study was performed to investigate the dependence of the  $\text{Fe}^{2+}/\Sigma\text{Fe}$  ratio in phono-tephritic melts on oxygen fugacity. The redox conditions were adjusted at prevailing  $f\text{H}_2$  using mixed  $\text{H}_2\text{O}-\text{CO}_2$  fluids which control the water activity in the system. The experimentally obtained relationship between  $f\text{O}_2$  and  $\text{Fe}^{3+}/\text{Fe}^{2+}$  for hydrous ultrapotassic melts is in general agreement with predictions from the models of Kress and Carmichael (1991) and Moretti (2005). This suggests that these models can be applied to phono-tephritic melts as well, although such compositions were not implemented in the model calibrations.

A small negative effect of dissolved water on  $\text{Fe}^{2+}/\Sigma\text{Fe}$  at given  $f\text{O}_2$  was found that confirms the predictions of the thermodynamic model of Moretti (2005). On the other hand, no effect of pressure and temperature on the redox state of iron was resolvable in the investigated P-T range. Compared to hydrous ferrobaltic melts systematically higher  $\text{Fe}^{2+}/\Sigma\text{Fe}$  ratios were found for the phono-tephrite in particular at low oxygen fugacity. This effect is most likely due to the much higher  $\text{K}_2\text{O}$  contents of the phono-tephrite (7.5 compared to 0.3 wt). However, the difference in  $\Sigma\text{FeO}$  (7.8 wt% in the phono-tephrite and 12.9 wt% in the basalt) may additionally contribute to the observed differences in  $\text{Fe}^{2+}/\Sigma\text{Fe}$ . The new data may be used to improve the computation models, i.e., to calibrate the effects of  $\text{H}_2\text{O}$ ,  $\text{K}_2\text{O}$  and  $\text{FeO}$  on the redox state of iron in silicate melts.

## **Chapter 2. The experimental calibration of the iron isotope fractionation factor between pyrrhotite and peralkaline rhyolitic melt**

### ABSTRACT

A first experimental study was conducted to determine the equilibrium iron isotope fractionation between pyrrhotite and silicate melt at magmatic conditions. Experiments were performed in internally heated gas pressure vessels at 500 MPa and temperatures between 840°C and 1000°C for 120 to 168 hours. Three different types of experiments were conducted and after phase separation the iron isotope composition of the run products was measured by MC-ICP-MS. (i) Kinetic experiments using  $^{57}\text{Fe}$ -enriched glass and natural pyrrhotite revealed that a close approach to equilibrium is attained already after 48 h. (ii) Isotope exchange experiments - using mixtures of hydrous peralkaline rhyolitic glass powder (~4 wt%  $\text{H}_2\text{O}$ ) and natural pyrrhotites ( $\text{Fe}_{1-x}\text{S}$ ) as starting materials - and (iii) crystallisation experiments, in which pyrrhotite was formed by reaction between elemental sulphur and rhyolitic melt, consistently showed that pyrrhotite preferentially incorporates light iron.

No temperature dependence of the fractionation factor was found between 840°C and 1000°C, within experimental and analytical precision. An average fractionation factor of  $\Delta^{56}\text{Fe}/^{54}\text{Fe}_{\text{pyrrhotite-melt}} = -0.35 \pm 0.04\text{‰}$  (2SE,  $n=13$ ) was determined for this temperature range. Predictions of Fe isotope fractionation between FeS and ferric iron-dominated silicate minerals are consistent with our experimental results, indicating that the marked contrast in both ligand and redox state of iron control the isotope fractionation between pyrrhotite and

silicate melt. Consequently, the fractionation factor determined in this study is representative for the specific  $\text{Fe}^{2+}/\Sigma\text{Fe}$  ratio of our peralkaline rhyolitic melt of  $0.38\pm 0.02$ . At higher  $\text{Fe}^{2+}/\Sigma\text{Fe}$  ratios a smaller fractionation factor is expected.

Further investigation on Fe isotope fractionation between other mineral phases and silicate melts is needed, but the presented experimental results already suggest that even at high temperatures resolvable variations in the Fe isotope composition can be generated by equilibrium isotope fractionation in natural magmatic systems.

## 2.1. INTRODUCTION

The range in iron isotope composition observed in nature cover about 4‰ in  $^{56}\text{Fe}/^{54}\text{Fe}$ . In particular low-temperature processes ( $< 100^\circ\text{C}$ ) show a high variability in Fe isotope composition, whereas bulk igneous rocks comprise a more narrow range of about  $\pm 0.1\%$  ( $2\sigma$ ) (Beard et al., 2003a). However, recent studies observed small but significant differences in Fe isotope compositions between mantle rocks and basalts (Weyer et al., 2005) and some silica-rich granitoids show heavier Fe isotope compositions than mafic rocks (Poitrasson and Freydier, 2005; Dauphas and Rouxel, 2006). At present, the experimental database on low-T Fe isotope fractionation processes is steadily growing, whereas experimental studies on high temperature Fe isotope fractionation in magmatic systems are still lacking.

Calculations based on Mössbauer spectroscopy data allow predictions of inter-mineral Fe isotope fractionation factors at high temperatures. For example, predicted equilibrium Fe isotope fractionation between clinopyroxene and olivine at  $800^\circ\text{C}$  is  $+0.15\%$  for the  $^{56}\text{Fe}/^{54}\text{Fe}$  ratio (Polyakov and Mineev, 2000). However, iron isotope results of

igneous rocks and their interpretations are often controversial. Zhu et al. (2002) and Williams et al. (2005) reported significant differences in the  $^{56}\text{Fe}/^{54}\text{Fe}$  ratio of -0.1 to -0.2‰ for coexisting olivine and pyroxene in mantle rocks, but an absence of differences between ortho- and clinopyroxene. The authors suggest that these findings reflect isotopic equilibrium at  $\sim 1000^\circ\text{C}$ . Beard and Johnson (2004b) confirmed differences in iron isotopes between coexisting olivine and clinopyroxene for some spinel peridotites, but attributed these to metasomatic alteration. On the other hand, these authors did not find any significant iron isotope fractionation between olivine and orthopyroxene in the investigated spinel peridotites. So far, the largest inter-mineral fractionation in mafic rocks interpreted as equilibrium fractionation was observed for clinopyroxene and garnet in eclogites and in garnet-bearing ultramafic rocks ( $\sim +0.3\%$  in  $^{56}\text{Fe}/^{54}\text{Fe}$ ; Beard and Johnson, 2004b).

A given mineral phase can show a considerable range in Fe isotope composition depending on the origin of its host rock (Beard and Johnson, 2004b; Williams et al. 2004; 2005). The largest variations in  $^{56}\text{Fe}/^{54}\text{Fe}$ , up to 1.1‰, were observed for mantle-derived spinels (Williams et al., 2004; 2005). Possible explanations for these variations are melt extraction in combination with changes in mantle redox conditions or metasomatism of the sub-arc mantle by iron-rich silicate melts from the subducting slab (Williams et al., 2004, 2005). The latter interpretation has already been proposed by Beard and Johnson (2004b). In contrast, andesitic volcanic rocks did not reveal any differences in Fe isotope composition between silicate minerals (olivine, biotite, amphibole) and magnetite (Beard and Johnson, 2004b).

To date, the mechanisms that cause Fe isotope fractionation in igneous rocks are still poorly understood and experimental calibrations of fractionation factors are missing. The motivation for our study is to clarify whether measurable high temperature equilibrium Fe

isotope fractionation does exist or not. Here we report a first experimental study on high temperature iron isotope fractionation under magmatic conditions. We present a detailed study on Fe isotope partitioning between pyrrhotite ( $\text{Fe}_{1-x}\text{S}$ ) and a hydrous peralkaline rhyolitic melt at temperatures between 840°C and 1000°C and at a pressure of 500 MPa. The pyrrhotite-melt system was chosen mainly because of the experimental simplicity of the system compared to, for example, olivine-melt or pyroxene-melt systems. We have chosen the peralkaline rhyolitic composition for two main reasons. (i) The high FeO content and the relatively low liquidus temperature facilitate experimental and analytical procedures, because pyrrhotite is the only iron-bearing mineral that is stable over a wide temperature range. (ii) The high alkalinity combined with a relatively low  $\text{Al}_2\text{O}_3$  concentration stabilises ferric over ferrous iron ( $\text{Fe}^{2+}/\text{Fe}_{\text{total}} \sim 0.4$ ) under our experimental conditions (e.g., Dickenson and Hess, 1986; Mysen, 1988; Gaillard et al., 2001). A pronounced contrast in the oxidation state of iron between the silicate melt and pyrrhotite ( $\text{Fe}_{1-x}\text{S}$  contains almost exclusively ferrous iron), is expected to support iron isotope fractionation (Polyakov and Mineev, 2000; Schauble, 2004). Studies on Fe isotope fractionation between aqueous ferric and ferrous species at low temperatures have shown that the heavier isotope is associated with the higher oxidation state of Fe (e.g., Johnson et al., 2002; Welch et al., 2003). Hence, for a first high temperature experimental study the chosen mineral-melt system provides the appropriate boundary conditions, where such predictions can be tested.

### 2.2. EXPERIMENTAL METHODS

Our experimental strategy involves three different experimental designs to distinguish between kinetic and thermodynamic isotope fractionation: (i) The timescale

required to attain isotopic equilibrium was determined with experiments using a glass that was artificially enriched in  $^{57}\text{Fe}$  and natural pyrrhotite. The large differences in  $^{57}\text{Fe}/^{54}\text{Fe}$  between the starting materials allow precise monitoring of isotope exchange towards equilibrium. (ii) The equilibrium fractionation factors between pyrrhotite and silicate melt were determined by the partial exchange method of Northrop and Clayton (1966). Synthetic glasses and natural pyrrhotites of known Fe isotope compositions were used as starting materials for these experiments. The large variation in Fe isotope composition of the pyrrhotites used allows the determination of fractionation factors even at incomplete equilibration. (iii) In addition, the equilibrium fractionation factor between pyrrhotite and silicate melt was determined by crystallisation experiments in which pyrrhotite was formed by reaction between sulphur and silicate melt.

### **2.2.1. Starting materials**

#### *2.2.1.1. Natural pyrrhotite samples*

Four different natural pyrrhotites were used for the experiments in our study. All samples were checked for purity by powder x-ray diffraction (XRD) and electron microprobe analysis (EMPA) (see Table A2.1.; all tables and figures with the prefix “A2” refer to appendix A2). No phases other than pyrrhotite were detected. In addition no elements other than Fe and S were detected by EMPA. Samples B and K show a single sharp  $d_{102}$  peak in the powder x-ray diffraction pattern that indicates hexagonal pyrrhotite. Splitting of this peak as observed for the samples MV and R is characteristic for monoclinic pyrrhotite (Vaughan and Craig, 1978). The  $^{56}\text{Fe}/^{54}\text{Fe}$  ratio of the pyrrhotite samples used in the experiments vary by 0.67‰ (Table 2.1). Additionally, another 12 natural sulphide samples – mainly pyrrhotites – from various geological setting were analysed for their Fe isotope composition (see appendix A2.4).

Table 2.1. Iron isotope compositions of the starting materials.

sample	analysis no. <sup>§</sup>	$\delta^{56}\text{Fe}$	$\delta^{57}\text{Fe}$	averages			
				$\delta^{56}\text{Fe}$	$2\sigma$ <sup>§</sup>	$\delta^{57}\text{Fe}$	$2\sigma$ <sup>§</sup>
<i>synthetic glasses</i>							
NSLsyn (dry)	NSL1	-0.234	-0.334	-0.247	0.043	-0.346	0.074
	NSL2	-0.276	-0.396				
	NSL3a	-0.252	-0.336				
	NSL3b	-0.282	-0.354				
	NSL4	-0.223	-0.299				
	NSL5a	-0.243	-0.341				
	NSL5b	-0.245	-0.315				
	NSL5c	-0.284	-0.420				
NSLsyn01 *	NSL6	-0.265	-0.382				
NSLsyn07 *	NSL7a	-0.225	-0.361				
	NSL7b	-0.225	-0.317				
	NSL7c	-0.231	-0.373				
NSLsyn05 *	NSL8a	-0.247	-0.330				
	NSL8b	-0.228	-0.289				
NSLsyn04 <sub>spike</sub>	NSL9a	0.720	1623.494	0.723	0.043	1623.487	0.364
	NSL9b	0.746	1623.666				
	NSL10	0.704	1623.302				
NSLsyn06 <sub>spike</sub>	NSL11a	-0.024	438.092	-0.009	0.025	438.138	0.121
	NSL11b	-0.002	438.206				
	NSL12	-0.002	438.115				
<i>natural pyrrhotites</i>							
MV	MV1a	-0.733	-1.106	-0.727	0.069	-1.063	0.107
	MV1b	-0.758	-1.079				
	MV2	-0.690	-1.003				
B	B1a	-1.065	-1.554	-1.035	0.084	-1.517	0.134
	B1b	-1.076	-1.589				
	B2a	-1.007	-1.440				
	B2b	-0.991	-1.485				
K	K1a	-0.345	-0.498	-0.369	0.037	-0.526	0.047
	K1b	-0.391	-0.530				
	K2a	-0.366	-0.507				
	K2b	-0.385	-0.558				
	K2c	-0.360	-0.535				
R	R1a	-0.725	-1.077	-0.720	0.022	-1.064	0.030
	R1b	-0.727	-1.057				
	R2a	-0.724	-1.045				
	R2b	-0.704	-1.075				

§ Each number refers to an analytical sequence involving dissolution of glass or pyrrhotite and chromatographic separation of iron. Characters a, b, c denote multiple Fe isotope analyses of the same solution.

\* Some of the hydrous glass batches were analysed to ensure that Fe isotope composition remained unchanged after the hydration  
 § Uncertainty given as the two standard deviation of replicate analyses. The long-term external reproducibility ( $2\sigma$ ) for "unspiked" samples on the Neptune mass spectrometer is  $\pm 0.049$  ‰ on  $\delta^{56}\text{Fe}$  and  $\pm 0.071$  ‰ on  $\delta^{57}\text{Fe}$ .

### 2.2.1.2. Synthetic peralkaline, rhyolitic glass

As starting glass, we chose a synthetic analogue of a peralkaline rhyolitic obsidian from New Zealand (composition in wt%: 75.5 SiO<sub>2</sub>, 10.4 Al<sub>2</sub>O<sub>3</sub>, 4.1 FeO, 5.3 Na<sub>2</sub>O, 4.7 K<sub>2</sub>O). The NSLsyn glass was prepared by fusing a mixture of oxides and carbonates at 1600°C (Table A2.2, NSLsyn dry). In the experiments we used prehydrated glasses as



starting materials to assure homogeneous H<sub>2</sub>O distribution and to avoid any possible complications due to a fluid phase which may initiate metastable reactions in the beginning of the experiment. Details on the preparation of the synthetic glasses are given in appendix A2.1. A H<sub>2</sub>O content of ~ 4 wt% was chosen to obtain a fluid-undersaturated melt (Behrens and Jantos, 2001) under the experimental conditions applied here, even in the presence of sulphur. The hydrous glass was ground to grain sizes of < 20 µm and used as starting material for the isotope exchange and crystallisation experiments. For this study eight batches of “isotopically normal” hydrous glass were synthesised, each analysed by electron microprobe (Table A2.2.). The difference to 100 % in the electron microprobe analysis was interpreted as the amount of H<sub>2</sub>O dissolved in the glasses (e.g., Devine et al., 1995; Morgan and London, 1996; Berndt et al., 2005). In addition, the H<sub>2</sub>O concentrations of selected glasses were determined by Karl-Fischer titration (KFT) (Behrens and Stuke, 2003; Leschik et al., 2004). Although, the “by-difference-method” for water determination using the EMPA has a relatively high uncertainty of at least ±0.5 wt%, the results of both methods are in very good agreement (Table A2.2.), with exception of NSLsyn01. The EMPA measurements show homogeneous distribution of water in the glasses.

#### 2.2.1.3. <sup>57</sup>Fe enriched glasses

For the kinetic tracer experiments we doped the NSLsyn glass with a <sup>57</sup>Fe isotope tracer. For this study two batches of hydrous <sup>57</sup>Fe-enriched NSLsyn glass were synthesised (Table A2.2., NSLsyn04<sub>spike</sub> and NSLsyn06<sub>spike</sub>). Electron microprobe transects were measured on three glass pieces of each charge to ensure compositional homogeneity. Fe isotope analyses were performed on two different glass pieces of each batch (Table 2.1). FeO<sub>total</sub> concentration of the <sup>57</sup>Fe-enriched glasses are slightly lower (~ 0.3 - 0.7 wt% FeO<sub>total</sub> less) than those of “unspiked” hydrous glasses (Table A2.2.). Probably small amounts of iron

were lost to the capsule during the initial melting under dry conditions in the internally heated pressure vessel (IHPV) (Berndt et al., 2005). No iron loss was observed after synthesis of water-bearing glasses.

## 2.2.2. Experimental design

### 2.2.2.1. Kinetic tracer experiments

The kinetics of iron isotope exchange between pyrrhotite and silicate melt were determined using the  $^{57}\text{Fe}$  enriched glass and natural pyrrhotite with “natural”  $^{57}\text{Fe}$  abundance. The use of enriched isotope tracers to evaluate the kinetics of isotope exchange has a long history (Mills and Urey, 1940) and was already successfully applied to the iron isotopic system by Johnson et al. (2002). The initial difference in  $^{57}\text{Fe}/^{54}\text{Fe}$  between pyrrhotite ( $^{57}\text{Fe}/^{54}\text{Fe} \sim 0.363$ ) and melt (NSLsyn04<sub>spike</sub>:  $^{57}\text{Fe}/^{54}\text{Fe} \sim 0.951$ ) is much larger than any kinetic or equilibrium isotope fractionation in nature. The high analytical precision allows an accurate assessment of the kinetics of iron isotope exchange and the timescale required to attain isotopic equilibrium at the given P-T-conditions. For each experiment approximately 80 mg of  $^{57}\text{Fe}$  enriched hydrous glass powder (NSLsyn04<sub>spike</sub>, Table 2.1) was mixed with  $\sim 5$  mg of natural pyrrhotite powder (sample K, Table 2.1) and sealed in a gold capsule. Experiments were performed in the IHPV at 900°C and 500 MPa for 2 h, 24 h, 48 h and 120 h, respectively, to obtain a time-resolved approach to isotopic equilibrium.

### 2.2.2.2. Isotope exchange experiments

For each of the investigated temperatures four or five capsules were prepared containing  $\sim 80$  mg of hydrous NSLsyn glass powder ( $\sim 4$  wt%  $\text{H}_2\text{O}$ ) mixed with  $\sim 5$  mg of natural pyrrhotite powder. Four different natural pyrrhotites (Table 2.1) were used to vary the initial differences in iron isotope composition between pyrrhotite and glass. All capsules

of each set were processed simultaneously in the IHPV at 500 MPa and either 840°C, 900°C or 1000°C, to ensure identical experimental conditions. Each experimental set also included at least one capsule with  $^{57}\text{Fe}$  enriched glass powder mixed with pyrrhotite to assess the extent of equilibration for the given experimental conditions.

### 2.2.2.3. Crystallisation experiments

Hydrous NSLsyn glass powder (~ 4 wt%  $\text{H}_2\text{O}$ , Table A2.2.) was mixed with various amounts of elemental sulphur (ChemPur<sup>®</sup>, 99.99 % purity) and sealed in Au capsules to crystallise pyrrhotite. Preliminary tests with relatively large amounts of sulphur (up to ~ 14 wt% S in the capsule) resulted in the formation of large Fe-S-rich fluid bubbles and an inhomogeneous Fe distribution in the melt (Fig. 2.1A). By reducing the concentration of elemental sulphur to < 0.53 wt%, pyrrhotite was crystallised with a coexisting homogeneous melt free of large Fe-S-rich fluid bubbles. Small bubbles (<1  $\mu\text{m}$ ) were occasionally present, probably due to trapped nitrogen during capsule preparation.

Three or four capsules with different initial Fe:S ratios (ranging from about 6:1 to 12:1) were processed simultaneously in the IHPV at 500 MPa and at a temperature of 840°C, 900°C or 1000°C. Pyrrhotite crystallised preferentially along the former grain boundaries of the glass powder (Fig. 2.1B) and was often accumulated in a few, large clusters probably due to initial inhomogeneous distribution of S in the loaded charge. To improve homogenous distribution of pyrrhotite in the samples, the experiments were interrupted after 24 h. Samples were reground, sealed again in new Au capsules and processed in the IHPV for another five to six days at identical experimental conditions. One capsule was added to each run that only contained hydrous glass powder. The redox state of iron in those samples was determined by wet chemistry using the colorimetric method described in chapter 1.3.2.

#### 2.2.2.4. Run conditions

During the experiments in the IHPV temperature was measured next to the capsules (typically capsules had an inner diameter of 4 mm, a wall thickness of 0.2 mm, and a length of ~ 15 mm) using three K-type thermocouples with an accuracy of better than  $\pm 7^\circ\text{C}$  (A. Meisen, pers. comm.). The temperature variation across the capsule assemblage was  $< 5^\circ\text{C}$  and temperature stability was always better than  $\pm 2^\circ\text{C}$ . Pressure was measured with an uncertainty of about 1 MPa and the stability was within 5 MPa. Heating to the desired run temperature was done isobarically at 500 MPa at a rate of  $30^\circ\text{C}/\text{min}$ . Oxygen fugacity is imposed by the intrinsic hydrogen fugacity of the IHPV. At water-saturated conditions in the capsule the oxygen fugacity is close to that of the MnO-Mn<sub>3</sub>O<sub>4</sub> buffer ( $\log f_{\text{O}_2} \sim \text{NNO}+3.5$ ; see Berndt et al. (2002)). In all experiments the melts were H<sub>2</sub>O undersaturated and, hence, the prevailing oxygen fugacity in the capsule was lower than NNO+3.5. For peralkaline rhyolite the relationship between water solubility in the melt and water activity is not known. To estimate the oxygen fugacity we assumed for simplicity that the water activity  $a_{\text{H}_2\text{O}}$  is proportional to the water concentration in the melt. At 4 wt% H<sub>2</sub>O dissolved in the melt and 500 MPa, this approach probably slightly overestimates the water activity (see Fig. 4 of Tamic et al. (2001) for the variation of water solubility in rhyolitic melts as a function of the mole fraction of water in the fluid), but  $a_{\text{H}_2\text{O}}$  is estimated to be accurate within a factor of two. Using a water solubility of 10.93 wt% determined for peralkaline rhyolite (NSL) at  $800^\circ\text{C}$  and 500 MPa (Behrens and Jantos, 2001), the estimated  $\log f_{\text{O}_2}$  is NNO+2.6. According to Gaillard et al. (2002) redox equilibrium is attained after ~ 3 hours under our experimental conditions.

After the run the samples were isobarically quenched to room temperature at an initial cooling rate of ~  $200^\circ\text{C}/\text{min}$  by turning off the power of the furnace. The capsules

were weighed before and after the IHPV runs to ensure that they remained closed during the experiments.

#### *2.2.2.5. Characterisation of run products*

Thin sections of all run products, except for samples E-840-5S and C-840-3, were prepared for electron microprobe analysis. The remaining sample was ground in an agate mortar to grain sizes of  $< 5\mu\text{m}$  for Fe isotope analysis. Selected samples were examined by XRD for phase identification. All microprobe analyses of pyrrhotites and glasses were done on a Cameca SX-100 (see appendix A2.2 for details on analytical conditions). Water concentrations in the glasses were estimated from electron microprobe analysis using the “by-difference-method”.

### **2.2.3. Isotope analysis**

#### *2.2.3.1. Phase separation*

The run products of all experiments, pyrrhotite and silicate glass, needed to be separated before chemical Fe purification and subsequent isotope analysis using solution multi collector inductively coupled plasma mass spectrometry (MC-ICP-MS). In most experiments, in particular in the crystallisation experiments, grain sizes of pyrrhotite were too small for physical separation by para-magnetism or heavy liquids. Therefore pyrrhotite was selectively removed from the glass by dissolution in hydrochloric acid. However, no complete phase separation could be attained with this method. This leads to a systematic underestimate of the measured fractionation factors. Therefore, a correction for this cross-contamination during phase separation was applied to the measured Fe isotope data of pyrrhotite and glass (see appendix A2.3 for details on the phase separation and the corrections). The extent of the corrections can be seen in Tables 2.2 and 2.3.

Iron was separated from other elements by anion-exchange chromatography as described in Schoenberg and von Blanckenburg (2005). Before and after column chemistry, Fe concentration was measured by ICP-OES to ensure quantitative elution of Fe from the anion exchange resin (DOWEX AG<sup>®</sup> 1x8 100-200 mesh) and to verify that matrix elements were removed efficiently. Total procedural Fe blanks were always below 60 ng. This is more than four orders of magnitude less than Fe processed and is considered negligible.

### 2.2.3.2. Mass spectrometry and data presentation

All iron isotope measurements were carried out on a ThermoFinnigan Neptune MC-ICP-MS using the analytical protocol described by Schoenberg and von Blanckenburg (2005). The standard-sample bracketing technique was used to correct for instrumental mass bias and the commercially available iron standard IRMM-014 was used as bracketing reference standard. Iron isotope data are reported in the  $\delta$ -notation, which gives the per mil deviation of the  $^{56}\text{Fe}/^{54}\text{Fe}$  or  $^{57}\text{Fe}/^{54}\text{Fe}$  ratio of the sample relative to that of the IRMM-014 standard, e.g.:

$$\delta^{56}\text{Fe}_{\text{sample}} = \left[ \left( \frac{^{56}\text{Fe}}{^{54}\text{Fe}}_{\text{sample}} \bigg/ \frac{^{56}\text{Fe}}{^{54}\text{Fe}}_{\text{IRMM-014}} \right) - 1 \right] \cdot 1000 \quad [\text{‰}] \quad (2.1)$$

The long-term external reproducibility for single Fe isotope measurements, determined by replicate analysis of standards and samples of different matrices, is  $\pm 0.049\text{‰}$  and  $\pm 0.071\text{‰}$  (2 standard deviation,  $2\sigma$ ) for  $\delta^{56}\text{Fe}$  and  $\delta^{57}\text{Fe}$ , respectively (Schoenberg and von Blanckenburg, 2005). We routinely analysed our internal laboratory standard JM (commercially available pure Fe wire) within each analytical session to assess the accuracy of the measurements. During the course of this study the measured Fe isotope composition of the JM standard was  $\delta^{56}\text{Fe} = 0.422 \pm 0.043\text{‰}$  and  $\delta^{57}\text{Fe} = 0.631 \pm 0.072\text{‰}$  ( $2\sigma$ ,  $n = 64$ ), which is in excellent agreement with previous measurements ( $\delta^{56}\text{Fe} = 0.423 \pm 0.046\text{‰}$  and

$\delta^{57}\text{Fe} = 0.624 \pm 0.073\%$ ) given by Schoenberg and von Blanckenburg (2005). Measured Fe isotope differences between pyrrhotite (p) and glass (g) are expressed by the fractionation factor  $\alpha$

$$\alpha_{\text{p-g}} = \frac{1000 + \delta^{56}\text{Fe}_p}{1000 + \delta^{56}\text{Fe}_g} \quad (2.2)$$

or by the approximation

$$\Delta^{56}\text{Fe}_{\text{p-g}} = \delta^{56}\text{Fe}_p - \delta^{56}\text{Fe}_g \approx 10^3 \ln \alpha_{\text{p-g}}. \quad (2.3)$$

### 2.3. RESULTS

All experiments contained pyrrhotite and glass as the only reaction products (Fig. 2.1), except for samples E-900-1, E-840-2 and E840-5S, where small amounts of additional quartz with crystal sizes  $< 10 \mu\text{m}$  were present. However, quartz is not expected to affect Fe isotope partitioning between pyrrhotite and silicate melt. In the crystallisation experiments small pyrrhotite crystals ( $< 1 \mu\text{m}$ ) were homogeneously distributed in the run products. Pyrrhotite crystal contents in these experiments, estimated by mass balance of iron, were below 1.5 wt%. EMPA transects through the samples revealed homogeneous melt compositions and  $\text{H}_2\text{O}$  concentrations identical with those of the starting materials within analytical uncertainty (Table A2.5). The redox state of Fe, expressed as  $\text{Fe}^{2+}/\Sigma\text{Fe}$  ratio, in the pure hydrous rhyolitic melt (measured by wet-chemistry) does not vary significantly with temperature ( $0.37 \pm 0.01$  ( $1\sigma$ ,  $n=3$ ) at  $840^\circ\text{C}$ ,  $0.39 \pm 0.01$  ( $1\sigma$ ,  $n=5$ ) at  $900^\circ\text{C}$ , and  $0.37 \pm 0.02$  ( $1\sigma$ ,  $n=7$ ) at  $1000^\circ\text{C}$ ). The constancy of the  $\text{Fe}^{2+}/\Sigma\text{Fe}$  ratio (average:  $0.38 \pm 0.02$ ,  $1\sigma$ ,  $n=15$ ) within a relatively limited temperature range is consistent with experimental findings presented in chapter 1.5.2 and results reported by Gaillard et al. (2001). In the crystallisation

experiments pyrrhotite crystallisation lowered the  $\text{FeO}_{\text{total}}$  in the glasses by 0.02 to 0.79 wt% compared to the starting material. On the other hand, in exchange experiments  $\text{FeO}_{\text{total}}$  slightly increased, because the added pyrrhotite was partially dissolved to saturate the melt with sulphur (Fig. 2.2, Table A2.5). The differences in the sulphur contents of the post-experimental glasses can be explained by variations in iron content of the melt and in temperature (Botcharnikov et al., 2004).

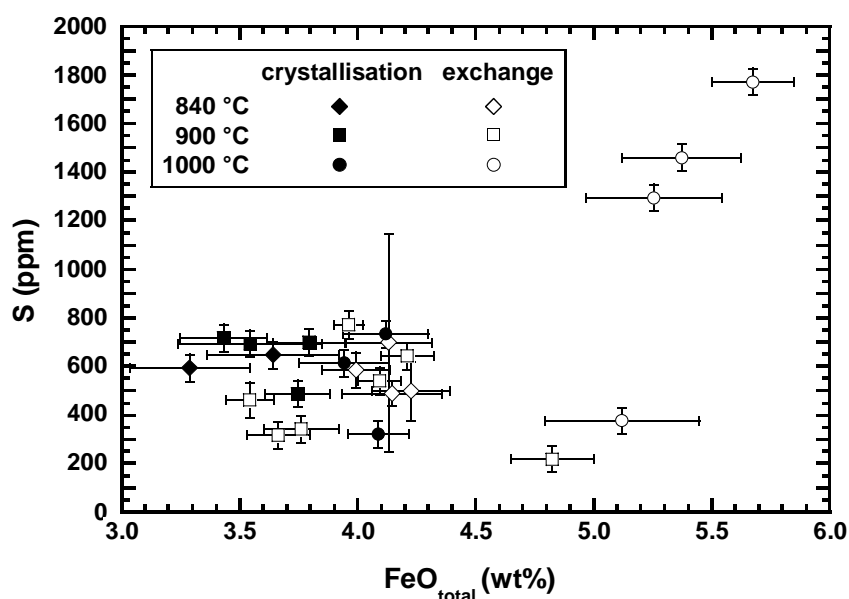


Figure 2.2. Sulphur contents in the post-experimental glasses of crystallisation and isotope exchange experiments as a function of  $\text{FeO}_{\text{total}}$ .

Only hexagonal pyrrhotite was found by XRD in run products of crystallisation and exchange experiments. The monoclinic pyrrhotites MV and R, used as starting material in several experiments (Table 2.2) changed to hexagonal crystal structure, as expected for high temperature pyrrhotites (Vaughan and Craig, 1978). Compositions of pyrrhotites after the exchange experiments are given in Table A2.5. Since the crystal size of pyrrhotites from the crystallisation experiments were  $< 1\mu\text{m}$  it was not possible to analyse them by EMPA.



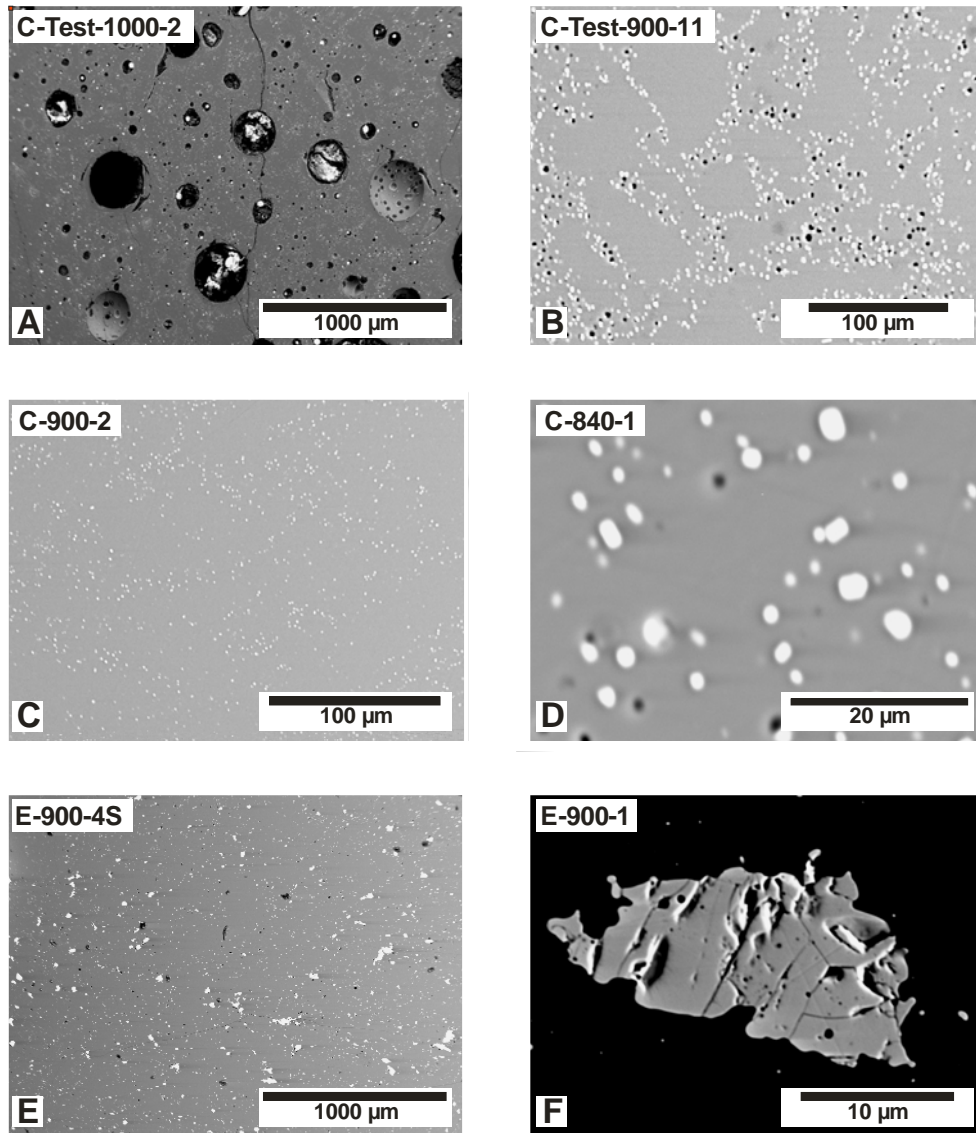


Figure 2.1. Back scattered electron images of representative experimental run products. (A) Preliminary crystallisation experiments (1000 °C, 500 MPa, 24 hours) with high amounts of sulphur (14.16 wt% S) resulted in formation of large Fe-S-rich fluid bubbles. (B) Short term crystallisation experiments (900 °C, 500 MPa, 24 hours, 0.29 wt% S added) show preferential pyrrhotite (light colour) formation along the former grain boundaries of the glass powder. (C and D) Typical images of run products from re-homogenised crystallisation experiments with initial S contents < 0.54 wt%. (E) Representative image of run products from exchange experiments. A pyrrhotite crystal is shown in detail in (F). The crystal shows a dissolution texture, but a subhedral crystal shape is still preserved.

Table 2.2. Summary of exchange and kinetic tracer experiments.

exchange experiments	experiment	starting materials #	phase <sup>s</sup>	replicate analyses		averages - measured <sup>r</sup>		averages - corrected <sup>s</sup>		$\Delta^{56}\text{Fe}_{\text{final}}^{\text{e}}$	$\Delta^{56}\text{Fe}_{\text{initial}}^{\text{e}}$	$\Delta^{56}\text{Fe}_{\text{final}}^{\text{e}}$	$\Delta^{56}\text{Fe}_{\text{initial}}^{\text{e}}$	$\Delta^{56}\text{Fe}_{\text{pyrrhotite-melt}}^{\text{e}}$ <sup>†</sup>	fractional approach to equilibrium <sup>†</sup>		
				$\delta^{56}\text{Fe}$	$\delta^{57}\text{Fe}$	$\delta^{56}\text{Fe}$	$\delta^{57}\text{Fe}$	$2\sigma$	$2\sigma$						$F(\Delta)$	$F(\delta)_p$	$F(\delta)_g$
<i>840 °C, 144 h experimental runtime</i>																	
	E-840-1	NSLsyn12 + B	g	-0.549	-0.790	-0.549	-0.790	-0.41	0.12	-0.57	0.19	-0.80 ± 0.07	-0.50 ± 0.13	0.30 ± 0.15	-0.37 ± 0.24	0.72	
			p	-0.908	-1.349	-0.908	-1.349										
	E-840-2	NSLsyn12 + K	g	-0.238	-0.355	-0.238	-0.355	-0.17	0.07	-0.26	0.10	-0.12 ± 0.07	-0.23 ± 0.09	-0.11 ± 0.11			
			p	-0.407	-0.599	-0.407	-0.599										
	E-840-3	NSLsyn12 + R	g	-0.317	-0.471	-0.317	-0.471	-0.15	0.14	-0.23	0.20	-0.80 ± 0.07	-0.60 ± 0.15	0.20 ± 0.17			
			p	-0.751	-1.080	-0.751	-1.080										
	E-840-4S	NSLsyn06 <sub>spike</sub> + K	g	-0.035	230.525	-0.025	230.544	0.11	0.12	243.49	10.2	-0.36 ± 0.07	-0.47 ± 0.13	-0.11 ± 0.14	0.89	0.98	0.82
			g	-0.016	230.563	-0.367	197.262										
			p	-0.391	197.218												
			p	-0.343	197.306												
	E-840-5S	NSLsyn06 <sub>spike</sub> + B	g	-0.382	209.934	-0.372	209.982	-0.24	0.11	219.31	7.3	-1.04 ± 0.07	-0.46 ± 0.12	0.58 ± 0.14	0.92	0.94	0.91
			g	-0.361	210.030												
			p	-0.719	185.968	-0.706	186.002										
			p	-0.693	186.037												
<i>900 °C, 120 h experimental runtime</i>																	
	E-900-1	NSLsyn09 + B	g	-0.613	-0.854	-0.613	-0.854	-0.49	0.11	-0.64	0.18	-0.80 ± 0.07	-0.44 ± 0.12	0.36 ± 0.14	-0.35 ± 0.10	0.86	
			p	-0.930	-1.399	-0.930	-1.399										
	E-900-2	NSLsyn09 + R	g	-0.339	-0.542	-0.339	-0.542	-0.21	0.11	-0.37	0.15	-0.47 ± 0.07	-0.46 ± 0.12	0.02 ± 0.14			
			p	-0.668	-0.980	-0.668	-0.980										
	E-900-3	NSLsyn09 + K	g	-0.292	-0.393	-0.292	-0.393	-0.22	0.08	-0.26	0.12	-0.12 ± 0.07	-0.26 ± 0.09	-0.14 ± 0.11			
			p	-0.482	-0.723	-0.482	-0.723										
	E-900-4S	NSLsyn04 <sub>spike</sub> + K	g	0.190	713.539	0.179	713.462	0.29	0.10	728.31	11.7	-1.09 ± 0.07	-0.40 ± 0.11	0.69 ± 0.13	0.97	0.96	0.97
			g	0.169	713.386												
			p	-0.108	675.286	-0.110	675.289										
			p	-0.111	675.293												
<i>1000 °C, 120 h experimental runtime</i>																	
	E-1000-1	NSLsyn11 + B	g	-0.635	-0.910	-0.635	-0.910	-0.48	0.13	-0.67	0.20	-0.80 ± 0.07	-0.57 ± 0.14	0.23 ± 0.16	-0.44 ± 0.10	0.93	
			p	-1.045	-1.537	-1.045	-1.537										
	E-1000-2	NSLsyn09 + R	g	-0.402	-0.557	-0.402	-0.557	-0.27	0.11	-0.38	0.16	-0.47 ± 0.07	-0.46 ± 0.12	0.02 ± 0.14			
			p	-0.735	-1.043	-0.731	-1.023										
			p	-0.727	-1.002												
	E-1000-3S	NSLsyn06 <sub>spike</sub> + K	g	-0.154	206.409	-0.144	206.446	-0.03	0.10	206.72	0.23	-0.36 ± 0.07	-0.40 ± 0.11	-0.04 ± 0.13	1.00	1.02	0.98
			g	-0.133	206.482												
			p	-0.416	205.776	-0.430	205.736										
			p	-0.443	205.695												
	E-1000-4S	NSLsyn06 <sub>spike</sub> + B	g	-0.435	237.067	-0.430	237.068	-0.31	0.11	238.11	0.83	-1.04 ± 0.07	-0.44 ± 0.12	0.60 ± 0.14	0.99	0.98	1.01
			g	-0.425	237.069	-0.746	234.377										
			p	-0.725	234.384												
			p	-0.766	234.369												

continued on next page

Table 2.2 - continued.

experiment	starting materials <sup>#</sup>	replicate analyses		averages - measured		averages - corrected <sup>§</sup>		fractional approach to equilibrium <sup>¶</sup>								
		phase <sup>§</sup>	$\delta^{56}\text{Fe}$	$\delta^{57}\text{Fe}$	$\delta^{56}\text{Fe}$	$\delta^{57}\text{Fe}$	$\delta^{56}\text{Fe}$	$\delta^{57}\text{Fe}$	$2\sigma$	$2\sigma$	$\Delta^{56}\text{Fe}_{\text{pyrrhotite-melt}}$ <sup>†</sup>	$F(\text{N\&C})$	$F(\Delta)$	$F(\delta)_p$	$F(\delta)_g$	
<i>kinetic tracer experiments, 900 °C, experiment runtimes varied</i>																
E-900-1S (2h)	NSLsyn04 <sub>spske</sub> + K	g	0.259	903.693	0.239	903.602	0.40	0.14	1104.06	1.57.7						
		g	0.218	903.512												
		p	-0.197	388.135	-0.184	388.135										
E-900-2S (24h)	NSLsyn04 <sub>spske</sub> + K	g	0.296	726.949	0.296	726.949	0.45	0.13	774.20	37.2						
		p	-0.110	605.452	-0.110	605.452										
E-900-3S (48h)	NSLsyn04 <sub>spske</sub> + K	g	0.186	689.599	0.186	689.599	0.32	0.11	715.54	20.4						
		p	-0.150	622.892	-0.150	622.892										

All experiments were performed at 500 MPa.

<sup>#</sup> Mixtures of hydrous glass (~4 wt% H<sub>2</sub>O) and pyrrhotite powder (see Tables 2.1 and A2.2). Numbers refer to the different synthesised NSLsyn glass batches. Suffix spike denotes <sup>57</sup>Fe enriched glass.

<sup>§</sup> Separated glass (g) or pyrrhotite (p) fraction.

<sup>¶</sup> Analytical uncertainty (long-term external reproducibility (2σ)) for "unspiked" samples on the Neptune mass spectrometer with standard-sample bracketing is ± 0.049 ‰ on δ<sup>56</sup>Fe and ± 0.071 ‰ on δ<sup>57</sup>Fe.

<sup>§</sup> Measured values of the separated glass fractions were corrected for incomplete separation from pyrrhotite (see appendix A2 for details).

<sup>‡</sup> Uncertainties for Δ<sup>56</sup>Fe values are calculated by error propagation of the uncertainties in δ<sup>56</sup>Fe values of the involved phases, including errors associated with corrections, if applied.

<sup>†</sup> Fractionation factor according to the method of Northrop & Clayton (1966). Given uncertainty is the error on the y-intercept derived from the error weighted linear regression.

<sup>¶</sup> F(δ)<sub>p</sub> and F(δ)<sub>g</sub> values were calculated according to equation 2.4, where p and g refer to the pyrrhotite or the glass fraction, respectively. F(Δ) values are calculated using equation 2.5. F(N&C) values are derived from Fig. 2.4, where F = (-1/slope).

Table 2.3. Summary of crystallisation experiments.

experiment	starting glass	Fe:S <sub>initial</sub> <sup>‡</sup>	S <sub>initial</sub> <sup>‡</sup> (wt%) <sup>‡</sup>	phase <sup>§</sup>	replicate analyses		averages - measured <sup>††</sup>		averages - corrected <sup>§</sup>		averages		f F <sub>transfer</sub> <sup>#</sup>
					δ <sup>56</sup> Fe	δ <sup>57</sup> Fe	δ <sup>56</sup> Fe	δ <sup>57</sup> Fe	δ <sup>56</sup> Fe	δ <sup>57</sup> Fe	Δ <sup>56</sup> Fe <sub>pyrrhotite-melt</sub>	Δ <sup>56</sup> Fe <sub>pyrrhotite-melt</sub> &	
<i>840 °C, experimental runtime 24+144 h<sup>¶¶</sup></i>													
C-840-1	NSLsyn08	9.1 : 1	0.36	g	-0.131	-0.213	-0.122	-0.193	-0.33 ± 0.070	-0.35 ± 0.10	0.189 ± 0.098		
				g	-0.113	-0.172	-0.438	-0.608					
				p	-0.427	-0.604							
				p	-0.449	-0.613							
C-840-2	NSLsyn08	8.8 : 1	0.37	g	-0.100	-0.219	-0.126	-0.192	-0.31 ± 0.081		0.101 ± 0.101		
				g	-0.152	-0.165							
				p	-0.416	-0.600	-0.404	-0.599					
				p	-0.392	-0.598							
C-840-3	NSLsyn08	8.5 : 1	0.40	g	-0.265	-0.354	-0.244	-0.349	-0.40 ± 0.073		~0.145*		
				g	-0.223	-0.343							
				p	-0.624	-0.948	-0.618	-0.933					
				p	-0.611	-0.918							
<i>900 °C, experimental runtime 24+120 h<sup>¶¶</sup></i>													
C-900-1	NSLsyn05	8.8 : 1	0.37	g	-0.207	-0.301	-0.198	-0.311	-0.41 ± 0.086	-0.38 ± 0.10	0.092 ± 0.078		
				g	-0.190	-0.321							
				p	-0.550	-0.800	-0.558	-0.821					
				p	-0.565	-0.841							
C-900-2	NSLsyn07	6.2 : 1	0.54	g	-0.217	-0.349	-0.217	-0.349	-0.37 ± 0.070		0.168 ± 0.049		
				p	-0.575	-0.815	-0.561	-0.808					
				p	-0.547	-0.801							
C-900-3	NSLsyn07	12.2 : 1	0.27	g	-0.212	-0.362	-0.220	-0.344	-0.32 ± 0.071		0.098 ± 0.039		
				g	-0.229	-0.326							
				p	-0.511	-0.735	-0.502	-0.723					
				p	-0.492	-0.710							
C-900-4	NSLsyn07	8.4 : 1	0.40	g	-0.240	-0.372	-0.246	-0.374	-0.43 ± 0.087		0.069 ± 0.042		
				g	-0.252	-0.376							
				p	-0.599	-0.871	-0.608	-0.877					
				p	-0.616	-0.883							

continued on next page

Table 3. - continued.

experiment	starting glass	Fe:S <sub>initial</sub> <sup>‡</sup>	S <sub>initial</sub> (wt%) <sup>‡</sup>	phase <sup>§</sup>	replicate analyses		averages - measured <sup>¶</sup>		averages - corrected <sup>§</sup>		averages			
					$\delta^{56}\text{Fe}$	$\delta^{57}\text{Fe}$	$\delta^{56}\text{Fe}$	$\delta^{57}\text{Fe}$	$\delta^{56}\text{Fe}$	$\delta^{57}\text{Fe}$	$\Delta^{56}\text{Fe}_{\text{pyrrhotite-melt}}$	$\Delta^{56}\text{Fe}_{\text{pyrrhotite-melt}} \& \Delta^{57}\text{Fe}_{\text{transfer}}^{\#}$		
1000 °C, experimental runtime 24+120 h <sup>¶¶</sup>														
C-1000-1	NSLsyn10	8.8 : 1	0.37	g	-0.149	-0.215	-0.145	-0.239	-0.145	-0.239	-0.37 ± 0.39	-0.30 ± 0.23	0.005 ± 0.052	
				g	-0.141	-0.262								
				p	-0.255	-0.362	-0.244	-0.328	-0.52	0.39	-0.57	0.35		
				p	-0.232	-0.293								
C-1000-2	NSLsyn07	6.0 : 1	0.53	g	-0.059	-0.086	-0.065	-0.088	-0.065	-0.088	-0.16 ± 0.09		0.041 ± 0.037	
				g	-0.072	-0.089								
				p	-0.185	-0.266	-0.191	-0.267	-0.23	0.08	-0.32	0.12		
				p	-0.197	-0.268								
C-1000-3	NSLsyn07	11.1 : 1	0.30	g	-0.170	-0.298	-0.162	-0.274	-0.162	-0.274	-0.35 ± 0.36		0.004 ± 0.047	
				g	-0.155	-0.250								
				p	-0.236	-0.349	-0.236	-0.349	-0.51	0.36	-0.63	0.37		

All experiments were performed at 500 MPa.

‡ Iron to sulphur weight ratio. The variation in this ratio was obtained by varying the amount of S added to the capsules.

§ Separated glass (g) or pyrrhotite (p) fraction.

¶ Runs were interrupted after one day to rehomogenise the charge.

¶¶ Measured values of the separated pyrrhotite fractions were corrected for contamination with Fe from glass during phase separation (see appendix A2 for details).

§ Analytical uncertainty (long-term external reproducibility (2σ)) on the Neptune mass spectrometer with standard-sample bracketing is ± 0.049 ‰ on  $\delta^{56}\text{Fe}$  and ± 0.071 ‰ on  $\delta^{57}\text{Fe}$ .

¶ The given error results from propagation of the uncertainties in  $\delta^{56}\text{Fe}$  values of the involved phases.

& The given error is the two standard deviation (2σ) of all  $\Delta^{56}\text{Fe}_{\text{pyrrhotite-melt}}$  values obtained at a certain temperature.

# Fraction of Fe transferred from the melt to pyrrhotite during the crystallisation experiments, calculated from measured FeO concentrations (H<sub>2</sub>O free normative concentrations; Tables A2.2 and A2.54)

in the glass before and after the experiments:  $f_{\text{Fe}_{\text{transfer}}} = (c_{\text{FeO}_{\text{melt}}^{\text{glass}}} - c_{\text{FeO}_{\text{melt}}^{\text{cryst}}}) / c_{\text{FeO}_{\text{melt}}^{\text{glass}}}$ . Given uncertainties result from propagation of analytical errors of FeO concentrations (EMPA).

\*  $f_{\text{Fe}_{\text{transfer}}}$  for C-840-2 was estimated on the basis of experiments C-840-1 and C-840-3, because no thin section for electron microprobe analysis was prepared from this sample. Therefore, correction on

the  $\delta^{56}\text{Fe}$  of pyrrhotite are also based on this estimate.

## 2.3.1. Isotope exchange kinetics

The kinetics of Fe isotope exchange and the time scale to attain isotopic equilibrium in the system was investigated in detail at 900°C and 500 MPa using  $^{57}\text{Fe}$  enriched glass. Figure 2.3 shows that the  $\delta^{57}\text{Fe}$  of the melt decreased rapidly with experimental runtime through isotope exchange with the coexisting pyrrhotite, which correspondingly increased in  $\delta^{57}\text{Fe}$ . A close approach to Fe isotope equilibrium (> 90 %) between these two phases is already attained after 24 hours.

The extent of isotope equilibration  $F(\delta)$  at a given runtime can be described for each phase by

$$F(\delta) = \frac{\delta^{57}\text{Fe}_{\text{final}} - \delta^{57}\text{Fe}_{\text{initial}}}{\delta^{57}\text{Fe}_{\text{equilibrium}} - \delta^{57}\text{Fe}_{\text{initial}}} \quad (2.4)$$

where  $\delta^{57}\text{Fe}_{\text{initial}}$  and  $\delta^{57}\text{Fe}_{\text{final}}$  denote the Fe isotope composition of this phase before and after the experiment (e.g., Criss et al., 1987; Johnson et al., 2004).  $\delta^{57}\text{Fe}_{\text{equilibrium}}$  is the equilibrium isotope composition of this phase, which is identical to the bulk Fe isotope composition of the mixture in the capsule if full equilibration is reached. This presumption is valid because any equilibrium Fe isotope fractionation between melt and pyrrhotite is insignificant compared to the difference in  $\delta^{57}\text{Fe}$  between the two phases even at  $F = 0.99$ . The bulk Fe isotope composition can be calculated from the respective amounts of iron and corresponding  $\delta^{57}\text{Fe}_{\text{initial}}$  values of the starting materials. Alternatively,  $F$  can also be expressed in terms of  $\Delta^{57}\text{Fe}$ :

$$F(\Delta) = \frac{\Delta^{57}\text{Fe}_{\text{final}} - \Delta^{57}\text{Fe}_{\text{initial}}}{\Delta^{57}\text{Fe}_{\text{equilibrium}} - \Delta^{57}\text{Fe}_{\text{initial}}} \quad (2.5)$$

Both expressions (Eqn. 2.4 and 2.5) were used to evaluate the fractional approach to equilibrium.

The atomic processes which control the isotope exchange kinetics in our experiments are not fully clear. However, isotope exchange kinetics observed in other experimental systems (e.g., Cole and Chakraborty, 2001) often follow the general form shown in Figure 2.3, i.e. rapid initial exchange is followed by slower exchange. Since small amounts of pyrrhotite are dissolved in the initial stages of the experiments, it is possible that the isotope exchange reaction is dominated by dissolution and recrystallisation in the early stages, as indicated by more than 50% exchange after the 2 hour experiment. Recrystallisation of pyrrhotite is also supported by XRD measurements on the run products, demonstrating a change from initially monoclinic to hexagonal symmetry. After 24 hours the approach to the equilibrium value slows (Fig. 2.3). This might be due to a diffusion-controlled exchange mechanism, governed by the diffusivity of Fe in pyrrhotite and in the melt. However, the experiments demonstrate that a very close approach to equilibrium is already reached after 48 hours.

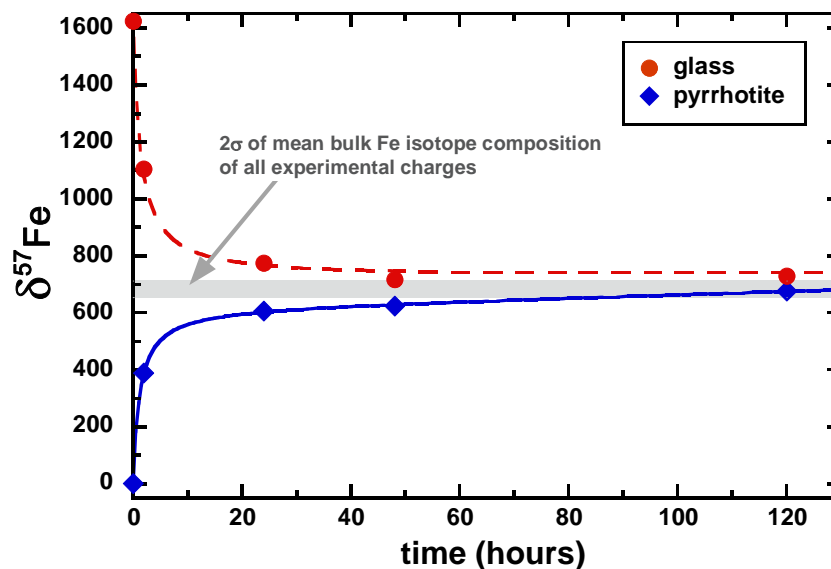


Figure 2.3. Kinetics of iron isotope exchange between pyrrhotite and  $^{57}\text{Fe}$  enriched silicate melt at 900°C and 500 MPa. A close approach to isotopic equilibrium (grey shaded band) is already attained after 24 hours. The solid trend line was fitted to the pyrrhotite data. This in turn was used to compute the corresponding dashed line for the glass fraction to satisfy mass balance. The grey area represents the variation in the bulk Fe isotope composition of all experimental charges (average =  $682 \pm 29\text{‰}$ ,  $2\sigma$ ). Each capsule was filled with an individually prepared mixture of pyrrhotite and glass powder.

### 2.3.2. Isotope exchange experiments

The method of Northrop and Clayton (1966), originally developed to determine oxygen and carbon isotope equilibrium fractionation factors, was applied to determine Fe equilibrium isotope fractionation factors between pyrrhotite and silicate melt at high temperatures. This method allows the determination of an equilibrium fractionation factor between two phases at given conditions from a set of partial exchange experiments. Partial isotope exchange reactions can be described mathematically by the following equation (Northrop and Clayton, 1966):

$$\ln\alpha_{initial} = \ln\alpha_{equilibrium} - 1/F \cdot (\ln\alpha_{final} - \ln\alpha_{initial}) \quad (2.6)$$

where  $\alpha_{initial}$  and  $\alpha_{final}$  represent the differences in isotope composition between the two phases of interest at the beginning and at the end of the experiment, respectively, expressed as fractionation factor (see equation 2.2).  $\alpha_{equilibrium}$  is the difference in isotope composition between the two phases when equilibrium is reached, and F is the degree of equilibration of the system (see equations 2.4 and 2.5) after a certain experimental runtime.

The equilibrium fractionation factor can be derived from the y-intercept of a plot of  $\ln\alpha_{initial}$  versus  $\ln\alpha_{final} - \ln\alpha_{initial}$  data. Alternatively, if  $\alpha$  values are close to unity, as in our study, plots of  $\Delta^{56}\text{Fe}_{initial}$  vs.  $(\Delta^{56}\text{Fe}_{final} - \Delta^{56}\text{Fe}_{initial})$  are equivalent (see Fig. 2.4).

The equilibrium fractionation factor between pyrrhotite and silicate melt at each experimental temperature was determined by a least squares fit accounting for individual errors using the method of York (1969) as implemented in *Isoplot* (Ludwig, 2001). The linearity of the data (Fig. 2.4) indicates that boundary conditions for application of the partial exchange method are satisfied. Criss (1999) proposed an iterative approach for solving equation 2.6. We applied both methods to our data and obtained identical results. For simplicity, we implemented the conventional method of Northrop and Clayton (1966).



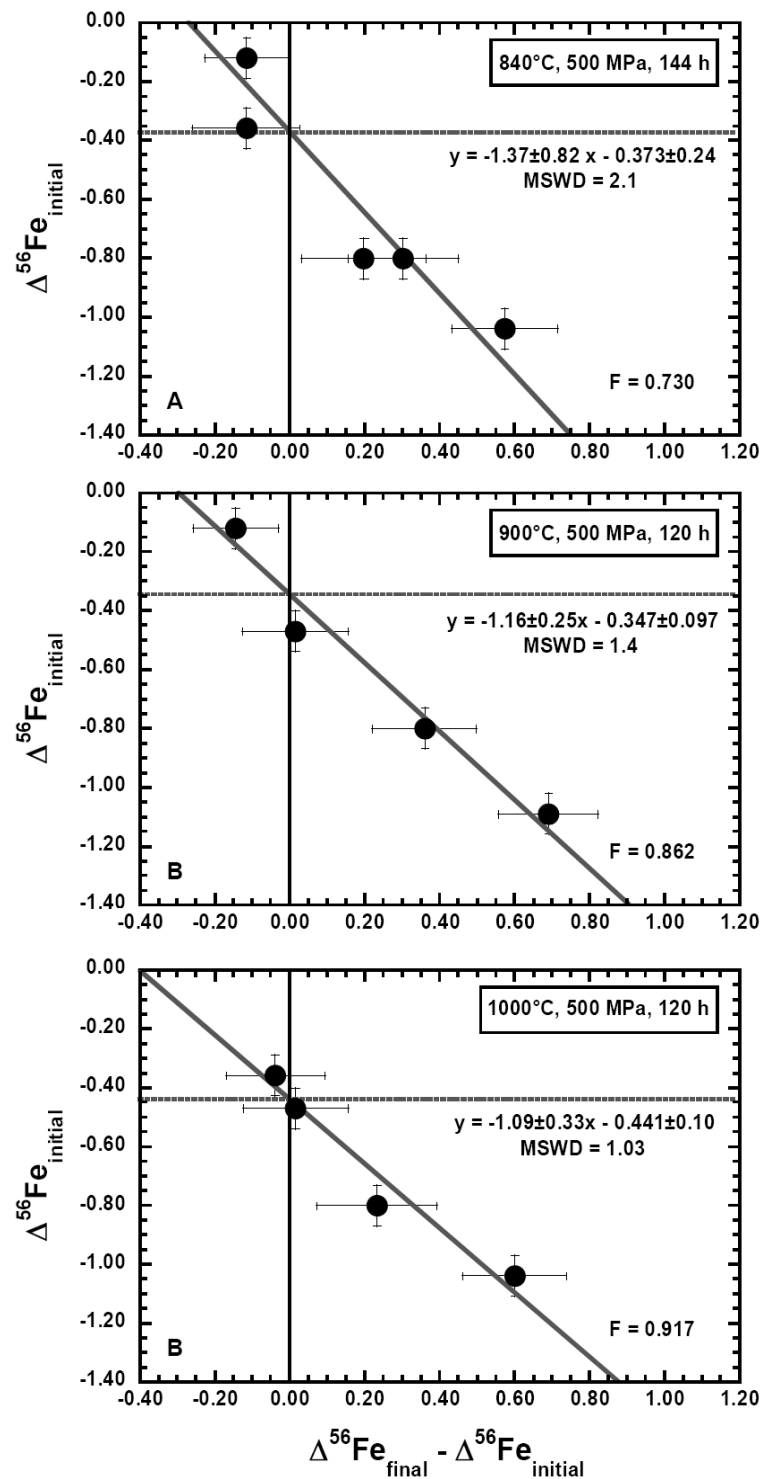


Figure 2.4. Iron isotope exchange between pyrrhotite and silicate melt at temperatures of (A) 840°C, (B) 900°C and (C) 1000°C presented according to Northrop and Clayton (1966).  $\Delta^{56}\text{Fe}_{\text{initial}}$  and  $\Delta^{56}\text{Fe}_{\text{final}}$  represent the differences in Fe isotope composition between pyrrhotite and glass at the start and at the end of each experiment (Table 2.5). The y-intercept of the linear regression corresponds to the equilibrium isotope fractionation factor and F ( $= -1/\text{slope}$ ) to the extent of equilibration.

The fractional approach to equilibrium, determined from the slopes in Fig. 2.4 ( $F = -1/\text{slope}$ ) was 0.72 at 840°C (6 days), 0.86 at 900°C (5 days) and 0.93 at 1000°C (5 days) (denoted as  $F(\text{N\&C})$  in Table 2.2). These values are generally lower than  $F(\delta)_p$  values calculated by equation 2.4 from the  $^{57}\text{Fe}$  enriched samples included in each experimental series. However, these discrepancies lie within the uncertainties of the slopes derived by linear regression. It must be noted that the slopes in Figure 2.4 are associated with relatively high uncertainties, but the y-intercepts, which are the quantitatively relevant values here, are more precise. The derived fractionation factors expressed as  $\Delta^{56}\text{Fe}_{\text{pyrrhotite-melt}}$  are  $-0.37 \pm 0.24\text{‰}$  at 840 °C,  $-0.35 \pm 0.10\text{‰}$  at 900°C and  $-0.44 \pm 0.10\text{‰}$  at 1000°C (Table 2.2). The negative sign of the fractionation factor indicates that pyrrhotite incorporates preferentially lighter Fe isotopes relative to the coexisting silicate melt.

### 2.3.3. Crystallisation experiments

The crystallisation experiments corroborate the result of the exchange experiments in that pyrrhotite is isotopically lighter than the silicate melt. The measured  $\Delta^{56}\text{Fe}_{\text{pyrrhotite-melt}}$  values of different samples, run at the same temperature, show good internal consistency, independent from the initial sulphur content (Table 2.3). Average  $\Delta^{56}\text{Fe}_{\text{pyrrhotite-melt}}$  values are  $-0.35 \pm 0.10\text{‰}$  at 840°C,  $-0.38 \pm 0.10\text{‰}$  at 900°C and  $-0.30 \pm 0.23\text{‰}$  at 1000°C (Table 2.3). Pyrrhotite crystal content varied in the experimental products and was quantified by comparing the iron concentration of the starting glass and the post-experimental glass. Since pyrrhotite is the only Fe bearing crystalline phase, the fraction of Fe transferred from the melt to pyrrhotite,  $f\text{Fe}_{\text{transfer}}$  can be calculated as  $(c\text{FeO}_{\text{start glass}} - c\text{FeO}_{\text{glass after exp}}) / c\text{FeO}_{\text{start glass}}$ . In the calculation we used H<sub>2</sub>O-free normative FeO concentrations derived from the analyses listed in Tables A2.2 and A2.5. The obtained values of  $f\text{Fe}_{\text{transfer}}$  range from 0.004 to 0.189 (Table 2.3). However, it must be noted that these calculations have high

uncertainties due to the low pyrrhotite contents and hence small changes in the Fe concentration in the melt, which are hardly detectable within analytical precision. This is also reflected in the large errors assigned to the corrected  $\delta^{56}\text{Fe}$  values of pyrrhotite of two of the 1000°C experiments, which have very low pyrrhotite contents (Table 2.3). Figure 2.5 shows the measured Fe isotope compositions of corresponding pyrrhotite-glass pairs in comparison with the theoretical mass balance lines for equilibrium Fe isotope fractionation in a closed system. Except for one 1000°C experiment (C-1000-2), there is good agreement between measured and predicted Fe isotope distributions.

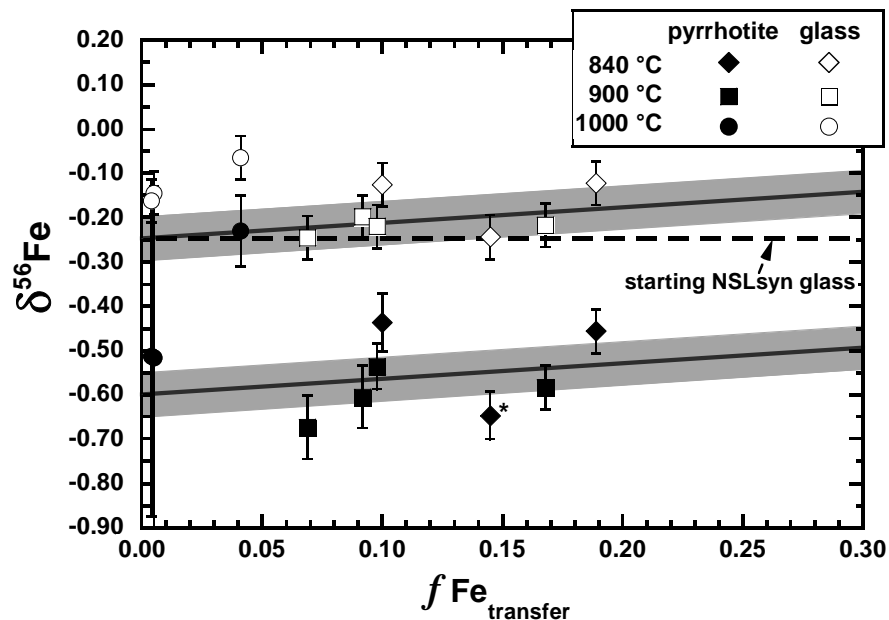


Figure 2.5.  $\delta^{56}\text{Fe}$  values of corresponding pyrrhotite (corrected for incomplete phase separation) and glass pairs from crystallisation experiments in comparison with calculated mass balance lines for equilibrium isotope fractionation in a closed system. Mass balance lines are constructed using the error weighted average of  $\Delta^{56}\text{Fe}_{\text{pyrrhotite-melt}}$  of  $-0.35\text{‰}$  obtained from crystallisation and isotope exchange experiments. The grey areas correspond to the analytical uncertainty ( $\pm 0.049\text{‰}$ ) of  $\delta^{56}\text{Fe}$  measurements. The pyrrhotite datum marked with an \* represents the uncorrected measured  $\delta^{56}\text{Fe}$  value (see Table 2.3).

## 2.4. DISCUSSION

### 2.4.1. Stability of pyrrhotite

The stability field of pyrrhotite is a complex function of thermodynamic parameters, such as temperature, pressure, and the fugacity of sulphur and oxygen. From observations in natural samples and from experimental studies it is known that silicate melts can coexist with immiscible sulphide liquids from which sulphide minerals crystallise rapidly during cooling (Whitney, 1984; Luhr, 1990; Vaughan and Lennie, 1991; Clemente et al., 2004). Hence, to interpret the measured Fe isotope partitioning we have to consider whether pyrrhotite found in the run products was a stable phase at the experimental conditions or represents a quench phase.

As already described in section 2.3 formation of a sulphur-rich liquid phase was observed for initial experiments with relatively high amounts of sulphur (up to 14.16 wt% S; Fig. 2.1A). This phase disappeared when the amount of sulphur was reduced ( $< 0.53$  wt% S) and pyrrhotite became the only sulphur-rich phase in the system (Fig. 2.1B-D). In crystallisation experiments pyrrhotite crystals are preferentially located at the former grain boundaries of the glass powder used as starting material (Fig. 2.1B) indicating heterogeneous nucleation of pyrrhotite under experimental conditions. If an immiscible sulphide liquid was present during the experiment, formation of a few larger pools is expected (to minimise surface energy), rather than numerous small droplets and even aggregates of droplets. Additional evidence that pyrrhotite is a stable phase at experimental conditions is given by the exchange experiments which show that the initially added pyrrhotite crystals were partly dissolved in the silicate melt until sulphur and iron saturation was reached. These crystals

show a typical dissolution texture (Fig. 2.1F). Their subhedral crystal shapes, however, are still preserved and no signs for formation of an immiscible sulphide liquid can be found.

#### 2.4.2. Iron isotope fractionation

Both experimental approaches show that resolvable iron isotope fractionation exists at magmatic conditions. Pyrrhotite incorporates preferentially lighter Fe isotopes relative to the coexisting silicate melt. The fractionation factors determined from the crystallisation experiments are in good agreement with the values obtained from the isotope exchange experiments (Tables 2.2 and 2.3, Fig. 2.6).

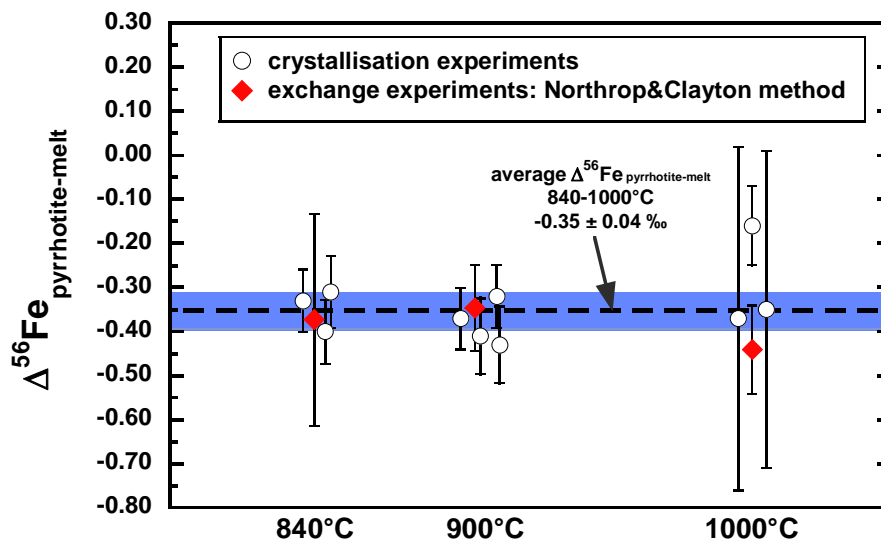


Figure 2.6. Summary of the Fe isotope dataset obtained from the partial exchange experiments and the crystallisation experiments. The results of the crystallisation experiment agree well with those of the exchange experiment. Uncertainties associated with crystallisation experiments at 1000°C are larger, due to higher uncertainties on the small changes in  $\text{FeO}_{\text{total}}$  (compare  $f_{\text{Fe}_{\text{transfer}}}$  in Table 2.3), which was used to correct the measured  $\delta^{56}\text{Fe}$  of pyrrhotite for contamination with Fe from the glass during phase separation. The dashed line represents the error-weighted average of all  $\Delta^{56}\text{Fe}_{\text{pyrrhotite-melt}}$  values from both the crystallisation experiments and the partial isotope exchange method.

Understanding the mechanisms of isotope fractionation is necessary to interpret natural Fe isotope variations in igneous systems. In doing so, it is important to distinguish between kinetic and equilibrium fractionation. This issue will be discussed in the following

section. Then we focus on the interpretation of the fractionation data in terms of structural and compositional parameters controlling the sign and magnitude of the Fe isotope fractionation factor by comparing the experimental data with predicted fractionations.

#### *2.4.2.1. Kinetic or equilibrium isotope fractionation?*

The two different experimental approaches (crystallisation and exchange experiments) follow two different reaction pathways. In the crystallisation experiments, Fe from the melt is transferred into pyrrhotite. Possible mechanisms controlling these experiments are diffusion of iron in the melt, reaction kinetics at the interfaces between sulphur/melt, pyrrhotite/sulphur and pyrrhotite/melt and diffusion of iron in the newly formed pyrrhotite. In the exchange experiments pyrrhotite is partly dissolved and controlling steps for the reaction may be diffusion of iron in the melt and in pyrrhotite, diffusion of sulphur into the melt and the interface reaction between pyrrhotite and melt.

There is no indication that interface reactions are important for the timescale required to achieve chemical and isotopic equilibrium in the system. Furthermore, diffusion of iron in pyrrhotite is very fast compared to the crystal sizes of pyrrhotite. According to Condit et al. (1974) the self diffusion coefficient  $D_{\text{Fe}}$  in  $\text{Fe}_{0.9}\text{S}$  at  $840^\circ\text{C}$  is  $1.08 \cdot 10^{-11} \text{ m}^2/\text{s}$ . Hence, the timescale to equilibrate pyrrhotite crystals of  $20 \mu\text{m}$  diameter is about 37 seconds, much lower than the experimental duration. In the crystallisation experiments the size of pyrrhotite crystals is much smaller and, hence, Fe isotopic equilibration of pyrrhotite is even faster. Thus, the mechanism which controls the equilibration of the samples is probably diffusion of iron in the melt. Experimental data for iron diffusion in the rhyolitic melts are not available, but data for lanthanum diffusion may serve as a lower limit for iron diffusion (La is in trivalent state whereas Fe is in a mixed divalent/trivalent state). At  $800^\circ\text{C}$  and 500 MPa in rhyolitic melt containing 5 wt% water La-diffusivity is  $6 \cdot 10^{-15} \text{ m}^2/\text{s}$  (Tegge-Schüring, 2003),

resulting after 144 h run duration in a diffusion length ( $\sqrt{(D \cdot t)}$ ) of 57  $\mu\text{m}$ . This is similar to the average distance between pyrrhotite crystals. Diffusion in the more depolymerised and thus less viscous peralkaline melt at 840°C can be expected to be significantly faster (Mungall, 2002). Hence, we conclude that iron diffusion in the melt should be always fast enough to equilibrate iron isotopes in the sample during the applied run durations, consistent with the findings of the kinetic  $^{57}\text{Fe}$  tracer experiments.

#### *2.4.2.2. Effect of temperature on iron isotope fractionation*

Equilibrium isotope fractionation typically shows a decrease in magnitude with increasing temperature with  $1/T$  or  $1/T^2$  (Urey, 1947). However, predicted changes of the fractionation factors for any mineral combination in the investigated temperature range between 840°C and 1000°C (Polyakov and Mineev, 2000) are below analytical resolution. Indeed, our experiments did not reveal any temperature dependence of the fractionation factor within experimental and analytical precision (Fig. 2.6). However, an alternative explanation for the lack of temperature dependence is that the fractionation measured in the quenched phases is overprinted by retrograde exchange processes. Thus, it has to be discussed whether the data reflect equilibrium at high temperature or the isotopic closure temperature of the system (Dodson, 1973). As discussed above Fe diffusion in the silicate melt is probably the limiting factor controlling equilibration. Thus, although Fe re-equilibration by diffusion within a pyrrhotite crystal might be possible during quenching, an isotope exchange between pyrrhotite and silicate melt would be limited by the Fe diffusivity in the silicate melt. The typical time to cool the experimental charges from the run temperature to 400°C (at this temperature cation diffusion in the melt can be considered as essentially frozen-in) was less than three minutes. As shown in Figure 2.3 this time interval is very short compared to the characteristic equilibration time of >24 h at 900°C. At lower

temperature the equilibration time is even longer. Thus, we conclude that only a minor fraction of iron isotopes can exchange during cooling and the measured fractionation factors reflect the near-equilibrium fractionation under the given experimental conditions.

We propose an average fractionation factor between pyrrhotite and silicate melt of  $\Delta^{56}\text{Fe}_{\text{pyrrhotite-melt}} = -0.35 \pm 0.04\text{‰}$  (2SE,  $n=13$ ) at 500 MPa and temperatures between 840°C to 1000°C. This value represents the error-weighted average of all fractionation data from the exchange experiments using the method of Northrop and Clayton (1966) and the crystallisation experiments (Tables 2.2 and 2.3) and was calculated using the *Isoplot* program (Ludwig, 2001). The given uncertainty ( $2\text{SE} = t \cdot \frac{\sigma}{\sqrt{n}}$ ) describes the 95% confidence level for the mean value of the population, with  $n=13$  and a *students-t* factor  $t = 2.18$  for 12 degrees of freedom at 95% confidence level.

### 2.4.3. Mechanisms of isotope fractionation

In order to develop insights into the mechanisms of Fe isotope fractionation between pyrrhotite and silicate melt, we compare our results to predictions based on Mössbauer spectroscopy data (Polyakov and Mineev, 2000; Polyakov et al., 2007) (Fig. 2.7). Currently, no predictions of Fe isotope fractionation between minerals and silicate melts are available. Therefore, we assume that the reduced isotopic partition function ratios ( $\beta$ -factors) of ferrous and ferric iron bearing silicate minerals can be used as reasonable approximations of  $\beta$ -factors for silicate melts. For ferric iron-dominated silicates we used the  $\beta$ -factor of aegirine (Polyakov and Mineev, 2000). The ferrous iron silicate “fields” shown in Figure 2.7 were calculated on the basis of the entire range of  $\beta$ -factors available for olivine, diopside, enstatite and hedenbergite from Polyakov and Mineev (2000). The  $\beta$ -factors of  $\text{FeS}_2$  and



$\text{Ni}_{0.95}\text{Fe}_{0.05}\text{S}_2$  are also from Polyakov and Mineev (2000). The  $\beta$ -factor of FeS (troilite) was calculated by Polyakov et al. (2007) on the basis of the partial phonon density of state (PDOS), obtained by inelastic nuclear resonant x-ray scattering (INRXS) at 1.5 GPa by Kobayashi et al. (2004). The stoichiometric polymorph of FeS, troilite that is stable only up to about 140°C at 1 atm (Craig and Scott, 1974), differs from high-temperature hexagonal pyrrhotite only by a slight distortion from the ideal NiAs structure. The NiAs structure type exhibits considerable chemical flexibility due to accommodation of metal vacancies, common for pyrrhotites. Thus, we conclude that the  $\beta$ -factor of FeS (troilite) can be considered as representative for pyrrhotite in our experimental temperature range.

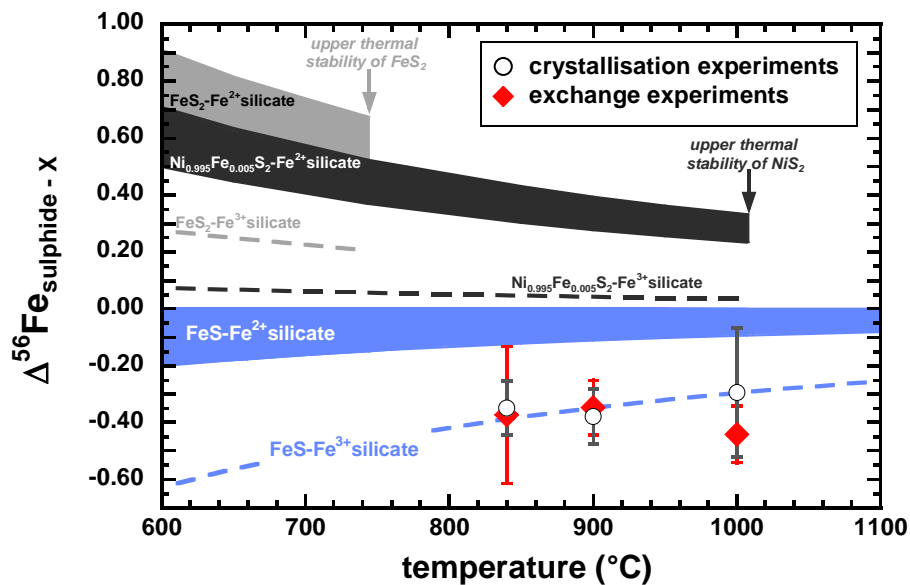


Figure 2.7. Experimentally determined Fe isotope fractionation between pyrrhotite ( $\text{Fe}_{1-x}\text{S}$ ) and rhyolitic melt. Also plotted are the predicted equilibrium isotope fractionations between sulphide minerals and ferric or ferrous Fe dominated silicate minerals, calculated on the basis of Mössbauer and INRXS data by Polyakov and Mineev (2000) and Polyakov et al. (2007). Thermal stability limits valid for 1 atm (Craig and Scott, 1974).

Our experimental findings are consistent with the predicted Fe isotope fractionation between FeS and a ferric iron dominated silicate (Fig. 2.7), suggesting that the Fe redox state in the silicate melt plays an important role for Fe isotope fractionation. Our experimentally

determined fractionation factor is representative for a specific  $\text{Fe}^{2+}/\Sigma\text{Fe}$  ratio ( $0.38\pm 0.02$ ). From Figure 2.7 it is evident that if the silicate melt becomes more reduced, a decrease in the fractionation factor between pyrrhotite and silicate melt is predicted, perhaps approaching zero.

Differences in coordination of Fe exist between pyrrhotite and the silicate melt present in our experiments that may affect Fe isotope fractionation as well (Schauble, 2004). Contrary to pyrrhotite, the peralkaline melt contains both ferric and ferrous iron. Ferric iron is predominantly tetrahedrally coordinated by oxygen. However, some  $\text{Fe}^{3+}$  may also be present in five-fold or six-fold coordination (Mysen and Richet, 2005). The coordination of  $\text{Fe}^{2+}$  in silicate melts is still debated. A continuous distribution of  $\text{Fe}^{2+}$  environments from four-fold to six-fold coordination in silicate melts has been suggested (e.g., Seifert et al., 1979; Virgo and Mysen, 1985; Rossano et al., 2000; Farges et al., 2004; Wilke et al., 2005). However, for silica-rich melts it can be expected that most  $\text{Fe}^{2+}$  is octahedrally coordinated (e.g., Mysen et al., 1982; Virgo and Mysen, 1985). Given that all other parameters are identical one might expect an enrichment of the heavier isotopes in the phase where Fe has a lower coordination number (Schauble, 2004). In our experiments octahedrally coordinated Fe in pyrrhotite is isotopically lighter than the silicate melt with primarily tetrahedrally coordinated Fe (possibly along with minor Fe in 5- and 6-fold coordination), which is consistent with theory.

Moreover, it can be seen from Figure 2.7, that considerable differences in isotope fractionation exist between the different Fe sulphides. For example, a change of the sign of the fractionation factor occurs comparing FeS with  $\text{FeS}_2$  and  $\text{Ni}_{0.95}\text{Fe}_{0.05}\text{S}_2$ , although all the three sulphides contain octahedrally coordinated ferrous Fe. Hence, there must be other factors governing Fe isotope fractionation besides the valency and the coordination of Fe. A possible explanation may lie in the nature of bonding in the sulphides and the related

electron configuration. In pyrrhotite iron is in the high-spin state (Prewitt and Rajamani, 1974), i.e. four of the six 3d electrons occupy the three  $t_{2g}$  orbitals, forming only one  $\pi$  bond. Additionally, a metallic Fe-Fe bond along the c-axis of the NiAs cell is present in the pyrrhotite structure, although it is subsidiary to the main Fe-S bond (e.g., Tokonami et al., 1972; Farrell and Fleet, 2001). On the other hand in the pyrite-type sulphides iron is in the low spin-state (Prewitt and Rajamani, 1974), i.e. all six 3d electrons fill the three  $t_{2g}$  orbitals, forming three  $\pi$  bonds. This  $\pi$  bond formation increases the covalency of the Fe-S bond in the sequence  $\text{FeS} < \text{Ni}_{1-x}\text{Fe}_x\text{S}_2 < \text{FeS}_2$  (Prewitt and Rajamani, 1974), consistent with the sequence of the respective  $\beta$ -factors (Fig. 2.7). This highlights the importance of the bond character as an influencing factor on inter-mineral Fe isotope fractionation, as already emphasised by Polyakov and Mineev (2000) and Schauble (2004).

For our experiments, we suggest that differences in ligands and Fe redox state (to which Fe coordination is linked) between pyrrhotite and silicate melt most likely control the sign and magnitude of isotope fractionation.

#### **2.4.4. Applications to natural systems – perspectives**

Pyrrhotite ( $\text{Fe}_{1-x}\text{S}$ ) is a common iron sulphide and an important constituent of mafic ore deposits. It is also found in pegmatites, in contact metamorphic deposits, in high temperature metamorphic veins and in sediments. Pyrrhotite has repeatedly been observed in felsic magmatic environments as an accessory mineral phase and as inclusions within phenocrysts (e.g., Ueda and Itaya, 1981; Whitney and Stormer, 1983). Natural pyrrhotites, like other sulphides such as pyrite and chalcopyrite (Graham et al., 2004; Rouxel et al., 2004), show a considerable range in Fe isotope compositions. For example the pyrrhotite samples analysed in this study cover a range from -1.09 to 0‰ in  $\delta^{56}\text{Fe}$  (see appendix A2.4), while the mean mafic Earth has a  $\delta^{56}\text{Fe}$  value of +0.069‰ (recalculated from the  $\delta^{57}\text{Fe}$

values reported by Poitrasson et al., 2004). If we consider the fractionation factor between pyrrhotite and ferric iron-rich peralkaline rhyolitic melt of  $\Delta^{56}\text{Fe}_{\text{pyrrhotite-melt}} = -0.35\text{‰}$  as a maximum value at magmatic temperatures, then primary pyrrhotites of igneous origin are expected to have  $\delta^{56}\text{Fe}$  values that are only slightly lower than or even equal to that of the mean mafic Earth (Fig. A2.3). Consequently, the very negative  $\delta^{56}\text{Fe}$  values of some pyrrhotites (Fig. A2.2, A2.3) cannot be explained solely by primary magmatic mineral-melt fractionation. Other processes, such as hydrothermal activity and metamorphism or other isotopically fractionated Fe-sources need to be involved in pyrrhotite formation to explain these values. Assuming crystallisation from a mafic melt having a  $\delta^{56}\text{Fe}$  value of  $+0.069\text{‰}$  (Fig. A2.3) a primary magmatic Fe isotope signature of pyrrhotites is expected to lie between  $+0.069\text{‰}$  and  $-0.281\text{‰}$  in  $\delta^{56}\text{Fe}$ , whereas sulphides of low-temperature origins are expected to display more negative  $\delta^{56}\text{Fe}$  values. However, since a considerable overlap exists between the  $\delta^{56}\text{Fe}$  values of “high-T sulphides” and “low-T sulphides” analysed in this study the Fe isotope composition of pyrrhotites alone does not allow a simple genetic classification. Hence, more work is needed to test whether Fe isotope systematics may be a useful tool to determine the processes of sulphide formation and evolution of sulphide ore deposits.

Another interesting aspect arises from the conclusion that the redox state of iron plays an important role on the Fe isotope fractionation in magmatic systems. In natural silicate melts a high variability of the redox state of Fe exists depending on the magma composition. On average the  $\text{Fe}^{2+}/\Sigma\text{Fe}$  decreases as magmatic liquids become more felsic (e.g., Fig. 8.19 in Mysen, 1988, and Fig. I.II). Our experimentally determined fractionation factor probably represents an upper limit for iron isotope fractionation during pyrrhotite crystallisation from magmas in nature. A much smaller fractionation (probably approaching

zero) than in our experiments can be expected for a MORB system, with  $\text{Fe}^{2+}/\Sigma\text{Fe}$  ratios of silicate melts typically  $> 0.8$  (e.g., Bezos and Humler, 2005, and Fig. I.II). Considering the variations in oxygen fugacity found in natural magmatic systems with different chemical compositions, and the related diversity in the redox state of Fe in silicate melts, a variation of mineral-melt Fe isotope fractionation in general is likely, assuming a sensitivity of the fractionation factor to the Fe redox state. If true, Fe isotopes may serve as a tracer for changing redox conditions in magmatic systems. However, a prerequisite to this application would be that the change in mineral-melt fractionation as a function of the  $\text{Fe}^{2+}/\Sigma\text{Fe}$  ratio of the melt is analytically resolvable. Up to date no such studies have been done and further investigation is needed.

## 2.5. CONCLUSIONS

The experimentally studied Fe isotope partitioning between coexisting iron sulphide (pyrrhotite) and a hydrous rhyolitic melt at magmatic conditions (840°C to 1000°C, 500 MPa) show that pyrrhotite preferentially incorporates lighter Fe isotopes relative to silicate melt. For the investigated temperature range from 840°C to 1000°C we determined an average equilibrium Fe isotope fractionation factor of  $\Delta^{56}\text{Fe}_{\text{pyrrhotite-melt}} = -0.35 \pm 0.04\%$  (2SE, n=13). In comparison to the relatively ferric iron-rich peralkaline rhyolitic composition used in our experiments a smaller Fe isotope fractionation factor is expected between pyrrhotite and a basaltic melt with a higher  $\text{Fe}^{2+}/\Sigma\text{Fe}$  ratio.

Ferrous iron bonded to sulphur in pyrrhotite forms a marked contrast in comparison to oxygen-coordinated Fe in a mixed divalent/trivalent state in the silicate melt (i.e. [Fe(II)-S] in pyrrhotite vs. [Fe(II)/Fe(III)-O] in the silicate melt). Thus, in view of the high

temperatures the relatively large isotope fractionation determined in this study is most likely a consequence of significant differences in the redox state and in the ligand of Fe between the phases. This might explain why Fe isotope fractionation observed between silicate minerals in igneous rocks (e.g., Beard and Johnson, 2004b), where Fe is solely coordinated by oxygen, is smaller or not resolvable at all.

**Chapter 3. Iron and lithium isotope systematics of the Hekla volcano,  
Iceland – Evidence for stable Fe isotope fractionation during magma  
differentiation**

ABSTRACT

In this study potential iron isotope fractionation in the Earth's crust by magmatic processes was systematically investigated. High precision iron isotope analyses by MC-ICP-MS were performed on a suite of rock samples representative for the volcanic evolution of the Hekla volcano, Iceland. The whole series of Hekla's rocks results from several processes. (i) Basaltic magmas rise and induce partial melting of meta-basalts in the lower part of the Icelandic crust. The resulting dacitic magma evolves to rhyolitic composition through crystal fractionation. During this differentiation the  $\delta^{56/54}\text{Fe}_{\text{IRMM-014}}$  values increase successively from 0.051 for the primitive dacites to 0.168 ( $\pm 0.021\%$  external reproducibility) for the rhyolites. This increase can be described by a Rayleigh fractionation model using a constant bulk fractionation factor between all mineral phases (M) and the silicate liquid (L) of  $\Delta^{56/54}\text{Fe}_{\text{M-L}} = -0.1\%$ . (ii) The basaltic magma itself differentiates by crystal fractionation to basaltic andesite composition. No Fe isotope fractionation was found in this series. All basalts and basaltic andesites have an average  $\delta^{56/54}\text{Fe}_{\text{IRMM-014}}$  value of  $0.062 \pm 0.042\%$  (2SD, n=9), identical to mean terrestrial basaltic values reported in previous studies. This observation is consistent with the limited decrease in iron concentration of the remaining silicate melt during crystal fractionation and small mineral-melt Fe isotope fractionation

factors expected at temperatures  $> 1050^{\circ}\text{C}$ . (iii) Andesites are produced by mixing of basaltic andesite with dacitic melts. The iron isotope composition of the andesites is matching that of the basaltic andesites and the less evolved dacites, in agreement with a mixing process. In the Hekla volcanic suite Li concentrations are positively correlated with indicators of magma differentiation. All Hekla rocks have  $\delta^7\text{Li}$  values typical for the upper mantle and demonstrate the absence of resolvable Li isotope fractionation during crystal fractionation. As a fluid-mobile trace element, Li concentrations and isotopes are a potential tracer of magma/fluid interaction. At Hekla, Li concentrations and isotope compositions do not indicate extensive fluid/melt interaction. Hence, the heavy Fe isotope composition of the dacites and rhyolites can be predominately attributed to fractional crystallisation. Iron isotope analyses on single samples from other Icelandic volcanoes (Torfajökull, Vestmannaeyjar) confirm heavy Fe isotope enrichment in evolving magmas. Our results suggest that the iron isotope composition of the crust can be slightly modified by magmatic processes.

### 3.1. INTRODUCTION

The rapidly evolving field of “non-traditional” stable isotope studies have improved our understanding of the behaviour of iron and lithium isotopes during a variety of geological processes (e.g., Johnson et al., 2004). During the last decade, pioneering work was done to characterise the isotopic inventory of planetary reservoirs and to explore fundamental principles governing isotopic fractionation. It has been shown that processes occurring in low temperature environments at Earth’s surface induce large isotope fractionation. With increasing temperature, the magnitude of stable isotope fractionation



decreases, limiting studies on high temperature geological processes to currently achievable analytical precision. Relatively large isotopic variations of up to 1.1‰ in  $^{56}\text{Fe}/^{54}\text{Fe}$  are observed in the Earth's mantle (e.g., Williams et al., 2005), while igneous crust is isotopically much more homogenous (e.g., Beard et al., 2003a). However, latest analytical improvements now allow resolving smallest Fe isotope variations. For example, differences as small as 0.1‰ in  $^{56}\text{Fe}/^{54}\text{Fe}$  were found between various igneous rocks and reservoirs, although their geological significance is highly debated (Poitrasson and Freydier, 2005; Weyer et al., 2005; Beard and Johnson, 2006; Poitrasson, 2006; Schoenberg and von Blanckenburg, 2006; Beard and Johnson, 2007; Poitrasson, 2007; Weyer et al., 2007; Weyer and Ionov, 2007). Several processes have been proposed to explain these systematic Fe isotope variations in igneous rocks – for instance, the role of partial melting (Williams et al., 2005; Schoenberg and von Blanckenburg, 2006; Weyer and Ionov, 2007), magma differentiation (Beard and Johnson, 2004b; Poitrasson and Freydier, 2005; Schoenberg and von Blanckenburg, 2006), late-stage magmatic fluids or post-magmatic alteration (Beard and Johnson, 2004b; Poitrasson and Freydier, 2005). However, it is difficult to clearly identify the underlying processes, because knowledge about mechanisms that fractionate Fe isotopes at high temperatures is limited. Calculations based on Mössbauer spectroscopy data indicate resolvable inter-mineral Fe isotope fractionation at high temperatures (Polyakov and Mineev, 2000). However, mineral-melt fractionation factors relevant for common magmatic systems (e.g., silicates and oxides vs. silicate melts) haven't been determined yet. Nevertheless, recent experimental work has given evidence for resolvable equilibrium Fe isotope fractionation between magnetite and fayalite at temperatures of 600 to 800°C (Shahar et al., 2007). Moreover, the experiments described in chapter 2 showed relatively large equilibrium Fe isotope fractionation between pyrrhotite and silicate melt at temperatures of 840 to 1000°C ( $\Delta^{56}\text{Fe}_{\text{pyrrhotite-melt}} = -0.35\text{‰}$ ), due to the marked contrast in Fe

redox state and bonding environments (i.e.  $^{[6]}\text{Fe(II)-S}$  in pyrrhotite vs.  $^{[6]}\text{Fe(II)}/^{[4]}\text{Fe(III)-O}$  in the silicate melt).

The question whether magma differentiation processes fractionate Fe isotopes has been addressed by Beard and Johnson (2004b), Poitrasson and Freydier (2005) and by Schoenberg and von Blanckenburg (2006). Beard et al. (2003a) and Beard and Johnson (2004b) analysed a global selection of igneous rock samples representative for various geological settings and covering a wide range of chemical compositions. They found this global igneous rock dataset to be homogeneous in  $^{56}\text{Fe}/^{54}\text{Fe}$  within  $\pm 0.1\%$  (2SD), and concluded from the absence of any correlation between Fe isotope composition and bulk rock  $\text{SiO}_2$  that magma differentiation does not induce Fe isotope fractionation. In contrast, Poitrasson and Freydier (2005) found  $\text{SiO}_2$ -rich granitoids to be significantly heavier in Fe isotope composition than basalts. However, these authors ruled out magma differentiation to be responsible for the heavy Fe isotope signatures of highly evolved rocks, arguing that Fe-rich minerals, which could potentially fractionate Fe isotopes, are absent in evolved granitic magmas. Rather, Poitrasson and Freydier (2005) suggested that exsolving aqueous fluids were preferentially enriched in light Fe isotopes leaving behind an isotopically heavy melt. Schoenberg and von Blanckenburg (2006) found systematic variations in the Fe isotope compositions of a genetically related suite of igneous rocks from the Bergell intrusion, Swiss Alps. However, the observed positive correlation between  $\text{SiO}_2$  and  $^{56}\text{Fe}/^{54}\text{Fe}$  could not unambiguously be attributed to fractional crystallisation, due to simultaneous assimilation of host rocks with ongoing fractional crystallisation (AFC), as is often the case in continental settings.

The primary goal of this study is to explore the ability of stable Fe isotope systematics as a tracer of magmatic processes. Therefore, a systematic investigation of the Hekla volcano, Iceland, with genetically related series of eruption products was performed.

The Hekla volcanic system is especially well-suited for such a study, since magma genesis at such young divergent settings is not influenced by assimilation of host rocks of possibly different Fe isotope composition. Furthermore, the geological setting of Iceland and particularly that of the Hekla volcanic system is ideal for studying the effect of magmatic differentiation processes on isotopic fractionation, since a wide range in magma compositions is produced contemporaneously and the volcanic history has been thoroughly studied. In this study, Fe isotope systematics were complemented with Li isotopes, providing isotopic information from a major and a trace element with different chemical behaviour during magmatic processes. Despite the large isotopic variability of lithium in the mantle (e.g., Seitz et al., 2004; Magna et al., 2006; Jeffcoate et al., 2007; Rudnick and Ionov, 2007), no resolvable Li isotope fractionation was found during basalt (Tomascak et al., 1999b) or granite differentiation (Teng et al., 2006). Analyses of olivine and matrix pairs from Hawaiian basalts showed also no significant differences in  $^7\text{Li}/^6\text{Li}$  ratios (Chan and Frey, 2003; Jeffcoate et al., 2007). Moreover, fresh basaltic rocks have a relatively homogenous Li isotope composition, i.e., within  $\pm 2\%$  in  $^7\text{Li}/^6\text{Li}$  (Elliott et al., 2004; Tomascak, 2004). However, since lithium is a fluid-mobile element, and thus a potential tracer of fluid/magma interaction (Brenan et al., 1998; Wunder et al., 2006; Wunder et al., 2007), Li concentration and isotope systematics bear the potential to evaluate the role of fluids on Fe isotope fractionation in the Hekla volcanic system.

### 3.2. GEOLOGICAL BACKGROUND AND SAMPLE SELECTION

Iceland is located at the intersection of the Mid-Atlantic ridge with the Iceland mantle plume leading to high magma productivity. The Hekla volcano is located in the South

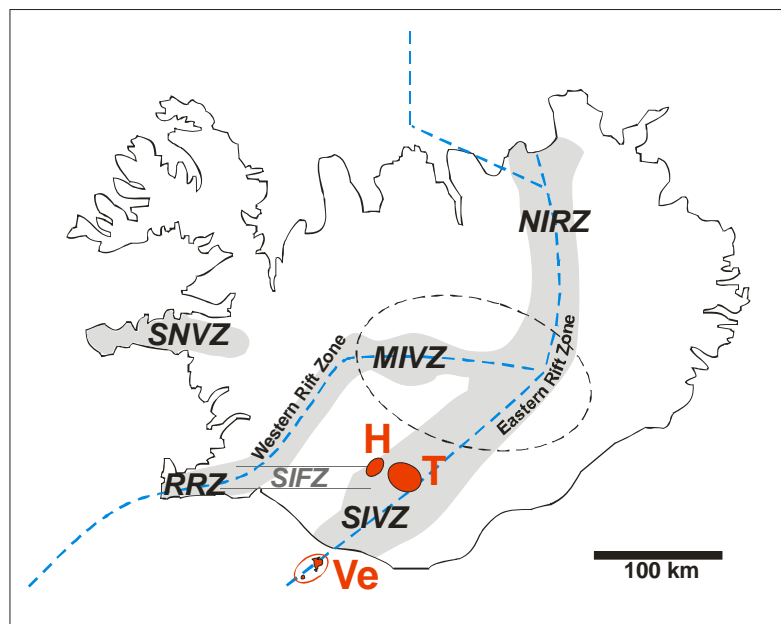


Figure 3.1. Map of Iceland showing the locations of the volcanic systems of Hekla (H), Torfajökull (T) and the Vestmannaeyjar (Ve). The Eldfell volcano is located on the island of Heimaey which is north east of Surtsey – both belonging to the Vestmannaeyjar. Main fault structures and volcanic zones are also shown. NIRZ (North Iceland Rift Zone), MIVZ (Mid Iceland Volcanic Zone), SIVZ (South Iceland Volcanic Zone), Snæfellsnes Volcanic Zone (SNVZ), Reykjanes Rift Zone (RRZ), South Iceland Fracture Zone (SIFZ). The inferred mantle plume centre is indicated by the dashed ellipse (Wolfe et al., 1997).

Iceland Volcanic Zone, at the western margin of a propagating rift (the Eastern Rift Zone) that intersects with the South Iceland Fracture Zone (Fig. 3.1). This area represents the most active volcanic area on Iceland. The present plumbing system beneath Hekla most likely established in the Holocene and a magma chamber has been inferred at a depth of >8 km (Kjartansson and Gronvold, 1983; Sigmarsson et al., 1992a). Eighteen historic eruptions from the Hekla central volcano were documented since 1104 A.D., the most recent one in the year 2000 (see Thordarson and Larsen, 2007, and references therein). The eruptions at the Hekla volcano are compositionally zoned, each usually beginning with an explosive Plinian or sub-Plinian phase followed by effusive activity and lava outpouring. During eruptive events, the composition commonly changes successively from andesite to basaltic andesite, occasionally from rhyolite/dacite to basaltic andesite. The initial SiO<sub>2</sub> content is related to the repose time between eruptions, where the longest inactive periods are followed by

eruptions of the most SiO<sub>2</sub>-rich tephras produced in the initial phases (Thorarinsson and Sigvaldason, 1972).

Major and trace element data of Hekla's rocks illustrate the volcanic evolution of the transitional alkaline series (Fig. 3.2), where incompatible elements like Th and Rb are enriched in the melt during differentiation.

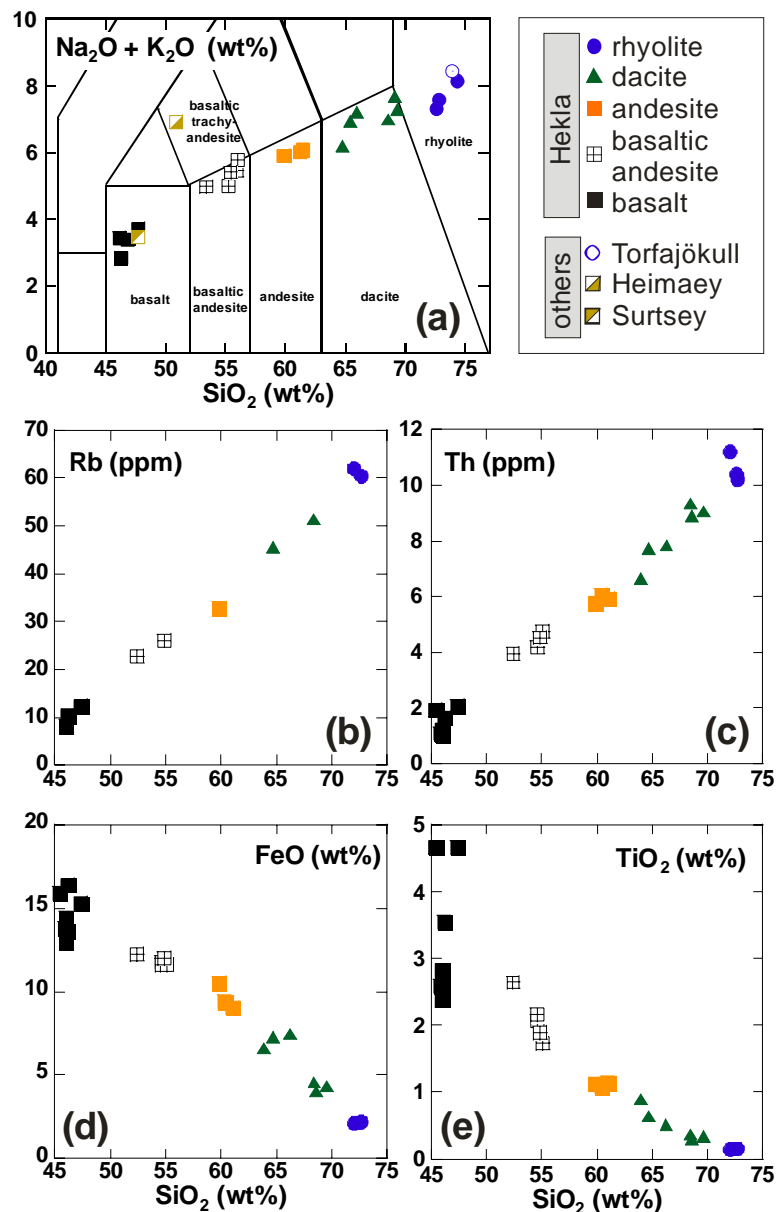


Figure 3.2. (a) Total alkali versus SiO<sub>2</sub> diagram (TAS) after Le Bas et al. (1986), illustrating the compositional range of samples analysed in this study. (b, c, d, e) Major and trace element variations for samples from the Hekla volcano as discussed in detail by Sigmarsson et al. (1992a).

The magmatic system of Hekla has been intensively studied, but particularly the combined Th, Sr and O isotope study by Sigmarsson et al (1992a) revealed detailed insights into its differentiation processes. A three-stage-model was developed for the Hekla magmatic system to explain the compositional variability of the eruption products (see Sigmarsson et al., 1992a, and discussion therein): (i) Partial melting of the mantle produces basaltic melts that probably interact with the lower Icelandic crust while ascending and then evolve by crystal fractionation to basaltic andesites. (ii) The rise of the hot basaltic melts induces partial melting of the Icelandic crust that leads to the formation of dacitic magmas. The latter then mix with the basaltic andesite melts to form andesitic magma. (iii) The dacitic magma itself evolves to rhyolitic composition through crystal fractionation. In combination, these processes lead to a stratified magma chamber and chemically zoned eruptions. Based on these differentiation mechanisms, we can study the behaviour of Fe and Li isotopes during different magmatic processes, such as crystal fractionation, magma mixing, partial crustal melting, and fluid exsolution.

A suite of samples representative for the volcanic evolution of Hekla and some samples from the surrounding area were selected for a detailed Fe and Li isotope study. Bulk rock sample powders analysed in this work have been used in earlier geochemical studies (Jakobsson, 1979; Sigmarsson et al., 1991; Sigmarsson et al., 1992a; Sigmarsson et al., 1992b; Sigmarsson, 1996; Moune et al., 2007; Sigmarsson et al., 2007). The investigated eruption products from the Hekla central volcano comprise a total of seventeen tephra and lava samples, ranging in composition from basaltic andesite to rhyolite (Table 3.1, Figure 3.2). Four basaltic rocks from the vicinity of Hekla were studied that most likely represent the parental magma of the basaltic andesites. We also included one xenolith sample erupted by Hekla belonging to the Torfajökull volcano, located about 20 km east from the Hekla

volcano. Two samples are from the Vestmannaeyjar (Westman islands), i.e., from Eldfell volcano at Heimaey and from the Surtsey volcano, respectively.

### 3.3. ANALYTICAL METHODS

#### 3.3.1. Sample preparation and purification

All reagents used during digestion and element separation were singly distilled, unless states otherwise. Between 50 and 200 mg of rock powder was dissolved in a 3:1 mixture of concentrated HF/HNO<sub>3</sub> in Savillex screw-top beakers on a hotplate at ~100°C. In addition, some samples were digested in HF/HNO<sub>3</sub> mixtures using microwave agitation (CEM Mars) at a temperature of 200°C and a pressure of ~11 bars. After HF/HNO<sub>3</sub> dissolution the samples were taken to dryness and subsequently taken up and dried again in concentrated HCl, aqua regia and HNO<sub>3</sub> until complete dissolution was achieved. The dried residues were finally taken up in 6M HCl for chromatographic separation of iron by anion exchange chromatography (DOWEX AG<sup>®</sup> 1X8 100-200 mesh), following the procedure described in Schoenberg and von Blanckenburg (2005). For each sample two separate dissolutions of rock powder were prepared. Each of the dissolutions was split into two aliquots from which iron was separately purified by anion exchange chromatography. This procedure resulted in four individually prepared iron separates for each sample, each of which was analysed at least twice by MC-ICP-MS yielding a minimum of eight analyses per rock sample. Total procedural Fe blanks were always below 30 ng, which is less than 0.01% of Fe processed from the samples and therefore considered negligible.

Sample preparation for Li isotope analysis was done following a procedure similar to the one described by Magna et al. (2004), but using a two column procedure. After

dissolution, aliquots equivalent to 15 - 20 mg of rock powder were used for subsequent separation of Li by cation exchange chromatography. For both column procedures DOWEX AG<sup>®</sup> 50W X8 (200-400 mesh) cation exchange resin was used. The first column (PP Spectrum<sup>®</sup>) had an inner diameter of 8 mm and a resin volume of 2.3 mL. Upon cleaning of the resin with 10 mL 2.5M HNO<sub>3</sub>, 2 mL 6M HCl and 8 mL 3M HCl, the resin was conditioned with 3 mL 0.67M HNO<sub>3</sub>/methanol(30%). In between each acid cleaning step the resin was rinsed with two column volumes of 18.2 MΩ H<sub>2</sub>O (Milli-Q<sup>®</sup> water). Then, samples were loaded onto the columns in 0.6 mL 0.67M HNO<sub>3</sub>/methanol(30%) and Li was subsequently eluted with 21 mL of 1M HNO<sub>3</sub>/methanol(80%). Reagents were prepared from concentrated HNO<sub>3</sub> diluted to the required acid concentrations with 18.2 MΩ H<sub>2</sub>O and methanol(100%), resulting in final methanol concentrations (v/v) of about 30% and 80%, respectively. Analytical grade methanol (Merck, p.a.) was found to be essentially Li-free and was used without further purification. The second set of columns was shaped to an inner diameter of 4 mm and a resin volume of 0.5 mL using shrink-fit Teflon. The resin was cleaned with 6 mL 2.5M HNO<sub>3</sub> and 3 mL 3M HCl and then conditioned with 1 mL 0.67M HNO<sub>3</sub>/methanol(30%). After drying down the Li fractions from the first column step, samples were loaded onto the second column in 0.5 mL 0.67M HNO<sub>3</sub>/methanol(30%) and Li was subsequently eluted with 8 mL of 1M HNO<sub>3</sub>/methanol(80%). After collection of the Li fractions from each column the sample matrix was eluted from the resin with > 10 times the column volume of 5M HNO<sub>3</sub>, H<sub>2</sub>O and 6M HCl and cleaned as described above for next usage. Since quantitative recovery of Li from the column chemistry is essential, the Li elution curves were determined using both mixtures of ICP standard solutions and dissolved rocks of basaltic and rhyolitic composition (see appendix A3, Fig. A3.1). To ensure quantitative recovery of Li, column cuts before and after the Li fractions were collected for each sample processed through the chemistry and



analysed for Li concentration. Only when the Li concentrations in these column cuts were below the normal blank levels, Li isotope measurements were done on the corresponding Li elutions. To test for any potential isotope fractionation induced by the Li separation procedure, four aliquots of the L-SVEC standard ( $\delta^7\text{Li} = 0\text{‰}$ ) were individually processed through the column chemistry and yielded an average  $\delta^7\text{Li}$  value of  $-0.04 \pm 0.28\text{‰}$  (2SD). Total procedure blanks were always below 130 pg Li, which is less than 0.1% of Li processed from the samples ( $>70$  ng Li) and is considered negligible.

### 3.3.2. Mass spectrometry

#### 3.3.2.1. Fe isotope analyses

All measurements were done in high mass resolution mode on a ThermoFinnigan Neptune multicollector inductively coupled plasma mass spectrometer (MC-ICP-MS) at the Leibniz University of Hannover. We followed the protocol of Schoenberg and von Blanckenburg (2005) using standard-sample-standard bracketing to correct for instrumental mass bias. Iron isotope data are reported in the  $\delta$ -notation, which gives the per mil deviation of the  $^{56}\text{Fe}/^{54}\text{Fe}$  or  $^{57}\text{Fe}/^{54}\text{Fe}$  ratio of the sample relative to that of the IRMM-014 standard, e.g.:

$$\delta^{56}\text{Fe}_{\text{sample}} = \left[ \left( \frac{^{56}\text{Fe}}{^{54}\text{Fe}}_{\text{sample}} \bigg/ \frac{^{56}\text{Fe}}{^{54}\text{Fe}}_{\text{IRMM-014}} \right) - 1 \right] \cdot 1000 \text{ [‰]}. \quad (3.1)$$

As mass dependent isotope fractionation decreases with increasing temperature, Fe isotope studies of magmatic processes are usually at the limit of the currently achievable analytical resolution. Comprehensive tests on sample processing and mass spectrometry revealed that our procedure allows precise and accurate Fe isotope determination. Identical results can be achieved on high purity Fe standard solutions and natural samples (of various

chemical compositions) given that the Fe separates are pure, which is routinely tested by ICP-OES measurements on the analyte solutions (Schoenberg and von Blanckenburg, 2005; Schoenberg and von Blanckenburg, 2006). Our results on the international reference materials BIR-1 ( $\delta^{56}\text{Fe} = 0.053 \pm 0.047\%$ , 2SD) and BHVO-1 ( $\delta^{56}\text{Fe} = 0.109 \pm 0.049\%$ , 2SD) are in good agreement with previously published results (see appendix A3.1, Table A3.1). During the course of this study, we tested the limits of precision and accuracy associated with our analytical approach that includes eight or more replicate measurements of each sample, precise concentration matching (within 5%) between samples and bracketing standard and high signal intensities for good counting statistics. We prepared mixtures of two well characterised pure Fe solutions of different isotopic compositions ( $n > 1000$ ) to obtain a set of six Fe solutions, whose  $\delta^{56}\text{Fe}$  values increase in steps of  $0.04\%$ . (Fig. 3.3).

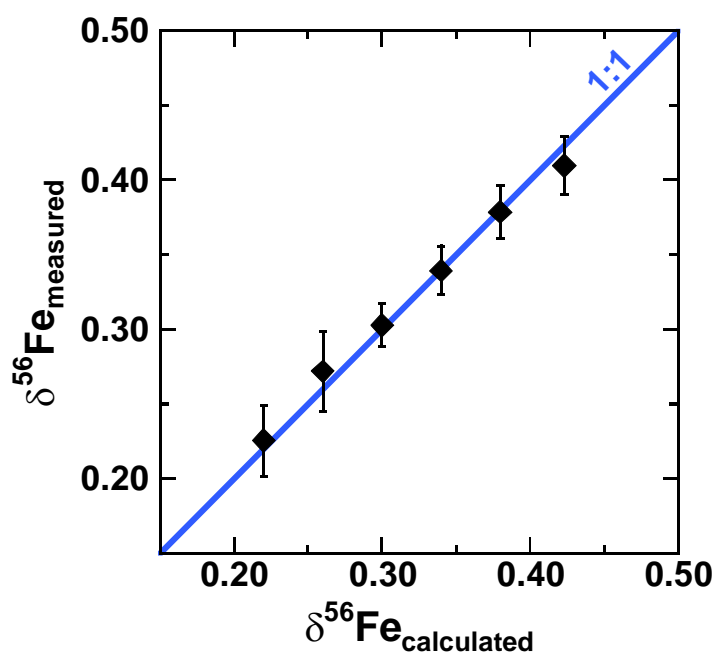


Figure 3.3. Results of measurements to test the limits of precision and accuracy associated with our analytical approach. Shown is the calculated versus measured Fe isotope composition. Each sample was made by precisely mixing two pure Fe isotope standard solutions. Each solution was analysed eight times. Deviations between calculated and measured  $\delta^{56}\text{Fe}$  are  $< 0.012\%$ .

Each solution was analysed eight times distributed over different analytical sessions. The small differences in Fe isotope composition were accurately resolved, with deviations between calculated and measured  $\delta^{56}\text{Fe} < 0.012\text{‰}$  (Fig. 3.3), demonstrating that with our approach the accuracy and precision can be drastically improved compared to single or duplicate analyses (i.e.,  $\pm 0.046\text{‰}$ , 2SD, on  $\delta^{56}\text{Fe}$  for a single measurement; Schoenberg and von Blanckenburg, 2005).

The long-term external reproducibility on  $\delta^{56}\text{Fe}$  and  $\delta^{57}\text{Fe}$  obtained from such pooled data with  $n \geq 8$  is  $\pm 0.021\text{‰}$  and  $\pm 0.031\text{‰}$  (2SD), respectively (Schoenberg and von Blanckenburg, 2006), comparable to the precision obtained by other groups on the ThermoFinnigan Neptune using a similar approach (e.g., Poitrasson and Freydier, 2005; Weyer et al., 2005). For samples analysed in this study, uncertainties for Fe isotope data is given as two standard deviations (2SD), representing the reproducibility of the replicate measurements and as 95% confidence intervals ( $2\text{SE} = t \cdot \frac{\sigma}{\sqrt{n}}$ , with  $t = \textit{students-t}$  correction factor, Table 3.2), the latter reflecting the accuracy and precision of the average of  $n \geq 8$  analyses that compare well with the long-term external reproducibility for pooled data of  $\pm 0.021\text{‰}$  on  $\delta^{56}\text{Fe}$ . () describes the 95% confidence level for the mean value of the population, with  $n=13$  and

### 3.3.2.2. Li isotope analyses

Lithium isotope measurements were done in low mass resolution mode ( $m/\Delta m \sim 2000$ , using 5 and 95% peak intensity limits) on the ThermoFinnigan Neptune in Hannover. We used a tandem quartz glass spray chamber (Finnigan SIS) combined with a self-aspirating Teflon microflow nebuliser ( $\sim 50 \mu\text{L}/\text{min}$ ) and high-sensitivity X-cones. Samples were dissolved in 0.3M  $\text{HNO}_3$  for mass spectrometric measurements and Li concentrations

between samples and the bracketing standard were closely matched and typically had concentrations of 100 ppb Li. However, no significant bias is caused due to even large deviations between the concentrations of samples and bracketing standards (see appendix A3.1, Fig. A3.2). Both,  $^6\text{Li}$  and  $^7\text{Li}$  were measured simultaneously on the two outermost Faraday cups. Each measurement consisted of 20 cycles with 4 seconds integration time, bracketed by the L-SVEC standard and blank measurements (for blanks 10 cycles of 4 seconds were measured). Li isotope data are reported in the  $\delta$ -notation, relative to the L-SVEC standard (Flesch et al., 1973):

$$\delta^7\text{Li}_{\text{sample}} = \left[ \left( \frac{^7\text{Li}}{^6\text{Li}}_{\text{sample}} \bigg/ \frac{^7\text{Li}}{^6\text{Li}}_{\text{L-SVEC}} \right) - 1 \right] \cdot 1000 \text{ [‰]} \quad (3.2)$$

Between each analysis the sample inlet system was rinsed with 0.3M  $\text{HNO}_3$  for 80 seconds. Differences between blank-corrected and uncorrected  $\delta^7\text{Li}$  values were always  $<0.05\%$ . The in-run precision was generally better than  $\pm 0.1\%$  (2SE).

Rosner et al. (2007) found that a sample introduction system similar to ours is less prone to matrix effects than desolvating systems that are used by other groups (e.g., Tomascak et al., 1999a; Magna et al., 2004; Jeffcoate et al., 2004). To test for potential matrix effects, L-SVEC solutions doped with different matrix elements having  $\Sigma\text{Element(s)}/\text{Li}$  ratios up to 25 were analysed. No systematic bias was found in this range of matrix impurities and all measurements gave  $\delta^7\text{Li}$  identical to pure L-SVEC within  $\pm 0.4\%$  (see appendix A3.1, Fig. A3.2). All sample solutions were analysed for Na, Mg, Al, Ca and Fe concentrations by MC-ICP-MS prior to Li isotope measurements to check for potential impurities. For the data reported here, separation of Li from matrix elements was found to be effective and the weight ratio of the sum of all matrix elements to Li ( $\Sigma\text{Elements}/\text{Li}$ ) was always below 1 for basalts to andesites and below 0.2 for dacites and rhyolites. This difference in the  $\Sigma\text{Elements}/\text{Li}$  ratio between basalt/andesite and dacite/rhyolite is solely due

to the differences in Li concentrations of the rocks, which is lower in mafic than in silicic samples. To evaluate the accuracy and precision of a new isotope measurement procedure, a large number of standards measurements over an extended time period is usually needed. In contrast to Fe isotope measurements, where a large dataset acquired over a time period of more than four years is available, no such long-term dataset exists for our Li isotope analytical protocol, yet. Therefore, we estimate our external reproducibility on  $\delta^7\text{Li}$  to  $\pm 0.5\text{‰}$  (2SD), based on multiple measurements of the natural samples over the course of this study (Table 3), comprising replicate sample dissolutions and passes through column chemistry, respectively. A somewhat inferior reproducibility in  $\delta^7\text{Li}$  is observed for some mafic rocks compared to that of silicic ones, although test of various  $^7\text{Li}_{\text{sample}}/^7\text{Li}_{\text{L-SVEC}}$  intensity ratios and  $\Sigma\text{Elements}/\text{Li}$  ratios did not reveal an influence on the accuracy of Li isotope measurements (see appendix A3.1). Accuracy of the measurements was evaluated by analyses of the two international basalt reference materials BHVO-1 ( $\delta^7\text{Li} = 5.60 \pm 0.55\text{‰}$ ,  $n=5$ ) and BIR-1 ( $\delta^7\text{Li} = 3.39 \pm 0.77\text{‰}$ ,  $n=9$ ). Our results for these standard materials are identical within uncertainty to previously published results (see appendix A3.1: Table A3.2 and Fig. A3.4). To our best knowledge, we publish the first data for RGM-1 ( $\delta^7\text{Li} = 2.59 \pm 0.15\text{‰}$ ,  $n=6$ ).

Lithium concentrations of the samples were measured on the ThermoFinnigan Neptune in free sample aspiration mode using an analogue detector and linear calibration of the  $^7\text{Li}$  intensities of a set of 5 standards of known Li concentrations. Based on replicate measurements, the uncertainty in the reported Li concentrations is estimated to be  $\pm 10\%$  (2SD).

Table 3.1. Major (wt%) and trace element (ppm) concentrations in the volcanic whole rock samples used in this study.

sample	SiO <sub>2</sub>	TiO <sub>2</sub>	Al <sub>2</sub> O <sub>3</sub>	FeO <sub>total</sub>	MnO	MgO	CaO	Na <sub>2</sub> O	K <sub>2</sub> O	H <sub>2</sub> O	Total	Th	Ba	Rb	Sr	Co	Ni	Sc	Nb	Zr	Yb	Ref.
<b>Hekla volcano</b>																						
H5-A	72.7	0.15	12.8	2.20	0.08	0.13	1.68	4.77	2.56	3.08	100.2	10.2	598	60.5	123	9	7	7	72.5	276	86.3	(1)
H4-5	72.0	0.14	12.6	2.12	0.09	0.07	1.44	4.79	2.71	2.94	98.9	11.2	638	62	107	5	5	4	84.5	329	96.8	(1)
H4-7	72.6	0.15	13.3	2.19	0.09	0.09	1.29	5.00	2.96		97.6	10.4										(2,1)
H4-3	66.3	0.52	14.8	7.43	0.25	0.37	3.53	5.16	2.08		100.4	7.85								1160		(2,1)
H2	68.6	0.29	14.0	3.98	0.12	0.30	2.49	5.03	2.18	1.90	98.9	8.9	540	188	19		9					(1)
H3-Haf	69.6	0.33	14.9	4.31	0.14	0.28	4.87	4.78	2.33		101.6	9.08										(2,1)
H1104-A	68.4	0.36	14.1	4.56	0.14	0.28	2.63	5.27	2.33	0.88	99.0	9.34	552	51.3	211	16	5	10	73.1	696	85	(1)
HZ-A	63.9	0.89	15.0	6.60	0.16	1.43	4.52	4.50	1.61		98.6	6.64										(3,4)
Hek-8	64.7	0.64	14.6	7.26	0.21	0.76	3.78	4.99	1.87	0.11	98.9	7.75	491	45.5	277	11	3	14	73.7	710	83	(1)
H4-T	59.8	1.13	15.3	10.50	0.27	1.65	5.21	4.37	1.54	0.11	99.9	5.78	387	32.7	325	12	4	19	63.7	718	78	(1)
H1300-M	60.3	1.08	14.8	9.37	0.25	1.58	5.12	4.47	1.47	0.00	98.4	6.06	417		324	21		19				(1)
H1947-A	61.0	1.14	14.9	9.06	0.24	1.65	5.11	4.55	1.48	0.11	99.2	5.94	419		340	25		19				(1)
HZ-B	54.6	2.07	15.1	11.79	0.28	3.20	6.82	3.73	1.22		98.8	4.21										(3,4)
HK2000T	54.6	2.16	14.4	11.61	0.37	2.50	6.61	4.10	1.23		97.6	4.52										(5)
H1300-L	55.1	1.72	14.9	11.60	0.29	2.68	6.40	4.32	1.36	0.08	98.5	4.77	347		374	20		21				(1)
H1846-L	54.8	1.89	14.8	12.00	0.29	2.90	6.73	4.08	1.27	0.16	98.9	4.55	341	26	380	23	4	22	67.2	508	81.2	(1)
Hek-11	52.4	2.64	14.2	12.20	0.27	3.54	7.42	3.86	1.03	0.60	98.2	3.98	22.7				4		58.1	458	78.8	(1,8)
<b>Vicinity of Hekla</b>																						
Hek-16T	45.4	4.66	13.3	15.90	0.29	4.48	9.56	2.68	0.62	0.00	96.9	1.92										(5,1)
Hek-28	46.2	3.54	14.1	16.40	0.26	6.18	9.92	2.90	0.56	0.12	100.2	1.66	150	10.4	335	54	58	32	21.2	225	38.3	(1)
Hek-18	47.3	4.66	13.2	15.30	0.25	5.17	9.23	3.03	0.67	0.35	99.2	2.07	12.3				14		42.8	272	46.8	(8,1)
Hek-4	46.0	2.37	16.0	13.00	0.20	7.73	11.20	2.42	0.40	0.14	99.5	1.08	109	8.2	372	51	114	33	19.9	141	24.7	(1)
<b>other volcanoes</b>																						
<i>Torfbjökull</i>																						
H1970-8	73.1	0.48	10.2	5.15	0.16	0.36	1.14	3.58	4.77		98.9	12.8										(2,1)
<i>Heimaey (Eldfell); Vestmannaeyjar (Westman Islands)</i>																						
4694	50.2	2.42	16.4	12.27	0.26	3.32	6.94	5.34	1.50		98.6	3.21	338	32.6	338							(3,6,9)
<i>Surtsey; Vestmannaeyjar (Westman Islands)</i>																						
8758H	47.1	1.92	15.0	11.33	0.16	9.26	10.50	3.02	0.41		98.7	0.96	114	10.1	265							(7,6,9)

References for major and trace element analyses, respectively:

- (1) Sigmarsson et al. (1992a)  
(2) ICP-OES analyses obtained at Hannover (this study)  
(3) ICP-OES or TIMS analyses obtained at Clermont-Ferrand (this study)  
(4) Sigmarsson et al. (1991)  
(5) Moune et al. (2007)  
(6) Sigmarsson et al. (1992b)  
(7) Sigmarsson, Jakobsson and Thordarson (2007)  
(8) Jakobsson (1979)  
(9) Sigmarsson (1996)

## 3.4. RESULTS

### 3.4.1. Iron isotope compositions

Iron isotope results are reported together with eruption dates (Thorarinsson, 1967; Jakobsson, 1979; Thorarinsson, 1971; Dugmore et al., 1991; Larsen et al., 2001) and rock types in Table 3.2. The  $\delta^{56}\text{Fe}$  values of rocks from the Hekla volcanic system, ranging in composition from basalt to rhyolite, vary from 0.021 to 0.168‰ (with an uncertainty of  $\pm 0.021$ ‰, 2SD). The xenolith sample (H1970-8) from Torfajökull represents the most evolved rhyolite analysed in this study and has the highest  $\delta^{56}\text{Fe}$  value of 0.187‰. The two samples from the Vestmannaeyjar have distinct Fe isotope compositions. The Fe isotope composition of the basalt from Surtsey is indistinguishable to that of the Holocene Hekla basalts, whereas the more evolved mugearite ( $\text{Na}_2\text{O}$ -rich basaltic trachyandesite) from Heimaey is remarkably heavier ( $\delta^{56}\text{Fe} = 0.177$ ‰).

The Fe isotope results of the Hekla volcanic rocks are described following the three-stage-model for magma evolution proposed by Sigmarsson et al., (1992a): (i) No systematic variation in  $\delta^{56}\text{Fe}$  was found during the evolution from basalt to basaltic andesite through closed-system crystal fractionation (Fig. 3.4 and 3.5).

The  $\delta^{56}\text{Fe}$  values of these basalts are in the range of previously reported Fe isotope compositions for terrestrial basalts (Beard et al., 2003a; Poitrasson et al., 2004; Weyer et al., 2005; Schoenberg and von Blanckenburg, 2006). They are also indistinguishable in  $\delta^{56}\text{Fe}$  from the basaltic andesites, andesites and the less evolved dacites with  $\text{SiO}_2 < 66$  wt% of Hekla (Fig. 3.4a). The average  $\delta^{56}\text{Fe}$  value of all basalts and basaltic andesites from Hekla is  $0.062 \pm 0.042$ ‰ (2SD,  $n=9$ ). (ii) In the silicic series of Hekla the  $\delta^{56}\text{Fe}$  values continuously

increase with ongoing magma differentiation from  $0.021 \pm 0.021\%$  for the dacite sample H4-3 ( $\text{SiO}_2 = 66.3 \text{ wt}\%$ ) to  $0.168 \pm 0.021\%$  for the rhyolite H4-5 ( $\text{SiO}_2 = 72.0 \text{ wt}\%$ ). Analogous correlations exist between  $\delta^{56}\text{Fe}$  and other major and trace element indicators of magma differentiation, such as FeO (Fig. 3.4b), CaO, MgO,  $\text{K}_2\text{O}$ , Th (Fig. 3.5), Rb (compare Tables 3.1 and 3.2). (iii) The Fe isotope compositions of the andesites are in agreement with a mixing process between the basaltic andesites and the less evolved dacites (Fig. 3.5).

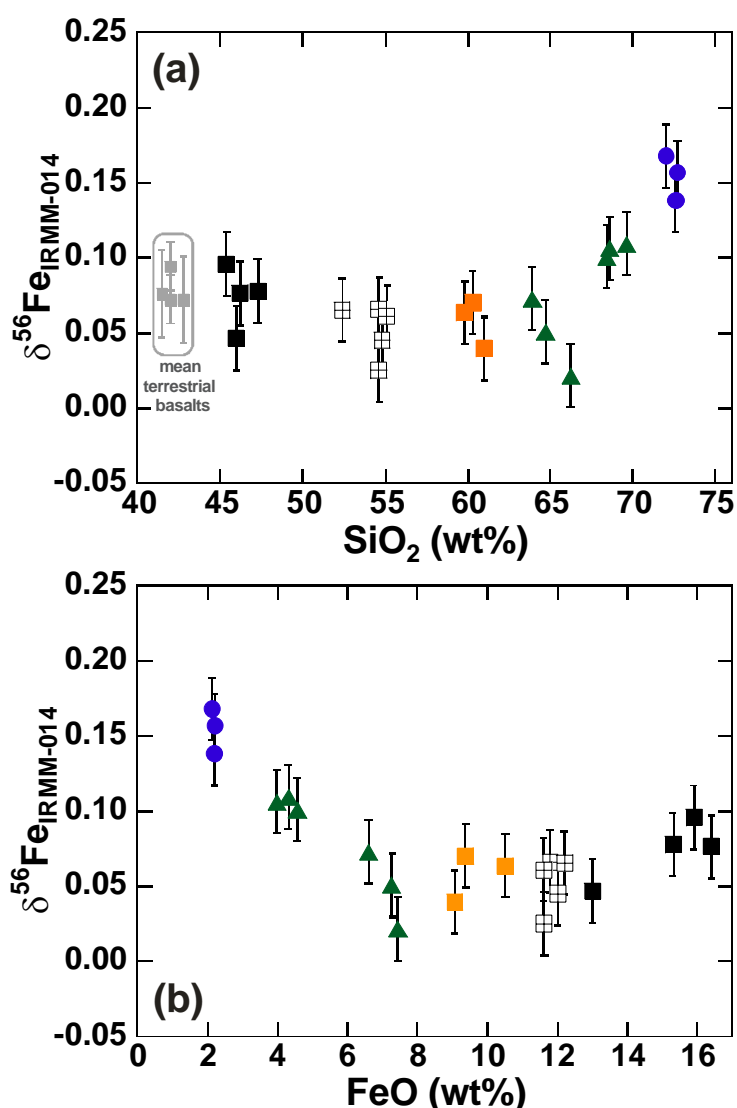


Figure 3.4. Iron isotope composition of Hekla volcanic rocks as a function of (a)  $\text{SiO}_2$  and (b) FeO (total iron content). Error bars represent  $\pm 0.021\%$  (2SD external reproducibility).  $\delta^{56}\text{Fe}$  values of mean terrestrial basalts as defined by other studies are shown for comparison (Beard et al., 2003a; Poitrasson et al., 2004; Weyer et al., 2005; Schoenberg and von Blanckenburg, 2006). Symbols as in Figure 3.2.



Table 3.2. Iron isotope compositions of volcanic rocks from Hekla and other Icelandic volcanoes.

sample	eruption date <sup>a</sup>	rock type	n <sup>b</sup>	$\delta^{56}\text{Fe}$	2SD <sup>c</sup>	2SE <sup>c</sup>	$\delta^{57}\text{Fe}$	2SD <sup>c</sup>	2SE <sup>c</sup>
<b><i>Hekla volcano</i></b>									
H5-A	7100 B.P.	Rhyolitic tephra	13	0.157	0.052	0.014	0.229	0.099	0.027
H4-5	4200 B.P.	Rhyolitic tephra	9	0.168	0.031	0.010	0.259	0.078	0.025
H4-7	4200 B.P.	Rhyolitic tephra	8	0.138	0.031	0.011	0.213	0.088	0.031
H4-3	4200 B.P.	Dacitic tephra	8	0.021	0.037	0.013	0.034	0.059	0.021
H2	3800 B.P.	Dacitic tephra	9	0.106	0.061	0.020	0.152	0.092	0.030
H3-Haf	3000 B.P.	Dacitic tephra	10	0.109	0.048	0.015	0.153	0.079	0.025
H1104-A	1104 A.D.	Dacitic tephra	8	0.101	0.067	0.023	0.155	0.083	0.029
HZ-A	<2800 B.P.	Dacitic tephra	8	0.073	0.035	0.012	0.090	0.070	0.024
Hek-8	1158 A.D.?	Dacitic lava	10	0.051	0.041	0.013	0.079	0.062	0.019
H4-T	4000 B.P.	Andesitic tephra	8	0.063	0.054	0.019	0.100	0.068	0.023
H1300-M	1300 A.D.	Andesitic tephra	8	0.070	0.048	0.017	0.088	0.070	0.024
H1947-A	1947 A.D.	Andesitic tephra	10	0.040	0.038	0.012	0.055	0.077	0.025
HZ-B	<2800 B.P.	Basaltic andesite tephra	9	0.066	0.051	0.017	0.096	0.096	0.031
HK2000T	2000 A.D.	Basaltic andesite tephra	9	0.025	0.057	0.019	0.038	0.079	0.026
H1300-L	1300 A.D.	Basaltic andesite lava	8	0.061	0.047	0.016	0.094	0.085	0.030
H1846-L	1846 A.D.	Basaltic andesite lava	10	0.045	0.056	0.017	0.065	0.103	0.032
Hek-11	<1500 B.P.	Basaltic andesite lava	8	0.065	0.024	0.008	0.097	0.041	0.014
<b><i>Vicinity of Hekla</i></b>									
Hek-16T	1913 A.D.	Basaltic tephra	10	0.096	0.045	0.014	0.145	0.089	0.028
Hek-28	6500 B.P.	Basaltic lava	8	0.076	0.038	0.013	0.104	0.055	0.019
Hek-18	1878 A.D.	Basaltic lava	9	0.078	0.072	0.024	0.112	0.096	0.031
Hek-4	Pleistocene	Basaltic lava	13	0.047	0.062	0.017	0.075	0.084	0.023
<b><i>other volcanoes</i></b>									
<b><i>Torfajökull</i></b>									
H1970-8	1970 A.D.	Rhyolitic xenolith erupted	9	0.187	0.049	0.016	0.277	0.070	0.023
<b><i>Heimaey (Eldfell); Vestmannaeyjar (Westman Islands)</i></b>									
4694	1973 A.D.	Mugearite	9	0.177	0.032	0.010	0.266	0.061	0.020
<b><i>Surtsey; Vestmannaeyjar (Westman Islands)</i></b>									
8758H	1965 A.D.	Basaltic lava	8	0.105	0.041	0.014	0.140	0.083	0.029

<sup>a</sup> Eruption dates from Thorarinsson (1967), Jakobsson (1979), Thorarinsson (1971), Dugmore et al. (1991), Larsen et al. (2001)

<sup>b</sup> Number of replicate measurements from two independent sample dissolutions and four chromatographic Fe separations.

<sup>c</sup> Uncertainties are given as two times the standard deviation (2SD) and 95% confidence intervals (2SE) of n replicate measurements, respectively. The 2SE uncertainties give a reliable estimate of the precision and accuracy, since for  $n \geq 8$  replicate measurements, the external long term reproducibility (2SD) of  $\delta^{56}\text{Fe}$  and  $\delta^{57}\text{Fe}$  is  $\pm 0.021\%$  and  $\pm 0.031\%$ ,

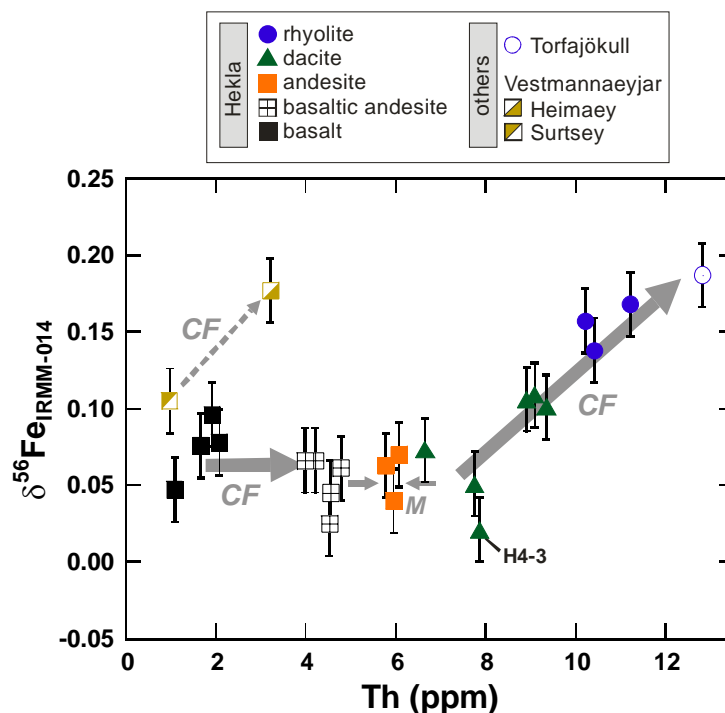


Figure 3.5. Iron isotope composition of volcanic rocks from Hekla and other Icelandic volcanoes as a function of Th concentration, used as differentiation index. Error bars represent  $\pm 0.021\text{‰}$  (2SD external reproducibility). Magmatic processes, i.e. crystal fractionation (CF) and magma mixing (M) are indicated by arrows. Sample H4-3 shows zircon accumulation, demonstrating crystallisation and subsequent crystal settling in the zoned magma chamber of Hekla (Sigmarsson et al. 1992a).

### 3.4.2. Lithium concentrations and isotope compositions

Lithium concentrations in the analysed bulk rock samples range from 2.9 to 42 ppm (Table 3.3) and systematically increase with increasing degree of magma differentiation as inferred from  $\text{SiO}_2$ ,  $\text{K}_2\text{O}$ , and Th contents (Fig. 3.6). The analysed samples have a limited range in Li isotope composition (Table 3.3, Fig. 3.6d, e), most of them identical within the limits of our analytical precision. The  $\delta^7\text{Li}$  of basalts, basaltic andesites and andesites range from 4.37 to 5.08‰ (average  $4.89 \pm 0.69\text{‰}$ , 2SD), excluding sample Hek-11, which has a slightly higher  $\delta^7\text{Li}$  of 6.22‰. This sample originates from a phreatomagmatic eruption (Jakobsson, 1979) and the elevated  $\delta^7\text{Li}$  is likely to reflect interaction with groundwater, which is enriched in heavy Li isotopes (Elliott et al., 2004). The  $\delta^7\text{Li}$  values of all Hekla dacites and rhyolites range from 3.83 to 4.60‰ (average  $4.27 \pm 0.57\text{‰}$ , 2SD).

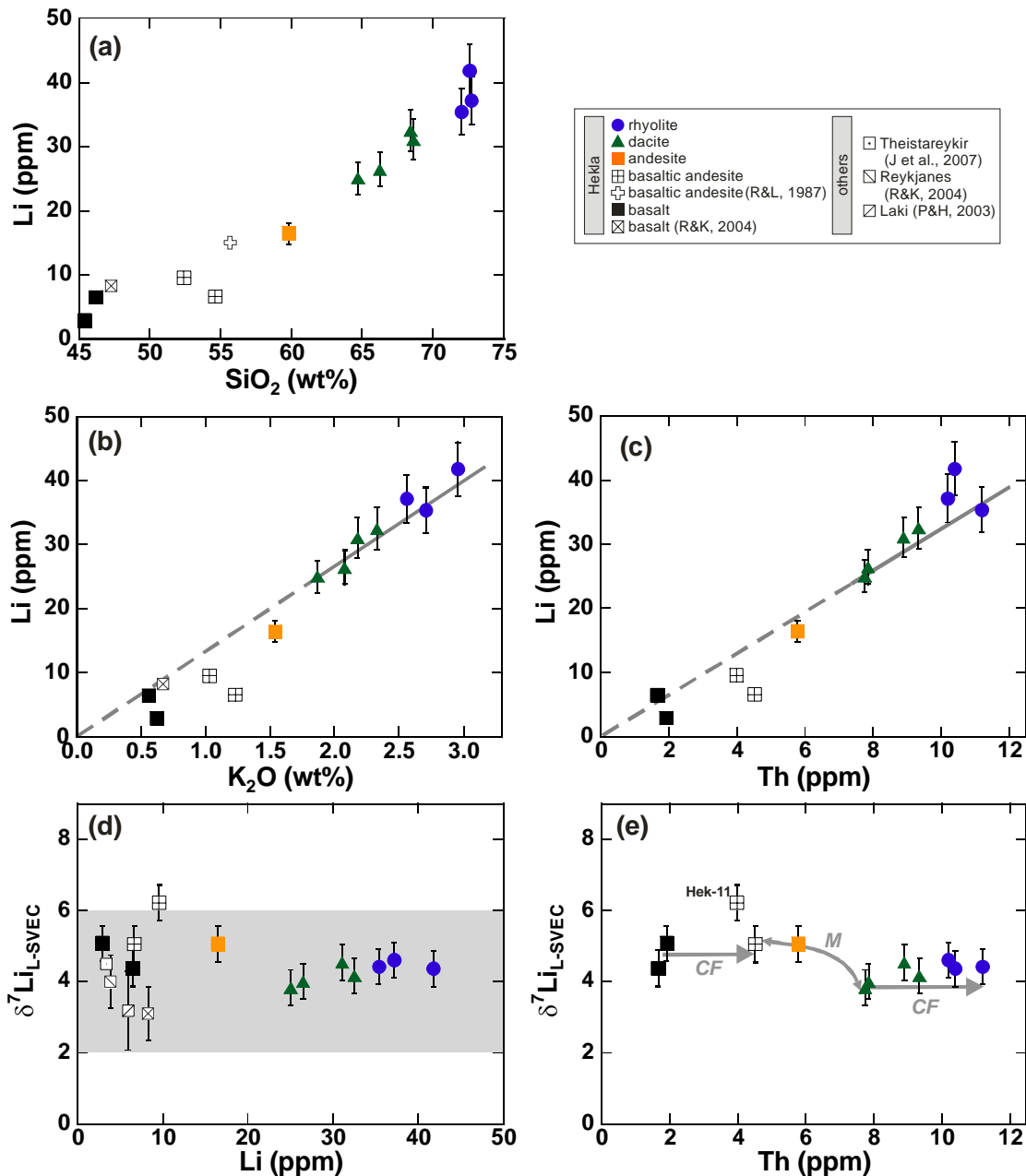


Figure 3.6. (a) Li concentrations in volcanic rocks from Hekla versus SiO<sub>2</sub> content. The results for a basalt and a basaltic andesite from the Hekla volcanic system reported by Ryan and Kyle (2004) and Ryan and Langmuir (1987), respectively, are also shown. (b, c) Li concentrations as a function of incompatible element contents, K<sub>2</sub>O and Th. Solid lines represent the expected evolution trends of the silicic series (dacites to rhyolites) produced by fractional crystallisation, assuming a similar (incompatible) behaviour for Li, Th, and K during crystal fractionation, hence, a straight line passing through the less evolved dacitic sample (Hek-8) was extrapolated to the origin (dashed line). (d) Li isotope compositions as a function of Li contents for volcanic rocks from Hekla (this study; Ryan and Langmuir, 1987; Ryan and Kyle, 2004) and for basalts from other Icelandic volcanoes (Jeffcoate et al., 2007; Pistiner and Henderson, 2003; Ryan and Kyle, 2004). The grey area represents the  $\delta^7\text{Li}$  value ( $4 \pm 2\%$ ) of the upper mantle as inferred from oceanic basalts and mantle xenoliths (Tomascak, 2004; Magna et al., 2006; Jeffcoate et al., 2007; Tomascak et al., 2007). Error bars for data from this study represent  $\pm 0.5\%$  (2SD, external reproducibility). (e) Li isotope compositions as a function of Th, used as differentiation index. Magmatic processes, i.e. crystal fractionation (CF) and magma mixing (M), are indicated by arrows. Sample Hek-11 is of phreatomagmatic origin.

Table 3.3. Li concentrations and isotope compositions for representative samples from the Hekla volcanic system.

sample	rock type	n <sup>a</sup>	d <sup>b</sup>	s <sup>c</sup>	$\delta^7\text{Li}$	2SD <sup>d</sup>	Li (ppm) <sup>e</sup>
<b><i>Hekla volcano</i></b>							
H5-A	Rhyolitic tephra	15	1	2	4.60	0.43	37.2
H4-5	Rhyolitic tephra	19	4	4	4.42	0.36	35.4
H4-7	Rhyolitic tephra	15	1	2	4.36	0.52	41.8
H4-3	Dacitic tephra	13	2	2	4.00	0.15	26.5
H2	Dacitic tephra	15	2	3	4.54	0.23	31.1
H1104-A	Dacitic tephra	14	1	2	4.16	0.31	32.5
Hek-8	Dacitic lava	16	1	2	3.83	0.47	25.0
H4-T	Andesitic tephra	4	2	2	5.06	0.70	16.5
HK2000T	Basaltic andesite tephra	3	1	1	5.05	0.27	6.6
Hek-11	Basaltic andesite lava	3	1	1	6.22	0.62	9.6
<b><i>Vicinity of Hekla</i></b>							
Hek-16T	Basaltic tephra	1	1	1	5.08	-	2.9
Hek-28	Basaltic lava	3	1	1	4.37	0.23	6.5

<sup>a</sup> Number of replicate Li isotope measurements. <sup>b</sup> Number of individual sample dissolutions.

<sup>c</sup> Number of chromatographic Li separations.

<sup>d</sup> Uncertainties are two times the standard deviation (2SD) of n replicate measurements. External reproducibility of  $\delta^7\text{Li}$  is  $\pm 0.50\%$  (2SD). <sup>e</sup> Uncertainties in Li concentrations are  $\pm 10\%$ .

### 3.5. DISCUSSION

#### 3.5.1. Behavior of Li and Li isotopes during fractional crystallisation

Lithium behaves as a moderately incompatible element during fractional crystallisation and the concentration of Li in the evolving melt is controlled by the partition coefficients between minerals and melt (e.g., Ryan and Langmuir, 1987). As illustrated in Figure 3.6 Li contents in the Hekla volcanic rocks are correlated with indicators for magma differentiation, demonstrating magmaphile behaviour of Li.

Absence of Li isotope fractionation during basalt differentiation at temperatures in excess of 1050°C was reported by Tomascak et al. (1999b). This agrees with our observations from the mafic Hekla series (Fig. 3.6e) that differentiated at similar temperatures (>1050°C, Baldrige et al., 1973), excluding the phreatomagmatic sample Hek-11. The compositional range of differentiated rocks covered in this study is extended from basalts up to rhyolites.

The temperatures during magma differentiation of the silicic series at Hekla of less than 950°C (Sigmarsson et al., 1992a) were lower than in the mafic magmas. Although this, in principal, would enlarge mineral-melt Li isotope fractionation factors, no resolvable isotopic difference was found between dacites and rhyolites (Fig. 3.6e). This is consistent with the absence of Li isotope fractionation during granite differentiation (Teng et al., 2006). Although not clearly resolvable within analytical uncertainties, the mafic series (average  $\delta^7\text{Li} = 4.89 \pm 0.69\%$ , 2SD) tends to be slightly heavier in Li isotopes than the silicic series (average  $\delta^7\text{Li} = 4.27 \pm 0.57\%$ , 2SD) (Fig. 3.6e). This could reflect a source effect, caused by minor compositional variability in  $\delta^7\text{Li}$  of the Icelandic crust, similar to observations made for oxygen isotopes (e.g., Hattori and Muehlenbachs, 1982). Moreover, the Li isotope compositions of all Hekla rocks analysed in this study are close to  $\delta^7\text{Li}$  values reported by other studies for Icelandic basalts (Pistiner and Henderson, 2003; Ryan and Kyle, 2004; Jeffcoate et al., 2007) and match the  $\delta^7\text{Li}$  inferred for the upper mantle ( $\delta^7\text{Li}$  of  $4 \pm 2\%$ , Tomascak, 2004; Magna et al., 2006; Jeffcoate et al., 2007; Tomascak et al., 2007) (Fig. 3.6d). These observations suggest that the Li isotope signature of a magma source is preserved during melt differentiation through crystal fractionation.

### **3.5.2. Behaviour of Li and Fe and their isotopes during fluid exsolution**

Given the fluid-mobile behaviour of Li and the absence of Li isotope fractionation during crystal fractionation, Li and its isotopes are potentially useful to trace magma/fluid interaction.

*3.5.2.1. Constraints from Li and Fe concentrations*

The influence of fluids that could potentially fractionate Fe isotopes in a magmatic system has to be considered for the observed systematic increase in  $\delta^{56}\text{Fe}$  values with ongoing magma differentiation (Fig. 3.5). Although, no hydrothermal system is associated with the volcanic activity at Hekla, the role of deuteric fluids exsolving from the magma itself will be discussed. Poitrasson and Freydier (2005) suggested that isotopically light Fe preferentially partitions in such a late-stage deuteric aqueous fluid exsolved from a highly evolved silicate melt. However, it remains to be tested experimentally whether this process indeed fractionates Fe isotopes. Nevertheless, the presence of such a fluid in the evolved series of Hekla should be traceable by a fluid mobile element, such as Li. During exsolution of a chlorite-bearing fluid Li strongly partitions into the fluid ( $D_{\text{fluid/melt}}^{\text{Li}}$  up to 2.5, Webster et al., 1989), resulting in a decrease in the coexisting silicate melt's Li concentration. The Li concentrations measured in Hekla's rocks increase with increasing degree of magma evolution (Fig. 3.6), demonstrating incompatible element behaviour during fractional crystallisation. Correlations between two incompatible elements (refractory vs. volatile) can be used to estimate the expected concentration of the volatile element in the magma prior to degassing (Moune et al., 2007). Here, we apply this approach to Li concentrations in the silicic series of Hekla (Fig. 3.6b, c). If both Li and Th (or Li and K) behave as incompatible elements then the fractional crystallisation vector in Li vs. Th (or Li vs.  $\text{K}_2\text{O}$ ) space has to pass through the origin. When a straight line is extrapolated from the primitive dacite sample Hek-8 to the origin, it appears as if the rhyolites tend to be slightly over-enriched in Li relative to the expected fractional crystallisation trend (solid line in Fig. 3.6b, c). This observation could be explained by fluid accumulation in the magma chamber during fractional crystallisation of the highly evolved Hekla series. In such a case, degassing would eventually cause a drop in fluid-mobile element contents in the residual magma of the

eruption products. Such a fluid accumulation most likely caused the highly explosive Plinian eruptions at Hekla. However, considering the size of the error bars in Figure 3.6, the trend towards slight enrichment in lithium for the rhyolites can not be unambiguously attributed to fluid accumulation. Moreover, it has to be noted that the approach taken to estimate the fractional crystallisation vector (Fig. 3.6b, c) is based on the assumption that partition coefficients are constant over the entire range of magma evolution from dacite to rhyolite, which is not necessarily true. Hence, more data on volatile element concentrations in melt inclusions (e.g., Cl, F, S), describing the evolution of the silicic series at Hekla, is needed to better constrain the role of exsolving fluids. Nevertheless, the discussed trends indicate, that exsolution and/or degassing of large amounts of fluid during crystal fractionation of the Hekla dacites to rhyolites is unlikely, since extensive partitioning of Li into a fluid would cause more pronounced deviations from the expected evolution trends (Fig. 3.6b, c). Thus, fluid exsolution alone must be considered an unlikely explanation for the observed Fe isotope fractionation in the evolved rocks. This conclusion arises from the fact that  $D_{\text{fluid/melt}}^{\text{Fe}}$  is much smaller than  $D_{\text{fluid/melt}}^{\text{Li}}$  and a large fraction of Fe would have to be extracted from the magma (which contains > 2wt% FeO) into the fluid to cause a resolvable shift in  $\delta^{56}\text{Fe}$  of the residual melt. Moreover, the fluid/melt ratio is probably very low, since the amount of exsolved fluid is limited by the initial volatile contents of the silicate melt (< 3 wt%, compare H<sub>2</sub>O in Table 3.1).

#### *3.5.2.2. Constraints from Li isotopes on the significance of fluids during magma differentiation*

Li isotope systematics may reveal further information about the significance of fluids during the differentiation of the Hekla volcanic series. There exist several experimental studies that determined equilibrium Li isotope fractionation between silicate minerals and

aqueous fluids at high temperatures. Thereby,  $\Delta^7\text{Li}_{\text{fluid-spodumene}}$  is about +2‰ at 2 GPa and 900°C (Wunder et al., 2006), while  $\Delta^7\text{Li}_{\text{fluid-stauroilite}}$  is about -1.5‰ at 3.5 GPa and 900°C (Wunder et al., 2007). A fluid inclusion study of Teng et al. (2006) suggested a +4‰ Li isotope fractionation during fluid exsolution from a pegmatite melt at >600°C. In addition to these results, experiments in a fluid-melt system were performed during this study, using H<sub>2</sub>O and rhyolite (USGS RGM-1, similar in composition to the evolved Hekla rocks) as starting materials. At 850°C, 200 MPa, and an experimental runtime of 72 hours it was found that preferentially light Li entered the fluid yielding a  $\Delta^7\text{Li}_{\text{fluid-melt}} = -1.6 \pm 0.7\text{‰}$ . Therefore, at temperatures relevant for the silicic Hekla magmas (<950°C), the presence of a fluid that continuously removed large fractions of Li from the magma should lead to heavy Li isotope signatures for the evolved eruption products. Assuming a  $\Delta^7\text{Li}_{\text{fluid-melt}}$  of -1.6‰, a Rayleigh distillation model for fluid exsolution predicts the residual magma to be 1.1‰ and 2.5‰ heavier in  $\delta^7\text{Li}$  than its source, after removal of 50% and 80% of Li, respectively. However, for such high fractions of Li removal (>50%) an external fluid source would be needed, since the amount of fluid that can exsolve from the magma itself is limited by the initial volatile content in the melt (about 3 wt%, compare H<sub>2</sub>O in Table 3.1). After exsolution of about 3 wt% H<sub>2</sub>O and transfer of about 10% Li from the magma into the fluid ( $D^{\text{Li}}_{\text{fluid/melt}} = 2.5$ ; Webster et al., 1989), the  $\delta^7\text{Li}$  of the residual magma is expected to change by about +0.2‰ only, which is not resolvable within analytical precision. Although the dacites and rhyolites with Th contents > 8 ppm (Fig. 3.6e) tend to be slightly heavier in  $\delta^7\text{Li}$  than their less evolved parental magmas (Hek-8, H4-3), they can not be distinguished at our analytical resolution and certainly show no isotope fractionation as large as those expected from extensive magma/fluid interaction (with Li transfer > 50%, see above). Hence, the virtually constant  $\delta^7\text{Li}$  of the dacites and rhyolites from Hekla (Fig. 3.6e) corroborate the conclusions



drawn from Li concentrations that fluid exsolution only played a subordinate role in the Hekla volcanic system.

### 3.5.3. Fe isotope fractionation through crystal fractionation

One mechanism to modify the Fe isotope composition of a melt is removal of isotopically lighter or heavier iron through crystallisation of minerals. Unfortunately, Fe isotope fractionation factors between silicate minerals and silicate melts are unknown to date, but preliminary results on magnetite-melt fractionation exist (Huang and Lundstrom, 2006; this study: appendix A3.3). Therefore, it is difficult to clearly assign the observed trend in the silicic series of Hekla (Fig. 3.5) to the removal of isotopically light Fe by crystallisation of a specific mineral. However, the integrated Fe isotope fractionation factor between the silicate melt and all liquidus phases (plagioclase, olivine, pyroxene and titanomagnetite) can be estimated by Rayleigh fractionation modelling using different mineral-melt fractionation factors  $1000 \cdot \ln \alpha^{56/54} \text{Fe}_{\text{mineral/melt}} \approx \Delta^{56}\text{Fe}_{\text{mineral-melt}} = \delta^{56}\text{Fe}_{\text{mineral}} - \delta^{56}\text{Fe}_{\text{melt}}$  (Figure 3.7). These calculations demonstrate that the rhyolites can be produced by fractional crystallisation of a dacitic melt with a bulk mineral-melt fractionation factor  $\Delta^{56}\text{Fe}_{\text{mineral-melt}}$  of about -0.1‰. In this model sample Hek-8 was taken as representative for the less evolved dacites (Th < 8 ppm), i.e. the source of the silicic series. As mentioned above, dacitic melts are produced by dehydration melting of meta-basalts in the local crust under amphibolite facies conditions (Sigmarsson et al., 1992a). Weyer and Ionov (2007) proposed that partial melting of mantle rocks induces Fe isotope fractionation, resulting in a heavier  $\delta^{56}\text{Fe}$  of basalts (+0.1‰) relative to residual mantle rocks. However, at Hekla, the primitive dacites are identical in  $\delta^{56}\text{Fe}$  to terrestrial basalts in general and also to the basalts erupted in the vicinity of Hekla (Fig. 3.4a). Although the Fe isotope composition of the meta-basaltic Icelandic crust is not known, it is most likely well represented by that of Hekla

basalts. Thus our results suggest that no Fe isotope fractionation occurs during partial melting beneath the Hekla volcanic system – at least at the prevailing degree of melting that produces the most primitive dacites (~10%, Sigmarsson et al., 1992a). If fractional crystallisation is responsible for the heavy Fe isotope composition of the Hekla rhyolites, then the accumulated crystals must contain the corresponding light Fe. Indeed, crystal settling in the zoned magma chambers at Hekla is demonstrated by the H4 eruption, where zircon accumulation took place as recorded in sample H4-3 (Sigmarsson et al., 1992a). In accord with this observation, sample H4-3 ( $\delta^{56}\text{Fe} = 0.021\text{‰}$ ) tends to be lighter than dacites that have a similar (Hek-8) or even less evolved (HZ-A) character, as inferred from  $\text{SiO}_2$  or Th contents (Fig. 3.5).

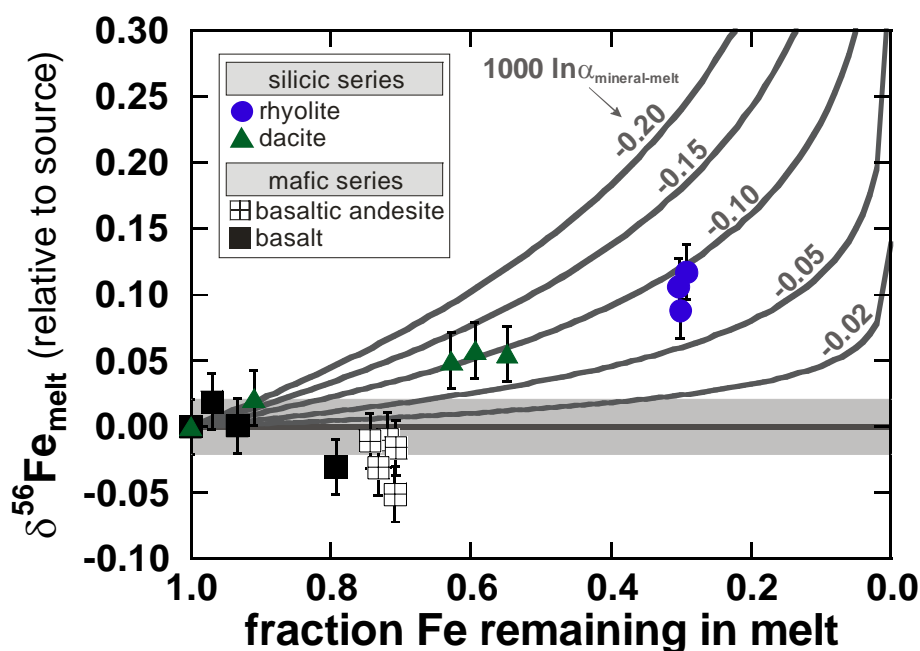


Figure 3.7. Comparison of Fe isotope composition of samples from the silicic and mafic series of the Hekla volcano with a Rayleigh fractionation model ( $\delta^{56}\text{Fe}_{\text{melt}} = \delta^{56}\text{Fe}_{\text{source}} + 1000f^{(\alpha-1)}$ ), using different bulk isotope fractionation factors ( $1000 \cdot \ln \alpha_{\text{mineral-melt}}$ ) between all crystallising minerals and the silicate melt. During magma differentiation, the FeO content of the melt decreases (see Fig. 3.2d), due to crystallisation of Fe bearing minerals and subsequent crystal settling. The Fe isotope composition is modelled relative to the source composition as a function of the fraction of iron remaining in the evolving melt ( $f$ ). For the silicic series that evolve by crystal fractionation from dacite to rhyolite, sample Hek-8 (formed by partial melting of Icelandic crust) is taken as representative for the source ( $\delta^{56}\text{Fe}_{\text{source}}$ ). Sample Hek-28 is representative for the less differentiated Holocene basalts and is used as  $\delta^{56}\text{Fe}_{\text{source}}$  for the mafic series model calculations. The grey area represents the analytical uncertainty ( $\delta^{56}\text{Fe} = 0 \pm 0.021\text{‰}$ , 2SD external long-term reproducibility).

Since extensive titanomagnetite crystallisation is recorded (Fig. 3.2d, e), partitioning of light Fe isotopes into titanomagnetite and subsequent crystal settling is a possible mechanism driving the evolving melt towards heavier  $\delta^{56}\text{Fe}$ . Experimental results from Fe isotope partitioning at 800°C between magnetite and andesitic melt at 0.5 GPa (Huang and Lundstrom, 2006) or rhyolitic melt at 0.1 and 0.2 GPa (this study, appendix A3.3) indicate that magnetite is isotopically lighter than the coexisting melt ( $\Delta^{56}\text{Fe}_{\text{magnetite-melt}} = -0.2$  to  $-0.26\%$ ). No experimental results for titanomagnetite-melt fractionation are available. Unfortunately, there is also only an iron  $\beta$ -factor (reduced isotope partition function ratio) – derived from Mössbauer spectroscopy data – available for magnetite (Polyakov et al., 2007), but not for titanomagnetite. However, a crystal chemical control on the  $\beta$ -factor due to Ti incorporation into the magnetite crystal structure is not unrealistic, as such an effect is observed for the iron oxide minerals hematite ( $\text{Fe}_2\text{O}_3$ ) and ilmenite ( $\text{FeTiO}_3$ ) (Polyakov and Mineev, 2000; Polyakov et al., 2007). As a consequence of  $\text{Ti}^{4+}$ -incorporation, titanomagnetite has a much higher ferrous iron content compared to pure magnetite. At a given temperature, following sequence of  $\beta$ -factor is observed:  $\beta(\text{Fe}_2\text{O}_3) > \beta((\text{Mg,Fe})_2\text{SiO}_4) > \beta(\text{FeTiO}_3)$ . This means that at equilibrium hematite is isotopically heavier than coexisting olivine, whereas ilmenite is lighter. Thus, ferrous iron rich titanomagnetite is expected to incorporate isotopically lighter Fe relative to a highly evolved silicic silicate melt which are known to be enriched in ferric iron (compare Fig. II.II). Hence, crystal fractionation of titanomagnetite could potentially explain the heavy Fe isotope enrichment in the evolving melts at Hekla.

In contrast to the silicic series, the mafic series does not reveal resolvable changes in Fe isotope composition during crystal fractionation (Fig. 3.5). There are different mechanisms that may explain this discrepancy:

- 1) Following the discussion above, a lower proportion of titanomagnetite crystallisation in the mafic magmas compared to the silicic magma could explain the lack of measurable Fe isotope fractionation in the mafic series.
- 2) An obvious difference between the mafic series and the silicic series is illustrated in Figure 3.7. The fraction of iron remaining in the residual melt of the basaltic series ( $>0.5$ ) is much larger than that of the silicic one (down to 0.3). Indeed, a Rayleigh fractionation process with a mineral-melt fractionation factor  $\Delta^{56}\text{Fe}_{\text{mineral-melt}}$  of  $-0.1\%$  or smaller does not produce an analytically resolvable shift in  $\delta^{56}\text{Fe}$  for the amount of iron removed during differentiation of the mafic series.
- 3) The magnitude of mineral-melt fractionation factors is expected to decrease with increasing temperature. Therefore, the high temperature prevailing during basalt to basaltic andesite differentiation ( $>1050^\circ\text{C}$ , Baldrige et al., 1973) could result in very small mineral-melt fractionation factors, whereas crystallisation of the silicic magmas at lower temperatures ( $<950^\circ\text{C}$ ), could be associated with larger fractionation factors.
- 4) Despite the relative abundance of the minerals, there is no drastic difference in the mineral assemblages between all Hekla rocks. Nevertheless, a compositional effect with respect to the evolving silicate melt could potentially influence Fe isotope fractionation. The less polymerised basaltic melts are expected to be more ferrous iron enriched ( $\text{Fe}^{2+}/\Sigma\text{Fe} > 0.9$ , Bezos and Humler, 2005) than the dacitic and rhyolitic melts, which have high alkali contents and therefore structurally stabilise more ferric iron (e.g., Dickenson and Hess, 1986; Mysen, 1988; Gaillard et al., 2001). The importance of marked differences in the Fe redox state for Fe isotope fractionation in mineral-melt systems has been already highlighted in chapter 2. Hence, a pronounced contrast in the redox state of Fe between the minerals and the melt in the evolved

Hekla magmas would be consistent with an enrichment of heavy Fe isotopes in the ferric Fe rich silicate melt.

The effect of magma differentiation processes on Fe isotope composition identified at the Hekla volcanic system can be compared to other Icelandic volcanoes. The Torfajökull volcano produced the largest volumes of silicic rocks in Iceland. The most likely process to generate the rhyolites of the Torfajökull volcano is similar to that of the neighbouring Hekla volcanic system, following a two-stage process that involves partial melting of hydrated metabasaltic crust and subsequent fractional crystallisation of the generated silicic magma with a minor role of magma mixing (see Martin and Sigmarsson, 2007, and references therein). The Fe isotope trend defined by the silicic series from Hekla is directly extended by the Torfajökull rhyolite (Fig. 3.5).

The eruption products from Heimaey and Surtsey most likely originate from a common parent magma, but represent different degrees of fractional crystallisation of predominantly plagioclase, clinopyroxene, olivine and iron oxides (Furman et al., 1991; Mattsson and Oskarsson, 2005; Higgins and Roberge, 2007). As such, the Heimaey sample represents a magma that resided in the crust and fractionated for about 10 years longer than the Surtsey magma (Sigmarsson, 1996). The  $\delta^{56}\text{Fe}$  of the evolved Heimaey mugearite is higher by 0.072‰ compared to that of the primitive Surtsey basalt (Table 3.2, Fig. 3.5). On a first view, this large increase in  $\delta^{56}\text{Fe}$  from the Surtsey basalt to the Heimaey mugearite is in contrast to the absence of a resolvable Fe isotope fractionation in the mafic series of Hekla (Fig. 3.5). However, compositional differences exist between the two systems (Table 3.1), particularly in terms of the more alkali-rich character of the evolved Vestmannaeyjar rocks compared to those of Hekla. This difference could have an effect on mineral-melt Fe isotope fractionation factors (as discussed above). Another possible explanation could be that the

Surtsey basalt is not exactly comparable to the parental magma of the Heimaey mugearite. Furthermore, at the Vestmannaeyjar volcanic system fluids could have played a more important role compared to the less volatile enriched magmas at Hekla. It is interesting to note that the sub-Plinian eruptive column of a typical 20<sup>th</sup> century Hekla eruption only lasts a few hours when the repose time between eruptions is only a decade, whereas during the 1973 eruption of Eldfell volcano at Heimaey lasted for a few days (Thordarson and Larsen, 2007). These durations and the column heights are probably the best proxies for the amount of gas release and accumulated fluids in the magma chambers. However, based on the available data, the process that resulted in the elevated  $\delta^{56}\text{Fe}$  value of the mugearite can not be unambiguously identified.

In summary, the enrichment of heavy Fe isotopes in evolving magmas is not restricted to the silicic series of Hekla, but seems to be a feature occurring in other magmatic systems too. Whether this systematic trend is valid for other geological settings and chemical compositions can not be constrained based on the currently available data. However, it has to be noted that a heavy iron isotope composition of granitoids was particularly found in highly evolved rocks with  $\text{SiO}_2$  from about 71 to 78 wt% (Poitrasson and Freydier, 2005). The samples analysed in this study have  $\text{SiO}_2$  contents up to about 73 wt% (Fig. 3.4a). Hence, if the positive correlation between the degree of magma differentiation and  $\delta^{56}\text{Fe}$  observed for the Icelandic volcanoes is extended towards higher  $\text{SiO}_2$ , heavy  $\delta^{56}\text{Fe}$  values at  $\text{SiO}_2$  contents as high as about 77 wt% could be explained.

### 3.6. CONCLUSIONS

The behaviour of Fe isotopes during magma differentiation was investigated on eruption products from the Hekla volcano. In the mafic series that differentiate from basalt to basaltic andesite through fractional crystallisation no systematic change in  $\delta^{56}\text{Fe}$  was found. Rayleigh fractionation modelling reveals that even a fractionation factor  $\Delta^{56}\text{Fe}_{\text{minerals-melt}}$  of up to -0.1‰ does not result in resolvable changes in Fe isotope composition of the evolving melt for the amount of Fe removed during crystal fractionation of this series. The silicic rocks at Hekla comprise rhyolites produced by high degrees of fractional crystallisation of a dacitic parent magma. Here, the Fe isotope composition of the eruption products is positively correlated with indicators of magma differentiation. In the Hekla volcanic system no Li isotope fractionation was found during crystal fractionation and thus the eruption products most likely represent the isotopic signature of the source. Furthermore, Li concentrations and isotopes in the Hekla rocks suggest that fluid exsolution and degassing did not play a dominating role regarding Fe isotope fractionation. Hence, the systematic change in  $\delta^{56}\text{Fe}$  in the silicic series of Hekla can be predominately attributed to crystal fractionation. A possible mechanism is removal of isotopically light Fe controlled by titanomagnetite crystallisation and subsequent crystal settling.

Our results demonstrate that the Fe isotope composition of the Earth's crust can be slightly modified by magmatic processes. Nevertheless, such relatively small variations in  $\delta^{56}\text{Fe}$  of highly evolved crustal rocks do not change the Earth's bulk igneous rock composition, as defined previously (Beard et al., 2003a; Poitrasson et al., 2004).

## References

- Allegre C., Manhès G., and Lewin E. (2001) Chemical composition of the Earth and the volatility control on planetary genetics. *Earth and Planetary Science Letters* **185**(1-2), 49-69.
- Amonette J. E. and Scott A. D. (1991) Determination of ferrous iron in nonrefractory silicate minerals .1. An improved semi-micro oxidimetric method. *Chemical Geology* **92**(4), 329-338.
- Amonette J. E. and Templeton J. C. (1998) Improvements to the quantitative assay of nonrefractory minerals for Fe(II) and total Fe using 1,10-phenanthroline. *Clays and Clay Minerals* **46**(1), 51-62.
- Anbar A. D. (2004) Iron stable isotopes: beyond biosignatures. *Earth and Planetary Science Letters* **217**(3-4), 223-236.
- Anbar A. D., Jarzecki A. A., and Spiro T. G. (2005) Theoretical investigation of iron isotope fractionation between Fe(H<sub>2</sub>O)(3+)(6) and Fe(H<sub>2</sub>O)(2+)(6) : Implications for iron stable isotope geochemistry. *Geochimica et Cosmochimica Acta* **69**(4), 825-837.
- Anbar A. D., Roe J. E., Barling J., and Neelson K. H. (2000) Nonbiological fractionation of iron isotopes. *Science* **288**(5463), 126-128.
- Anbar A. D. and Rouxel O. (2007) Metal stable isotopes in paleoceanography. *Annual Review of Earth and Planetary Sciences* **35**, 717-746.
- Andrade S., Hypolito R., Ulbrich H., and Silva M. L. (2002) Iron(II) oxide determination in rocks and minerals. *Chemical Geology* **182**(1), 85-89.
- Aranovich L. Y. and Newton R. C. (1999) Experimental determination of CO<sub>2</sub>-H<sub>2</sub>O activity-composition relations at 600-1000 degrees C and 6-14 kbar by reversed decarbonation and dehydration reactions. *American Mineralogist* **84**(9), 1319-1332.
- Aulbach S., Rudnick R. L., and McDonough W. F. (2007) Li-Sr-Nd isotope signatures of the plume and cratonic lithospheric mantle beneath the margin of the rifted Tanzanian craton (Labait). *Contributions to Mineralogy and Petrology*.
- Baker L. L. and Rutherford M. J. (1996) The effect of dissolved water on the oxidation state of silicic melts. *Geochimica et Cosmochimica Acta* **60**(12), 2179-2187.
- Baldrige W. S., McGetchin T. R., and Frey F. A. (1973) Magmatic evolution of Hekla, Iceland. *Contributions to Mineralogy and Petrology* **42**(3), 245-258.



- Beard B. L. and Johnson C. M. (1999) High precision iron isotope measurements of terrestrial and lunar materials. *Geochimica et Cosmochimica Acta* **63**(11-12), 1653-1660.
- Beard B. L. and Johnson C. M. (2004a) Fe isotope variations in the modern and ancient earth and other planetary bodies. In *Geochemistry of Non-Traditional Stable Isotopes - Reviews in Mineralogy & Geochemistry*, Vol. **55**, pp. 319-357.
- Beard B. L. and Johnson C. M. (2004b) Inter-mineral Fe isotope variations in mantle-derived rocks and implications for the Fe geochemical cycle. *Geochimica et Cosmochimica Acta* **68**(22), 4727-4743.
- Beard B. L. and Johnson C. M. (2006) Comment on "Heavy iron isotope composition of granites determined by high resolution MC-ICP-MS", by F. Poitrasson and R. Freydisier [Chem. Geol. 222 132-147]. *Chemical Geology* **235**(1-2), 201-204.
- Beard B. L. and Johnson C. M. (2007) Comment on "Iron isotope fractionation during planetary differentiation" by S. Weyer et al., Earth Planet. Sci. Lett. V240, pages 251-264. *Earth and Planetary Science Letters* **256**(3-4), 633-637.
- Beard B. L., Johnson C. M., Cox L., Sun H., Neelson K. H., and Aguilar C. (1999) Iron isotope biosignatures. *Science* **285**(5435), 1889-1892.
- Beard B. L., Johnson C. M., Skulan J. L., Neelson K. H., Cox L., and Sun H. (2003a) Application of Fe isotopes to tracing the geochemical and biological cycling of Fe. *Chemical Geology* **195**(1-4), 87-117.
- Beard B. L., Johnson C. M., Von Damm K. L., and Poulson R. L. (2003b) Iron isotope constraints on Fe cycling and mass balance in oxygenated Earth oceans. *Geology* **31**(7), 629-632.
- Behrens H. and Jantos N. (2001) The effect of anhydrous composition on water solubility in granitic melts. *American Mineralogist* **86**(1-2), 14-20.
- Behrens H. and Stuke A. (2003) Quantification of H<sub>2</sub>O contents in silicate glasses using IR spectroscopy - a calibration based on hydrous glasses analyzed by Karl-Fischer titration. *Glass Science and Technology* **76**(4), 176-189.
- Behrens H., Zhang Y. X., and Xu Z. G. (2004) H<sub>2</sub>O diffusion in dacitic and andesitic melts. *Geochimica et Cosmochimica Acta* **68**(24), 5139-5150.
- Berndt J., Liebske C., Holtz F., Freise M., Nowak M., Ziegenbein D., Hurkuck W., and Koepke J. (2002) A combined rapid-quench and H<sub>2</sub>-membrane setup for internally heated pressure vessels: Description and application for water solubility in basaltic melts. *American Mineralogist* **87**, 1717-1726.
- Bertoldi C., Dachs E., and Appel P. (2007) Heat-pulse calorimetry measurements on natural chlorite-group minerals. *American Mineralogist* **92**(4), 553-559.

## References

---

- Bezou A. and Humler E. (2005) The Fe<sup>3+</sup>/Sigma Fe ratios of MORB glasses and their implications for mantle melting. *Geochimica et Cosmochimica Acta* **69**(3), 711-725.
- Bigeleisen J. and Mayer M. G. (1947) Calculation of Equilibrium Constants for Isotopic Exchange Reactions. *Journal of Chemical Physics* **15**(5), 261-267.
- Blumel P. and Schreyer W. (1977) Phase relations in pelitic and psammitic gneisses of sillimanite-potash feldspar and cordierite-potash feldspar zones in Moldanubicum of Lam-Bodenmais area, Bavaria. *Journal of Petrology* **18**(3), 431-459.
- Boctor N. Z. (1980) Sphalerite geobarometry in Bodenmais ore, Bavaria. *American Mineralogist* **65**(9-10), 1031-1037.
- Borisov A. A. and Shapkin A. I. (1989) New empiric equation of dependence of Fe<sup>3+</sup>/Fe<sup>2+</sup> ratio in natural melts on their composition, oxygen fugacity and temperature. *Geokhimiya* **6**, 892-897.
- Botcharnikov R. E., Behrens H., and Holtz F. (2006) Solubility and speciation of C-O-H fluids in andesitic melt at T = 1100-1300 °C and P = 200 and 500 MPa. *Chemical Geology* **229**(1-3), 125-143.
- Botcharnikov R. E., Behrens H., Holtz F., Koepke J., and Sato H. (2004) Sulfur and chlorine solubility in Mt. Unzen rhyodacitic melt at 850 °C and 200 MPa. *Chemical Geology* **213**(1-3), 207-225.
- Botcharnikov R. E., Koepke J., Holtz F., McCammon C., and Wilke M. (2005) The effect of water activity on the oxidation and structural state of Fe in a ferro-basaltic melt. *Geochimica et Cosmochimica Acta* **69**(21), 5071-5085.
- Bouman C., Elliott T., and Vroon P. Z. (2004) Lithium inputs to subduction zones. *Chemical Geology* **212**(1-2), 59-79.
- Brantley S. L., Liermann L. J., Guynn R. L., Anbar A., Icopini G. A., and Barling J. (2004) Fe isotopic fractionation during mineral dissolution with and without bacteria. *Geochimica et Cosmochimica Acta* **68**(15), 3189-3204.
- Brenan J. M., Neroda E., Lundstrom C. C., Shaw H. F., Rverson F. J., and Phinney D. L. (1998) Behaviour of boron, beryllium, and lithium during melting and crystallization: constraints from mineral-melt partitioning experiments. *Geochimica et Cosmochimica Acta* **62**(12), 2129-2141.
- Bryant C. J., Chappell B. W., Bennett V. C., and McCulloch M. T. (2004) Lithium isotopic compositions of the New England Batholith: correlations with inferred source rock compositions. *Transactions of the Royal Society of Edinburgh-Earth Sciences* **95**, 199-214.

- Bullen T. D., White A. F., Childs C. W., Vivit D. V., and Schulz M. S. (2001) Demonstration of significant abiotic iron isotope fractionation in nature. *Geology* **29**(8), 699-702.
- Burgisser, A., and Scaillet, B. (2007) Redox evolution of a degassing magma rising to the surface. *Nature*, **445**(7124), 194-197.
- Butler I. B., Archer C., Vance D., Oldroyd A., and Rickard D. (2005) Fe isotope fractionation on FeS formation in ambient aqueous solution. *Earth and Planetary Science Letters* **236**(1-2), 430-442.
- Carmichael I. S. E. (1991) The redox states of basic and silicic magmas - a reflection of their source regions. *Contributions to Mineralogy and Petrology* **106**(2), 129-141.
- Carroll M. R. and Rutherford M. J. (1988) Sulfur speciation in hydrous experimental glasses of varying oxidation-state - results from measured wavelength shifts of sulfur X-rays. *American Mineralogist* **73**(7-8), 845-849.
- Chacko T., Cole D. R., and Horita J. (2001) Equilibrium oxygen, hydrogen and carbon Isotope fractionation factors applicable to geologic systems. In *Stable Isotope Geochemistry, Reviews in Mineralogy and Geochemistry*, Vol. **43**, pp. 1-83.
- Chan L. H. and Frey F. A. (2003) Lithium isotope geochemistry of the Hawaiian plume: Results from the Hawaii Scientific Drilling Project and Koolau volcano. *Geochemistry Geophysics Geosystems* **4**(3), 8707.
- Chou I. M. (1986) Permeability of precious metals to hydrogen at 2 kbar total pressure and elevated temperatures. *American Journal of Science* **286**, 638-658.
- Clemente B. (1998) Etude expérimentale et modélisation de la solubilité du soufre dans les liquides magmatiques. Ph.D. thesis, Université d'Orléans.
- Clemente B., Scaillet B., and Pichavant M. (2004) The solubility of sulphur in hydrous rhyolitic melts. *Journal of Petrology* **45**(11), 2171-2196.
- Cohen B. A., Levasseur S., Zanda B., Hewins R. H., and Halliday A. N. (2006) Kinetic isotope effect during reduction of iron from a silicate melt. *Geochimica et Cosmochimica Acta* **70**(12), 3139-3148.
- Cole D. R. and Chakraborty S. (2001) Rates and mechanisms of isotopic exchange. In *Stable Isotope Geochemistry - Reviews in Mineralogy & Geochemistry*, Vol. **43**, pp. 83-223.
- Condit R. H., Hobbins R. R., and Birchenall C. E. (1974) Self-diffusion of iron and sulfur in ferrous sulfide. *Oxidation of Metals* **8**(6), 409-455.
- Cook N. J. and Damian G. S. (1997) New data on "plumosite" and other sulphosalt minerals from the Herja hydrothermal vein deposit, Baia Mare district, Rumania. *Geologica Carpathica* **48**(6), 387-399.

## References

---

- Craig J. R. and Scott S. D. (1974) Sulfide phase equilibria. In *Sulfide Mineralogy - Reviews in Mineralogy*, Vol. **1**, pp. CS1-104.
- Criss R. E. (1999) *Principles of stable isotope distribution*. Oxford University Press, 254 p.
- Criss R. E., Gregory R. T., and Taylor H. P. (1987) Kinetic theory of oxygen isotopic exchange between minerals and water. *Geochimica et Cosmochimica Acta* **51**(5), 1099-1108.
- Crosby H. A., Johnson C. M., Roden E. E., and Beard B. L. (2005) Coupled Fe(II)-Fe(III) electron and atom exchange as a mechanism for Fe isotope fractionation during dissimilatory iron oxide reduction. *Environmental Science & Technology* **39**(17), 6698-6704.
- Dauphas N. and Rouxel O. (2006) Mass spectrometry and natural variations of iron isotopes. *Mass Spectrometry Reviews* **25**(4), 515-550.
- Devine J. D., Gardner J. E., Brack H. P., Layne G. D., and Rutherford M. J. (1995) Comparison of microanalytical methods for estimating H<sub>2</sub>O contents of silicic volcanic glasses. *American Mineralogist* **80**(3-4), 319-328.
- Dickenson M. P. and Hess P. C. (1986) The structural role and homogeneous redox equilibria of iron in peraluminous, metaluminous and peralkaline silicate melts. *Contributions to Mineralogy and Petrology* **92**(2), 207-217.
- Dodson M. H. (1973) Closure temperature in cooling geochronological and petrological systems. *Contributions to Mineralogy and Petrology* **40**(3), 259-274.
- Dugmore, A.J., Cook, G.T., Shore, J.S., Newton, A.J., Edwards, K.J., and Larsen, G. (1995) Radiocarbon dating tephra layers in Britain and Iceland. *Radiocarbon*, **37**(2), 379-388.
- Elliott T., Jeffcoate A., and Bouman C. (2004) The terrestrial Li isotope cycle: light-weight constraints on mantle convection. *Earth and Planetary Science Letters* **220**(3-4), 231-245.
- Engrand C., McKeegan K. D., Leshin L. A., Herzog G. F., Schnabel C., Nyquist L. E., and Brownlee D. E. (2005) Isotopic compositions of oxygen, iron, chromium, and nickel in cosmic spherules: Toward a better comprehension of atmospheric entry heating effects. *Geochimica et Cosmochimica Acta* **69**(22), 5365-5385.
- Farges F., Lefrere Y., Rossano S., Berthereau A., Calas G., and Brown G. E. (2004) The effect of redox state on the local structural environment of iron in silicate glasses: a molecular dynamics, combined XAFS spectroscopy, and bond valence study. *Journal of Non-Crystalline Solids* **344**(3), 176-188.
- Farrell S. P. and Fleet M. E. (2001) Sulfur K-edge XANES study of local electronic structure in ternary monosulfide solid solution (Fe, Co, Ni)<sub>0.923</sub>S. *Physics and Chemistry of Minerals* **28**(1), 17-27.
- Flesch G., Anderson A. R., and Svec H. J. (1973) A secondary isotopic standard for <sup>6</sup>Li/<sup>7</sup>Li determinations. *International Journal of Mass Spectrometry and Ion Physics* **12**, 265-272.

- Frost B. R. (1991) Introduction to oxygen fugacity and its petrologic importance. In *Reviews in Mineralogy*, Vol. **25**, pp. 1-9.
- Furman T., Frey F. A., and Park K. H. (1991) Chemical constraints on the petrogenesis of mildly alkaline lavas from Vestmannaeyjar, Iceland - the Eldfell (1973) and Surtsey (1963-1967) eruptions. *Contributions to Mineralogy and Petrology* **109**(1), 19-37.
- Gaeta M., Freda C., Christensen J. N., Dallai L., Marra F., Karner D. B., and Scarlato P. (2006) Time-dependent geochemistry of clinopyroxene from the Alban Hills (Central Italy): Clues to the source and evolution of ultrapotassic magmas. *Lithos* **86**(3-4), 330-346.
- Gaillard F., Pichavant M., and Scaillet B. (2003) Experimental determination of activities of FeO and Fe<sub>2</sub>O<sub>3</sub> components in hydrous silicic melts under oxidizing conditions. *Geochimica et Cosmochimica Acta* **67**(22), 4389-4409.
- Gaillard F., Scaillet B., and Pichavant M. (2002) Kinetics of iron oxidation-reduction in hydrous silicic melts. *American Mineralogist* **87**(7), 829-837.
- Gaillard F., Scaillet B., Pichavant M., and Beny J.-M. (2001) The effect of water and fO<sub>2</sub> on the ferric-ferrous ratio of silicic melts. *Chemical Geology* **174**(1-3), 255-273.
- Govindaraju K. (1994) 1994 compilation of working values and sample description for 383 geostandards. *Geostandards Newsletter* **18**, 1-158.
- Govindaraju K. (1995) 1995 working values with confidence-limits for 26 CRPG, ANRT and IWG-GIT geostandards. *Geostandards Newsletter* **19**, 1-33.
- Graham S., Pearson N., Jackson S., Griffin W., and O'Reilly S. Y. (2004) Tracing Cu and Fe from source to porphyry: in situ determination of Cu and Fe isotope ratios in sulfides from the Grasberg Cu-Au deposit. *Chemical Geology* **207**(3-4), 147-169.
- Guelke M. and von Blanckenburg F. (2007) Fractionation of stable iron isotopes in higher plants. *Environmental Science & Technology* **41**(6), 1896-1901.
- Gunnarsson B., Marsh B. D., and Taylor H. P. (1998) Generation of Icelandic rhyolites: silicic lavas from the Torfajokull central volcano. *Journal of Volcanology and Geothermal Research* **83**(1-2), 1-45.
- Halama R., McDonough W. F., Rudnick R. L., Keller J., and Klaudius J. (2007) The Li isotopic composition of Oldoinyo Lengai: Nature of the mantle sources and lack of isotopic fractionation during carbonatite petrogenesis. *Earth and Planetary Science Letters* **254**(1-2), 77-89.
- Hattori K. and Muehlenbachs K. (1982) Oxygen isotope ratios of the Icelandic crust. *Journal of Geophysical Research* **87**(NB8), 6559-6565.

## References

---

- Heimann A., Beard B., and Johnson C. (2007) Fe isotopes in siliceous igneous rocks: Evidence for fluid-rock interaction in plutons. *Geochimica et Cosmochimica Acta* **71**(15), (Goldschmidt conference abstract) A390-A390.
- Higgins M. D. and Roberge J. (2007) Three magmatic components in the 1973 eruption of Eldfell volcano, Iceland: Evidence from plagioclase crystal size distribution (CSD) and geochemistry. *Journal of Volcanology and Geothermal Research* **161**(3), 247-260.
- Hoefs J. (2004) *Stable Isotope Geochemistry*. Springer, 244 p.
- Holloway J. R. and Blank J. G. (1994) Application of experimental results to C-O-H species in natural melts. In *Volatiles in Magmas - Reviews in Mineralogy*, Vol. **30**, pp. 187-230.
- Horn I. and von Blanckenburg F. (2007) Investigation on elemental and isotopic fractionation during 196 nm femtosecond laser ablation multiple collector inductively coupled plasma mass spectrometry. *Spectrochimica Acta Part B-Atomic Spectroscopy* **62**(4), 410-422.
- Horn I., von Blanckenburg F., Schoenberg R., Steinhoefel G., and Markl G. (2006) In situ iron isotope ratio determination using UV-femtosecond laser ablation with application to hydrothermal ore formation processes. *Geochimica et Cosmochimica Acta* **70**(14), 3677-3688.
- Huang F. and Lundstrom C. C. (2006) Iron isotopic fractionation factor between magnetite and hydrous silicic melt. *American Geophysical Union (AGU) Fall Meeting abstract*, V21B-0575.
- Huang F., Lundstrom C. C., and Ianno A. J. (2007) Mg and Fe isotopes as tracers of temperature gradient driven diffusive differentiation. *Geochimica et Cosmochimica Acta* **71**(15) (Goldschmidt conference abstract), A422-A422.
- Huber P. and Muresan I. (1996) Eisen-, Blei- und Antimonminerale aus der Erzlagerstätte Herja (Herzabánya). *Lapis* **27**(7/8), 20-27.
- Huebner J. S. and Sato M. (1970) The oxygen fugacity-temperature relationships of manganese and nickel oxide buffers. In *American Mineralogist*, Vol. 55, pp. 934-952.
- Icopini G. A., Anbar A. D., Ruebush S. S., Tien M., and Brantley S. L. (2004) Iron isotope fractionation during microbial reduction of iron: The importance of adsorption. *Geology* **32**(3), 205-208.
- Jakobsson S. P. (1979) Petrology of recent basalts of the eastern volcanic zone, Iceland. *Acta Naturalia Islandica* **II 26**, 1-103.
- James R. H. and Palmer M. R. (2000) The lithium isotope composition of international rock standards. *Chemical Geology* **166**(3-4), 319-326.
- Jayasuriya K. D., O'Neill H. S., Berry A. J., and Campbell S. J. (2004) A Mossbauer study of the oxidation state of Fe in silicate melts. *American Mineralogist* **89**(11-12), 1597-1609.

- Jeffcoate A. B., Elliott T., Kasemann S. A., Ionov D., Cooper K., and Brooker R. (2007) Li isotope fractionation in peridotites and mafic melts. *Geochimica et Cosmochimica Acta* **71**(1), 202-218.
- Jeffcoate A. B., Elliott T., Thomas A., and Bouman C. (2004) Precise, small sample size determinations of lithium isotopic compositions of geological reference materials and modern seawater by MC-ICP-MS. *Geostandards and Geoanalytical Research* **28**(1), 161-172.
- Johnson C. M. and Beard B. L. (2004) Isotopic constraints on Biogeochemical Cycling of Fe. In *Geochemistry of Non-Traditional Stable Isotopes - Reviews in Mineralogy & Geochemistry*, Vol. **55**, pp. 359-408.
- Johnson C. M., Beard B. L., and Albarede F. (2004) *Geochemistry of Non-Traditional Stable Isotopes - Reviews in Mineralogy & Geochemistry*. Vol. **55**, 454 p.
- Johnson C. M., Roden E. E., Welch S. A., and Beard B. L. (2005) Experimental constraints on Fe isotope fractionation during magnetite and Fe carbonate formation coupled to dissimilatory hydrous ferric oxide reduction. *Geochimica et Cosmochimica Acta* **69**(4), 963-993.
- Johnson C. M., Skulan J. L., Beard B. L., Sun H., Nealon K. H., and Braterman P. S. (2002) Isotopic fractionation between Fe(III) and Fe(II) in aqueous solutions. *Earth and Planetary Science Letters* **195**(1-2), 141-153.
- Kappler A. and Newman D. K. (2004) Formation of Fe(III)-minerals by Fe(II)-oxidizing photoautotrophic bacteria. *Geochimica et Cosmochimica Acta* **68**(6), 1217-1226.
- Kehm K., Hauri E. H., Alexander C. M. O., and Carlson R. W. (2003) High precision iron isotope measurements of meteoritic material by cold plasma ICP-MS. *Geochimica et Cosmochimica Acta* **67**(15), 2879-2891.
- Kilinc A., Carmichael I. S. E., Rivers M. L., and Sack R. O. (1983) The ferric-ferrous ratio of natural silicate liquids equilibrated in air. *Contributions to Mineralogy and Petrology* **83**(1-2), 136-140.
- Kjartansson E. and Gronvold K. (1983) Location of a magma reservoir beneath Hekla volcano, Iceland. *Nature* **301**(5896), 139-141.
- Kobayashi H., Kamimura T., Alfe D., Sturhahn W., Zhao J. Y., and Alp E. E. (2004) Phonon density of states and compression behavior in iron sulfide under pressure. *Physical Review Letters* **93**(19), 1955031-1955034.
- Kress V. C. and Carmichael I. S. E. (1988) Stoichiometry of the iron oxidation reaction in silicate melts. *American Mineralogist* **73**(11-12), 1267-1274.
- Kress V. C. and Carmichael S. E. (1991) The compressibility of silicate liquidus containing Fe<sub>2</sub>O<sub>3</sub> and the effect of composition, temperature, oxygen fugacity and pressure on their redox states. *Contributions to Mineralogy and Petrology* **108**, 82-92.

## References

---

- Lalonde A. E., Rancourt D. G., and Ping J. Y. (1998) Accuracy of ferric/ferrous determinations in micas: A comparison of Mossbauer spectroscopy and the Pratt and Wilson wet-chemical methods. *Hyperfine Interactions* **117**(1-4), 175-204.
- Larsen, C., Newton, A.J., Dugmore, A.J., and Vilmundardottir, E.G. (2001) Geochemistry, dispersal, volumes and chronology of Holocene from the Katla volcanic silicic tephra layers system, Iceland. *Journal of Quaternary Science*, **16**(2), 119-132.
- Le Bas M. J., Le Maitre R. W., Streckeisen A., and Zanettin B. (1986) A chemical classification of volcanic rocks based on the total alkali-silica diagram. *Journal of Petrology* **27**, 745-750.
- Leschik M., Heide G., Frischat G. H., Behrens H., Wiedenbeck M., Wagner N., Heide K., Geissler H., and Reinholz U. (2004) Determination of H<sub>2</sub>O and D<sub>2</sub>O contents in rhyolitic glasses. *Physics and Chemistry of Glasses* **45**(4), 238-251.
- Liebske C., Behrens H., Holtz F., and Lange R. A. (2003) The influence of pressure and composition on the viscosity of andesitic melts. *Geochimica et Cosmochimica Acta* **67**(3), 473-485.
- Lobato L. M., Ribeiro-Rodrigues L. C., and Vieira F. W. R. (2001) Brazil's premier gold province. Part II: Geology and genesis of gold deposits in the Archean Rio das Velhas greenstone belt, Quadrilátero Ferrífero. *Mineralium Deposita* **36**(3-4), 249-277.
- Ludwig K. R. (2001) Isoplot - A geochronological toolkit for Microsoft Excel, Version 2.49. *Berkeley Geochronology Center Special Publication No. 1a*, 55 p.
- Luhr J. F. (1990) Experimental phase-relations of water-saturated and sulfur-saturated arc magmas and the 1982 eruptions of El-Chichon volcano. *Journal of Petrology* **31**(5), 1071-1114.
- Macdonald R., McGarvie D. W., Pinkerton H., Smith R. L., and Palacz Z. A. (1990) Petrogenetic evolution of the Torfajökull Volcanic Complex, Iceland .1. Relationship between the magma types. *Journal of Petrology* **31**(2), 429-459.
- Magna T., Wiechert U., and Halliday A. N. (2006) New constraints on the lithium isotope compositions of the Moon and terrestrial planets. *Earth and Planetary Science Letters* **243**(3-4), 336-353.
- Magna T., Wiechert U. H., and Halliday A. N. (2004) Low-blank isotope ratio measurement of small samples of lithium using multiple-collector ICPMS. *International Journal of Mass Spectrometry* **239**(1), 67-76.
- Mandernack K. W., Bazylnski D. A., Shanks W. C., and Bullen T. D. (1999) Oxygen and iron isotope studies of magnetite produced by magnetotactic bacteria. *Science* **285**(5435), 1892-1896.
- Markl G., von Blanckenburg F., and Wagner T. (2006) Iron isotope fractionation during hydrothermal ore deposition and alteration. *Geochimica et Cosmochimica Acta* **70**(12), 3011-3030.



- Marra F., Freda C., Scarlato P., Taddeucci J., Karner D. B., Renne P. R., Gaeta M., Palladino D. M., Trigila R., and Cavarretta G. (2003) Post-caldera activity in the Alban Hills volcanic district (Italy): Ar-40/Ar-39 geochronology and insights into magma evolution. *Bulletin of Volcanology* **65**(4), 227-247.
- Martin E. and Sigmarsson O. (2007) Crustal thermal state and origin of silicic magma in Iceland: the case of Torfajökull, Ljosufjöll and Snaefellsjökull volcanoes. *Contributions to Mineralogy and Petrology* **153**(5), 593-605.
- Matthews A., Zhu X. K., and O'Nions K. (2001) Kinetic iron stable isotope fractionation between iron (-II) and (-III) complexes in solution. *Earth and Planetary Science Letters* **192**(1), 81-92.
- Mattsson H. B. and Oskarsson N. (2005) Petrogenesis of alkaline basalts at the tip of a propagating rift: Evidence from the Heimaey volcanic centre, south Iceland. *Journal of Volcanology and Geothermal Research* **147**(3-4), 245-267.
- Mills G. A. and Urey H. C. (1940) The kinetics of isotopic exchange between carbon dioxide, bicarbonate ion, carbonate ion and water. *Journal of the American Chemical Society* **62**, 1019-1026.
- Mineev S. D., Polyakov V. B., and Permyakov Y. V. (2007) Equilibrium iron isotope fractionation factors for magnetite from Mössbauer spectroscopy and inelastic nuclear resonant X-ray scattering data. *Geochimica et Cosmochimica Acta* **71**(15) (Goldschmidt conference abstract), A669.
- Misiti V., Behrens H., Freda C., Vetere F., Botcharnikov R. E., and Scarlato P. (2007) Solubility of H<sub>2</sub>O and CO<sub>2</sub> in potassic melts at 1200 and 1250 °C and pressure from 50 to 500 MPa. *American Mineralogist* (in review).
- Moore G., Righter K., and Carmichael I. S. E. (1995) The effect of dissolved water on the oxidation-state of iron in natural silicate liquids. *Contributions to Mineralogy and Petrology* **120**(2), 170-179.
- Moretti R. (2005) Polymerisation, basicity, oxidation state and their role in ionic modelling of silicate melts. *Annals of Geophysics* **48**(4-5), 583-608.
- Moretti, R., and Ottonello, G. (2003) Polymerization and disproportionation of iron and sulfur in silicate melts: insights from an optical basicity-based approach. *Journal of Non-Crystalline Solids*, **323**(1-3), 111-119.
- Moretti, R., and Papale, P. (2004) On the oxidation state and volatile behavior in multicomponent gas-melt equilibria. *Chemical Geology*, **213**(1-3), 265-280.
- Morgan G. B. and London D. (1996) Optimizing the electron microprobe analysis of hydrous alkali aluminosilicate glasses. *American Mineralogist* **81**(9-10), 1176-1185.

## References

---

- Moune S., Gauthier P. J., Gislason S. R., and Sigmarsson G. (2006) Trace element degassing and enrichment in the eruptive plume of the 2000 eruption of Hekla volcano, Iceland. *Geochimica et Cosmochimica Acta* **70**(2), 461-479.
- Moune S., Sigmarsson O., Thordarson T., and Gauthier P. J. (2007) Recent volatile evolution in the magmatic system of Hekla volcano, Iceland. *Earth and Planetary Science Letters* **255**(3-4), 373-389.
- Mullane E., Russell S. S., and Gounelle M. (2005) Nebular and asteroidal modification of the iron isotope composition of chondritic components. *Earth and Planetary Science Letters* **239**(3-4), 203-218.
- Mungall J. E. (2002) Empirical models relating viscosity and tracer diffusion in magmatic silicate melts. *Geochimica et Cosmochimica Acta* **66**(1), 125-143.
- Mysen B. O. (1988) *Structure and properties of silicate melts*. Elsevier, 354 p.
- Mysen B. O. and Richet P. (2005) Silicate glasses and melts - properties and structure. *Developments in Geochemistry* **10**, 544 p.
- Mysen B. O., Virgo D., and Seifert F. A. (1982) The Structure of Silicate Melts - Implications for Chemical and Physical-Properties of Natural Magma. *Reviews of Geophysics* **20**(3), 353-383.
- Nikolaev G. S., Borisov A. A., and Ariskin A. A. (1996) Calculation of the ferric-ferrous ratio in magmatic melts: Testing and additional calibration of empirical equations for various magmatic series. *Geokhimiya* **8**, 713-722.
- Northrop D. A. and Clayton R. N. (1966) Oxygen isotope fractionations in systems containing dolomite. *Journal of Geology* **74**(2), 174-196.
- Oberthur T., Weiser T. W., Gast L., and Kojonen K. (2003) Geochemistry and mineralogy of platinum-group elements at Hartley Platinum Mine, Zimbabwe - Part I. Primary distribution patterns in pristine ores of the Main Sulfide Zone of the Great Dyke. *Mineralium Deposita* **38**(3), 327-343.
- O'Neill H. S. C., Berry A. J., McCammon C. C., Jayasuriya K. D., Campbell S. J., and Foran G. (2006) An experimental determination of the effect of pressure on the Fe<sup>3+</sup>/Sigma Fe ratio of an anhydrous silicate melt to 3.0 GPa. *American Mineralogist* **91**(2-3), 404-412.
- Ottonello G., Moretti R., Marini L., and Zuccolini M. V. (2001) Oxidation state of iron in silicate glasses and melts: a thermochemical model. *Chemical Geology* **174**(1-3), 157-179.
- Partzsch G. M., Lattard D., and McCammon C. (2004) Mossbauer spectroscopic determination of Fe<sup>3+</sup>/Fe<sup>2+</sup> in synthetic basaltic glass: a test of empirical fO<sub>2</sub> equations under superliquidus and subliquidus conditions. *Contributions to Mineralogy and Petrology* **147**(5), 565-580.
- Pistiner J. S. and Henderson G. M. (2003) Lithium-isotope fractionation during continental weathering processes. *Earth and Planetary Science Letters* **214**(1-2), 327-339.

- Pitzer K. S. and Sterner S. M. (1994) Equation of state valid continuously from zero to extreme pressures for H<sub>2</sub>O and CO<sub>2</sub>. *Journal of Chemical Physics* **102**, 3111-3116.
- Poitrasson F. (2006) On the iron isotope homogeneity level of the continental crust. *Chemical Geology* **235**(1-2), 195-200.
- Poitrasson F. (2007) Does planetary differentiation really fractionate iron isotopes? *Earth and Planetary Science Letters* **256**(3-4), 484-492.
- Poitrasson F. and Freydier R. (2005) Heavy iron isotope composition of granites determined by high resolution MC-ICP-MS. *Chemical Geology* **222**(1-2), 132-147.
- Poitrasson F., Halliday A. N., Lee D. C., Levasseur S., and Teutsch N. (2004) Iron isotope differences between Earth, Moon, Mars and Vesta as possible records of contrasted accretion mechanisms. *Earth and Planetary Science Letters* **223**(3-4), 253-266.
- Polyakov V. B. (1993) On ideality of isotope mixture in solids. *Russian Journal of Physical Chemistry* **67**, 422-425.
- Polyakov V. B. (1997) Equilibrium fractionation of the iron isotopes: Estimation from Mossbauer spectroscopy data. *Geochimica et Cosmochimica Acta* **61**(19), 4213-4217.
- Polyakov V. B., Clayton R. N., Horita J., and Mineev S. D. (2007) Equilibrium iron isotope fractionation factors of minerals: Reevaluation from the data of nuclear inelastic resonant X-ray scattering and Mossbauer spectroscopy. *Geochimica et Cosmochimica Acta* **71**(15), 3833-3846.
- Polyakov V. B. and Mineev S. D. (2000) The use of Mössbauer spectroscopy in stable isotope geochemistry. *Geochimica et Cosmochimica Acta* **64**(5), 849-865.
- Pouchou J. L. and Pichoir F. (1991) Quantitative analysis of homogeneous or stratified microvolumes applying the model "PAP". In *Electron probe quantitation* (ed. K. F. J. Heinrich and D. E. Newbury), pp. 31-75. Plenum Press.
- Prewitt C. T. and Rajamani V. (1974) Electron interactions and chemical bonding in sulfides. In *Sulfide Mineralogy - Reviews in Mineralogy*, Vol. **1**, pp. PR1-41.
- Robie R. A., Hemingway B. S., and Fischer J. R. (1978) Thermodynamic properties of minerals and related substances at 298.15 K and 1 bar (105 Pascals) pressure and at higher temperature. *Geological Survey Bulletin* **1452**, 456.
- Roskosz M., Luais B., Watson H. C., Toplis M. J., Alexander C. M. O., and Mysen B. O. (2006) Experimental quantification of the fractionation of Fe isotopes during metal segregation from a silicate melt. *Earth and Planetary Science Letters* **248**(3-4), 851-867.
- Rosner M., Ball L., Peucker-Ehrenbrink B., Blusztajn J., Bach W., and Erzinger J. (2007) A simplified, accurate and fast method for lithium isotope analysis of rocks and fluids, and

## References

---

- delta Li-7 values of seawater and rock reference materials. *Geostandards and Geoanalytical Research* **31**(2), 77-88.
- Rossano S., Ramos A., Delaye J. M., Creux S., Filipponi A., Brouder C., and Calas G. (2000) EXAFS and Molecular Dynamics combined study of CaO-FeO-2SiO(2) glass. New insight into site significance in silicate glasses. *Europhysics Letters* **49**(5), 597-602.
- Rouxel O., Fouquet Y., and Ludden J. N. (2004) Subsurface processes at the Lucky Strike hydrothermal field, Mid-Atlantic Ridge: Evidence from sulfur, selenium, and iron isotopes. *Geochimica et Cosmochimica Acta* **68**(10), 2295-2311.
- Rudnick R. L. and Ionov D. A. (2007) Lithium elemental and isotopic disequilibrium in minerals from peridotite xenoliths from far-east Russia: Product of recent melt/fluid-rock reaction. *Earth and Planetary Science Letters* **256**(1-2), 278-293.
- Rudnick R. L., Tomascak P. B., Njo H. B., and Gardner L. R. (2004) Extreme lithium isotopic fractionation during continental weathering revealed in saprolites from South Carolina. *Chemical Geology* **212**(1-2), 45-57.
- Ryan J. G. and Kyle P. R. (2004) Lithium abundance and lithium isotope variations in mantle sources: insights from intraplate volcanic rocks from Ross Island and Marie Byrd Land (Antarctica) and other oceanic islands. *Chemical Geology* **212**(1-2), 125-142.
- Ryan J. G. and Langmuir C. H. (1987) The systematics of lithium abundances in young volcanic rocks. *Geochimica et Cosmochimica Acta* **51**(6), 1727-1741.
- Sack R. O., Carmichael I. S. E., Rivers M., and Ghiorso M. S. (1980) Ferric-ferrous equilibria in natural silicate liquids at 1bar. *Contributions to Mineralogy and Petrology* **75**(4), 369-376.
- Schauble E. A. (2004) Stable isotope fractionation theory applied to new systems. In *Geochemistry of Non-Traditional Stable Isotopes - Reviews in Mineralogy & Geochemistry*, Vol. **55**, pp. 65-101.
- Schauble E. A., Rossman G. R., and Taylor H. P. (2001) Theoretical estimates of equilibrium Fe-isotope fractionations from vibrational spectroscopy. *Geochimica Et Cosmochimica Acta* **65**(15), 2487-2497.
- Schoenberg R. and von Blanckenburg F. (2005) An assessment of the accuracy of stable Fe isotope ratio measurements on samples with organic and inorganic matrices by high-resolution multicollector ICP-MS. *International Journal of Mass Spectrometry* **242**(2-3), 257-272.
- Schoenberg R. and von Blanckenburg F. (2006) Modes of planetary-scale Fe isotope fractionation. *Earth and Planetary Science Letters* **252**(3-4), 342-359.
- Seifert F., Virgo D., and Mysen B. O. (1979) Melt Structures and Redox Equilibria in the System Na<sub>2</sub>O-FeO-Fe<sub>2</sub>O<sub>3</sub>-Al<sub>2</sub>O<sub>3</sub>-SiO<sub>2</sub>. *Carnegie Institution Washington Yearbook* **78**, 511-519.

- Seitz H. M., Brey G. P., Lahaye Y., Durali S., and Weyer S. (2004) Lithium isotopic signatures of peridotite xenoliths and isotopic fractionation at high temperature between olivine and pyroxenes. *Chemical Geology* **212**(1-2), 163-177.
- Shahar A., Manning C. E., and Young E. D. (2007) An experimental approach to high-temperature iron isotope fractionation. *Geochimica et Cosmochimica Acta* **71**(15) (Goldschmidt conference abstract), A920-A920.
- Sigmarsson O. (1996) Short magma chamber residence time at an Icelandic volcano inferred from U-series disequilibria. *Nature* **382**(6590), 440-442.
- Sigmarsson O., Condomines M., and Fourcade S. (1992a) A Detailed Th, Sr and O Isotope Study of Hekla - Differentiation Processes in an Icelandic Volcano. *Contributions to Mineralogy and Petrology* **112**(1), 20-34.
- Sigmarsson O., Condomines M., and Fourcade S. (1992b) Mantle and crustal contribution in the genesis of recent basalts from off-rift zones in Iceland - Constraints from Th-isotopes, Sr-isotopes and O-isotopes. *Earth and Planetary Science Letters* **110**(1-4), 149-162.
- Sigmarsson O., Hemond C., Condomines M., Fourcade S., and Oskarsson N. (1991) Origin of silicic magma in Iceland revealed by Th isotopes. *Geology* **19**(6), 621-624.
- Sigmarsson O., Jakobsson S. P., and Thordarson T. (2007) Segregations in Surtsey lavas, Iceland, reveal extreme magma differentiation during lava emplacement. In *A Joint Special IAVCEI and GSL Publication: Studies in Volcanology: The Legacy of George Walker (accepted manuscript)* (ed. T. Thordarson, G. Larsen, S. Self, S. Rowland, and A. Höskuldsson).
- Sisson T. W. and Grove T. L. (1993) Experimental investigations of the role of H<sub>2</sub>O in calc-alkaline differentiation and subduction zone magmatism. *Contributions to Mineralogy and Petrology* **113**(2), 143-166.
- Skulan J. L., Beard B. L., and Johnson C. M. (2002) Kinetic and equilibrium Fe isotope fractionation between aqueous Fe(III) and hematite. *Geochimica et Cosmochimica Acta* **66**(17), 2995-3015.
- Tamic N., Behrens H., and Holtz F. (2001) The solubility of H<sub>2</sub>O and CO<sub>2</sub> in rhyolitic melts in equilibrium with a mixed CO<sub>2</sub>-H<sub>2</sub>O fluid phase. *Chemical Geology* **174**(1-3), 333-347.
- Tangeman J. A., Lange R., and Forman L. (2001) Ferric-ferrous equilibria in K<sub>2</sub>O-FeO-Fe<sub>2</sub>O<sub>3</sub>-SiO<sub>2</sub> melts. *Geochimica et Cosmochimica Acta* **65**(11), 1809-1819.
- Taylor J. R., Wall V. J., and Pownceby M. I. (1992a) The calibration and application of accurate redox sensors. In *American Mineralogist*, Vol. **77**, pp. 284-295.
- Taylor P. D. P., Maeck R., and Debievre P. (1992b) Determination of the absolute isotopic composition and atomic-weight of a reference sample of natural iron. *International Journal of Mass Spectrometry and Ion Processes* **121**(1-2), 111-125.

## References

---

- Tegge-Schüring A. S. (2003) Cation diffusion in silicate melts. Ph.D. thesis, University of Hannover.
- Teng F. Z., McDonough W. F., Rudnick R. L., Walker R. J., and Sirbescu M. L. C. (2006) Lithium isotopic systematics of granites and pegmatites from the Black Hills, South Dakota. *American Mineralogist* **91**(10), 1488-1498.
- Teutsch N., von Gunten U., Hofstetter T. B., and Halliday A. N. (2004) Iron isotope fractionation during adsorption of Fe(II) on Fe(III) oxides. *Geochimica et Cosmochimica Acta* **68**(11), A361-A361.
- Thorarinsson S. (1967) The eruption of Hekla in historical times, eruption of Hekla 1947-1948. *Soc. Sci. Islandica* **1**, 1-170.
- Thorarinsson, S. (1971) The age of the light Hekla tephra layers according to corrected <sup>14</sup>C datings (in Icelandic). *Náttúrufræðingurinn*, **41**, 99-105.
- Thorarinsson S. and Sigvaldason G. E. (1972) The Hekla eruption of 1970. *Bulletin of Volcanology* **26**, 1-20.
- Thordarson T. and Larsen G. (2007) Volcanism in Iceland in historical time: Volcano types, eruption styles and eruptive history. *Journal of Geodynamics* **43**(1), 118-152.
- Tokonami M., Nishiguc.K, and Morimoto N. (1972) Crystal-structure of a monoclinic pyrrhotite (Fe<sub>7</sub>S<sub>8</sub>). *American Mineralogist* **57**(7-8), 1066-1080.
- Tomascak P. B. (2004) Developments in the understanding and application of lithium isotopes in the earth and planetary sciences. In *Geochemistry of Non-Traditional Stable Isotopes - Reviews in Mineralogy & Geochemistry*, Vol. 55, pp. 153-195.
- Tomascak P. B., Carlson R. W., and Shirey S. B. (1999a) Accurate and precise determination of Li isotopic compositions by multi-collector sector ICP-MS. *Chemical Geology* **158**(1-2), 145-154.
- Tomascak P. B., Langmuir C. H., Le Roux P. J., and Shirey S. B. (2007) Lithium isotopes in global mid-ocean ridge basalts. *Geochimica et Cosmochimica Acta*, (in press).
- Tomascak P. B., Tera F., Helz R. T., and Walker R. J. (1999b) The absence of lithium isotope fractionation during basalt differentiation: New measurements by multicollector sector ICP-MS. *Geochimica et Cosmochimica Acta* **63**(6), 907-910.
- Ueda A. and Itaya T. (1981) Microphenocrystic Pyrrhotite from Dacite Rocks of Satsuma-Iwojima, Southwest Kyushu, Japan and the Solubility of Sulfur in Dacite Magma. *Contributions to Mineralogy and Petrology* **78**(1), 21-26.
- Urey H. C. (1947) The thermodynamic properties of isotopic substances. *Journal of the Chemical Society*, 562-581.

- Valley G. E. and Anderson H. H. (1947) A Comparison of the Abundance Ratios of the Isotopes of Terrestrial and of Meteoritic Iron. *Journal of the American Chemical Society* **69**(8), 1871-1875.
- Valley J. W. and Cole D. R. (2001) Stable isotope geochemistry - *Reviews in Mineralogy & Geochemistry*, Vol. **43**, 662 p.
- Vaughan D. J. and Craig J. R. (1978) *Mineral chemistry of metal sulfides*. University Press, Cambridge, 493 p.
- Vaughan D. J. and Lennie A. R. (1991) The iron sulfide minerals - Their chemistry and role in nature. *Science Progress* **75**(298), 371-388.
- Vetere F., Behrens H., Schuessler J. A., Holtz F., Misiti V., and Borchers L. (2006) Viscosity of andesite melts – implication for magma mixing prior to Unzen 1991-1995 eruption. *Journal of Volcanology and Geothermal Research*, (in press).
- Virgo D. and Mysen B. O. (1985) The structural state of iron in oxidized vs reduced glasses at 1 atm - a Fe-57 Mossbauer study. *Physics and Chemistry of Minerals* **12**(2), 65-76.
- Volkening J. and Papanastassiou D. A. (1989) Fe isotope anomalies. *Meteoritics* **24**(4), 335-335.
- Walczyk T. and von Blanckenburg F. (2002) Natural iron isotope variations in human blood. *Science* **295**(5562), 2065-2066.
- Walczyk T. and von Blanckenburg F. (2005) Deciphering the iron isotope message of the human body. *International Journal of Mass Spectrometry* **242**(2-3), 117-134.
- Watson E. B. and Baxter E. F. (2007) Diffusion in solid-Earth systems. *Earth and Planetary Science Letters* **253**(3-4), 307-327.
- Webster J. D., Holloway J. R., and Hervig R. L. (1989) Partitioning of lithophile trace-elements between H<sub>2</sub>O and H<sub>2</sub>O + CO<sub>2</sub> fluids and topaz rhyolite melt. *Economic Geology* **84**(1), 116-134.
- Wedepohl H. K. (1995) The composition of the continental crust. *Geochimica et Cosmochimica Acta* **59**(7), 1217-1232.
- Welch S. A., Beard B. L., Johnson C. M., and Braterman P. S. (2003) Kinetic and equilibrium Fe isotope fractionation between aqueous Fe(II) and Fe(III). *Geochimica et Cosmochimica Acta* **67**(22), 4231-4250.
- Weyer S., Anbar A. D., Brey G. P., Munker C., Mezger K., and Woodland A. B. (2005) Iron isotope fractionation during planetary differentiation. *Earth and Planetary Science Letters* **240**(2), 251-264.
- Weyer S., Anbar A. D., Brey G. P., Munker C., Mezger K., and Woodland A. B. (2007) Fe-isotope fractionation during partial melting on Earth and the current view on the Fe-isotope budgets

## References

---

- of the planets (reply to the comment of F. Poitrasson and to the comment of B.L. Beard and C.M. Johnson on "Iron isotope fractionation during planetary differentiation" by S. Weyer, A.D. Anbar, G.P. Brey, C. Munker, K. Mezger and A.B. Woodland). *Earth and Planetary Science Letters* **256**(3-4), 638-646.
- Weyer S. and Ionov D. A. (2007) Partial melting and melt percolation in the mantle: The message from Fe isotopes. *Earth and Planetary Science Letters* **259**(1-2), 119-133.
- Whipple E. R. (1974) Study of Wilson's determination of ferrous iron in silicates. *Chemical Geology* **14**(3), 223-238.
- Whitney J. A. (1984) Fugacities of sulfurous gases in pyrrhotite-bearing silicic magmas. *American Mineralogist* **69**(1-2), 69-78.
- Whitney J. A. and Stormer J. C. (1983) Igneous sulfides in the Fish Canyon Tuff and the role of sulfur in calc-alkaline magmas. *Geology* **11**(2), 99-102.
- Wiesli R. A., Beard B. L., and Johnson C. M. (2004) Experimental determination of Fe isotope fractionation between aqueous Fe(II), siderite and "green rust" in abiotic systems. *Chemical Geology* **211**(3-4), 343-362.
- Wilke M., Behrens H., Burkhard D. J. M., and Rossano S. (2002) The oxidation state of iron in silicic melt at 500 MPa water pressure. *Chemical Geology* **189**(1-2), 55-67.
- Wilke M., Schmidt C., Farges F., Malavergne V., Gautron L., Simionovici A., Hahn M., and Petit P.-E. (2006) Structural environment of iron in hydrous aluminosilicate glass and melt-evidence from X-ray absorption spectroscopy. *Chemical Geology* **229**(1-3), 144-161.
- Williams H. M., McCammon C. A., Peslier A. H., Halliday A. N., Teutsch N., Levasseur S., and Burg J. P. (2004) Iron isotope fractionation and the oxygen fugacity of the mantle. *Science* **304**(5677), 1656-1659.
- Williams H. M., Peslier A. H., McCammon C., Halliday A. N., Levasseur S., Teutsch N., and Burg J. P. (2005) Systematic iron isotope variations in mantle rocks and minerals: The effects of partial melting and oxygen fugacity. *Earth and Planetary Science Letters* **235**(1-2), 435-452.
- Wilson A. D. (1960) The micro-determination of ferrous iron in silicate minerals by a volumetric and colorimetric method. *Analyst* **85**, 823-827.
- Wolfe C. J., Bjarnason I. T., VanDecar J. C., and Solomon S. C. (1997) Seismic structure of the Iceland mantle plume. *Nature* **385**(6613), 245-247.
- Wood B. J. (1991) Oxygen barometry of spinel peridotites. *Reviews in Mineralogy*, Vol. **25**, pp. 417-431.
- Woodhead J. D. (2006) Isotope ratio determination in the earth and environmental sciences: Developments and applications in 2004/2005. *Geostandards and Geoanalytical Research* **30**(3), 187-196.



- Wunder B., Meixner A., Romer R. L., Feenstra A., Schettler G., and Heinrich W. (2007) Lithium isotope fractionation between Li-bearing staurolite, Li-mica and aqueous fluids: An experimental study. *Chemical Geology* **238**(3-4), 277-290.
- Wunder B., Meixner A., Romer R. L., and Heinrich W. (2006) Temperature-dependent isotopic fractionation of lithium between clinopyroxene and high-pressure hydrous fluids. *Contributions to Mineralogy and Petrology* **151**(1), 112-120.
- Yokoyama T. and Nakamura E. (2002) Precise determination of ferrous iron in silicate rocks. *Geochimica et Cosmochimica Acta* **66**(6), 1085-1093.
- York D. (1969) Least squares fitting of a straight line with correlated errors. *Earth and Planetary Science Letters* **5**, 320-324.
- Young E. D., Galy A., and Nagahara H. (2002) Kinetic and equilibrium mass-dependent isotope fractionation laws in nature and their geochemical and cosmochemical significance. *Geochimica et Cosmochimica Acta* **66**(6), 1095-1104.
- Yund R. A. and Hall H. T. (1969) Hexagonal and monoclinic pyrrhotites. *Economic Geology* **64**(4), 420-&.
- Zhu X. K., Guo Y., Williams R. J. P., O'Nions R. K., Matthews A., Belshaw N. S., Canters G. W., de Waal E. C., Weser U., Burgess B. K., and Salvato B. (2002) Mass fractionation processes of transition metal isotopes. *Earth and Planetary Science Letters* **200**(1-2), 47-62.

## Appendix A1 to chapter 1

### A1.1. REAGENTS USED FOR WET-CHEMICAL COLORIMETRIC IRON DETERMINATION

All reagents were freshly prepared before each analytical session:

*Ammonium vanadate solution.* 0.165 g  $\text{NH}_4\text{VO}_3$  (Alfa Aesar, 99.93% metals basis) was diluted in 100 mL distilled water and  $\text{H}_2\text{SO}_4$  (Merck, p.a.). The final concentration of  $\text{H}_2\text{SO}_4$  was generally 1M, or in some cases up to 5M to test whether the sulphuric acid concentration has an influence on the ferrous iron determination (see text). 1 mL of this solution was added to each sample (corresponds to  $\sim 14.1 \mu\text{mol NH}_4\text{VO}_3$ ), capable to oxidize about 800  $\mu\text{g}$  ferrous Fe. We always processed  $<500 \mu\text{g}$  Fe to ensure  $\text{V}^{5+}$  excess.

*Boric acid solution.* Approximately 20 g  $\text{H}_3\text{BO}_3$  (Merck, p.a.) were dissolved in  $\sim 100$  mL distilled water at  $\sim 80^\circ\text{C}$  to obtain a saturated solution. After sample dissolution 5 mL of the hot solution was added to each sample.

*2:2'bipyridyl solution.* 0.15g  $\text{C}_{10}\text{H}_8\text{N}_2$  (Alfa Aesar, p.a.) was dissolved in 100 mL distilled water. 5 mL of this solution (corresponds to  $\sim 9.6 \mu\text{mol C}_{10}\text{H}_8\text{N}_2$ ) was added to each sample. This amount can complex about 900  $\mu\text{g}$  ferrous Fe to form the colored chromophore. Less than  $<500 \mu\text{g}$  Fe was processed to ensure bipyridyl excess.

*Ammonium acetate solution:* Approximately 20 g  $\text{CH}_3\text{COONH}_4$  was dissolved in 200 mL distilled water.

*Hydroxylamine hydrochloride.* Between 5 and 10 mg  $\text{NH}_2\text{OH}\cdot\text{HCl}$  (Merck, p.a.) were added to each 10-mL-sample-aliquot containing  $<50 \mu\text{g}$  ferric Fe, to ensure quantitative reduction. At least 8 mg ferric Fe can be reduced by this amount ( $>72 \mu\text{mol NH}_2\text{OH}\cdot\text{HCl}$ ).

*Hydrofluoric acid* was 24% or 48% (Merck, p.a.) (see text).

## A1.2. WATER SOLUBILITY IN PHONO-TEPHRITIC MELTS

Table A1.1. Water concentrations and experimental run products (from Misiti et al., 2007).

sample	P (MPa)	T (°C)	H <sub>2</sub> O <sup>a</sup> (wt%)		experimental products <sup>b</sup>
<b>Ar-IHPV (fH<sub>2</sub> intrinsic)</b>					
<b>H<sub>2</sub>O fluid, aH<sub>2</sub>O = 1</b>					
Alb1-20	50	1250	2.43 ± 0.12	IR	gl, fl
Alb1-21	50	1250	2.49 ± 0.12	IR	gl, fl
Alb1-22	100	1250	3.44 ± 0.18	IR	gl, fl
Alb1-23	100	1250	3.41 ± 0.18	IR	gl, fl
Alb1-36	200	1200	5.07 ± 0.25	IR	gl, fl
Alb1-37	200	1200	4.31 ± 0.21	IR	gl, fl
Alb1-10	200	1250	4.87 ± 0.26	IR	gl, fl
Alb1-24	300	1250	5.90 ± 0.08	KFT	gl, fl, xx(quench)
Alb1-25	300	1250	6.20 ± 0.08	KFT	gl, fl, xx(quench)
Alb1-35	400	1200	8.36 ± 0.10	KFT	gl, fl, xx(quench)
Alb1-26	400	1250	7.61 ± 0.08	KFT	gl, fl, xx(quench)
Alb1-27	400	1250	8.16 ± 0.08	KFT	gl, fl, xx(quench)
Alb1-5	500	1200	11.95 ± 0.08	KFT	gl, fl, xx(quench)
Alb1-15	500	1250	8.08 ± 0.08	KFT	gl, fl, xx(quench)
Alb1-28	500	1250	9.78 ± 0.18	KFT	gl, fl, xx(quench)
Alb1-41	200	1200	3.76 ± 0.19	KFT	gl, fl
<b>Ar-IHPV (fH<sub>2</sub> intrinsic)</b>					
<b>H<sub>2</sub>O-CO<sub>2</sub> fluid</b>					
Alb1-7	200	1250	2.43 ± 0.10	KFT	
Alb1-8	200	1250	3.10 ± 0.10	KFT	gl, fl
Alb1-6bis	200	1250	0.89 ± 0.14	IR	gl, fl
Alb1-6a	200	1250	1.41 ± 0.15	IR	gl, fl
Alb1-1	500	1200	0.94 ± 0.07	KFT	gl, fl, cpx
Alb1-2	500	1200	2.82 ± 0.07	KFT	gl, fl
Alb1-3	500	1200	5.54 ± 0.08	KFT	gl, fl
Alb1-4	500	1200	9.27 ± 0.08	KFT	gl, fl, xx(quench)
Alb1-12	500	1250	3.80 ± 0.20	IR	gl, fl
Alb1-13	500	1250	6.91 ± 0.09	KFT	gl, fl, xx(quench)
Alb1-14	500	1250	6.97 ± 0.07	KFT	gl, fl, xx(quench)
<b>Ar-H<sub>2</sub>-IHPV (fH<sub>2</sub> varied)</b>					
<b>H<sub>2</sub>O fluid and H<sub>2</sub>O-CO<sub>2</sub> fluid</b>					
AbH-42	200	1200	5.32 ± 0.09	KFT	gl, fl
AbH-43	200	1200	4.73 ± 0.14	KFT	gl, fl
AbH-44	200	1200	2.67 ± 0.09	KFT	gl, fl
AbH-45	200	1200	1.41 ± 0.05	KFT	gl, fl
AbH-47	200	1200	5.32 ± 0.06	KFT	gl, fl
AbH-48	200	1200	4.64 ± 0.06	KFT	gl, fl
AbH-49	200	1200	2.78 ± 0.18	KFT	gl, fl
AbH-50	200	1200	1.97 ± 0.18	KFT	gl, fl
AbH-51	200	1200	1.57 ± 0.17	KFT	gl, fl
AbH-52	200	1200	4.81 ± 0.07	KFT	gl, fl
AbH-54	200	1200	2.84 ± 0.07	KFT	gl, fl
AbH-56	200	1200	1.08 ± 0.06	KFT	gl, fl

<sup>a</sup>Water concentration in the glasses measured by IR spectroscopy (IR) or Karl Fischer titration (KFT).

<sup>b</sup>gl=glass, fl=fluid phase, cpx= clinopyroxene crystals formed in equilibrium with silicate melt at experimental conditions, xx(quench)= crystals formed during cooling at the end of the experiment

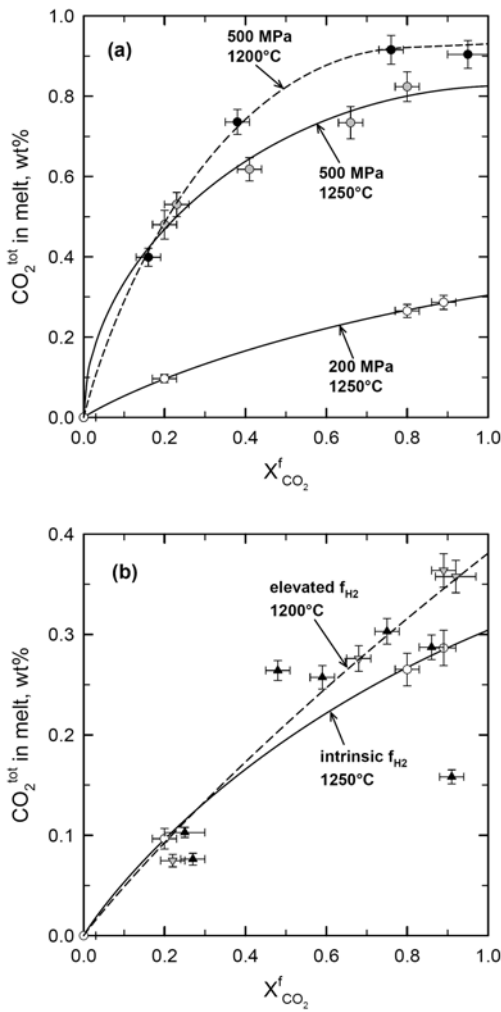


Figure A1.1. Relationship between the mole fraction of  $\text{CO}_2$  in the fluid phase and the concentration of  $\text{CO}_2$  dissolved in the melt (from Misiti et al., 2007). (a) intrinsic  $f_{\text{H}_2}$  of the IHPV. (b) Various  $f_{\text{H}_2}$  at a pressure of 200 MPa. Open circles:  $T = 1250^\circ\text{C}$ ,  $f_{\text{H}_2} \sim 0.02$  MPa; grey triangle down:  $T = 1200^\circ\text{C}$ ,  $f_{\text{H}_2}$  nominal = 0.25 MPa; black triangles up:  $T = 1200^\circ\text{C}$ ,  $f_{\text{H}_2}$  nominal = 2.44 MPa. Lines illustrate the trends at intrinsic  $f_{\text{H}_2}$  (solid) and elevated  $f_{\text{H}_2}$  (dashed). Only sample Alb1H-56 (on the lower right in (b)) deviates from the general trends.

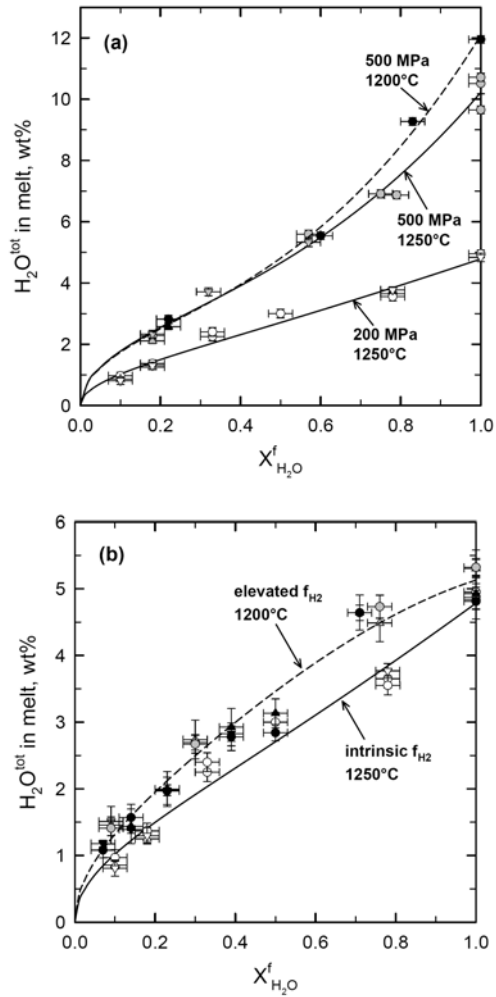


Figure A1.2. Relationship between the mole fraction of  $\text{H}_2\text{O}$  in the fluid phase and the concentration of total water dissolved in the melt at intrinsic  $f_{\text{H}_2}$  (from Misiti et al., 2007). Open symbols:  $1250^\circ\text{C}$ , 200 MPa; grey symbols:  $1250^\circ\text{C}$ , 500 MPa; black symbols:  $1200^\circ\text{C}$ , 500 MPa. The dashed line displays the trend at  $1200^\circ\text{C}$ , 500 MPa. Solid lines show trends at  $1250^\circ\text{C}$ . Circles represent KFT data, triangle down represent MIR data and triangle up represent NIR data. (b) Effect of hydrogen fugacity on the relationship between  $X^f_{\text{H}_2\text{O}}$  and  $\text{H}_2\text{O}_{\text{tot}}$  in the melt at 200 MPa and temperatures of 1200 – 1250°C. Open symbols:  $T = 1250^\circ\text{C}$ ,  $f_{\text{H}_2} \sim 0.02$  MPa; grey symbols:  $T = 1200^\circ\text{C}$ ,  $f_{\text{H}_2}$  nominal = 0.25 MPa; black symbols:  $T = 1200^\circ\text{C}$ ,  $f_{\text{H}_2}$  nominal = 2.44 MPa.

## Appendix A2 to chapter 2

### A2.1. DETAILS ON THE STARTING MATERIALS

#### *Natural pyrrhotites used in experiments*

Sample B originates from a sulphide ore deposit near Bodenmais, Bavaria, Germany. Sample MV is from the massive sulphide deposit Morro Velho (Minas Gerais), Brazil. Sample R is a pyrrhotite from the ore deposit Kisbanya (Herja Mine), Romania. The origin of sample K is unknown. It was obtained from the mineralogical museum of the University of Köln, Germany. Specimens MV and R were kindly provided by the German Geological Survey (BGR, collection numbers: MV: 4289WE; R: 318WE). Handpicked mm-sized crystal pieces were cleaned with dilute HCl to remove surface alteration products, and then ground in an agate mortar to grain sizes of  $< 20 \mu\text{m}$ . The chemical compositions (Table A2.1.) of the hexagonal pyrrhotites (K and B) were also determined by XRD using the calibration of Yund and Hall (1969). These analyses gave slightly higher Fe concentrations compared to the EMPA results, similar to findings reported by Clemente (1998).

Table A2.1. Chemical compositions of natural pyrrhotites used as starting materials.

sample	MV	B	K	R
<i>EMPA</i>				
n	9	9	9	9
(wt%)				
Fe	59.10 $\pm$ 0.30	59.50 $\pm$ 0.15	59.50 $\pm$ 0.21	59.42 $\pm$ 0.17
S	40.90 $\pm$ 0.78	40.50 $\pm$ 0.05	40.18 $\pm$ 0.06	40.58 $\pm$ 0.86
(at%)				
Fe	45.34 $\pm$ 0.54	45.75 $\pm$ 0.06	46.09 $\pm$ 0.08	45.67 $\pm$ 0.52
S	54.64 $\pm$ 0.55	54.24 $\pm$ 0.08	53.93 $\pm$ 0.08	54.32 $\pm$ 0.52
Fe:S	0.830 $\pm$ 0.013	0.843 $\pm$ 0.002	0.855 $\pm$ 0.002	0.841 $\pm$ 0.012
<i>XRD</i>				
Fe <sup>S</sup>	n.d.	47.48 $\pm$ 0.13	47.54 $\pm$ 0.13	n.d.
Fe:S	n.d.	0.904 $\pm$ 0.009	0.906 $\pm$ 0.009	n.d.

n Number of electron microprobe analyses. n.d. Not determined. Given uncertainties of microprobe analyses are standard errors (95% confidence level) of the average of n replicate analyses.

\$ Atomic proportion of Fe (at%) of hexagonal pyrrhotites calculated after Yund and Hall (1969) from the  $d_{102}$  peak position determined by XRD.

*Synthetic glasses*

The NSLsyn glass was prepared from a mixture of oxides ( $\text{SiO}_2$ ,  $\text{Al}_2\text{O}_3$ ,  $\text{Fe}_2\text{O}_3$ ) and carbonates ( $\text{Na}_2\text{CO}_3$ ,  $\text{K}_2\text{CO}_3$ ), ground in an agate rotary mill and melted at 1 atm in an open  $\text{Pt}_{90}\text{Rh}_{10}$  crucible at  $1600^\circ\text{C}$  over a time period of about 8 hours. The melt was quenched to glass by rapid cooling of the crucible in a water bath. The glass was then ground, re-melted and quenched to improve its homogeneity. The major element composition of the synthetic glass was analysed by a Cameca SX-100 electron microprobe, with 15 keV accelerating voltage, 6 nA beam current, and a 20  $\mu\text{m}$  electron beam diameter (Table A2.2., NSLsyn dry).

Table A2.2. Chemical compositions of synthetic glasses used as starting materials (EMPA).

(wt%)	NSLsyn (dry)	NSLsyn01	NSLsyn04 <sub>spike</sub>	NSLsyn05	NSLsyn06 <sub>spike</sub>	NSLsyn07
n	8	20	20	30	30	30
$\text{SiO}_2$	75.74±0.28	70.49±0.25	73.97±0.24	73.25±0.16	73.05±0.15	73.00±0.11
$\text{Al}_2\text{O}_3$	10.38±0.08	9.34±0.09	9.56±0.09	9.59±0.06	9.60±0.06	9.68±0.05
$\text{FeO}_{\text{total}}$	4.13±0.19	3.94±0.14	3.36±0.13	3.99±0.11	3.72±0.08	4.16±0.10
$\text{Na}_2\text{O}$	5.28±0.18	4.98±0.15	4.98±0.12	5.06±0.06	4.98±0.05	5.04±0.06
$\text{K}_2\text{O}$	4.65±0.03	4.55±0.10	4.33±0.06	4.39±0.03	4.38±0.03	4.39±0.03
Total	100.19±0.40	93.30±0.39	96.20±0.33	96.27±0.23	95.73±0.20	96.28±0.20
$\text{H}_2\text{O}^*$	n.d.	3.91±0.07	n.d.	n.d.	n.d.	n.d.
$\text{Fe}^{2+}/\Sigma\text{Fe}^{\S}$	0.25±0.02	0.40±0.02	n.d.	0.38±0.02	n.d.	n.d.

	NSLsyn08	NSLsyn09	NSLsyn10	NSLsyn11	NSLsyn12
n	20	20	20	20	20
$\text{SiO}_2$	72.89±0.59	73.15±0.19	72.69±0.45	72.91±0.26	72.81±0.22
$\text{Al}_2\text{O}_3$	9.64±0.20	9.64±0.08	9.61±0.09	9.59±0.08	9.74±0.05
$\text{FeO}_{\text{total}}$	4.04±0.32	3.99±0.11	3.97±0.10	4.23±0.15	4.14±0.13
$\text{Na}_2\text{O}$	5.10±0.14	5.06±0.08	5.10±0.09	5.02±0.08	5.09±0.05
$\text{K}_2\text{O}$	4.40±0.07	4.40±0.03	4.42±0.04	4.42±0.03	4.43±0.03
Total	96.06±0.55	96.24±0.24	95.78±0.60	96.18±0.34	96.21±0.21
$\text{H}_2\text{O}^*$	4.07±0.29	4.11±0.05	3.90±0.05	n.d.	n.d.
$\text{Fe}^{2+}/\Sigma\text{Fe}^{\S}$	n.d.	n.d.	n.d.	n.d.	n.d.

n Number of electron microprobe analyses. Given uncertainties are standard errors (95% confidence level) of the average of n replicate analysis.

\*  $\text{H}_2\text{O}$  determined by Karl Fischer titration (KFT). Given values were corrected for unextracted water during KFT analysis (+0.10 wt%  $\text{H}_2\text{O}$ ) according to Leschik et al. (2004).

§ Determined by wet chemical analysis (see text). Given value is the average of three replicate analyses and the uncertainty is  $1\sigma$  of the average. n.d. Not determined.

To produce hydrous glasses the nominally dry glass was ground in an agate mortar. Between 800 and 900 mg of the mixed powder were sealed together with ~ 4 wt%  $\text{H}_2\text{O}$  in  $\text{Au}_{80}\text{Pd}_{20}$  capsules (6.4 mm outer diameter, ~ 30 mm in length, 0.2 mm wall thickness).

Water loss during welding was avoided by cooling the capsules with liquid nitrogen. The capsules were then placed in a vertically oriented internally heated pressure vessel (IHPV) at 1250°C and 500 MPa for 24 hours to produce a homogeneous melt. The glass obtained after quench was ground to grain sizes of < 20 µm and used as starting material for the isotope exchange and crystallisation experiments.

## A2.2. CHARACTERISATION OF THE RUN PRODUCTS

### *Analytical conditions of electron microprobe analysis*

All microprobe analyses were done on a Cameca SX-100 using 15 keV accelerating voltage. For pyrrhotite analyses we used a focussed electron beam (~1 µm diameter), a beam current of 15 nA and a counting time of 10 s on peak and background for Fe and S. Silicate glasses were analysed with a beam current of 4 nA, an electron beam diameter of 10 µm and a counting time of 5 s for Fe, Al, Si and 2 s for K, Na on peak and background. S was always analysed as the last element of each point analysis and beam current and counting time were increased to 30 nA and 30 s, respectively. It must be noted that routine analyses of sulphur in the glasses were performed consistently at the peak position of sulphate (e.g., Carroll and Rutherford, 1988), because the peak position of the S K $\alpha$  x-rays slightly varied non-systematically with glass composition and run condition. Additionally, the peak was often not well resolved due to generally low S contents of the glasses. This approach may result in slight underestimation (up to 15 %) of the sulphur content for glasses with a relatively high sulphide/sulphate ratio. Nevertheless, comparison of pyrrhotite crystal contents calculated by mass balance of sulphur on one hand, and by mass balance of iron on the other hand, gives no indication of a major underestimation of sulphur concentrations in the glasses.

### A2.3. PHASE SEPARATION AND CORRECTIONS APPLIED TO THE MEASURED ISOTOPIC COMPOSITIONS

Phase separation for isotopic analysis was done by selective dissolution of pyrrhotite with 5M HCl. The ground run products were placed in 7 mL Savillex<sup>®</sup> vials and leached with distilled 5M HCl at room temperature for 48 to 60 hours. After centrifugation for 10 minutes the supernate HCl containing the dissolved pyrrhotite was transferred to a second 7 mL Savillex<sup>®</sup> vial. The residual glass in the first vial was thoroughly washed with ultra pure H<sub>2</sub>O (resistance 18 MΩ) and then completely dissolved in a 3:1 mixture of distilled concentrated HF and HNO<sub>3</sub>. However, together with pyrrhotite small amounts of glass were dissolved by the HCl as well. Leaching experiments of pure glass powder with 5M HCl revealed that 1.90±0.10 % of Fe from the glass is released into the pyrrhotite fraction (Table A2.3). This contamination was found to be insignificant for Fe isotope analysis of the pyrrhotite fraction from the kinetic tracer and the exchange experiments, having a weight-ratio of Fe in pyrrhotite to Fe in glass of about 1:1. The crystallisation experiments, however, are characterised by very low pyrrhotite contents of < 1.5 wt%, corresponding to a weight-ratio of Fe in pyrrhotite to Fe in glass of 1:3, or less. In this case, Fe contamination of the pyrrhotite fraction by the Fe from glass significantly changes the measured <sup>56</sup>Fe/<sup>54</sup>Fe and <sup>57</sup>Fe/<sup>54</sup>Fe ratios of the pyrrhotite fraction.

We performed phase separation experiments to quantify the cross-contamination during the HCl leaching. Mixtures of glass and pyrrhotite - in proportions resembling the exchange experiments and the crystallisation experiments - of known isotopic compositions were leached with 5M HCl (Table A2.4).



Table A2.3. HCl-leaching experiments on pure glasses.

experiment	HCl leaching time (hours)	HCl leachate		Fe dissolved (%)*
		$\delta^{56}\text{Fe}$	$\delta^{57}\text{Fe}$	
<i>starting material</i>				
NSLsyn		$-0.247 \pm 0.049$	$-0.346 \pm 0.071$	
<i>leaching experiments</i>				
NSL1	44	$-0.305 \pm 0.049$	$-0.372 \pm 0.071$	$1.91 \pm 0.10$
NSL2	44	$-0.270 \pm 0.049$	$-0.437 \pm 0.071$	$1.89 \pm 0.10$
NSL3	44	$-0.256 \pm 0.049$	$-0.403 \pm 0.071$	$1.89 \pm 0.10$
<b>Average</b>		<b>-0.277</b>	<b>-0.404</b>	<b>1.90</b>
<i>NSLsyn01 in Au capsule, 500 MPa, 900°C, 24h</i>				
Fe-0	64	$-0.255 \pm 0.049$	$-0.365 \pm 0.071$	

\* Calculated from ICP-OES measurements of Fe concentration in untreated bulk NSLsyn and in the HCl leachate:  $\text{Fe}_{\text{dissolved}} = (\text{cFe}_{\text{leached}}/\text{cFe}_{\text{total in glass}}) \times 100$ .

Those leaching tests representative for the kinetic tracer and the exchange experiments, with relatively high pyrrhotite contents, show that the separated pyrrhotite is isotopically identical to the starting material, within analytical uncertainty (Fig. A3.2.1a), and therefore we did not correct the measured isotopic composition of pyrrhotite. The separated glass fraction, however, shows a significant isotopic contamination with Fe from undissolved pyrrhotite. From the leaching tests we estimate a contamination of Fe from pyrrhotite in the analysed glass fraction of our experimental products of  $28 \pm 13\%$  (Table A2.4). Based on these estimate we corrected the measured  $\delta^{56}\text{Fe}_{\text{glass}}$  and  $\delta^{57}\text{Fe}_{\text{glass}}$  for contamination with residual pyrrhotite (see Table 2.2 for results), e.g. for  $\delta^{56}\text{Fe}_{\text{glass}}$ :

$$\delta^{56}\text{Fe}_{\text{glass}}^{\text{corrected}} = \frac{\delta^{56}\text{Fe}_{\text{glass}}^{\text{measured}} - \delta^{56}\text{Fe}_{\text{pyrrhotite}}^{\text{measured}} \cdot f_{\text{Fe from pyrrhotite}}^{\text{contaminant}}}{1 - f_{\text{Fe from pyrrhotite}}^{\text{contaminant}}} \quad (\text{A2.1})$$

The uncertainties given in Table 2.2 were calculated incorporating upper and lower error bounds of  $f_{\text{contaminant (Fe from pyrrhotite)}}$  ( $0.28 \pm 0.13$ ) and error propagation of uncertainties assigned to the electron microprobe analyses of the glasses (Tables A2.2 and A2.5) and from analytical uncertainties of Fe isotope measurements.

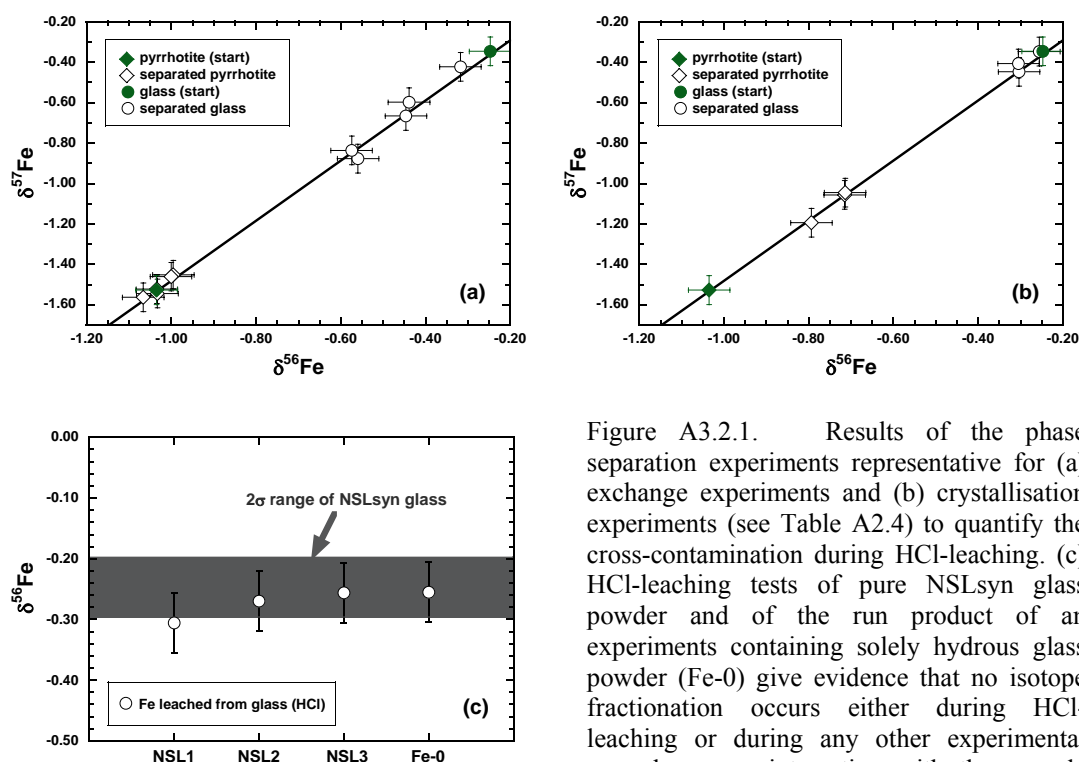


Figure A3.2.1. Results of the phase separation experiments representative for (a) exchange experiments and (b) crystallisation experiments (see Table A2.4) to quantify the cross-contamination during HCl-leaching. (c) HCl-leaching tests of pure NSLsyn glass powder and of the run product of an experiment containing solely hydrous glass powder (Fe-0) give evidence that no isotope fractionation occurs either during HCl-leaching or during any other experimental procedure, e.g. interaction with the capsule material.

For the crystallisation experiments, with low pyrrhotite contents, the results of the separation experiments show a significant isotopic contamination of the pyrrhotite fraction with Fe from the glass (Fig. A3.2.1b). On the other hand, the separated glass is isotopically identical to the starting composition, within analytical uncertainty and therefore, no correction to the measured  $\delta^{56}\text{Fe}_{\text{glass}}$  and  $\delta^{57}\text{Fe}_{\text{glass}}$  values was applied.

The extent of Fe contamination with Fe leached from the glass into the pyrrhotite fraction depends on the pyrrhotite content, which varies in the run products of the crystallisation experiments, and therefore, has to be considered for the corrections. Based on the amount of iron leached from the glass into the pyrrhotite fraction ( $1.90 \pm 0.10$  %, Table A2.3), the Fe concentration in the post-experimental glasses (see Table A2.5) and the pyrrhotite content in the sample, which can be calculated by mass balance compared to the starting glass (Table A2.2, see also expressed as  $f_{\text{Fe transfer}}$  in Table 2.3), we can correct the measured  $\delta^{56}\text{Fe}$  and  $\delta^{57}\text{Fe}$  values of pyrrhotite individually for each experiment, analogue to equation A2.1.

(results see Table 2.3). For experiment C-840-3 (Table 2.3), no thin section for EMPA was prepared. Therefore we estimated the  $\text{FeO}_{\text{total}}$  contents of the post-experimental glass from the other two crystallisation experiments run under similar conditions at 840°C. The uncertainties given in Table 2.3 result from error propagation of uncertainties assigned to the electron microprobe analyses of the glasses before and after the experiments, from analytical uncertainties in Fe isotope measurements by MC-ICP-MS and from the uncertainty in the fraction of Fe leached from the glasses ( $1.90 \pm 0.10$  %).

Table A2.4.. Phase separation experiments on pyrrhotite-glass mixtures

experiment	HCl leaching time (hours)	HCl leachate		residue after HCl leaching		cross contamination*	
		(pyrrhotite fraction)		(glass fraction)		$f$ Fe from glass in pyrr	$f$ Fe from pyrr in glass
		$\delta^{56}\text{Fe}$	$\delta^{57}\text{Fe}$	$\delta^{56}\text{Fe}$	$\delta^{57}\text{Fe}$		
<i>starting materials (from Table 1)</i>							
pyrrhotite B		-1.035	-1.528				
NSLsyn				-0.247	-0.346		
<i>phase separation experiments with glass + 6% pyrrhotite</i>							
P1	44	-1.033	-1.545	-0.560	-0.877	0.2%	39.7%
P2	44	-1.034	-1.523	-0.317	-0.423	0.1%	8.9%
P3	44	-1.066	-1.564	-0.574	-0.837	-4.0%	41.5%
L27	64	-0.995	-1.452	-0.446	-0.666	5.0%	25.3%
L28	64	-1.001	-1.461	-0.439	-0.598	4.3%	24.3%
<b>average</b>						<b>1.1%</b>	<b>28.0%</b>
<b>1-SD</b>						<b>3.7%</b>	<b>13.3%</b>
<i>phase separation experiments with glass + 0.5% pyrrhotite</i>							
P4	44	-0.793	-1.195	-0.303	-0.447	30.7%	7.1%
P5	44	-0.715	-1.057	-0.305	-0.407	40.6%	7.3%
P6	44	-0.714	-1.045	-0.255	-0.347	40.7%	1.1%
<b>average</b>						<b>37.3%</b>	<b>5.2%</b>
<b>1-SD</b>						<b>5.8%</b>	<b>3.6%</b>

\* Calculated from a simple isotope mixing equation, using the starting pyrrhotite and glass as end-members.

For the crystallisation experiments, the corrected  $\delta^{56}\text{Fe}$  values of pyrrhotite differ between -0.02 to -0.07‰ from the uncorrected values (Table 2.3), except for experiments C-1000-1 and C-1000-3, where the correction was -0.27 and -0.28‰, respectively, due to the very low crystal contents in these two samples and therefore a more pronounced

contamination of the pyrrhotite fraction with Fe from the glass. For the kinetic and exchange experiments the differences between corrected and uncorrected  $\delta^{56}\text{Fe}$  values of the glass fraction range from +0.07 to +0.17 (Table 2.2).

To test whether the experimental and analytical procedure causes any iron isotope fractionation that is not due to pyrrhotite-melt interaction we performed a run with pure hydrous glass at 500 MPa and 900°C (Fe-0 in Table A2.3) without any addition of sulphur (as in crystallisation experiments) or natural pyrrhotite (as in exchange experiments). The measured Fe isotope composition of the processed glass of sample Fe-0 is isotopically identical to the starting material within analytical uncertainty (Fig. A3.2.1c). Moreover, the results from HCl leaching experiments of pure glass (Table A2.3) and pyrrhotite-glass mixtures (Table A2.4) indicate no change in Fe isotope composition during phase separation.

Table A2.5. Chemical compositions of silicate glasses and pyrrhotites after experiments.

experiment*	silicate glasses (wt%)							pyrrhotites (at%)				
	n	SiO <sub>2</sub>	Al <sub>2</sub> O <sub>3</sub>	FeO <sub>total</sub>	Na <sub>2</sub> O	K <sub>2</sub> O	S	Total	n	Fe	S	Fe:S
E-840-1	7	73.12 ± 0.27	9.66 ± 0.13	4.23 ± 0.17	4.90 ± 0.20	4.29 ± 0.09	0.050 ± 0.012	96.24 ± 0.12	6	48.02 ± 0.06	51.86 ± 0.02	0.926 ± 0.001
E-840-2	9	72.92 ± 0.37	9.73 ± 0.08	4.15 ± 0.21	4.78 ± 0.19	4.42 ± 0.09	0.049 ± 0.005	96.05 ± 0.46	5	48.33 ± 0.25	51.55 ± 0.29	0.938 ± 0.007
E-840-3	9	73.05 ± 0.32	9.73 ± 0.11	4.13 ± 0.18	4.68 ± 0.06	4.41 ± 0.10	0.070 ± 0.045	96.06 ± 0.23	6	48.03 ± 0.59	51.86 ± 0.57	0.926 ± 0.015
E-840-4S	9	72.50 ± 0.25	9.67 ± 0.10	3.99 ± 0.15	4.75 ± 0.16	4.37 ± 0.09	0.058 ± 0.007	95.34 ± 0.46	2	47.91 ± 0.20	52.00 ± 0.25	0.921 ± 0.006
E-900-1S	10	72.60 ± 0.32	9.79 ± 0.09	3.54 ± 0.10	4.38 ± 0.15	4.29 ± 0.06	0.046 ± 0.007	94.66 ± 0.40	8	47.11 ± 0.13	52.78 ± 0.11	0.893 ± 0.003
E-900-2S	9	74.21 ± 0.39	9.73 ± 0.09	3.76 ± 0.16	5.00 ± 0.09	4.37 ± 0.07	0.034 ± 0.006	97.12 ± 0.37	13	45.44 ± 0.28	54.48 ± 0.30	0.834 ± 0.007
E-900-3S	12	74.28 ± 0.25	9.94 ± 0.10	3.66 ± 0.13	4.89 ± 0.12	4.35 ± 0.07	0.032 ± 0.006	97.14 ± 0.25	10	45.71 ± 0.55	54.20 ± 0.56	0.843 ± 0.013
E-900-4S	6	72.08 ± 0.29	9.72 ± 0.13	3.96 ± 0.06	4.63 ± 0.26	4.39 ± 0.11	0.077 ± 0.006	94.85 ± 0.57	8	47.16 ± 0.32	52.75 ± 0.31	0.894 ± 0.008
E-900-1	6	72.21 ± 0.56	10.30 ± 0.15	4.82 ± 0.18	5.37 ± 0.10	4.75 ± 0.08	0.022 ± 0.006	97.47 ± 0.72	7	48.25 ± 0.30	51.68 ± 0.30	0.933 ± 0.008
E-900-2	12	72.12 ± 0.29	9.67 ± 0.10	4.09 ± 0.09	4.75 ± 0.20	4.38 ± 0.06	0.054 ± 0.006	95.07 ± 0.41	8	47.14 ± 0.20	52.79 ± 0.17	0.893 ± 0.005
E-900-3	10	72.33 ± 0.26	9.73 ± 0.12	4.21 ± 0.11	4.76 ± 0.15	4.37 ± 0.08	0.064 ± 0.006	95.46 ± 0.36	6	46.69 ± 0.44	53.22 ± 0.39	0.877 ± 0.010
E-1000-1	8	71.79 ± 0.18	9.75 ± 0.09	5.37 ± 0.25	4.81 ± 0.25	4.40 ± 0.10	0.146 ± 0.006	96.28 ± 0.38	5	48.14 ± 0.43	51.80 ± 0.47	0.929 ± 0.012
E-1000-2	8	73.44 ± 0.52	9.82 ± 0.08	5.12 ± 0.33	5.15 ± 0.25	4.44 ± 0.05	0.038 ± 0.006	97.99 ± 0.47	5	49.05 ± 0.03	50.87 ± 0.10	0.964 ± 0.002
E-1000-3S	16	71.46 ± 0.30	9.58 ± 0.06	5.67 ± 0.17	4.81 ± 0.10	4.27 ± 0.07	0.177 ± 0.006	95.96 ± 0.29	5	48.89 ± 0.24	51.11 ± 0.25	0.957 ± 0.007
E-1000-4S	8	71.58 ± 0.90	9.61 ± 0.09	5.25 ± 0.29	4.94 ± 0.25	4.32 ± 0.10	0.129 ± 0.006	95.83 ± 0.79	3	48.78 ± 0.23	51.15 ± 0.29	0.954 ± 0.007
C-840-1	9	74.10 ± 0.41	9.88 ± 0.06	3.29 ± 0.26	4.67 ± 0.11	4.41 ± 0.08	0.059 ± 0.006	96.41 ± 0.30			n.d.	
C-840-2	5	73.53 ± 0.20	9.78 ± 0.19	3.64 ± 0.28	4.84 ± 0.06	4.40 ± 0.04	0.065 ± 0.006	96.26 ± 0.57			n.d.	
C-900-1	10	71.76 ± 0.48	9.93 ± 0.11	3.54 ± 0.30	4.49 ± 0.14	4.37 ± 0.05	0.069 ± 0.006	94.16 ± 0.48			n.d.	
C-900-2	8	73.17 ± 0.43	9.84 ± 0.10	3.43 ± 0.19	4.62 ± 0.07	4.34 ± 0.04	0.072 ± 0.006	95.47 ± 0.43			n.d.	
C-900-3	10	73.40 ± 0.19	9.95 ± 0.10	3.75 ± 0.14	4.61 ± 0.13	4.40 ± 0.06	0.049 ± 0.006	96.15 ± 0.29			n.d.	
C-900-4	10	71.73 ± 0.41	9.80 ± 0.12	3.79 ± 0.15	4.55 ± 0.14	4.42 ± 0.04	0.070 ± 0.006	94.37 ± 0.44			n.d.	
C-1000-1	10	72.62 ± 0.20	9.74 ± 0.10	3.94 ± 0.19	4.86 ± 0.18	4.42 ± 0.06	0.061 ± 0.006	95.64 ± 0.36			n.d.	
C-1000-2	4	75.01 ± 0.97	9.95 ± 0.05	4.09 ± 0.13	5.19 ± 0.10	4.47 ± 0.10	0.032 ± 0.006	98.74 ± 0.89			n.d.	
C-1000-3	10	72.47 ± 0.27	9.76 ± 0.11	4.12 ± 0.18	4.87 ± 0.15	4.41 ± 0.05	0.073 ± 0.006	95.71 ± 0.38			n.d.	

n Number of electron microprobe analyses. n.d. Not determined. Given uncertainties are standard errors (95% confidence level) of the average of n replicate analyses.

\* See Tables 2.1 and 2.2 for starting compositions, runtimes and temperatures of the experiments. The chemical compositions of the starting glasses are given in Table A2.2.

## A2.4. IRON ISOTOPE COMPOSITIONS OF NATURAL SULPHIDES

Sulphide mineral separates (mainly pyrrhotites) from various locations (Table A2.6.) were analysed for their iron isotope composition following the analytical protocol described in chapter 2.2.3. Mineral separates were produced by handpicking under a binocular microscope. Some sulphide fractions were further purified by density liquid separation using methylene iodide (density = 3.3 g/cm<sup>3</sup>). Each mineral separate was analysed by powder x-ray diffraction for mineral identification. The results are given in Table A2.7 and Figures A2.2 and A2.3.

Table A2.6. Background information on natural sulphide samples.

sample abbreviation	locality	sample source <sup>a</sup> and number	sulphide genesis	ref.
K	<i>unknown</i>	Institut für Mineralogie, Uni Köln	<i>unknown</i>	-
R	Kisbanya (Romania), Herja Mine	BGR: WE 318 Schr. 389 L10	hydrothermal, pyrrhotite mineralisation at ~300°C	(1)
A-1	St. Andreasberg (Germany, Harz Mountains)	BGR: 265 WE	hydrothermal	(2)
MQ	Okehampton (GB), Meldon Quarry	BGR: 323 WE	hydrothermal (280-380°C)	(2)
WBE	Erzberg (Austria, Steiermark)	BGR: WBE	hydrothermal, sediment related	(2)
BW	New Brunswick (Canada), Base Metal Zone	BGR: Brunswick 13	volcanogenic-hydrothermal (black smoker), ~300°C	(2)
MV-1	Morro Velho, Nova Lima (Brazil), Minas Gerais	BGR: 4289 WE	hydrothermal; several mineralisation generations exist,	(2,3)
MV-2	Morro Velho, Nova Lima (Brazil), Minas Gerais	BGR: Putzer Nr.: 9	represented by MV-1 (first hydrothermal generation), MV-2 (main lode, first hydrothermal generation), MV-3	
MV-3	Morro Velho, Nova Lima (Brazil), Minas Gerais	BGR: Putzer Nr.: 10	(Passagem, first hydrothermal generation) and M-4	
MV-4	Morro Velho, Nova Lima (Brazil), Minas Gerais	BGR: (collection U. Vetter)	(second hydrothermal generation); later ov	
B	Bodenmais (Germany, Bayern)	Institut für Mineralogie, Uni Hannover	metamorphic: 650-750°C, 200-500 MPa	(4)
T	Trojan mine (Zimbabwe)	BGR: TN	magmatic, mafic, later metamorphosed	(2)
SP	Selebi-Phikwe (Botswana)	BGR: SP-14	magmatic, mafic layered intrusion, later metamorphosed	(2)
CM	Sudbury (Canada, Ontario), Craig Mine	BGR: SUD-CR-01	magmatic, mafic layered intrusion, later metamorphosed	(2)
GD	Great Dike (Zimbabwe), Hartley Mine (MSZ)	BGR: GD-4-CC	magmatic, mafic layered intrusion, later metamorphosed	(5)
HG	Bad Harzburg (Germany), Bärenstein quarry	BGR: HG02	magmatic, mafic	(2)
S	Sohland (Germany, Sachsen)	BGR: Putzer Nr.: 99	magmatic, mafic	(2)
BU	Bühl/ Weimar (Germany)	BGR: 315 WE	magmatic, basalt intrusion in coal bed	(2)

<sup>a</sup>BGR: Bundesanstalt für Geowissenschaften und Rohstoffe, Hannover, Germany

References: (1) Cook and Damian (1997), Huber and Muresan (1996); (2) Melcher, F. and Vetter, U. (BGR, pers. comm.); (3) Lobato et al. (2001); (4) Boctor (1980), Blumel and Schreyer (1977); (5) Oberthür (2003)

Table A2.6. Fe isotope compositions of natural iron sulphide samples.

sample	mineral separate <sup>a</sup>	individual analyses <sup>b</sup>		averages			
		$\delta^{56}\text{Fe}$	$\delta^{57}\text{Fe}$	$\delta^{56}\text{Fe}$	2SD	$\delta^{57}\text{Fe}$	2SD
CM	pyrrhotite (m)	-0.383	-0.548	-0.379	0.046	-0.571	0.051
		-0.401	-0.598				
		-0.355	-0.568				
BU	pyrrhotite (h)	-0.332	-0.491	-0.397	0.102	-0.593	0.148
		-0.455	-0.666				
		-0.387	-0.594				
		-0.413	-0.620				
GD	60% pyrrhotite (m), 30% pentlandite, 10% chalcopyrite	-0.307	-0.454	-0.258	0.087	-0.390	0.111
		-0.245	-0.360				
		-0.223	-0.356				
HG	97% pyrrhotite (h), 3% clinopyroxene	-0.003	0.027	-0.001	0.026	0.011	0.053
		-0.009	-0.026				
		0.004	0.030				
		-0.014	-0.008				
		0.019	0.032				
S	30% pyrrhotite (m), 70% plagioclase, <1% chalcopyrite + magnetite	-0.052	-0.040	-0.088	0.069	-0.118	0.149
		-0.066	-0.071				
		-0.122	-0.161				
		-0.113	-0.198				
K	pyrrhotite (h)	-0.345	-0.498	-0.369	0.037	-0.526	0.047
		-0.391	-0.530				
		-0.366	-0.507				
		-0.385	-0.558				
		-0.360	-0.535				
B	pyrrhotite (h)	-1.065	-1.554	-1.035	0.084	-1.517	0.134
		-1.076	-1.589				
		-1.007	-1.440				
		-0.991	-1.485				
R	pyrrhotite (m)	-0.725	-1.077	-0.720	0.022	-1.064	0.030
		-0.727	-1.057				
		-0.724	-1.045				
		-0.704	-1.075				

*continued on next page*

Table A2.6. - continued.

sample	mineral separate <sup>a</sup>	individual analyses <sup>b</sup>		averages			
		$\delta^{56}\text{Fe}$	$\delta^{57}\text{Fe}$	$\delta^{56}\text{Fe}$	2SD	$\delta^{57}\text{Fe}$	2SD
MV-1	pyrrhotite (m)	-0.733	-1.106	-0.727	0.069	-1.063	0.107
		-0.758	-1.079				
		-0.690	-1.003				
MV-2	pyrrhotite (h)	-0.486	-0.754	-0.484	0.014	-0.733	0.429
		-0.477	-0.709				
		-0.490	-0.736				
MV-3	pyrrhotite (m)	-0.232	-0.327	-0.239	0.021	-0.343	0.046
		-0.247	-0.359				
MV-4	pyrrhotite (m)	-0.469	-0.651	-0.472	0.010	-0.650	0.003
		-0.476	-0.649				
MQ	pyrrhotite (m)	-0.411	-0.616	-0.422	0.019	-0.610	0.028
		-0.428	-0.594				
		-0.426	-0.619				
A-1	pyrrhotite (m)	-0.222	-0.391	-0.244	0.064	-0.397	0.018
		-0.267	-0.403				
BW	90% pyrrhotite (m), 10% chalcopyrite	-1.028	-1.545	-1.025	0.017	-1.525	0.050
		-1.015	-1.497				
		-1.031	-1.534				
WBE	70% pyrrhotite (m), 25% pyrite, <5% sphalerite	-1.112	-1.658	-1.087	0.049	-1.605	0.088
		-1.101	-1.621				
		-1.074	-1.558				
		-1.059	-1.585				

<sup>a</sup> Modal composition of each mineral separate estimated from x-ray powder diffraction pattern. Monoclinic (m) or hexagonal (h) pyrrhotite crystal structure indicated in parentheses.

<sup>b</sup> Individual analyses of at least two independent sample dissolutions and chromatographic Fe separations.



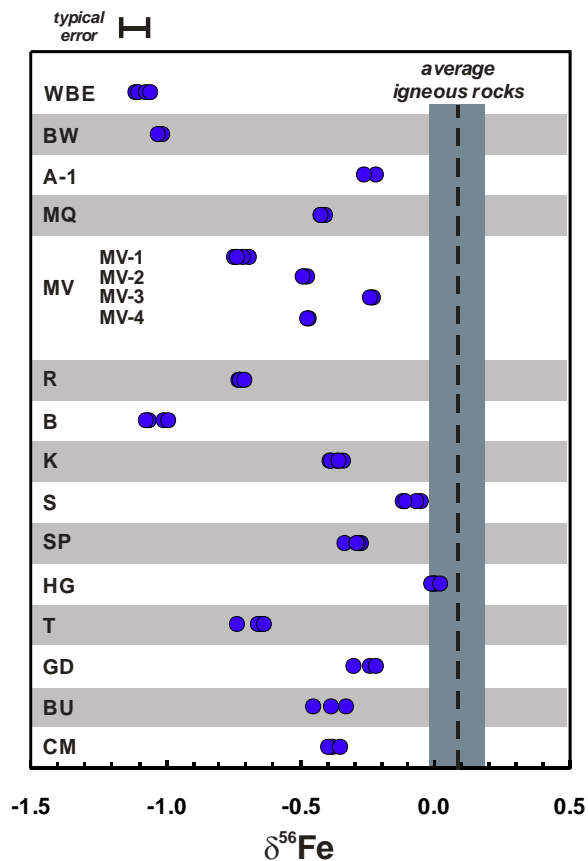


Figure A2.2. Summary of individual Fe isotope analyses of natural sulphide mineral separates (Table A2.6). The vertical dashed line represents the average igneous rock Fe isotope composition as defined by Beard et al. (2003a).

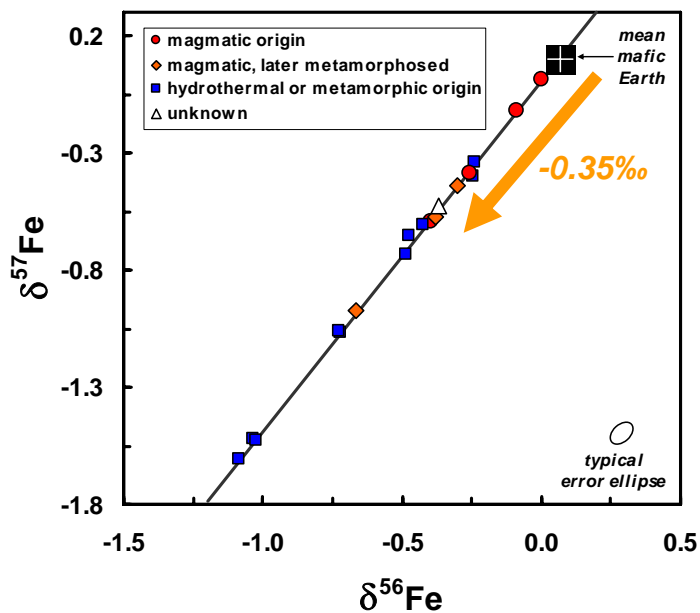


Figure A2.3. Three isotope plot comparing the Fe isotope composition of sulphides of different origin. Solid line is the mass dependent isotope fractionation line. Mean mafic Earth Fe isotope composition from Poitrasson et al. (2005). The arrow represents the experimentally determined Fe fractionation factor  $\Delta^{56}\text{Fe}_{\text{pyrrotite-melt}} = -0.35\text{‰}$ .

## Appendix A3 to chapter 3

### A3.1. IRON ISOTOPE ANALYSES OF REFERENCE MATERIALS

Table A3.1. Comparison of published Fe isotope data of reference materials.

Reference material	$\delta^{56}\text{Fe}$	2SD	$\delta^{57}\text{Fe}$	2SD	Reference
BHVO-1	0.110	0.110	0.150	0.130	Volkening and Papanastassiou (1989)
	0.117	0.030	0.174		Beard et al. (2003a)
	0.148		0.220	0.130	Beard et al. (2003b)
	0.110		0.164	0.032	Kehm et al. (2003)
	0.110		0.164	0.032*	Poitrasson et al. (2004)
	0.117	0.028*	0.174		Weyer et al. (2005)
	0.085	0.050	0.111	0.086	Schoenberg and von Blanckenburg (2006)
	0.109	0.020*	0.169	0.023*	this study (n=8)
BIR-1	0.054	0.040	0.080		Beard et al. (2003a)
	0.040		0.060	0.200	Beard et al. (2003b)
	0.069		0.102	0.015	Kehm et al. (2003)
	0.054		0.080	0.090	Mullane et al. (2005)
	0.055	0.025*	0.082		Weyer et al. (2005)
	0.060		0.090	0.015*	Poitrasson et al. (2004)
	0.051	0.046	0.063	0.073	Schoenberg and von Blanckenburg (2006)
	0.056	0.019*	0.083		Weyer and Ionov (2007)
	0.053	0.019*	0.085	0.033*	this study (n=8)

\* These values represent 2SE uncertainties (95% confidence). All iron isotope compositions expressed relative to the IRMM-014 standard.

Values without errors were recalculated from  $\delta^{56}\text{Fe}$  or  $\delta^{57}\text{Fe}$ , respectively, assuming mass dependent isotope fractionation.

### A3.2. LITHIUM ISOTOPE ANALYTICS

#### *Li purification chemistry*

Prior to isotopic analyses, we used cation exchange chromatography to purify Li from other matrix elements. A two-step column procedure using different volumes of cation exchange resin (DOWEX AG50W<sup>®</sup> X8, 200-400 mesh) was applied (Fig. A3.1).

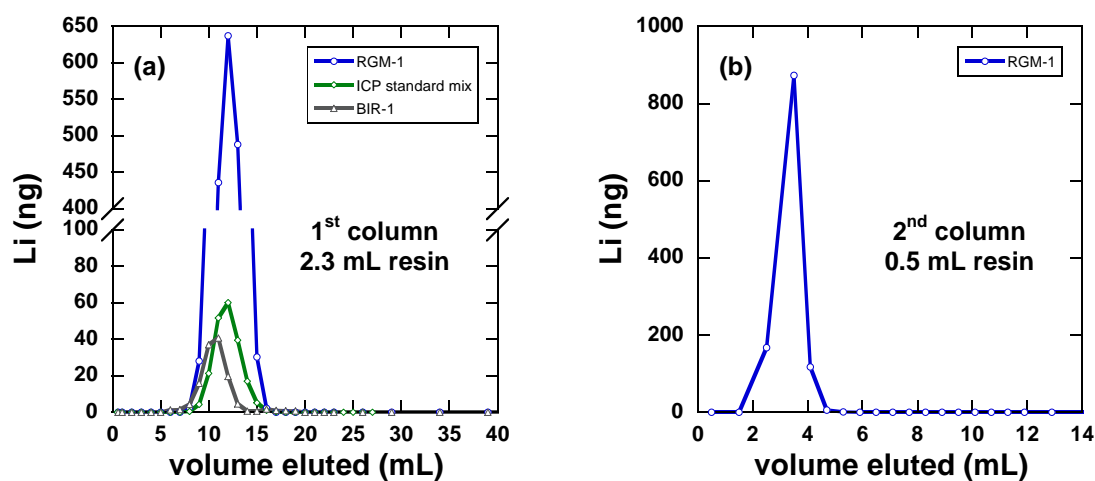


Figure A3.1. Elution curves of Lithium during chromatographic separation. (a) The first column was calibrated using basaltic (BIR-1) and rhyolitic (RGM-1) rock reference materials, and mixtures of ICP standard solutions (containing Li, Al, B, Ba, Ba, Ca, Cd, Co, Cr, Cr, Cu, Fe, Fe, K, Li, Mg, Mn, Na, Ni, Pb, Sr, Tl, Zn). (b) The second column was calibrated using RGM-1.

*Effect of Li concentration matching between samples and bracketing standard*

We analysed pure L-SVEC solutions having Li concentrations from about 20 to 240 ppb Li relative to a bracketing standard with 120 ppb Li. The signal intensities of  ${}^7\text{Li}$  (Volts) measured in the respective Faraday cup were used to calculate the intensity ratio of each solution relative to the L-SVEC bracketing standard ( ${}^7\text{Li}_{\text{sample}}/{}^7\text{Li}_{\text{L-SVEC}}$ ). A range from about 0.2 to 2 was covered (Fig. A3.2). Although, a slight negative correlation may exist, all solutions gave  $\delta^7\text{Li}$  values identical to the L-SVEC standard, within our analytical uncertainty of  $\pm 0.5\text{‰}$ , and even within  $\pm 0.25\text{‰}$ .

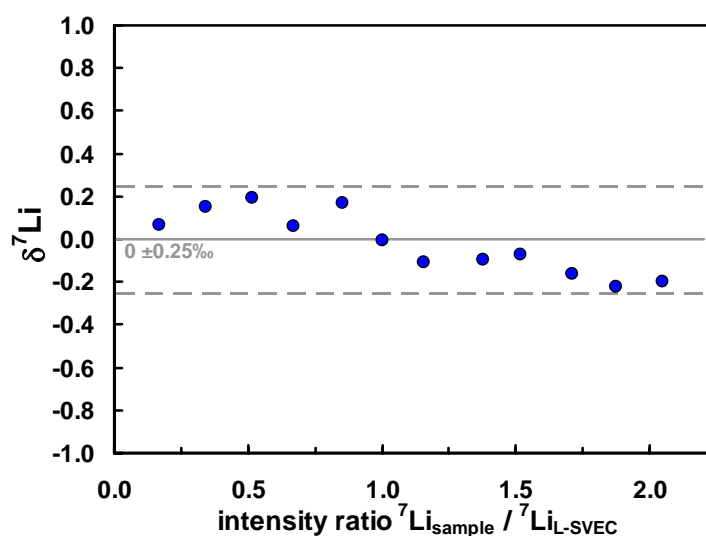


Figure A3.2. Li isotope composition of pure Li L-SVEC solutions (sample) with different Li concentrations relative to the L-SVEC bracketing standard ( $\delta^7\text{Li} = 0$ ).

*Matrix effects on Li isotope measurements*

The influence of matrix elements present in the Li sample solutions on the accuracy of Li isotope measurements by MC-ICP-MS was tested. Pure Li L-SVEC solutions, having Li concentrations of 100 ppb (in 0.3M  $\text{HNO}_3$ ), were doped with different amounts of single elements or element mixtures, that are major constituents of the volcanic rocks analysed in this study (Fig. A3.3). The reported  $\Sigma\text{Element(s)}/\text{Li}$  ratios (Fig. A3.3) of multi-element

solutions were calculated using the sum of all matrix element concentrations (having all equal concentrations from 5 to 165 ppb). In total, a range in  $\Sigma\text{Element(s)}/\text{Li}$  concentration ratios from 0.1 to 25 was covered. All solutions gave  $\delta^7\text{Li}$  values identical to the pure L-SVEC standard, within our analytical uncertainty ( $\pm 0.5\text{‰}$ ).

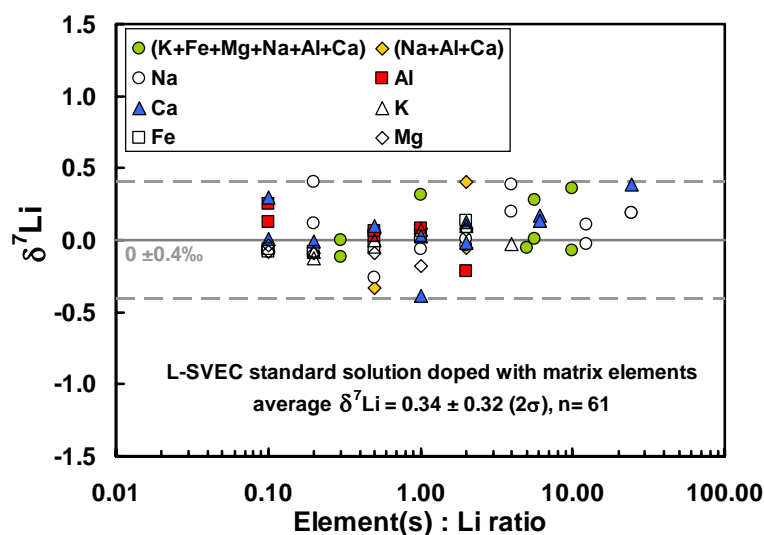


Figure A3.3. Measured Li isotope compositions of matrix-element-doped Li L-SVEC solutions. The dashed lines represent  $\pm 0.4\text{‰}$  relative to the pure Li L-SVEC solution ( $\delta^7\text{Li} = 0$ ).

Table A3.2. Comparison of Li isotope data of international reference materials

Reference material	$\delta^7\text{Li}$	2SD	Reference
BHVO-1	5.31	0.20	Magna et al. (2004)
	5.00	1.60	Bouman et al. (2004)
	5.80	1.60	James and Palmer (2000)
	5.20	0.50	Chan and Frey (2003)
	5.10	1.00	Pistiner and Henderson (2003)
	6.10	1.00	Bryant et al. (2004)
	4.30	1.00	Rudnick et al. (2004)
	4.68	0.16	Rosner et al. (2007)
	4.54	1.02	Aulbach et al. (2007)
	4.40	0.70	Halama et al. (2007)
	5.65	0.55	this study (n=5)
BIR-1	3.90	1.00	Rudnick et al. (2004)
	3.39	0.77	this study (n=9)
RGM-1	2.59	0.15	this study (n=6)

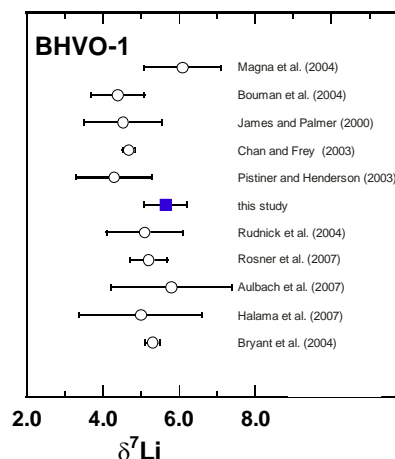


Figure A3.4. Comparison of Li isotope results from different studies for the reference material BHVO-1.

### A3.3. IRON ISOTOPE FRACTIONATION BETWEEN MAGNETITE AND RHYOLITIC MELT

Iron isotope exchange experiments between magnetite and hydrous peralkaline rhyolitic melt were carried out, using a similar approach as described in chapter 2.2. As starting materials mixtures of hydrous glass powder (Table A2.2) and various amounts of magnetite ( $\text{Fe}_3\text{O}_4$ ) or hematite ( $\text{Fe}_2\text{O}_3$ ) were sealed in Au capsules (Fig. A3.5).



Figure A3.5. Photograph of an Au capsule used for isotope exchange experiments.

To monitor the extent of isotopic exchange towards equilibrium some experiments were carried out with  $^{57}\text{Fe}$ -enriched glass and isotopically “normal” magnetite (see chapter 2.2.1.3 for details of this approach). Experiments were carried out in a hydrothermal autoclave (cold seal pressure vessel:  $\text{H}_2\text{O}$ -CSPV) at a pressure of 100 or 200 MPa and a temperature of  $800^\circ\text{C}$  for 164 to 406 hours. The oxygen fugacity in the autoclave was buffered at NNO (Ni-NiO buffer assemblage). The prevailing oxygen fugacity inside the capsules was slightly below NNO, since the melt was water-undersaturated, i.e., the melt contained about 4 wt%  $\text{H}_2\text{O}$ , whereas the maximum solubility is 7.2 wt%  $\text{H}_2\text{O}$  at  $800^\circ\text{C}$ , 200 MPa (Behrens and Jantos, 2001). At these conditions magnetite was a stable phase and

hematite (that was used as starting materials in some charges) recrystallised to magnetite during the runs. Experimental products were glass and magnetite crystals (Fig. A3.6).

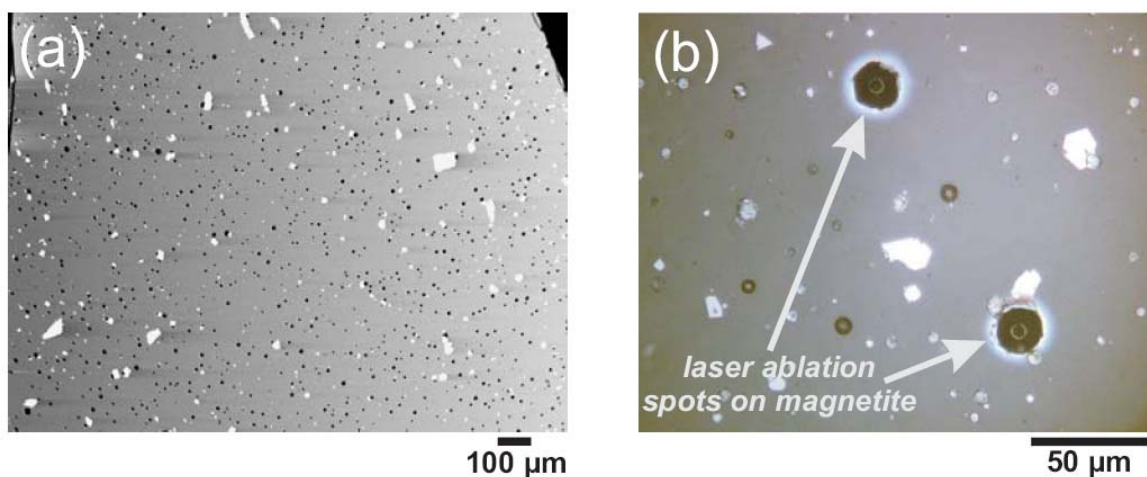


Figure A3.6. (a) Back scattered electron image of a typical experimental run product (sample M8; bright magnetite crystals and vesiculated silicate glass matrix). (b) Reflected light image shows laser ablation Fe isotope analyses spots on magnetite (sample M6).

The Fe isotope composition of the two phases was measured by solution MC-ICP-MS upon selective acid dissolution. Additionally, the Fe isotope composition of magnetite in two samples (M1, M8) was analysed using UV-femtosecond laser ablation coupled to MC-ICP-MS, following the analytical protocol described in Horn et al. (2006). For Fe isotope analyses in solution a similar approach as described in chapter 2.2.3.1 was used: First, magnetite was dissolved in HCl and the virtually magnetite-free glass fraction was then dissolved in HF/HNO<sub>3</sub>. The  $\delta^{56}\text{Fe}$  values of magnetite determined by the two methods are in agreement, although the solution results tend to systematically underestimate the magnetite-glass fractionation factor compared to laser ablation results or mass balance calculations (Fig. A3.7). This can be explained by a slight contamination of the magnetite Fe fraction with Fe from the glass, due to dissolution of very fine grained glass particles by HCl. Therefore, the solution magnetite analyses have to be treated with caution, since their  $\delta^{56}\text{Fe}$  values are probably too high.

Figure A3.7. Fe isotope compositions of starting materials and run products from isotope exchange experiments as a function of experiment duration. Note the change in sign of  $\Delta^{56}\text{Fe}_{\text{mag-melt}}$  values from starting mixtures ( $t = 0$ ) to experimental products.

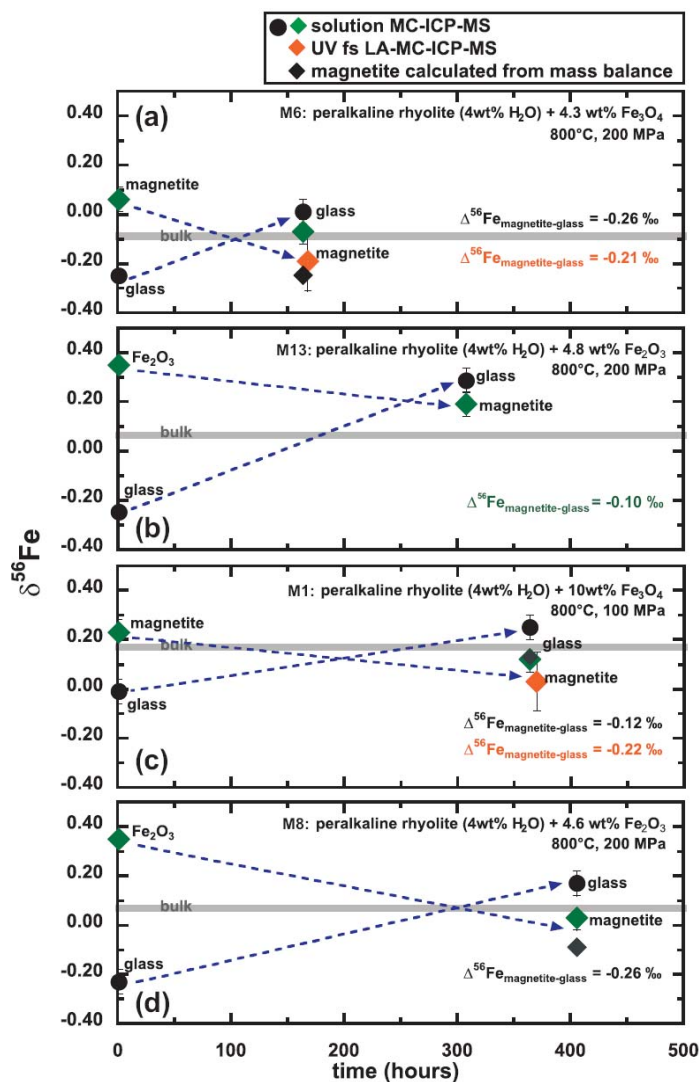
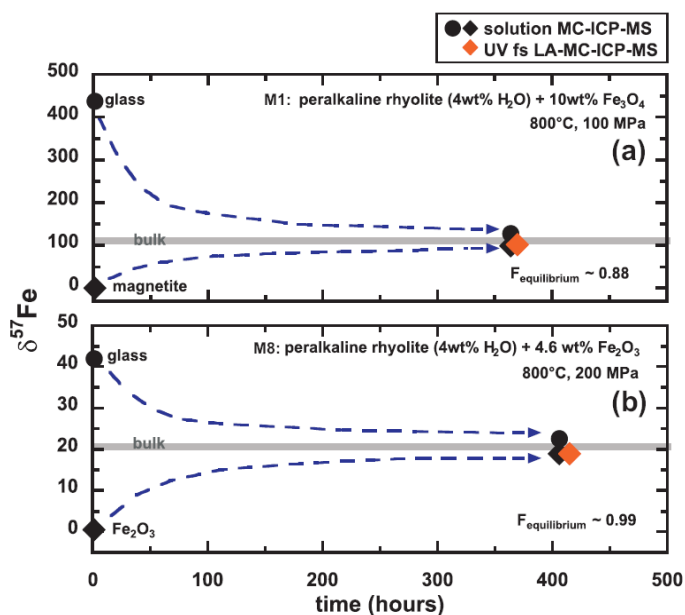


Figure A3.8. Experiments with  $^{57}\text{Fe}$ -enriched silicate glass were used to monitor the extent of Fe isotope exchange. A close approach to equilibrium (grey line) was attained.  $F_{\text{equilibrium}}$  values calculated according to equation 2.5.



Therefore, more experiments are needed with an improved HCl-dissolution technique (i.e., removal of the finest glass fraction before selective dissolution of magnetite with HCl) in combination with *in-situ* laser ablation analyses.

Nevertheless, based on these first experiments important systematics can be reliably obtained. The results consistently show that magnetite preferentially incorporates isotopically light Fe relative to the coexisting rhyolite melt (Fig. A3.7). The isotope exchange experiments done at different run times (Fig. A3.7) and the experiments with  $^{57}\text{Fe}$  enriched glass (Fig. A3.8) indicate that the system is close to isotopic equilibrium. Thus, from the most reliable analytical results (solution values for glass and laser values for magnetite) an equilibrium iron isotope fractionation factor of  $\Delta^{56/54}\text{Fe}_{\text{magnetite-rhyolite melt}} \sim -0.2\text{‰}$  is proposed (Figure A3.9). This is in good agreement with results reported by Huang and Lundstrom (2006) ( $\Delta^{56/54}\text{Fe}_{\text{magnetite-andesite melt}} < -0.26\text{‰}$ ; see chapter 3.5.3).

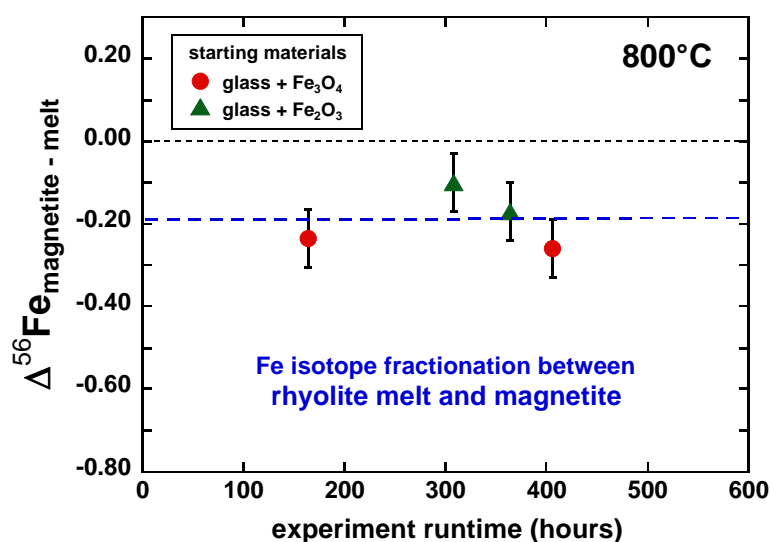


Figure A3.9. Summary of Fe isotope exchange experiments between magnetite and rhyolite melt at 800°C as a function of experiment runtime. Magnetite preferentially incorporates isotopically light Fe relative to the coexisting rhyolite melt.

The specific mechanisms causing the observed fractionation cannot be clearly clarified. However, some important observations can be made from comparison of the results



in the magnetite-melt system to the pyrrhotite-melt system (chapter 2). In the latter, marked contrasts in the ligand and the redox state of Fe between pyrrhotite and the ferric iron-rich silicate melt cause a significant isotope fractionation ( $[\text{Fe(II)-S}]$  vs.  $[\text{Fe(II)/Fe(III)-O}]$ ). In the magnetite-silicate melt system more similar bonding environments and redox states of Fe in both phases ( $\text{Fe}^{2+}/\Sigma\text{Fe}_{\text{pyrrhotite melt}} = 0.55$  vs.  $\text{Fe}^{2+}/\Sigma\text{Fe}_{\text{magnetite}} \sim 0.33$ ) possibly lead to a smaller isotope fractionation. Moreover, in the pyrrhotite-silicate melt system the heavier isotopes are associated with  $\text{Fe}^{3+}$  and the lower Fe coordination (as expected from theory). However, this simple rule does not seem to be applicable in the magnetite-silicate melt system (Fig. A3.10). Hence, mechanisms governing isotope fractionation in mineral-melt systems are probably more complex than expected from simple redox state and coordination considerations.

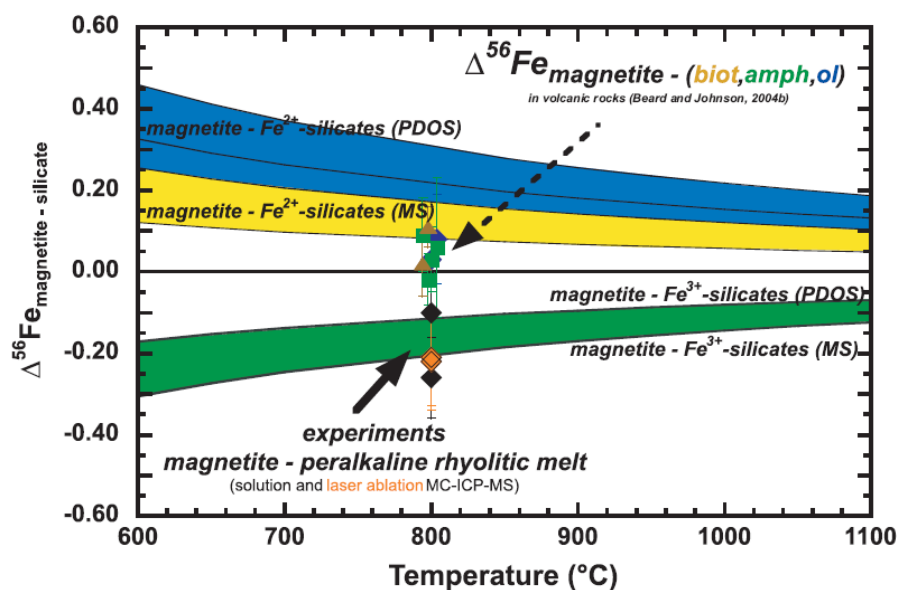


Figure A3.10. Comparison between the results from Fe isotope fractionation experiments and the predicted equilibrium isotope fractionations between magnetite and ferric or ferrous Fe dominated silicate minerals, calculated from Mössbauer (MS) and INRXS (PDOS) data (Polyakov and Mineev, 2000; Polyakov et al., 2007). No fractionation was found between magnetite and silicate minerals in natural volcanic rocks, within analytical uncertainties (Beard and Johnson, 2004b)

## Lebenslauf

### Jan Arne Schüssler

Edenstr. 24

D-30161 Hannover

janschuessler@gmx.de

### Persönliche Angaben

---

Geburtstag, -ort      19. Mai 1979, Stuttgart

Familienstand      verheiratet, 1 Kind

### Schulbildung

---

#### Baden-Württemberg

1985 – 1989 Grundschule Krauchenwies

1989 – 1994 Realschule Liebfrauenschule Sigmaringen

#### Niedersachsen

1994 – 1995 Heinrich-Prüve-Realschule Winsen: Realschul-Abschluss

1995 – 1998 Axel-Bruns-Schule Celle, Fachgymnasium Technik: Abitur

### Hochschulbildung

---

#### *Gottfried Wilhelm Leibniz Universität Hannover*

1999 – 2004      Studium der Geowissenschaften

    Juni 2003      Bachelor of Science im Studiengang Geowissenschaften

    Okt. 2004      Diplom im Studiengang Geowissenschaften

Nov. 2004 – Dez. 2007    Wissenschaftlicher Angestellter/Doktorand  
am Institut für Mineralogie der Leibniz Universität Hannover